MULTI-OBJECTIVE OPTIMISATION OF LOW-THRUST TRAJECTORIES

Federico Zuiani

Submitted in fulfilment of the requirements of the Degree of Doctor of Philosophy

School of Engineering

University of Glasgow

August 2014

Abstract

This research work developed an innovative computational approach to the preliminary design of low-thrust trajectories optimising multiple mission criteria.

Low-Thrust (LT) propulsion has become the propulsion system of choice for a number of near Earth and interplanetary missions. Consequently, in the last two decades a good wealth of research has been devoted to the development of computational method to design low-thrust trajectories. Most of the techniques, however, minimise or maximise a single figure of merit under a set of design constraints. Less effort has been devoted to the development of efficient methods for the minimisation (or maximisation) of two or more figures of merit. On the other hand, in the preliminary mission design phase, the decision maker is interested in analysing as many design solutions as possible against different trade-off criteria.

Therefore, in this PhD work, an innovative Multi-Objective (MO), memetic optimisation algorithm, called Multi-Agent Collaborative Search (MACS2), has been implemented to tackle low-thrust trajectory design problems with multiple figures of merit. Tests on both academic and real-world problems showed that the proposed MACS2 paradigm performs better than or as well as other state-of-the-art Multi-Objective optimisation algorithms.

Concurrently, a set of novel approximated, first-order, analytical formulae has been developed, to obtain a fast but reliable estimation of the main trade-off criteria. These formulae allow for a fast propagation of the orbital motion under a constant perturbing acceleration. These formulae have been shown to allow for the fast and relatively accurate propagation of long LT trajectories under the typical acceleration level delivered by current engine technology.

Various applications are presented to demonstrate the validity of the combination of the analytical formulae with MACS2. Among them, the preliminary design of the JAXA low-cost DESTINY mission to L_2, a novel approach to the optimisation under uncertainty of deflection actions for Near Earth Objects (NEO), and the de-orbiting of space debris with low-thrust and with a combination of low-thrust and solar radiation pressure.

To my parents, Ennia and Fabiano.

To my aunt Cinzia and my uncle Daniele.

To my cousin Piergiorgio.

To my uncle Paolo, my grandparents Margherita, Giuseppina, Luigi and Giuseppe, whom I will never forget.

To my honorary grandmother Bruna.

To my honorary uncle Tito and my honorary aunt Pia

To my friend and former 8, Ruthven Str.-flatmate Massimo.

To the Glaswegian (but mostly Italian) friends: Willem, Luca, Daniele, Simone, Salvatore, Flora, Eirini, Petros, Aldo, Daniel, Camilla, Edmondo, Thomas, Marcel.

To my friends in Udine: Andrea, Filippo, Giuseppe, Marco, Matteo, Riccardo.

To my “Milanese” friends: Pietro, Davide R., Davide M., Marco, Dario and Philipp.

To my “Japanese” friends: Yoshihide, Stefano, Marco, Lucas and Hiroko.

To all those whom my failing memory made me forget to mention here.

And, last but not least, to Beatrice, undisputed Sovereign of my Heart.

I declare that, except where explicitly stated, the work contained in this dissertation is my own.

Federico Zuiani, August 2014.

Contents

List of Figures

List of Tables

List of Acronyms

2PBVP	Two-point, Boundary Value Problem
AAS	American Astronautical Society
AIAA	American Institute of Aeronautics and Astronautics
BPA	Basic Probability Assignment
CPU	Central Processing Unit
DAE	Differential Algebraic Equations
DE	Differential Evolution
DFPET	Direct Finite Perturbative Element Transcription
EP	Electric Propulsion
ESA	European Space Agency
FE	Focal Element
IBSC	Ion Beaming Spacecraft
IES	Ion Engine System
ISAS	Institute of Space and Astronautical Science
JAXA	Japanese Aerospace Exploration Agency
LT	Low-Thrust
MACS	Multi-Agent Collaborative Search
MMO	Memetic Multi-Objective
MO	Multi-Objective
MOID	Minimum Orbit Intersection Distance
MOO	Multi-Objective Optimisation
NEO	Near Earth Object
NASA	National Aeronautics and Space Administration
ODE	Ordinary Differential Equations
OUU	Optimisation under Uncertainty
SEP	Solar-Electric Propulsion
SRP	Solar radiation pressure
TRL	Technology Readiness Level

Acknowledgements

This research was funded through a James Watt Scholarship of the University of Glasgow.

The research work on DESTINY was carried out during a 6.5 months visit at ISAS/JAXA and was funded through the Short-Term Post-doctoral Fellowship of the Japan Society for the Promotion of Science (JSPS).

I am deeply grateful to my supervisor, Prof. Massimiliano Vasile, for his continuous and dedicated support during my Ph.D. It is difficult to quantify how much I learned from him during my years in Glasgow.

I would also like to thank Prof. Kawakatsu Yasuhiro of ISAS/JAXA for his supervision during my stay in Japan. I very much enjoyed working with him on DESTINY.

A special thanks also to Dr. Stefano Campagnola for many useful discussions and suggestions before and during my stay in Japan.

Chapter 1.Introduction

Low Thrust (LT) propulsion systems, delivering a controllable acceleration in the order of 10^{-4}-10^{-5} m/s^2 with a mass flow rate of 10^{-6} to 10^{-8} kg/s, have become the propulsion system of choice for a number of past, current and future space missions. LT propulsion has been proposed for a wide range of applications, from the attitude control of Geosynchronous platforms, to the active removal of space debris, from the exploration of difficult to access targets in the solar system to the deflection of asteroids.

The prospect of an increasing use of LT propulsion in the future comes along with the need to develop new effective and flexible mission design tools. While this need has already been partially satisfied by previous research, there are still a number of open problems that this work is going to address. In particular, this thesis will address the preliminary design of Low-Thrust trajectories that need to be optimal with respect to multiple criteria.

In the early stage of the design of a space mission, scientists and decision makers are interested in exploring as many options as possible and to assess them against a number of criteria. In this phase, therefore, a set of solutions, satisfying multiple, and often conflicting, performance indicators, is required. The exploration of multiple options demands for the quick and reliable evaluation of the performance criteria. In this respect, model fidelity plays a fundamental role as very detailed and accurate solutions are not generally required at this stage but the value of the performance indicators needs to be sufficiently accurate to make reliable decisions. Therefore, the trade-off is between response fidelity and computational cost. The high fidelity design of LT trajectories would require, generally, the numerical solution of an expensive optimal control problem. Models representing the whole thrust arc as a single impulsive change of the velocity are too inaccurate to be applicable to extended LT arcs. Therefore, given the need of evaluating the cost of many LT transfer options, it is desirable to have a low-fidelity model for LT trajectories, which is at the same time realistic and computationally efficient.

This thesis proposes a novel low-fidelity analytical model for the design of low-thrust transfers with constraint conditions at the boundaries of the transfer arc, and a new memetic Multi-Objective solver that delivers sets of Pareto efficient solutions with a contained computational cost.

1.1 Past, Present and Future of Low Thrust Propulsion

From the 60s up to the early 90s the use of LT propulsion was limited to attitude control and station keeping, but since the end of the last century the number of missions which adopted LT as the primary propulsion system is steadily increasing. The first major breakthrough was NASA's technology demonstrator mission Deep Space 1 (1998-2001), which used its NSTAR Ion engine to flyby asteroid 9969 Braille[1]. It was followed in 2003 by JAXA's Hayabusa[2], which performed a rendezvous of asteroid 1998 SF_{36} Itokawa and returned samples to Earth in 2010. Despite some reliability issues with its four μ10 Ion engines and other on-board systems, it was regarded as a great success, since it was the first human-made object to reach an asteroid and return to the Earth. In the same year ESA launched SMART-1, a technology demonstrator, which used Hall Effect thrusters to reach the Moon. A rather exotic spacecraft which also employed ion propulsion, the Gravity Field and Steady-State Ocean Circulation Explorer (GOCE)[3], was also launched by the European Space Agency in 2009 to study the terrestrial gravity field and other atmospheric phenomena. It completed its mission successfully and re-entered the atmosphere after running out of propellant in November 2013.

NASA's Dawn[4,5] is under development and aims at shedding light on the formation of planets by visiting two dwarf planets in the asteroid belt, Vesta and Ceres. It is currently the only space mission bound to enter the orbit of two different extra-terrestrial bodies, something made possible by the high efficiency of its Ion propulsion system. Dawn left Vesta's orbit in July 2012 and is expected to enter Ceres' orbit in early 2015.

Hayabusa-2[6], the follow-on mission of Hayabusa, is expected to be launched in 2014-2015 and will follow a similar mission profile to its predecessor, reaching its target asteroid 1999JU3 in 2018-2019.

BepiColombo[7], a joint effort by JAXA and ESA, will send two orbiters in Mercury's orbit via a Low-thrust Multiple Gravity Assist (LTMGA) trajectory. Launch is planned for 2016 with Mercury's orbit insertion in 2024.

In addition, LT propulsion is being, or has been, considered for a number of future missions, like the cancelled Jupiter Icy Moon Orbiter (JIMO)[8] or JAXA's proposed technology validation mission DESTINY[9], which will also be one of the test applications of this thesis work.

In this thesis, the term "Low Thrust" describes any propulsion system which generates a low but continuous acceleration for extended periods of time. In this sense, it does not refer to any particular class of propulsion devices, but only to relative magnitude of the thrust

acceleration they produce and, therefore, it can apply to a broad class of propulsion methods, as will be seen later.

The term is often associated to Electric Propulsion (EP) technologies, in contrast to "High Thrust" propulsion, commonly associated to liquid or solid rocket engines. Both classes belong to the broader family of non-air-breathing jet engines but while in the latter case the exhaust fluid is accelerated as a result of a chemical reaction (combustion/decomposition followed by gas expansion), in the former the propellant is accelerated by exploiting electrical energy and principles of electromagnetism. EP is characterised by a very low thrust-to-mass ratio. By way of comparison, a state-of-the-art, chemically-propelled Mercury probe such as MESSENGER[10] has a ratio around 0.60 m/s^2 while BepiColombo[7], ESA's planned Mercury probe with Solar Electric Propulsion (SEP), has a ratio in the range of just $7 \cdot 10^{-5}$ m/s^2, or four orders of magnitude smaller than MESSENGER. The low thrust-to-mass ratio is offset by a much higher efficiency of Electric Propulsion compared to chemical propulsion. This is usually measured as the specific force per unit weight of mass flow, or Specific Impulse I_{sp}. In the case of chemical engine, I_{sp} can reach a maximum of 450s in the case of H_2/O_2 combinations while it can be in the range of 1500s for Hall Effect thrusters, 2000-3000s or more for Ion thruster and ongoing research (project VASIMR[11,12] and DS4G[13]) foresees specific impulses up to 20000s. This means that, for the same mass of propellant, the total velocity change (or ΔV) an EP system can provide is much higher than that of a chemical propulsion system.

The velocity change provided by chemical systems is so short compared to the whole transfer time that can be confidently modelled as an *impulse*. On the contrary, LT propulsion systems need to thrust for extended periods of time, compared to the total transfer time, in order to achieve the same velocity change. This has three important consequences: the first is that a longer transfer time is required, the second is that gravity losses are typically higher (a higher total ΔV is required to reach the same target), and the third is that the impulsive approximation is no adequate to correctly model a thrust arc. While chemical trajectories can be decomposed in a finite (and usually small) number of impulsive velocity changes, interweaved with long coasting arcs, in the LT case it is necessary to define a continuous optimal control policy at each time instant. In this sense the complexity of the design of an optimal LT transfer is comparably higher than the design of a multi-impulse transfer.

As pointed out earlier, in this dissertation the term LT is not necessarily restricted just to electrical propulsion, but embraces any propulsion system which generates a low but continuous acceleration for extended periods of time. As it will be seen in another test case,

an example of this is the deflection of asteroids by means of laser ablation, in which the propelling acceleration is produced by the sublimation of the asteroid's surface material irradiated by a high power laser (see Chapter 8).

1.1.1 Low Thrust Trajectory Design

The design of low-thrust (LT) trajectories requires the definition of the thrust profile that satisfies a Two-point Boundary Value Problem (2PBVP). In the literature, the design of low-thrust trajectories has been tackled in a number of different ways[14,15], generally classified in two families: indirect methods and direct methods. Indirect methods [16] translate the design of a low-thrust trajectory into the solution of an optimal control problem and derive explicitly the associated first-order optimality conditions. The first-order optimality conditions are a system of mixed differential-algebraic equations (DAE). Shooting, multiple-shooting, collocation and approximated analytical approaches have been proposed to solve the DAE system and satisfy the boundary conditions.

Direct methods[17,18,19,20] instead, do not derive the optimality conditions but transcribe the differential dynamic equations of motion into a system of algebraic equations and then solve a nonlinear programming problem. Numerical integration and collocation techniques have been proposed to transcribe the differential dynamic equations. Direct methods are generally computationally intensive while indirect methods can display some convergence problems. Both require some form of first guess solution. In the past decade, some low-fidelity approximation techniques have been proposed to generate the first guess solution, based on shaping approaches[21],[22],[23],[24].

No matter which approach is used, the differential equations governing the motion of the spacecraft are generally integrated numerically. Alternatively, albeit in few special cases, an analytical solution is also possible[25]. Some authors have proposed ways to alleviate the computational cost associated with the numerical integration of the dynamics in direct methods by computing approximated analytical solutions. Sims and Flanagan[26], Vavrina and Howell[27] and Yam et al.[28] used an approximation of the continuous thrust profile made of a sequence of impulsive ΔVs and analytically propagated Keplerian arcs.

Analytical solutions have been proposed for the integration of long low thrust, many-revolution transfers. In particular, the works of J.A. Kechichian proposed various analytical or semi-analytical solutions to specific LT trajectory design problems[29,30,31,32,33,34]. Kechichian[31] tackled the problem of the planar, eccentricity-constrained, LT orbit raising, producing a closed form solution for the thrust control which takes advantage of the condition of constant eccentricity. In Ref. 32, instead, Kechichian

dealt with the problem of orbit raising with Earth shadow under tangential thrust and presented a solution in series expansion with respect to the eccentricity for the equations of motion, which is valid up to eccentricities of 0.2. Similarly, in Ref. 33, he treated the problem of optimal inclination change for quasi-circular orbits. Another work[29] reformulated Edelbaum's problem with optimal control and applied the resulting solution to the design of transfers between non-coplanar, circular orbits. Other works[30,34] investigated the problem of LT trajectory optimisation under the effect of the J_2 effect and derived the set of dynamical and adjoint equations for the solution of optimal control problems. Note that, the differential equation are not solved in closed form but integrated numerically. Similarly, Refs. 35 and 36 studied the integrability of the motion under continuous tangential acceleration and derived some interesting closed form solutions, for example for escape spirals.

Kluever also proposed a number of design techniques based on averaging, and in particular in combination with a direct optimisation algorithm[37]. Gao and Kluever[38] proposed an analytical averaging technique on the eccentric anomaly for motion under tangential thrust. The resulting solution depends, however, on the approximate evaluation of elliptic integrals, the accuracy of which decreases with the eccentricity. Geoffroy and Epenoy[39] also investigated the use of averaging techniques to problems under a set of environmental and technological constraints. The latter group includes boundaries on thrust magnitude and direction, while the former encompasses, for example, J_2 perturbation and shadow effects. The resulting generalised method was applied to a number of minimum-time and minimum-fuel optimisation problems. Ferrier and Epenoy[40] proposed a further development of this approach by introducing an improved methodology for treating the shadow effects. The methodology envisions that the discontinuity due to the shadow is handled by introducing two modified optimization problems in which this transition is smoothed, i.e. no longer discontinuous. The authors demonstrated that the solution of the original problem is bounded by those of the two auxiliary problems.

Petropolous et al.[41], proposed a thrust profile derived from a feedback Lyapunov controller, as a function of the mismatch between the current and target values of the orbital parameters. More recently Colombo et al.[42] proposed a semi-analytical solution for the case of tangential thrust, with modulus as a function of distance from the central attractor, which was applied to the Low-Thrust deflection of Near Earth Objects. Bombardelli et al.[43], proposed a first order analytical solution based on perturbation theory for the case of purely tangential thrust. Lantoine and Russell developed an analytical solution to the case of inertial thrust by reformulating the perturbed Two Body problem as

a Stark problem (a well-known problem in quantum physics)[44,45]. Zuiani et al.[46] proposed a first-order analytical solution based on a perturbative expansion of the perturbed Keplerian motion, which will be amply described in this dissertation.

1.1.2 Multi-Objective Optimisation of Low-Thrust Trajectories

While the design and optimisation of low thrust trajectories has generated a vast literature in the past decades, the optimisation with respect to multiple criteria has received less attention. Coverstone-Carroll et al.[47] presented a very interesting methodology, for the Multi-Objective optimisation of interplanetary rendezvous transfers: a genetic algorithm-based Multi-Objective evolutionary algorithm, NSGA[48], generates pairs of departure and arrival dates each defining a 2PBVP, which is then solved with an algorithm implementing an indirect method[49].

Lee et al.[50] further developed the Q-law concept by having an evolutionary algorithm specify the parameters of the feedback law. This methodology was then employed to the Multi-Objective design of LT transfers around the Earth.

Schütze et al.[51] devised a methodology for the Multi-Objective optimisation of Low-Thrust, Multiple Gravity Assist trajectories (LT-MGA), adopting a shaped-based approach and a branch and prune method. The trajectory is modelled in a similar fashion to what is done for impulsive MGAs with the *patched conics*[52] method, although here the Lambert arcs are replaced by exponential sinusoid arcs.

Vasile[53] proposed a novel methodology for the robust design of LT missions, in which uncertainties are modelled by means of Evidence Theory, while a memetic algorithm is used to solve the MOO problem.

1.2 Motivations and Objectives

This dissertation will explore the possibility of applying Memetic Multi-Objective (MMO) optimisation algorithms to the preliminary design of Low Thrust transfers. In this sense, one of key objectives will be that of developing and testing an efficient MMO algorithm. The proposed algorithm is to be assessed both on a standard set of benchmark problems and on a set of specific space-related test problems. At the same time, its performance will also be compared with other state-of-the-art stochastic algorithms. The metrics used to assess the quality of the algorithm will be: the *reliability* in identifying an approximation of the Pareto-optimal set, the *quality* of the approximation (closeness to the actual Pareto set and extent to which the approximation covers the real Pareto set)and the associated *computational cost* measured in function calls. The computational cost, in

particular, is a key issue. Since the cost is measured as the total number of evaluations of the objective function(s), and since each evaluation translates in the propagation of a trajectory, it is desirable to keep the number of evaluations as low as possible and to minimise the computational cost of the propagation. Nevertheless, one has to take into consideration that, even with a high performance algorithm, and with a very simple optimisation problem (small number of design parameters and objective functions, and a very simple problem structure), the total number of function evaluations is likely to be in the range of a few thousand and can rise up to hundreds of thousands or even millions for complex problems. The high number of function evaluation derives from the need to reconstruct a set rather than identifying a single solution.

Therefore, a second key objective will be that of reducing the computational cost of each function evaluation itself, by developing a fast propagation methodology for the LT-perturbed orbital motion.

Finally, since the number of function evaluations required to solve a MOO problem is also linked to the number of design parameters, this research will aim at developing a suitable control parameterisation that reduces the number of control variables while keeping a sufficient degree of flexibility for modelling realistic trajectories.

1.3 Methodology and Expected Results

This dissertation will focus on two main areas of research. The first will be the development of an efficient Multi-Objective optimisation algorithm. A hybrid-memetic approach will be adopted, which combines different heuristics. The selection criteria for candidate solutions will be based in a combination of Pareto optimality and a scalar figure of merit based on Tchebycheff decomposition. The entire population will performed a set of independent, explorative actions, defined *individualistic*, while a subset will interact with each other in order to exploit the most promising solutions found so far (*social* actions). In particular, *social* individuals will always try to improve the scalar Tchebycheff function assigned to each of them. It is expected that the latter feature will considerably improve the quality of the output solutions, by ensuring their uniform distribution on the Pareto front. The performance of the proposed algorithm will be validated on a number of both academic and space related test cases and compared to that of other state MOO algorithms.

The other research path aims at the development of a set of analytical formulae for the propagation of perturbed Keplerian motion. This is achieved by means of a perturbative approach and by introducing some simplifying assumptions on the perturbative

acceleration. The configurations explored include a constant acceleration in the radial-transverse reference frame, a constant tangential acceleration, a constant inertial acceleration and finally a perturbing acceleration of J_2-like behaviour. It is expected to derive a set of formulae for each of these configurations, which describe the first-order evolution of the orbital elements and which will allow for a fast propagation of perturbed trajectory arc. Moreover, it is also envisioned to superimpose the effects of the above mentioned acceleration patterns in order to model more complex thrust and perturbation profiles. It will be shown that the formulae guarantee an adequate accuracy at a lower computational cost compared to numerical propagation methods.

The accuracy of the analytical formulae is inversely proportional to the length of the propagated arc. One remedy proposed in this work is to periodically *rectify* the reference conditions for the analytical formulae. The rectification process implies a higher number of evaluations of the analytical formulae but provides an accurate description of the evolution of the osculating orbital elements and of the LT acceleration pattern.

The other remedy explored in this thesis work is to use the analytical formulae for accurately and efficiently computing the average variation of the orbital elements over a single orbital revolution and then study the evolution of the averaged elements. This approach is particularly suited to the propagation of long, multiple-revolution trajectories.

The combination of low-thrust analytical formulae and memetic Multi-Objective optimisation will be applied to the solution of a range of innovative problems from the disposal of space debris to the deflection of asteroids under uncertainty.

1.4 Thesis Structure

This dissertation is organised as follows: Chapter 2 will present in detail MACS, the MO stochastic algorithm developed by the author. Its performance is assessed on a wide range of test cases and compared to that of other state-of-the-art MOO algorithms.

Chapter 3 introduces the approximate analytical solution for the perturbed Keplerian motion. The derivation of the analytical formulae is presented in detail as well as their numerical accuracy and computational time under a wide range of test propagations. Their performance is compared to a number of numerical integration methods. Some of the analytical expressions, cited in this chapter, are reported in full in Appendix A. A technique for the propagation of long, LT spiralling arcs, based on the *rectification* of the reference conditions for the analytical propagator.

Chapter 4 describes Direct Finite Perturbative Element Transcription (DFPET), a direct transcription method for LT trajectory optimisation, based on the analytical formulae of

Chapter 3. As it will be shown, this allows for a fast solution of 2PBVPs compared to similar, but more computationally expensive, methods. Thanks to this feature, it can be embedded in a MOO instance, for the ΔV vs. time of flight design trade-off for an interplanetary rendezvous transfer, as in the test case presented at the end of the chapter.

Chapter 5 presents methodologies, again based on the analytical formulae, for the propagation and optimisation of long, many-revolution transfers. A technique is proposed for the fast and accurate long-term propagation of LT transfer. This draws inspiration from orbital averaging techniques, but includes the analytical formulae for the short term propagation of the orbital motion along a revolution (see Chapter 5 for more details). A simplified control model is also proposed, which allows for a significant reduction of optimisation parameters, while retaining enough flexibility for describing typical LT many-revolution trajectories.

Chapter 6 presents an interesting test problem, in which a hypothetical Debris removal spacecraft is to rendezvous with and de-orbit a number of different pieces of debris. The objective is that of finding the optimal removal sequence and timing with respect to time and propellant consumption. The problem has been therefore formulated as a MOO problem and solved with MACS. In order to attain a reasonable computational time, the simplified control model described in Chapter 5, together with the *rectification* technique, for the modelling of the trajectory.

Chapter 7 details a “real world” application, in which the methodologies described in the previous chapters are applied to the preliminary mission study for JAXA’s mission DESTINY, a technology demonstrator for interplanetary exploration with LT propulsion.

Finally, Chapter 8 presents an interdisciplinary study, which analyses the problem of deflecting an Earth-threatening asteroid with a space-based, solar-pumped, laser ablation system. Detailed models for the trajectory, system and ablation models will be described. In addition epistemic uncertainties are also introduced and treated by means of Evidence Theory. The complex Multi-Objective design problem that follows, is solved with a variant of MACS, which deals also with uncertain parameters in the objective functions. The deflected trajectory of the asteroid, in fact a LT arc, is modelled and efficiently propagated with the proposed *rectification* technique.

1.5 Contributions

The key contributions of this thesis are:

- The development of a set of analytical formulae for the fast propagation of perturbed Keplerian motion.

- The development of a low-fidelity model for the optimal design of extended thrust arcs with boundary conditions.
- The development of a new efficient Memetic Multi-Objective Optimisation algorithm based on a combination of population-based search and individual neighbourhood exploration.
- The application of the above mentioned techniques to the solution of very challenging mission design problems, from the active removal of space debris to the optimal design of very long low-thrust spirals, to the deflection of asteroids (see Chapter 6, Chapter 7 and Chapter 8).
- The introduction of two new problems in space mission design: the optimal sequential disposal of multiple pieces of debris and the optimisation of asteroid deflection manoeuvres under epistemic uncertainty

The content of this dissertation was published in five journal papers and were presented in seven conference papers and presentations.

Part of the Low Thrust analytical formulation was first presented at the 61st International Astronautical Conference in Prague, Czech Republic in 2010 and subsequently published as a journal article in Acta Astronautica[46]. An extension of the analytical formulation was presented at the 63rd International Astronautical Conference in Naples, Italy in 2012.

An early version of MACS was presented at the 12th Congress on Evolutionary Computation (CEC 2010) in Barcelona, Spain in 2010 and appeared in the Proceedings of the Institution of Mechanical Engineers[54]. The new version, MACS2, described in this dissertation, was first presented at BIOMA2012 in Bohinij, Slovenia[55] and then published in an issue of Computational Optimisation and Applications[56].

The test case of Chapter 6 on the optimisation of debris removal missions was published in the International Journal of Aerospace Engineering[57], while the one on the robust design of asteroid deflection actions in Chapter 8 was presented at the conference “New Trends in Astrodynamics and Applications VI” in New York, U.S.A. in 2011 and then published in the journal Celestial Mechanics and Dynamical Astronomy[58].

The analyses for the preliminary design for DESTINY’s orbit raising (as in Chapter 7) were partially presented at the 23rd AIAA/AAS Space Flight Mechanics meeting in Kauaii, U.S.A., in 2013[59] and an internal report at the end of my JSPS fellowship at ISAS/JAXA[60].

Journal publications

1. Zuiani, F., Vasile, M.: "Multi-Agent Collaborative Search based on Tchebycheff Decomposition", Computational Optimisation and Applications, Vol. 56, No. 1, 189-208 (2013).
2. Zuiani, F., Vasile, M., Gibbings, A.: "Evidence-based Robust Design of Deflection Actions for Near Earth Objects", Celestial Mechanics and Dynamical Astronomy, Vol. 114, No. 1, 107-136 (2012).
3. Zuiani, F., Vasile, M.: "Preliminary Design of Debris Removal Missions by means of Simplified Models for Low-Thrust, Many Revolution Transfers", International Journal of Aerospace Engineering, (2012).
4. Zuiani, F., Vasile, M., Palmas, A. and Avanzini, G.: "Direct Transcription of Low-Thrust Trajectories with Finite Trajectory Elements", Acta Astronautica, Vol.72, March–April 2012, 108-120 (2012).
5. Vasile, M. and Zuiani, F.: "Multi-Agent Collaborative Search: an Agent-based Memetic Multi-Objective Optimization Algorithm applied to Space Trajectory Design", Proceedings of the Institution of Mechanical Engineers, Part G: Journal of Aerospace Engineering, Vol.25, No.11, 1211-1227 (2011).

Conference papers

1. Zuiani, F., Kawakatsu Y., Vasile, M.: "Multi-Objective Optimisation of Many-Revolution, Low-Thrust Orbit Raising for DESTINY Mission", Paper AAS 13-257, 23rd AAS/AIAA Space Flight Mechanics Meeting, Kauaii, Hawaii, U.S.A. (2013).
2. Zuiani, F., Vasile, M.: "Extension of Finite Perturbative Elements for Multi-Revolution, Low-Thrust Propulsion Transfer Optimisation", Paper C.1.4.6, Proceedings of the 63st International Astronautical Congress (IAC2012), Naples, Italy (2012).
3. Vasile, M., Zuiani, F.: "Evidence-based Robust Design Optimisation of Space Systems", EVOLVE2012, Mexico City, Mexico (2012).
4. Zuiani, F., Vasile, M.: "Multi-Agent Collaborative Search with Tchebycheff Decomposition and Monotonic Basin Hopping Steps", BIOMA2012, Bohinij, Slovenia (2012).
5. Zuiani, F., Vasile, M., Palmas, A., Avanzini, G.: "Direct Transcription of Low-Thrust Trajectories with Finite Trajectory Elements", Proceedings of the 61st International Astronautical Congress (IAC2010), Prague, Czech Republic (2010).

6. Vasile, M., Zuiani, F.: “A Hybrid Multi-Objective Optimization Algorithm applied to Space Trajectory Optimization”, Proceedings of the 12th conference on Congress on Evolutionary Computation (CEC 2010), Barcelona, Spain (2010).

Conference presentations

1. Zuiani, F., Gibbings, A., Vasile, M.: “Robust Design of Deflection Actions for Non-Cooperative Targets”, New Trends in Astrodynamics and Applications VI, New York, U.S.A. (2011).

Other

2. Zuiani, F.: “Multi-Objective Optimisation of Many-Revolution, Low-Thrust Orbit Raising for DESTINY Mission”, JSPS short-term fellowship final report (2013).

Chapter 2.Multi Agent Collaborative Search

This chapter presents a novel formulation of Multi Agent Collaborative Search (MACS), for Multi-Objective optimization, based on Tchebycheff decomposition.

The original version of MACS[61,62,54] has been applied to a number of standard problems and real applications with good results, if compared to existing algorithms[53,63,64]. MACS is a hybrid population-based approach that blends a number of heuristics. In particular, the search for Pareto optimal solutions is carried out globally by a population of agents implementing classical social heuristics and more locally by a subpopulation implementing a number of individualistic actions. The reconstruction of the set of Pareto optimal solutions is handled through two archives: a local and a global one.

The individualistic actions were devised to allow each agent to independently converge to the Pareto optimal set, thus creating its own partial representation of the Pareto front. Therefore, they can be regarded as memetic mechanisms associated to a single individual. It will be shown that individualistic actions significantly improve the performance of the algorithm. The Multi-Objective version of MACS[54] also included a modified selection criterion, for both global and local moves, to handle Pareto dominance as well as new heuristics to allow the agents to move towards and along the Pareto front.

The algorithm proposed here (referred to as MACS2) implements some key elements of innovation. Most of the search mechanisms have been simplified, but more importantly in this version Pareto dominance is not the only criterion used to rank and select the outcomes of each action. Instead, agents are using Tchebycheff decomposition to solve a number of single objective optimization problems in parallel.

Furthermore, opposite to previous implementations of MACS, here all agents perform individualistic actions while social actions are performed only by selected sub-populations of agents.

Recent work by Zhang et al.[65] has demonstrated that Tchebycheff decomposition can be effectively used to solve difficult Multi-Objective optimization problems. Another recent example is Sindhya et al.[66], that uses Tchebycheff scalarisation to introduce a local search mechanism in NSGA-II. In this paper, it will be demonstrated how MACS2 based on Tchebycheff decomposition can achieve very good results on a number of cases, improving over previous implementations and state-of-the-art multi-objective optimization (MOO) algorithms.

The new algorithm is here applied to a set of known standard test cases and to two space mission design problems. The space mission design cases consider spacecraft equipped with a chemical engine and performing a multi-impulse transfer. They are part of a test benchmark for multi-impulsive problems that has been extensively studied in the single objective case but for which only a few comparative studies exist in the Multi-Objective case[93].

The chapter is organized as follows: Section 2.1 contains the general formulation of the problem with a brief introduction to Tchebycheff decomposition; Section 2.2 gives an overview of the state of the art; Section 2.3 starts with a general introduction to the multi-agent collaborative search framework and with a description of its first implementation, MACS, underlining the key difference between MACS and MACS2. Section 2.4 will first give a general overview of MACS2 and its heuristics before going into some of the implementation details. Section 2.5 contains a set of comparative tests that demonstrates the effectiveness of the new heuristics implemented in MACS2. The section briefly introduces the performance metrics and ends with the results of the comparison. Finally, Section 2.6 details the hybridisation of MACS2 with Monotonic Basin Hopping (MBH).

2.1 Problem Formulation

Multi-Objective Optimisation (MOO) is a branch of multi-criteria decision making which involves the solution of an optimisation problem in which multiple figures of merits are to be concurrently optimised (minimised or maximised). In mathematical terms this is usually formulated as:

$$\min_{\mathbf{x}\in D} \mathbf{f}(\mathbf{x}) \tag{2.1}$$

where D is the domain for the parameter vector $\mathbf{x}$ and $\mathbf{f}$ is the vector of the m scalar objective functions to be minimised:

$$\mathbf{f}: D \to \mathbb{R}^m, \quad \mathbf{f}(\mathbf{x}) = \begin{bmatrix} f_1(\mathbf{x}) & f_2(\mathbf{x}) & \dots & f_m(\mathbf{x}) \end{bmatrix}^T \tag{2.2}$$

Note that, without loss of generality, from now onwards it will be assumed that all objective functions are to be minimised. The domain D is also assumed to be a hyperrectangle defined as $D = \left\{ x_j \mid x_j \in \begin{bmatrix} b_j^l & b_j^u \end{bmatrix} \subseteq \mathbb{R}, j = 1,\dots,n \right\}$. In a general Multi-Objective optimisation problem, there is no single solution vector $\mathbf{y}$ which minimises all the scalar functions of $\mathbf{f}(\mathbf{x})$ at the same time. However, it will possible to identify a *set* of $\mathbf{x}$ vectors in which none of its members is indisputably better than the others. In a more

rigorous way, this is usually referred to as the Pareto set*, and is defined as the set of the non-dominated solution vectors. The concept of dominance, defines the optimality of a particular solution. With reference to (2.1), one can say that :

$$\begin{gathered} \mathbf{x} \prec \mathbf{y} \\ \Leftrightarrow \\ \left\{ f_l(\mathbf{x}) \le f_l(\mathbf{y}) \quad l = 1,...,m \quad \wedge \quad \exists k \mid f_k(\mathbf{x}) \ne f_k(\mathbf{y}) \right\} \end{gathered} \tag{2.3}$$

where $\mathbf{x} \prec \mathbf{y}$ indicates the statement "**x** dominates **y**". A solution vector in *D* that is not dominated by any other vector in *D* is said to be Pareto optimal. All non-dominated decision vectors in *D* form the Pareto set D_p and the corresponding image in criteria space is the Pareto front. Note that, starting from the concept of dominance, it is possible to associate, to each solution in a finite set of solutions, the scalar dominance index:

$$I_d(\mathbf{x}_i) = \left| \left\{ i^* \mid i, i^* \in N_p \wedge \mathbf{x}_{i^*} \prec \mathbf{x}_i \right\} \right| \tag{2.4}$$

where the symbol |.| is used to denote the cardinality of a set and N_p is the set of the indices of all the solutions. All non-dominated and feasible solutions $\mathbf{x}_i \in D$ with $i \in N_p$ form the set:

$$X = \{ \mathbf{x}_i \in D \mid I_d(\mathbf{x}_i) = 0 \} \tag{2.5}$$

The set *X* is a subset of D_P, therefore, the solution of problem (2.1) translates into finding the elements of *X*. If D_P is made of a collection of compact sets of finite measure in $\mathbb{R}^n$, then once an element of *X* is identified, it makes sense to explore its neighbourhood to look for other elements of *X*. On the other hand, the set of non-dominated solutions can be disconnected and its elements can form islands in *D*. Hence, multiple parallel explorations can increase the collection of elements of *X*.

2.1.1 Tchebycheff Decomposition

In Tchebycheff's approach to the solution of problem (2.1), a number of scalar optimization problems are solved in the form:

$$\min_{\mathbf{x} \in D} \left(g(\mathbf{f}(\mathbf{x}), \boldsymbol{\lambda}, \mathbf{z}) \right) = \min_{\mathbf{x} \in D} \left(\max_{l=1,...,m} \{ \lambda_l \mid f_l(\mathbf{x}) - z_l \mid \} \right) \tag{2.6}$$

where $\mathbf{z} = [z_1, ..., z_m]^T$ is the reference objective vector whose components are $z_l = \min_{\mathbf{x} \in D} f_l(\mathbf{x})$, for $l = 1,...,m$, and λ_l is the *l*-th component of the weight vector $\boldsymbol{\lambda}$. By solving a number of problems (2.6), with different weight vectors, one can obtain different Pareto optimal solutions. Although the final goal is always to find the set X_g, using the

* The term Pareto set is here used to refer to the non-dominated solution set in the domain of the parameter vector **x**. Similarly, the term Pareto front will be used to describe the map of the Pareto set in the space of the objective vector **f**(**x**).

solution of problem (2.6) or index (2.4) has substantially different consequences in the way samples are generated and selected. In the following, the solution to problem (2.6) will be used as selection criterion in combination with index (2.4).

2.2 Related Works

Multi-Objective optimisation problems are widely found in economics[†], finance (e.g. portfolio optimisation) and engineering. Various methodologies have been proposed to solve this mathematical problem. Some simply involve the scalarisation of the minimisation problem by combining the various objective functions through a weighted sum. Thus, the well-established techniques for the solution of single objective problem can be easily applied to the scalarised function[67]. However, different weights also produce different solutions, which means that one has to solve many single-objective problems in order to extract sufficient knowledge of the Pareto set. Other proposals[68,69], extend the techniques of deterministic, gradient-based methods to the multi-criteria case. In similar way to the methods based on scalarisation, these methods too require an arbitrary definition of a search direction on the objectives' space. The main issue with this class of methods is that they lack in global exploration of the search space and, therefore, are likely to converge to locally optimally Pareto sets. At the same time, they also require information on the gradient of the objective functions which, if not available analytically, has to be computed numerically (e.g. by Finite Differences).

Alternative approaches, in the form of Metaheuristics have been successfully applied to Multi-Objective problems. The term Metaheuristics defines a wide class of techniques to solve optimisation problem and are characterised as being *non-deterministic*, in the sense that they rely on some form of randomisation to guide the search for solutions; in general, they do not rely on specific assumptions on problem structure and, therefore, are not problem-specific, at least on principle.

Metaheuristics and in particular the subclass Evolutionary Algorithms have been first proposed in the 60s and since then have been successfully applied to Single Objective optimisation problems. While a rigorous definition of the class of Evolutionary Computation is beyond the scope of this dissertation, it is still possible to identify the main common points. All algorithms in this class are characterised by:

- A *population* of candidate solutions, usually referred to as *agents* or *individuals.*

[†] The concept of Pareto dominance was originally proposed by the Italian economist Vilfredo Pareto at the beginning of the 20th Century.

- The population is progressively modified through a set of evolutionary mechanisms, which can be inspired from a wide range of phenomena, from physical (e.g. Simulated Annealing[70]), macro- (e.g. Ant Colony Optimisation, Particle Swarm Optimisation) or micro-biological (e.g. Genetic Algorithms).
- A *heuristic* is used to select good candidate solutions.
- The *knowledge* is inherited by the next generation.

Algorithms in this family are be broadly classified into:

- Genetic/Evolutionary Algorithms, which typically apply the genetic heuristics of mutation, cross-over and recombination to a set of binary-coded or real valued chromosomes.
- Evolutionary Strategies, which generate new candidate solutions through a combination of evolution a probabilistic model. See for example the well-known Differential Evolution and its derivatives [71, 72], or the Covariance Matrix Adaption Evolutionary Strategy (CMA-ES)[73].
- Swarm-based Intelligence, in which the population is evolved in the search space by mimicking the behaviour of swarms normally found in biology; the most famous representatives of this class are the Particle Swarm Optimisation (PSO)[74] and the Ant Colony Optimisation (ACO)[75].

Early examples of Multi-Objective evolutionary algorithms were obtained by modifying some of the above mentioned algorithms, usually by introducing selection and archiving criteria based on Pareto dominance[76,77,78]. The focus of current developments is mainly oriented towards improving the overall efficiency of the algorithms by adding mechanisms which address specific issues in algorithms behaviour (e.g. global exploration, local search, stagnation). The results of this effort are Hybrid Memetic Algorithms, a superclass in which different heuristics and metaheuristics, both deterministic and stochastic, are merged together[79]. In most cases, they aim at improving local search by combining stochastic-based, global exploration with gradient-based methods[80,81,66]. Lara et al.[82] proposed an innovative local search based on mathematical programming. Rigoni and Poles [83] hybridised an Evolutionary Algorithm with a Normal Boundary Intersection (NBI) technique. Another fairly successful algorithm, MOEA/D[65], combines Differential Evolution and a selection criterion based on Tchebycheff Decomposition.

2.2.1 Structure of an Evolutionary Algorithm

A detailed background on Evolutionary computation is beyond the scope of the present dissertation and is widely available in the relevant literature[84,85]. However, it has been

chosen to devote this section to the description of a generic stochastic algorithm in order to help the reader in understanding the detailed algorithmic description of MACS2, which appears in this chapter. In the typical evolutionary algorithm one finds a set P, usually called *population*, which collects a fixed, finite number of *agents* or *individuals*. Each individual is assigned with one candidate solution vector $\mathbf{x}$ of the problem to be solved (see Eq. (2.1)), and also the related value of the objective function $\mathbf{f}(\mathbf{x})$. The population is evolved in a number of discrete steps, commonly called *generations* or also *iterations*, in order to find the set of $\mathbf{x}$ which best solves Problem (2.1). Although the actions performed at each generation to evolve the population can vary widely depending on the specific operations, one can nevertheless identify the most recurring set of actions, as shown in Figure 2.1

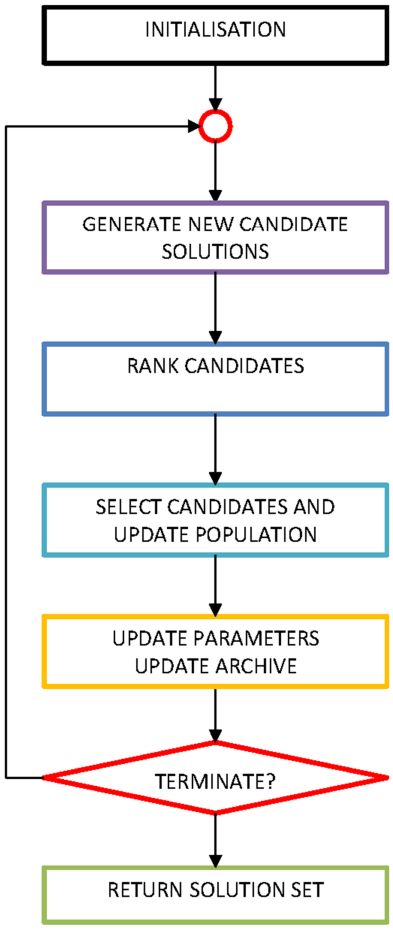

Figure 2.1: Flowchart of a typical sthocastic algorithm.

The first step consists in the initialisation of the algorithmic iterations. The initial population P_0 is generated, normally by random sampling in the solution domain D. Also, some adaptive parameters which govern the evolution of the population are also initialised at this stage. After the initialisation, the iterative process starts. In the single iteration the first action involves the generation of a set of candidates solutions, with which to

eventually replace some or all the individuals of the current population P_k. The strategy, with which the candidates are generated and selected, is the core feature of each algorithm and the factor which more than others determines its performance. Therefore, all sorts of heuristics can be found in the literature, and they can generically be summarised as follows:

$$\mathbf{y}_i = F\left(\mathbf{x}_i, \mathbf{x}_{j/\,j\neq i}, \mathbf{p}^k, \mathbf{e}\right) \tag{2.7}$$

which means that, each candidate solution $\mathbf{y}_i$ (*child* of *offspring*), meant for replacing the agent $\mathbf{x}_i$ (also called *parent* in this case), can be a function of:

- its parent, $\mathbf{x}_i$.
- one or more other members $\mathbf{x}_j$ of the population P_k.
- a set of algorithmic parameters $\mathbf{p}^k$, which can either be constant or be *adapted* iteration by iteration.
- a set of one or more random numbers $\mathbf{e}$.

While the dependancy of $\mathbf{y}_i$ on the stochastic component $\mathbf{e}$ and on $\mathbf{p}^k$ is almost always present, the child might not always depend from its parent or from other elements of the population. For example when the *child* only from $\mathbf{e}$ and $\mathbf{p}^k$ one has a simple random sampling. In addition, each parent can generate more than one offspring.

The following step, involves the *ranking* of the candidate solutions according to a specific performance metric. For MOO, this is typically done with the dominance index, but other criteria have been proposed, like the Tchebycheff scalarisation presented here. Also, the choice of the subset on which the ranking is performed might considerably affect the evolution of the population. For example, one can simply rank the children against their own parent individual. On the opposite, one could rank the entire set of candidate solutions against the entire current population P_k.

After the ranking, one has to select the candidates which will contribute to form the new population P_{k+1}. In most cases, one might simply choose to replace a number of the worst individuals in P_k with a similar number of the best candidates. However, one might for example also choose to preserve some of the worst individuals, if these are in less crowded areas of the domain D, in order to keep enough diversity in the population.

In the final step of an algorithmic iteration, the set of parameters $\mathbf{p}^k$ is updated according to an arbitrary rule. If present, the archive A_g might also be updated at this stage. The archive is a set which is specifically meant for storing the current best approximation, of the solution to Problem (2.1). In MOO, the archive will usually collect all the non-dominated solutions found so far.

At the end of the iteration, a termination condition is evaluated to decide whether to exit the algorithm. The criteria normally adopted normally check whether a maximum number of iterations or function evaluations has been exceeded.

2.3 The MACS framework

As mentioned above, the key idea underneath Multi-Agent Collaborative Search is to combine local and global search in a coordinated way such that local convergence is improved while retaining global exploration[86]. This combination of local and global search is achieved by endowing a set of agents with a repertoire of actions producing either the sampling of the whole search space or the exploration of a neighbourhood of each agent. Actions are classified into two categories: *social*, or *collaborative*, and *individualistic*. The next section will detail how these actions were performed in the first implementation of MACS[54].

2.3.1 The first implementation of MACS

As a first step, a population P_0 of n_{pop} individuals, one for each solution vector $\mathbf{x}_i$, with $i = 1,...,n_{pop}$, is deployed in the problem domain D. The population evolves through a number of generations.

At every generation k, all individuals perform a set of *collaborative* actions, which consist of the following:

- Two individuals $\mathbf{x}_i$ and $\mathbf{x}_j$ are selected such that $\mathbf{x}_i \prec \mathbf{x}_j$
- A new candidate is generated by *linear interpolation* between $\mathbf{x}_i$ and $\mathbf{x}_j$.
- A second candidate is generated by *linear extrapolation* between $\mathbf{x}_i$ and $\mathbf{x}_j$, on the side of $\mathbf{x}_i$.
- Two more candidates are generated by *recombination* of $\mathbf{x}_i$ and $\mathbf{x}_j$, by *single-point crossover*. Given a randomly selected component j, the two agents are split in two at the j-th component, one from component 1 to component j and the other from component j+1 to component n; and then we combine the two parts of each of the agents in order to generate two new solutions.
- A *tournament selection* is performed among the four new candidate solutions, by which the one with the lowest dominance index is selected.

A local restart mechanism is also implemented at this stage to avoid overcrowding of individuals.

After all the collaborative and restart actions have been implemented, the resulting updated population P_h is ranked according to I_d and split in two subpopulations: P^l, which contains the *best* n_{elite} inviduals, and P^u, with the *worst* n_{pop}-n_{elite} individuals. The agents in each subpopulation implement sets of, so called, *individualistic actions* to collect samples of the surrounding space and to modify their current location. In particular, the individuals belonging to P^u are simply randomly mutated.

The remaining n_{elite} agents $\mathbf{x}_i$ belong to P^l and implement a mix of actions that aim at either improving their location or exploring their neighbourhood $N_\rho(\mathbf{x}_i)$, a hyperectangle centred in $\mathbf{x}_i$. The actions described below are performed sequentially until an improved solution is found:

- *inertia*, which consists in generating a new sample by moving along the direction given by $\mathbf{x}_i$ at the current and at the previous generation, if the former is an improvement of the latter:

$$\begin{aligned} &\mathbf{y}_{ine} = \mathbf{x}_i^{\,k} + r(\mathbf{x}_i^{\,k} - \mathbf{x}_i^{\,k-1}) \\ &\mathbf{x}_i^{\,k} \prec \mathbf{x}_i^{\,k-1} \end{aligned} \tag{2.8}$$

  where r is a random number between 0 and 1.

- *differential*, which performs a step inspired by Differential Evolution[71] between $\mathbf{x}_i$ and three randomly selected individuals $\mathbf{x}_1$, $\mathbf{x}_2$ and $\mathbf{x}_3$ in $N_\rho(\mathbf{x}_i)$:

$$\mathbf{y}_{DE} = \mathbf{x}_i + \mathbf{e}\left[\mathbf{x}_1 + 0.8\left(\mathbf{x}_3 - \mathbf{x}_2\right)\right] \tag{2.9}$$

  where $\mathbf{e}$ is a vector of random numbers between 0 and 1.

- *mutation*, simple generation of a random sample $\mathbf{y}_{mut}$ in $N_\rho(\mathbf{x}_i)$.
- *linear extrapolation*, a sample $\mathbf{y}_{lin}$ is extrapolated on the side of the best between $\mathbf{x}_i$ and $\mathbf{y}_{mut}$.
- *quadratic extrapolation*, if all the previous steps were unsuccessfull, a quadratic model $\lambda(\mathbf{y})$ of I_d is constructed from $\mathbf{x}_i$, $\mathbf{y}_{lin}$ and $\mathbf{y}_{mut}$, and the point $\mathbf{y}_{quad}$ corresponding to the local minima of is generated.

In some implementations, these solutions are collected in a local archive $A_i^{\,l}$ associated to $\mathbf{x}_i$ and a dominance index is computed for all the elements in $A_i^{\,l}$. If at least one element in $A_i^{\,l}$ has I_d=0, then it will replace $\mathbf{x}_i$. If multiple elements of $A_i^{\,l}$ have I_d=0, then the one with the largest distance w.r.t. $\mathbf{x}_i$ is selected.11

Once the *individualistic* actions have been performed, the non-dominated solutions ar stored in the global archive A_g. The archive A_g is used to implement an attraction mechanism that improves the convergence of the worst individuals. During the global

archiving process a second restart mechanism that reinitialises a portion of the population (*bubble restart*) is implemented.

2.3.2 From MACS to MACS2

Compared to the first MACS, this work proposes a number of key innovations, which are introduced here and will be described in detail in Section 2.4:

- The first involves the selection criteria. As seen in the previous section, MACS selected the new candidate solutions on the basis of the dominance index I_d. In MACS2, Tchebycheff decomposition is used in combination with dominance-based ranking to accept the outcome of an action. The idea is that each agent can either try to improve its dominance index or can try to improve one particular objective function by working on a subproblem characterized by a subset of weights λ. This combination extends the accepted individualistic moves and improves the spreading of the solutions in the criteria space.
- The second innovation comes from an inversion of the policy to schedule *individualistic* and *social*/*collaborative* actions. In MACS, the first step of each algorithmic iteration consisted in the whole the whole performing a set of *collaborative* actions. In MACS2, this is now replaced by *individualistic* actions, performed independently by each individual. This inversion is quite significant as it translates into a parallel local search performed by the whole population, rather than having the local search performed by a selected number of individuals at a particular time of the evolution.
- In line with this, a similar change has been made on the second main step performed at each generation. In MACS the *collaborative* actions where followed by *individualistic* actions, in which each agent of the *elite* population performed a set of actions to search locally for improvements in its neighbourhood. In MACS2, the first step of *individualistic* actions is followed by a set of actions performed among *social* individuals (somehow equivalent to the *elite* population) only.
- The search heuristics have been somewhat simplified compared to MACS. The combination of *interpolation*, *extrapolation* and *recombination* of the collaborative actions in MACS has been replaced by the simple *pattern search* performed in the *individualistic* actions of MACS2. Similarly, the sequence of *inertia*, DE, *mutation* and *linear/quadratic extrapolation* of the *individualistic*

actions of MACS has been changed into a slightly different variant of DE in the *social* actions of MACS2.

2.4 MACS2 with Tchebycheff Decomposition

In this section, the key heuristics underneath MACS2 will be described in details. Compared to previous implementations of MACS[54], this work proposes a number of key innovations. First of all, Tchebycheff decomposition is used in combination with dominance-based ranking to accept the outcome of an action. The idea is that each agent can either try to improve its dominance index or can try to improve one particular objective function by working on a subproblem characterized by a subset of weights λ. This combination extends the accepted individualistic moves and improves the spreading of the solutions in the criteria space. The second innovation comes from an inversion of the policy to schedule individualistic and social actions. In previous implementations, the whole population was participating in the implementation of social actions at every generation, while an elite of agents was implementing individualistic actions. In this version of MACS, this policy is inverted and now all the agents perform individualistic actions while selected subpopulations perform social actions either with other agents in the current population or with elements in the archive. This inversion is quite significant as it translates into a parallel local search performed by the whole population at each iteration, rather than having the local search performed by a selected number of individuals at a particular time of the evolution. More specific heuristics are described in the next sections.

The use of either dominance or Tchebycheff scalarisation leads to the selection of different outcomes of the actions executed by the agents. With reference to Figure 2.2a, the dominance criterion can be used to select a displacement of agent **x** in the dominating region. In this case only strongly dominant solutions are accepted as admissible for a displacement of agent **x**. Tchebycheff scalarisation, instead, allows for movements in the region of decreasing g(**x)** in Figure 2.2a.

This region extends the dominating region of Figure 2.2a and includes part of the non-dominating region. Therefore, Tchebycheff scalarisation, as defined in (2.6) allows for the selection of weakly efficient solutions. If λ is kept constant the agent would progressively try to align along the direction ζ (see Figure 2.2b). The rectilinear line ζ divides the criteria space in Figure 2.2b in two half-planes, one, below ζ, where $\lambda_1 \mid f_1(\mathbf{x}) - z_1 \mid \rhd \lambda_2 \mid f_2(\mathbf{x}) - z_2 \mid$, the other, above ζ, where $\lambda_1 \mid f_1(\mathbf{x}) - z_1 \mid \lhd \lambda_2 \mid f_2(\mathbf{x}) - z_2 \mid$. The rectilinear line ζ is, therefore, the locus of points, in the criteria space, for which $\lambda_1 \mid f_1(\mathbf{x}) - z_1 \mid = \lambda_2 \mid f_2(\mathbf{x}) - z_2 \mid$. Figure 2.2b shows that by solving problem (2.6) one would

take displacements in any direction that improves f_1, starting from a solution that is under the ζ line. If one of these displacements crosses the ζ line, the solution of problem (2.6) would then generate displacements that improve f_2. This mechanism allows for the generation of dominating steps (see Figure 2.2c) as well as side steps (see Figure 2.2d). Side steps are important to move along the Pareto front (see Lara et al.[82] for more details on the effect of side steps).

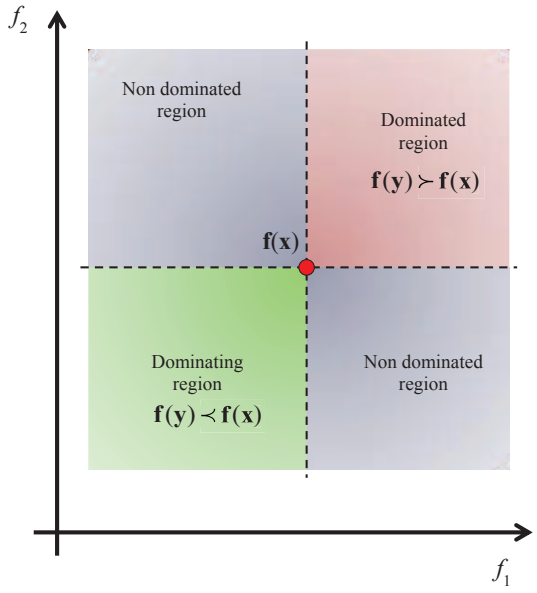

a) Selection based on dominance index

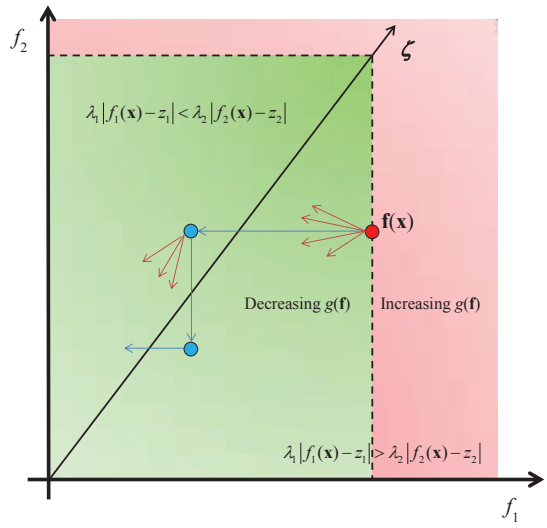

c) Selection based on Tchebycheff scalarisation

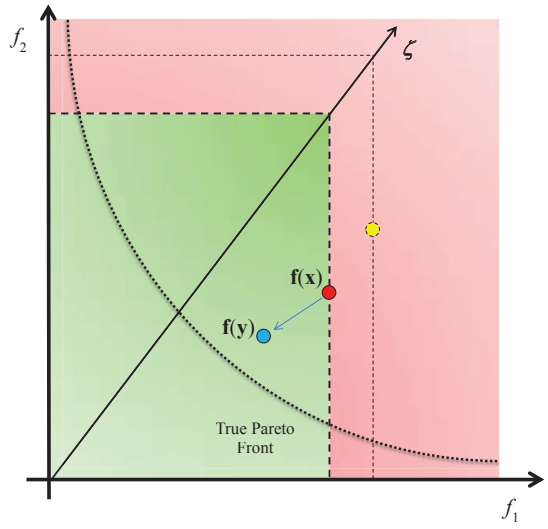

c) Selection based on Tchebycheff scalarisation, strong dominance step

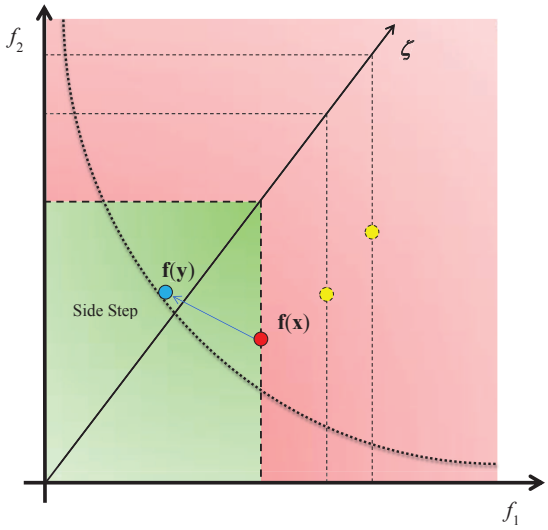

d) Selection based on Tchebycheff scalarisation, side step

Figure 2.2: Selection criteria.

In MACS side steps were generated by accepting displacements in the non-dominating regions of Figure 2.2a when no dominant solutions were available. In MACS2 instead side steps are generated by selecting displacements according to Tchebycheff scalarisation when strongly dominant solutions are not available. Note however, that although

displacements are computed considering a combination of strong dominance and Tchebycheff scalarisation, the archive is filled with all the solutions that have dominance index I_d=0 and a large reciprocal distance (see Section 2.4.4).

2.4.1 General Algorithm Description

A population P_0 of n_{pop} virtual agents, one for each solution vector $\mathbf{x}_i$, with $i = 1,...,n\_\{pop\}$, is deployed in the problem domain D, and is evolved according to Algorithm 2.1.

The population P_h at iteration h=0 is initialized using a Latin Hypercube distribution. Each agent then evaluates the associated objective vector $\mathbf{f}_i = \mathbf{f}(\mathbf{x}_i)$ and all non-dominated agents are cloned and inserted in the global archive A_g (lines 4 and 5 in Algorithm 2.1). The archive A_g contains the current best estimation of the target set X_g. The q-th element of the archive is the vector $\mathbf{a}_q = [\xi_q \quad \phi_q]^T$ where ξ_q is a vector in the parameter space and ϕ_q is a vector in the criteria space.

Each agent is associated to a neighbourhood D_{ρ_i} with size ρ_i. The size ρ_i is initially set to 1, i.e. representing the entire domain D (line 6 in Algorithm 2.1).

A set of n_λ, m-dimensional unit vectors $\boldsymbol{\lambda}_k$ is initialized such that the first m vectors are mutually orthogonal. The remaining n_λ-m vectors have random components instead. In two dimensions the vectors are initialized with a uniform sampling on a unit circle and in three dimensions with a uniform sampling on a unit sphere, while in n-dimensions with a Latin Hypercube sampling plus normalization, such that the length of each vector is 1 (see line 7 in Algorithm 2.1).

For each vector $\boldsymbol{\lambda}_k$, the value of an associated utility function U_k is set to 1 (see line 8 in Algorithm 2.1). The utility function is the one defined in Zhang et al.[65] and its value is updated every u_{iter} iterations using Algorithm 2.5. In this work it was decided to maintain the exact definition and settings of the utility function as can be found in[65], which the interested reader can therefore refer to for further details.

Each $\boldsymbol{\lambda}_k$ represents a subproblem in Eq. (2.6), i.e. it is used to compute the scalar function g_k. A total of $n_{social} = round(\rho_{pop} n_{pop})$ $\boldsymbol{\lambda}$ vectors are inserted in the index set I_a. The first m indexes in I_a correspond to the m orthogonal $\boldsymbol{\lambda}$ vectors, the other n_{social}-m are initially chosen randomly (line 9 of Algorithm 2.1).

Each $\boldsymbol{\lambda}_k$ for $k = 1,...,n_\lambda$ is associated to the element in A_g that minimizes g_k such that:

$$\underline{\phi}_k = \arg\min_{\phi_q} g(\phi_q, \lambda_k, \mathbf{z}) \tag{2.10}$$

where **z** is the vector containing the minimum values of each of the objective functions.

Then, for each $\boldsymbol{\lambda}_l$, with $l \in I_a$ and associated vector $\underline{\phi}_l$, a *social* agent $\mathbf{x}_q$ is selected from the current population P_h such that it minimizes $g(\mathbf{f}_q, \lambda_l, \mathbf{z})$. The indexes of all the selected social agents are inserted in the index set I_λ (see lines 14 to 17 in Algorithm 2.1). The indexes in I_a and I_λ are updated every u_{iter} iterations. At the h-th iteration, the population P_h is evolved through two sets of heuristics: first, every agent $\mathbf{x}_i$ performs a set of *individualistic actions* which aims at exploring a neighbourhood D_{ρ_i} of $\mathbf{x}_i$ (line 20 of Algorithm 2.1), the function *explore* described in Algorithm 2.2 is used to implement individualistic actions. All the samples collected during the execution of individualistic actions are stored in the local archive A_l. The elements of A_l and the outcome of social actions are inserted in the global archive A_g if they are not dominated by any element of A_g (line 22 in Algorithm 2.1). Then, a sub-population I_λ of n_{social} selected social agents performs a set of *social actions* (see line 23 of Algorithm 2.1). Social actions aim at sharing information among agents. More details about individualistic and social actions are provided in the following sections. The function *com* described in Algorithm 2.3 is used to implement social actions.

At the end of each iteration the global archive A_g is resized if its size has grown larger than $n_{A,max}$ (line 25 in Algorithm 2.1). The resizing is performed by function *resize* described in Algorithm 2.4.

The value $n_{A,max}$ was selected to be the largest number between $1.5n_\lambda$ and $1.5n_{A,out}$, where $n_{A,out}$ is the desired number of Pareto optimal elements in A_g at the last iteration. This resizing of the archive is done in order to reduce the computational burden required by operations like the computation of the dominance index. It also provides an improved distribution of the solutions along the Pareto front as it discards solutions that are excessively cluttered.

At the end of each iteration the algorithm also checks if the maximum number of function evaluations $n_{feval,max}$, defined by the user, has been reached and if so, the algorithm terminates. At termination, the archive A_g is resized to $n_{A,out}$ if its cardinality is bigger than $n_{A,out}$.

Algorithm 2.1 MACS2

Set $n_{feval,max}, n_{pop}, n_{social} = round(\rho_{pop} n_{pop}), F, tol_{conv}, n_{A,out}, u_{iter}$
Set $n_\lambda = 100m, n_{A,max} = round(1.5 \max([n_\lambda, n_{A,out}]))$
Set $n_{feval} = 0$
Initialize population P_h, $h = 0$
Insert the non-dominated elements of P_0 in the global archive A_g
$\rho_i = 1, \forall i \in \{1, ..., n_{pop}\}$
Initialize λ_k for $k \in \{1, ..., n_\lambda\}$ such that $\|\lambda_k\| = 1$
Initialize utility function vector $U_k = 1, \forall k \in \{1, ..., n_\lambda\}$
Select the n_{social} active subproblems λ_l, and save their indexes l in the index set I_a
Initialize $\delta_l = \max_q \phi_{q,l} - \min_q \phi_{q,l}$, $z_l = \min_q \phi_{q,l}$, $q \in \{1, ..., |A_g|\}$, $l = 1, ..., m$,
for all $k \in \{1, ..., n_\lambda\}$ **do**
    $\underline{\phi}_k = \arg\min_{\phi_q} g(\phi_q, \lambda_k, \mathbf{z}), q = 1, ..., |A_g|$
end for
for all $\lambda_l, l \in I_a$ **do**
    Select the $[\mathbf{x}_q \mathbf{f}_q] \in P_h$ which minimises $g(\mathbf{f}_q, \lambda_l, \mathbf{z}), l \in I_a$
    and save its index in the list of the social agents I_λ
end for
while $n_{feval} < n_{feval,max}$ **do**
    $h = h + 1$
    $[P_h, n_{feval}, A_l, \rho] = explore(P_{h-1}, n_{feval}, n, \rho, \mathbf{b}^l, \mathbf{b}^u, \mathbf{f}, \lambda, I_\lambda, I_a)$
    If necessary, update the vector of the best objectives $\mathbf{z}$, with A_l
    Update archive A_g with non dominated elements of A_l
    $[\mathbf{y}, \varphi, n_{feval}, P_h, A_g] = com(P_h, A_g, \mathbf{b}^l, \mathbf{b}^u, n_{feval}, n, F, \mathbf{f}, \lambda, I_\lambda, I_a)$
    if $|A_g| > n_{A,max}$ **then**
        $A_g = resize(A_g, m, n_{A,max})$
    end if
    if ($\mod (h, u_{iter}) = 0$) **then**
        $[I_a, I_\lambda, \mathbf{U}, \underline{\phi}] = select(\mathbf{U}, \lambda, \underline{\phi}, P_k, A_g, \mathbf{z}, m, n_{social}, n_\lambda)$
    end if
end while
$A_g = resize(A_g, m, n_{A,out})$

2.4.2 Individualistic Actions

Individualistic actions perform an independent exploration of the neighbourhood D_{ρ_i} of each agent. As in the original version of MACS[54] the neighbourhood is progressively resized so that the exploration is over the entire D when the size ρ_i is equal to 1 and becomes progressively more and more local as the neighbourhood shrinks down. In this new implementation of MACS each agent performs only a simple sampling along the coordinates. The neighbourhood D_{ρ_i} is a hypercube centred in $\mathbf{x}_i$ with size defined by ρ_i such that each edge of the hypercube has length $\rho_i(\mathbf{b}^u - \mathbf{b}^l)$. Algorithm 2.2 describes individualistic actions.

The search is performed along a single component of $\mathbf{x}_i$ at a time, in a random order: given an agent $\mathbf{x}_i$, a sample $\mathbf{y}^+$ is taken within D_{ρ_i} along the *j*-th coordinate with random step size $r \in \mathcal{U}(-1,1)$, where $\mathcal{U}(-1,1)$ is a uniform distribution over the closed interval [-1 1], leaving the other components unchanged. If $\mathbf{y}^+$ dominates $\mathbf{x}_i$, $\mathbf{y}^+$ replaces $\mathbf{x}_i$, otherwise

another sample $\mathbf{y}^-$ is taken in the opposite direction with step size *rr*, with $rr \in \mathcal{U}(0,1)$. Again, if $\mathbf{y}^-$ dominates $\mathbf{x}_i$, $\mathbf{y}^-$ replaces $\mathbf{x}_i$.

If $\mathbf{y}_i$ is not dominating and is not dominated by $\mathbf{x}_i$ and the index i of $\mathbf{x}_i$ belongs to I_λ, then $\mathbf{y}_i$ replaces $\mathbf{x}_i$ if $\mathbf{y}_i$ improves the value of the subproblem associated to $\mathbf{x}_i$. Whether a dominant sample or a sample that improves the value of the subproblem is generated the exploration terminates. This is a key innovation that exploits Tchebycheff decomposition and allows the agents to perform moves that improve one objective function at the time.

Algorithm 2.2 *explore*: Individualistic Actions

1: $\Delta = (\mathbf{b}^u - \mathbf{b}^l)/2$
2: **for all** $i = 1 : n_{pop}$ **do**
3: Set $A_{l,i} = \emptyset$, $p_i \in I_a$
4: Take a random permutation I_E of $\{1, ..., n\}$
5: **for all** $j \in I_E$ **do**
6: Take a random number $r \in \mathcal{U}(-1, 1)$
7: $\mathbf{y}^+ = \mathbf{x}_i$
8: **if** $r > 0$ **then**
9: $y_j^+ = \min\{y_j^+ + r\rho_i\Delta_j, b_j^u\}$
10: **else**
11: $y_j^+ = \max\{y_j^+ + r\rho_i\Delta_j, b_j^l\}$
12: **end if**
13: **if** $\mathbf{y}^+ \neq \mathbf{x}_i$ **then**
14: Evaluate $\varphi^+ = \mathbf{f}(\mathbf{y}^+)$
15: $n_{feval} = n_{feval} + 1$
16: **if** $(\mathbf{y}^+ \not\succ \mathbf{x}_i)$ **then**
17: $A_{l,i} = A_{l,i} \cup \{[\mathbf{y}^+ \ \varphi^+]\}$
18: **end if**
19: **if** $\mathbf{y}^+ \prec \mathbf{x}_i \vee (i \in I_\lambda \wedge g(\varphi^+, \lambda_{p_i}, \mathbf{z}) < g(\mathbf{f}_i, \lambda_{p_i}, \mathbf{z}))$ **then**
20: $\mathbf{x}_i = \mathbf{y}^+$; break
21: **end if**
22: **end if**
23: $\mathbf{y}^- = \mathbf{x}_i$
24: Take a random number $rr \in \mathcal{U}(0, 1)$
25: **if** $r > 0$ **then**
26: $y_j^- = \max\{y_j^- - rr\rho_i\Delta_j, b_j^l\}$
27: **else**
28: $y_j^- = \min\{y_j^- + rr\rho_i\Delta_j, b_j^u\}$
29: **end if**
30: **if** $\mathbf{y}^- \neq \mathbf{x}_i$ **then**
31: Evaluate $\varphi^- = \mathbf{f}(\mathbf{y}^-)$
32: $n_{feval} = n_{feval} + 1$
33: **if** $\mathbf{y}^- \not\succ \mathbf{x}_i$ **then**
34: $A_{l,i} = A_{l,i} \cup \{[\mathbf{y}^- \ \varphi^-]\}$
35: **end if**
36: **if** $\mathbf{y}^- \prec \mathbf{x}_i \vee (i \in I_\lambda \wedge g(\varphi^-, \lambda_{p_i}, \mathbf{z}) < g(\mathbf{f}_i, \lambda_{p_i}, \mathbf{z}))$ **then**
37: $\mathbf{x}_i = \mathbf{y}^-$; break
38: **end if**
39: **end if**
40: **end for**
41: **if** $\mathbf{y}^- \succ \mathbf{x}_i \wedge \mathbf{y}^+ \succ \mathbf{x}_i$ **then**
42: $\rho_i = \eta_\rho\rho_i$
43: **if** $\rho_i < tol_{conv}$ **then**
44: $\rho_i = 1$
45: **end if**
46: **end if**
47: **end for**
48: $A_l = \bigcup_{i=1,...,n_{pop}} A_{l,i}$

The search terminates also when all the components of $\mathbf{x}_i$ have been examined, even if all the generated samples are dominated (see Algorithm 2.2 lines 3 to 40).

If all children are dominated by their parent, the size of the neighbourhood ρ_i is reduced by a factor η_ρ. Finally, if ρ_i is smaller than a tolerance tol_{conv}, it is reset to 1 (see Algorithm 2.2 lines 41 to 46). In all the tests in this paper η_ρ was taken equal to 0.5 as this value provided good results, on average, across all test cases.

All the non-dominated children generated by each agent $\mathbf{x}_i$ during the exploration form the local archive $A_{l,i}$. The elements of $A_{l,i}$ are inserted in the global archive A_g if they are not dominated by any element in A_g.

Algorithm 2.3 *com*: Social Actions

1: $p_{AvsP} = 1 - e^{-|A_g|/n_{social}}$
2: **for all** $i \in I_\lambda$ **do**
3: $AvsP = r < p_{AvsP}, r \in \mathcal{U}(0,1), p_i \in I_a$
4: **if** $AvsP \wedge |A_g| \geq 3$ **then**
5: Select the n_{social} closest elements of the archive A_g to the agent $\mathbf{x}_i$ and save their indexes in the set I_T
6: **else**
7: Select the n_{social} closest agents of the population P_k to the agent $\mathbf{x}_i$ and save their indexes in the set I_T
8: **end if**
9: $K \in \mathcal{U}(0,1)$
10: Randomly select $s_1 \neq s_2 \neq s_3 \in I_T$
11: $\mathbf{y} = \mathbf{x}_i + K(\mathbf{s}_3 - \mathbf{x}_i) + KF(\mathbf{s}_1 - \mathbf{s}_2)$
12: **for all** $j \in \{1, ..., n\}$ **do**
13: $r \in U(0,1)$
14: **if** $y_j < b_j^l$ **then**
15: $y_j = b_j^l + r(y_j - b_j^l)$
16: **else if** $y_j > b_j^u$ **then**
17: $y_j = b_j^u - r(b_j^u - y_j)$
18: **end if**
19: **end for**
20: **if** $\mathbf{y} \neq \mathbf{x}_i$ **then**
21: Evaluate $\varphi = \mathbf{f}(\mathbf{y})$
22: $n_{feval} = n_{feval} + 1$
23: **end if**
24: If necessary, update $\mathbf{z}$ with φ
25: **if** $g(\varphi, \lambda_{p_i}, \mathbf{z}) < g(\mathbf{f}_i, \lambda_{p_i}, \mathbf{z})$ **then**
26: $\mathbf{f}_i = \varphi, \mathbf{x}_i = \mathbf{y}$
27: **end if**
28: Update archive A_g with non-dominated elements of $\{[\mathbf{y} \ \ \varphi]\}$
29: **end for**

2.4.3 Social Actions

Social actions are performed by each agent whose index is in the set I_λ. Social actions are meant to improve the subproblem defined by the weight vectors $\boldsymbol{\lambda}_k$ in I_a and associated to the agents $\mathbf{x}_i$ in I_λ. This is done by exploiting the information carried by either the other agents in the population P_h or the elements in the archive A_g.

Social actions implement the Differential Evolution (DE) heuristic:

$$\mathbf{y}_i = \mathbf{x}_i + K[(\mathbf{s}_1 - \mathbf{x}_i) + F(\mathbf{s}_2 - \mathbf{s}_3)] \tag{2.11}$$

where the vectors $\mathbf{s}_l$, with $l = 1,..,3$, are randomly taken from the local social network I_T of each social agent $\mathbf{x}_i$. The local social network is formed by either the n_{social} agents closest to $\mathbf{x}_i$ or the n_{social} elements of A_g closest to $\mathbf{x}_i$. The probability of choosing the archive vs. the population is directly proportional to p_{AvsP} (see line 3 of Algorithm 2.3). The parameter

p_{AvsP} is defined as $1-e^{-|A_g|/n_{social}}$. This means that in the limit case in which the archive is empty, the population is always selected. on the other hand, if the archive is much larger than the population, it is more likely to be selected. Note that, if the size of A_g is below 3 elements, then the population is automatically chosen instead (line 4 of Algorithm 2.3) as the minimum number of elements to form the step in (2.11) is 3. The offspring $\mathbf{y}_i$ replaces $\mathbf{x}_i$ if it improves the subproblem associated to $\mathbf{x}_i$ otherwise $\mathbf{y}_i$ is added to the archive A_g if it is not dominated by any of the elements of A_g. The value of F in this implementation is 0.9. Social actions, described in Algorithm 2.3, dramatically improve the convergence speed once a promising basin of attraction has been identified. On the other hand, in some cases social actions lead to a collapse of the subpopulation of social agents in one or more single points. This is in line with the convergence behaviour of DE dynamics presented in Vasile et al.[87]. This drawback is partially mitigated by the remaining agents, which perform only *individualistic actions*. Algorithm 2.3 implements social actions.

2.4.4 Archive Resizing

If the size of A_g exceeds a specified value (as detailed in Section 2.4.1), a resizing procedure is initiated. The resizing procedure progressively selects elements from the current archive and adds them to the resized archive until its specified maximum size $n_{A,max}$ is reached.

First the normalized Euclidean distances, in the objective space, between all the elements of the current archive are computed (lines 3-8 of Algorithm 2.4).

Then, the l-th element, minimizing the l-th objective function, with $l=1,...,m$, is inserted in the resized archive (lines 9 to 12 of Algorithm 2.4). The remaining $n_{A,max}$ -m elements are iteratively selected by considering each time the element of the current archive (excluding those which are already in the resized one) which has the largest distance from its closet element in the resized archive (lines 13 to 17 of Algorithm 2.4). This procedure provides a good uniformity in the distribution of samples. Future work will investigate the comparative performance of different archiving strategies like the one proposed in Laumanns et al.[88] and Schütze et al.[89].

Algorithm 2.4 *resize*: Archive Resizing

$n_A = |A_g|$, $S = \emptyset$
$\delta_j = \max_i \phi_{q,j} - \min_i \phi_{q,j}, \forall j = 1, ..., m$
for all $q \in \{1, ..., (n_A - 1)\}$ **do**
  for all $i \in \{(q + 1), ..., n_A\}$ **do**
    $d_{q,i} = \|(\phi_q - \phi_i)/\delta\|$
    $d_{i,q} = d_{q,i}$
  end for
end for
for all $l \in \{1, ..., m\}$ **do**
  $S = S \cup \{\arg\min_q(\phi_{q,l})\}$
end for
$S_n = \{1, ..., n_A\} \setminus S$
for all $i \in \{m + 1, ..., n_{A,max}\}$ **do**
  $l_S = \text{argmax}_l(\min_q(d_{q,l}))$, $q \in S, l \in S_n$
  $S = S \cup \{l_S\}$
  $S_n = S_n \setminus \{l_S\}$
end for
$A_g = \{\mathbf{a}_i | \forall i \in S\}$

Algorithm 2.5 *select*: Subproblem Selection

$\underline{\phi}_{old} = \underline{\phi}$
for all $k \in \{1, ..., n_\lambda\}$ **do**
  $\underline{\phi}_k = \arg\min_{\phi_q} g(\phi_q, \lambda_k, \mathbf{z})$, $q \in \{1, ..., |A_g|\}$
  $\gamma = (g(\underline{\phi}_{old,k}, \lambda_k, \mathbf{z}) - g(\underline{\phi}_k, \lambda_k, \mathbf{z}))$
  if $\gamma > 0.001$ **then**
    $U_k = 1$
  else
    $U_k = (0.95 + 50\gamma)U_k$
  end if
end for
$t_{size} = round(n_\lambda/60)$
$I_a = \{1, ..., m\}$
for all $i \in \{m + 1, ..., n_{social}\}$ **do**
  Randomly select a subset I_{sel} of t_{size} elements of $\{1, .., n_\lambda\}$
  $\bar{k} = \text{argmax}_k U_k, k \in I_{sel}$
  $I_a = I_a \cup \{\bar{k}\}$
end for
for all $\lambda_l, l \in I_a$ **do**
  Select the $[\mathbf{x}_q \mathbf{f}_q] \in P_h$ which minimises $g(\mathbf{f}_q, \lambda_l, \mathbf{z}), l \in I_a$
  and save its index in the list of the social agents I_λ
end for

2.4.5 Subproblem Selection

Every u_{iter} iterations the active subproblems in I_a and the associated agents in I_λ performing *social* actions are updated. The agents performing social actions are updated through function *select* described in Algorithm 2.5.

The improvement γ between $\underline{\phi}_k$ (i.e. the best value of g_k at current iteration in the global archive) and $\underline{\phi}_{old,k}$ (the best value of g_k, u_{iter} iterations before) is calculated. Then, the

utility function U_k associated to $\boldsymbol{\lambda}_k$ is updated according to the rule described in Zhang et al.[65] and reported in Algorithm 2.5, lines 2 to 10.

Once a value U_k is associated to each $\boldsymbol{\lambda}_k$, n_{social} new subproblems and associated $\boldsymbol{\lambda}$ vectors are selected. The first m $\boldsymbol{\lambda}$ vectors are always the orthogonal ones. The remaining n_{social}-m vectors are selected by taking $t_{size} = round(n_\lambda / 60)$ random indexes and then choosing the one with the largest value of U_k. This is repeated till I_a is full (see lines 11 to 17 in Algorithm 2.5). Note that t_{size} cannot exceed the size of I_{tmp} in Algorithm 2.5 if the number of social agents n_{social} is small compared to n_λ.

Finally, the agent $\mathbf{x}_i$, that minimizes the scalar objective function in Eq. (2.6), is associated to each $\boldsymbol{\lambda}_k$ with index in I_a, and its index is included in the new subset I_λ (lines 18 to 21 in Algorithm 2.5).

2.5 Experimental Results

This section presents the performance of MACS2 on a standard benchmark for Multi-Objective optimization algorithms and on some space-related test cases. Through an experimental analysis an optimal settings for MACS2 is derived. The results obtained with MACS2 will also be compared with those of MACS and other known Multi-Objective optimization algorithms[90].

The standard benchmark problems aim at optimizing the UF1-10 functions in the CEC'09 test suite[91] and the test instances ZDT2, ZDT4, ZDT6[92]. UF1 to UF7 are bi-objective test functions with 30 optimization parameters. UF8 to UF10 are tri-objective functions, again with 30 optimization parameters.

The CEC'09 competition rules specified 300000 function evaluations and 100 and 150 elements for the output Pareto fronts for the bi- and tri-objective functions respectively. ZDT2 ZDT4 and ZDT6 are bi-objective test cases with 30 parameters for the first one and 10 for the remaining two. They are tested running the algorithm for 25000 evaluations and taking an output front of 200 elements.

The space-related test instances are given by two trajectory optimization problems as described in Minisci and Avanzini[93] and Vasile and Zuiani[54]. The former is a 3-impulse transfer between a circular Low Earth Orbit (LEO) with radius r_0=7000km to a Geostationary Orbit (GEO) with radius r_f=42000km.

The latter test case, Cassini, describes a trajectory optimization instance from Earth to Jupiter with four intermediate gravity assists at Venus (twice), Earth and Jupiter respectively.

For both test cases the objective functions to be minimized are total ΔV and time of flight. The 3-impulse test case has 5 optimization parameters and is run for 30000 function evaluations while Cassini has 6 parameters and is run for 600000 evaluations as it was demonstrated, in the single objective case, to have multiple nested local minima with a funnel structure[87].

The metrics which will be used in order to evaluate the performance of the algorithms are chosen so to have a direct comparison of the results in this paper with those in previous works. Therefore, for the CEC'09 test set the *IGD* performance metric will be used[91]:

$$IGD(A,P^*) = \frac{1}{|P^*|}\sum_{\mathbf{v}\in P^*} \min_{\mathbf{a}\in A} \|\mathbf{v}-\mathbf{a}\| \tag{2.12}$$

where P^* is a set of equally spaced points on the true Pareto front, in the objective space, while A is the set of points from the approximation of the Pareto front. As in Zhang et al.[91], performance will be assessed as mean and standard deviation of the *IGD* over 30 independent runs. Note that a second batch of tests was performed taking 200 independent runs but the value of the *IGD* was providing similar indications.

For the ZDT test set and for the space problems, the success rate on the convergence M_{conv} and spreading M_{spr} metrics are used instead. Note that, the *IGD* metric has been preferred for the UF test problems in order to keep consistency with the results presented in the CEC'09 competition. Convergence and spreading are defined as:

$$M_{conv} = \frac{1}{|A|}\sum_{\mathbf{a}\in A} \min_{\mathbf{v}\in P^*} \|\frac{\mathbf{v}-\mathbf{a}}{\boldsymbol{\delta}}\| \tag{2.13}$$

$$M_{spr} = \frac{1}{|P^*|}\sum_{\mathbf{v}\in P^*} \min_{\mathbf{a}\in A} \|\frac{\mathbf{v}-\mathbf{a}}{\boldsymbol{\delta}}\| \tag{2.14}$$

with $\boldsymbol{\delta} = \max_i \mathbf{a}_{f,i} - \min_i \mathbf{a}_{f,i}$. It is clear that M_{spr} is the *IGD* but with the solution difference, in objective space, normalized with respect to the exact (or best-so-far) solution. In the case of the ZDT test set, the two objective functions range from 0 to 1, therefore no normalization is required and M_{spr} is in fact the *IGD*.

The success rates for M_{conv} and M_{spr} is defined as $p_{conv} = P(M_{conv} < \tau_{conv})$ and $p_{spr} = P(M_{spr} < \tau_{spr})$ respectively, or the probability that the indexes M_{conv} and M_{spr} achieve a value less than the threshold τ_{conv} and τ_{spr} respectively. The success rates p_{conv} and p_{spr} are computed over 200 independent runs, hence they account for the number of times M_{conv} and M_{spr} are below their respective thresholds. According to the theory developed in Minisci and Avanzini[93] and Vasile et al.[94], 200 runs provide a 5% error interval with a 95% confidence level. Values for thresholds for each test case are reported in Table 2.1.

Table 2.1: Convergence tolerances

	3-impulse	Cassini	UF1	UF2	UF3	UF4	UF5	UF6
τ_{conv}	$5\cdot10^{-2}$	$7.5\cdot10^{-3}$	$5\cdot10^{-3}$	$5\cdot10^{-3}$	$2\cdot10^{-2}$	$3.5\cdot10^{-2}$	$3\cdot10^{-2}$	$3\cdot10^{-2}$
τ_{spr}	$5\cdot10^{-2}$	$5\cdot10^{-2}$	$1\cdot10^{-2}$	$1\cdot10^{-2}$	$3\cdot10^{-2}$	$3.5\cdot10^{-2}$	$5\cdot10^{-2}$	$3\cdot10^{-2}$
	UF7	UF8	UF9	UF10	ZDT2	ZDT4	ZDT6	
τ_{conv}	$5\cdot10^{-3}$	$2\cdot10^{-2}$	$3\cdot10^{-2}$	$3\cdot10^{-2}$	$1\cdot10^{-3}$	$1\cdot10^{-2}$	$1\cdot10^{-3}$	
τ_{spr}	$1\cdot10^{-2}$	$6\cdot10^{-2}$	$4\cdot10^{-2}$	$6\cdot10^{-2}$	$3\cdot10^{-3}$	$1.5\cdot10^{-2}$	$3\cdot10^{-3}$	

MACS2 was initially set with some arbitrary values reported in Table 2.2. The size of the population was set to 60 for all the test cases except for the 3-impulse and ZDT functions. For these test cases the number of agents was set to 30. In the following, these values will identify the *reference* settings.

Table 2.2: Reference settings for MACS2. Values within parenthesis are for 3-impulse and ZDT test cases.

n_{pop}	ρ_{pop}	F	Tol_{conv}
60 (30)	0.33	0.5	$1\cdot10^{-4}$

Starting from this reference settings a number of tuning experiments were run to investigate the reciprocal influence of different parameters and different heuristics within the algorithm. Different combinations of n_{pop}, ρ_{pop}, F and Tol_{conv} were considered. Furthermore, the social moves were activated or de-activated to assess their impact. The success rates were then used to tune the algorithm in order to improve the spreading, and therefore the *IGD*. After an extensive testing of the algorithms, it was realized that the use of the success rates offers a clearer metric, than the mean and variance of the *IGD*, to understand the impact of some user-defined parameters.

In the following, only the most significant results with the most significant metric are presented. Table 2.3 summarizes the success rates on the Cassini test case for different values of n_{pop} and ρ_{pop} but with all the heuristics active.

Table 2.3: Tuning of n_{pop} and r_{pop} on the Cassini test case.

p_{conv}				p_{spr}			
$\rho_{pop}\backslash n_{pop}$	20	60	150	$\rho_{pop}\backslash n_{pop}$	20	60	150
0.2	0.22	0.34	0.76	0.2	0.32	0.45	0.31
0.5	0.16	0.41	0.78	0.5	0.45	0.48	0.26
0.8	0.35	0.40	0.77	0.8	0.37	0.40	0.26

Table 2.4: Tuning of MACS2 on the 3-impulse and Cassini test cases.

	3-impulse		Cassini	
	p_{conv}	p_{spr}	p_{conv}	p_{spr}
Reference	0.99	0.99	0.38	0.36
no social	0.47	1	0	0.18
n_{pop}=150, ρ_{pop}=0.2	1	1	0.76	0.31
F=0.9	0.97	0.99	0.50	0.36
Tol_{conv}=10^{-6}	0.99	0.99	0.38	0.45
Tol_{conv}=10^{-2}	0.97	0.99	0.33	0.39

Table 2.5: Tuning of MACS2 on the UF test cases.

		Reference	no social	n_{pop}=150, ρ_{pop}=0.2	n_{pop}=20, ρ_{pop}=0.8	Tol_{conv}=10^{-6}
UF1	p_{conv}	1	1	1	1	1
	p_{spr}	1	1	1	0.11	1
UF2	p_{conv}	1	1	1	1	1
	p_{spr}	1	1	1	0.46	1
UF3	p_{conv}	0.95	0.32	0.99	0.86	0.95
	p_{spr}	0.99	0.11	1	0.97	1
UF4	p_{conv}	1	1	1	0.06	1
	p_{spr}	1	1	1	0.54	1
UF5	p_{conv}	0.59	0.10	0.62	0.91	0.58
	p_{spr}	0.85	0.21	1	0.39	0.85
UF6	p_{conv}	0.58	0.50	0.32	0.54	0.61
	p_{spr}	0.40	0.42	0.45	0	0.37
UF7	p_{conv}	1	0.91	1	0.94	1
	p_{spr}	0.98	0	0.98	0.74	0.97
UF8	p_{conv}	0.86	0	0.88	0.89	0.88
	p_{spr}	0.8	0.01	1	0.04	0.54
UF9	p_{conv}	0.68	0.12	0.84	0.31	0.74
	p_{spr}	0.60	0	1	0	0.64
UF10	p_{conv}	0	0.01	0	0.28	0.01
	p_{spr}	0	0	0	0	0

One can see that the best convergence is obtained for n_{pop}=150 and in particular when combined with ρ_{pop}=0.5. On the other hand, best spreading is obtained with medium sized populations with n_{pop}=60. A good compromise seems to be n_{pop} =150 and ρ_{pop}=0.2.

Results on the other test cases (as shown in Table 2.4, Table 2.5 and Table 2.6, with n_{pop}=150 and ρ_{pop}=0.2) show in general that large populations and small ρ_{pop} are preferable. This also means that social actions on a large quota of the populations are undesirable and it is better to perform social moves among a restricted circle of agents. Table 2.4 reports the results of the tuning of MACS2 on the 3-imp and Cassini test cases. Table 2.5 and Table 2.6 report the results of the tuning of MACS2 on the UF and ZDT test sets respectively.

Table 2.4 shows a marked improvement of p_{conv} on the Cassini when the population size is 150. Likewise, Table 2.5 shows that in general, with a population of 150 agents, there is an improvement in performance and on p_{spr}, in particular on the UF1, 2, 6, 8 and 9 test cases. Notable exceptions are the ZDT in Table 2.6, for which the best performance is obtained for a small population with n_{pop}=20.

Table 2.6: Tuning of MACS2 on ZDT test cases.

		ZDT2	ZDT4	ZDT6
Reference	p_{conv}	1	0	0.93
	p_{spr}	1	0	1
no social	p_{conv}	1	0	0.91
	p_{spr}	1	0	0.98
n_{pop}=150, ρ_{pop}=0.2	p_{conv}	0.20	0	0.60
	p_{spr}	0.17	0	1
n_{pop}=20, ρ_{pop}=0.8	p_{conv}	1	0.02	0.96
	p_{spr}	1	0.02	1
F=0.9	p_{conv}	1	0	0.96
	p_{spr}	1	0	1
Tol_{conv}=10^{-6}	p_{conv}	1	0	0.96
	p_{spr}	1	0	1
MACS2 (tuned)	p_{conv}	1	0	0.96
	p_{spr}	1	0	1
MACS	p_{conv}	0.82	0.81	0.63
	p_{spr}	0	0.93	0

The impact of F is uncertain in many cases, however, Table 2.7 shows for example that on the UF8 test case a better performance is obtained for a high value of F. Table 2.5 and Table 2.6 show that the default value for Tol_{conv} already gives good performance and it does not seem advantageous to reduce it or make it larger.

The impact of social actions can be seen in Table 2.4, Table 2.5 and Table 2.6. Table 2.4 shows that on the 3-impulse and Cassini test cases the impact is clearly evident, since there is a marked worsening of both p_{conv} and p_{spr}. On the UF benchmark, see Table 2.5, removing social actions induces a sizeable worsening of the performance metrics. This is true in particular for functions UF1, UF3, UF5, UF6, UF7, UF8 and UF9. Notable exceptions are UF2, UF4 and UF10.

As a result of the tuning test campaign, the settings reported in Table 2.8 are recommended. Note that the recommended population size for all the cases except the ZDT functions, is 150 agents, while for the ZDT functions it remains 20 agents.

Table 2.7: Tuning of *F* on the UF8 test case.

F	0.1	0.5	0.9
average *IGD* (variance)	$6.75 \cdot 10^{-2}$ ($3.20 \cdot 10^{-5}$)	$6.06 \cdot 10^{-2}$ ($2.56 \cdot 10^{-5}$)	$5.57 \cdot 10^{-2}$ ($1.87 \cdot 10^{-5}$)

Table 2.8: Settings for MACS2 after tuning.

n_{pop}	ρ_{pop}	F	Tol_{conv}
150 (20)	0.2 (0.8)	0.9	$1 \cdot 10^{-4}$

With these settings, the performance of MACS2 was compared, on the UF test suite in Table 2.9, with that of MACS, Multi-Objective Evolutionary Algorithm based on Decomposition (MOEA/D[65]), Multiple Trajectory Search (MTS[95]) and Dynamical Multi-Objective Evolutionary Algorithm (DMOEADD[96]). The last three are the best performing algorithms in the CEC09 competition[90].

Table 2.9: Performance comparison on UF test cases: average *IGD* (variance within parenthesis.

	MACS2	MACS	MOEA/D	MTS	DMOEADD
UF1	$4.37 \cdot 10^{-3}$ ($1.67 \cdot 10^{-8}$)	$1.15 \cdot 10^{-1}$ ($1.66 \cdot 10^{-3}$)	$4.35 \cdot 10^{-3}$	$6.46 \cdot 10^{-3}$	$1.04 \cdot 10^{-2}$
UF2	$4.48 \cdot 10^{-3}$ ($1.16 \cdot 10^{-8}$)	$5.42 \cdot 10^{-2}$ ($4.19 \cdot 10^{-4}$)	$6.79 \cdot 10^{-3}$	$6.15 \cdot 10^{-3}$	$6.79 \cdot 10^{-3}$
UF3	$2.29 \cdot 10^{-2}$ ($5.21 \cdot 10^{-6}$)	$6.56 \cdot 10^{-2}$ ($1.42 \cdot 10^{-3}$)	$7.42 \cdot 10^{-3}$	$5.31 \cdot 10^{-2}$	$3.34 \cdot 10^{-2}$
UF4	$2.64 \cdot 10^{-2}$ ($3.48 \cdot 10^{-7}$)	$3.36 \cdot 10^{-2}$ ($1.66 \cdot 10^{-5}$)	$6.39 \cdot 10^{-2}$	$2.36 \cdot 10^{-2}$	$4.27 \cdot 10^{-2}$
UF5	$2.95 \cdot 10^{-2}$ ($1.56 \cdot 10^{-5}$)	$6.44 \cdot 10^{-2}$ ($1.17 \cdot 10^{-3}$)	$1.81 \cdot 10^{-1}$	$1.49 \cdot 10^{-2}$	$3.15 \cdot 10^{-1}$
UF6	$3.31 \cdot 10^{-2}$ ($7.42 \cdot 10^{-4}$)	$2.40 \cdot 10^{-1}$ ($1.43 \cdot 10^{-2}$)	$1.76 \cdot 10^{-1}$	$5.91 \cdot 10^{-2}$	$6.67 \cdot 10^{-2}$
UF7	$6.12 \cdot 10^{-3}$ ($3.14 \cdot 10^{-6}$)	$1.69 \cdot 10^{-1}$ ($1.22 \cdot 10^{-2}$)	$4.44 \cdot 10^{-3}$	$4.08 \cdot 10^{-2}$	$1.03 \cdot 10^{-2}$
UF8	$4.98 \cdot 10^{-2}$ ($2.05 \cdot 10^{-6}$)	$2.35 \cdot 10^{-1}$ ($1.77 \cdot 10^{-3}$)	$5.84 \cdot 10^{-2}$	$1.13 \cdot 10^{-1}$	$6.84 \cdot 10^{-2}$
UF9	$3.23 \cdot 10^{-2}$ ($2.05 \cdot 10^{-6}$)	$2.68 \cdot 10^{-1}$ ($1.71 \cdot 10^{-2}$)	$7.90 \cdot 10^{-2}$	$1.14 \cdot 10^{-1}$	$4.90 \cdot 10^{-2}$
UF10	$1.41 \cdot 10^{-1}$ ($5.59 \cdot 10^{-5}$)	1.25 ($4.28 \cdot 10^{-1}$)	$4.74 \cdot 10^{-1}$	$1.53 \cdot 10^{-1}$	$3.22 \cdot 10^{-1}$

As shown in Table 2.9, the tuned version of MACS2 outperforms the other algorithms on UF2, 3, 6, 8, 9 and 10, on UF1 is very close to MOEA/D, while it ranks second on UF5 and 10 and finally third on UF7. In Table 2.6 one can find the comparison against the old version MACS on the ZDT test set. MACS2 results generally better except on the ZDT4 case. Note that M_{spr} of MACS for both ZDT2 and ZDT6 is always between $6 \cdot 10^{-3}$ and $9 \cdot 10^{-3}$, therefore always above the chosen threshold τ_{spr}. The poor performance of MACS2 on ZDT4, might be due to the relative ineffectiveness of the pattern search along the coordinates on this particular test case. In the attempt to improve performance on ZDT4, a second test set was run with a slightly modified version of MACS2: the number of components which are explored by each agent at the h-th iteration was reduced to 1 only, compared to the n in Algorithm 2.2, at the same time, all individuals were performing social actions, i.e. $n_{social}=n_{pop}$. With these modifications, a success rate of 0.66 both on convergence and spreading is achieved although the p_{conv} and p_{spr} on ZDT2 drops to 0 and the p_{conv} on ZDT6 drops to 0.23.

Table 2.10: Comparison of MACS, MACS2 and MOEA/D on 3-impulse and Cassini test cases.

	3-impulse		Cassini	
	p_{conv}	p_{spr}	p_{conv}	p_{spr}
MACS	0.99	0.99	0.87	0.49
MACS2 (tuned)	0.99	1	0.77	0.34
MOEA/D	1	0.49	0.51	0.01
MTS	0.57	1	0.05	0.32
NSGA-II	0.03	1	0.90	0.26

Table 2.10 shows a comparison of the performance of MACS2 on 3-impulse and Cassini, against MACS, MOEA/D, MTS and NSGA-II. Both MACS and MACS2 are able to reliably solve the 3-impulse case, while MOEA/D manages to attain good convergence but with only mediocre spreading. On the contrary, both MTS and NSGA-II achieve good spreading but worse convergence, indicating that their fronts are quite well distributed but probably too distant from the true Pareto front.

Cassini is a rather difficult problem and this is reflected by the generally lower metrics achieved by most algorithms. Only MACS, MACS2 and NSGA-II reach a high convergence ratio, but for the last two, their spreading is still rather low. After inspection of each of the 200 Pareto fronts one can see that such a low spreading implies that the algorithm did not converge to the global Pareto front. Figure 2.3 illustrates the difference

between MACS and NSGA-II. The behaviour of MACS2 is similar to the one of NSGA-II. MACS achieves the best known value for objective function Δv. Both NSGA-II and MACS2 instead fall in the basin of attraction of the second best value for objective function Δv[Error! Bookmark not defined.].

The performance of MOEA/D and MTS on Cassini is rather poor, with the former attaining only 50% convergence but with almost zero p_{spr}; conversely, only one third of the latter's runs are below the spreading threshold and almost none meets the convergence criterion.

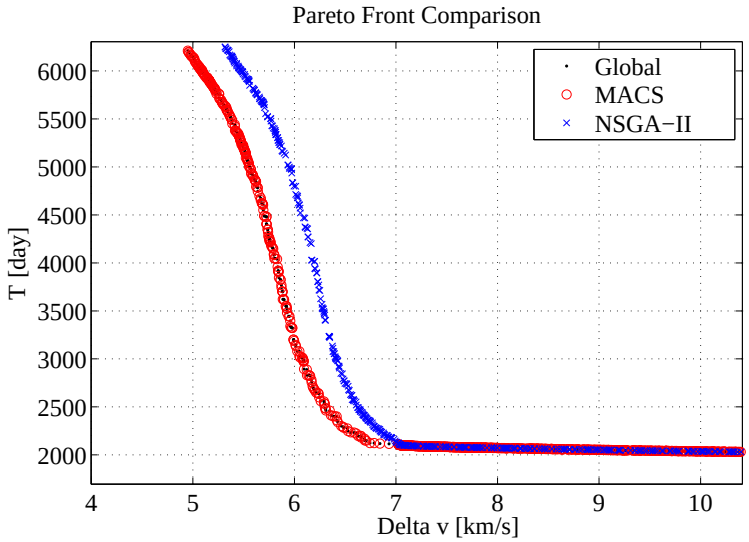

Figure 2.3: Comparison of Pareto fronts for the Cassini test case.

2.6 MACS2 with Monotonic Basin Hopping

The use of Tchebycheff decomposition leads to the possibility to introduce Monotonic Basin Hopping steps[97] in the action set of each agent. MBH steps are introduced as a sampling technique in the individualistic actions but only for the individuals which are solving the m pure single objective subproblems.

In this variant of the individualistic actions, at each iteration, first the standard search along the coordinates is performed (as described in Section 2.4.2); then, the actions described in Algorithm 2.6, are performed. For each of the m single-objective subproblems, a sample is taken in the domain D and then MatLab®'s *fmincon* is used to solve this subproblem using this point as a first guess, attaining convergence to a local minimum. If this latter point is better than the current individual which solves this subproblem, it will replace it. Otherwise, the new point could still replace the current individual with a probability $1/n$.

This variant has been tested on the Cassini introducing the MBH step only in the action set of the two agents that are solving the extremal single objective problems. The Cassini

case resulted to be quite challenging for MACS2 it is known to have an interesting funnel structure[87]. The MBH steps yield a marked improvement in both convergence and spreading compared to the standard version of MACS2, with a p_{conv} increasing to 85% and p_{spr} to 99%. This improvement is related essentially to a much closer convergence in the part of the front corresponding to the minimum ΔV solution.

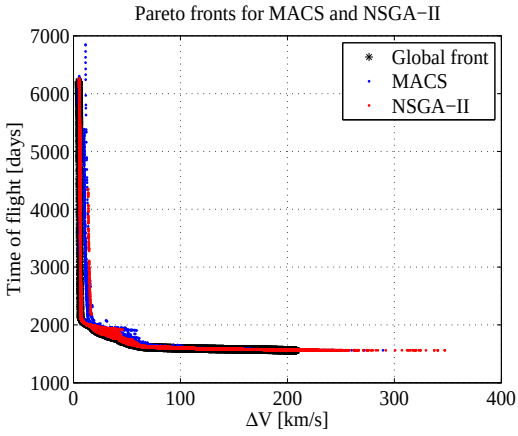

a) NSGA-II and MACS full fronts

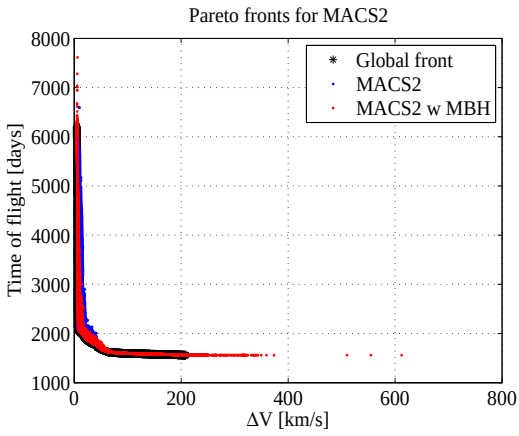

c) MACS2 and MACS2+MBH full fronts

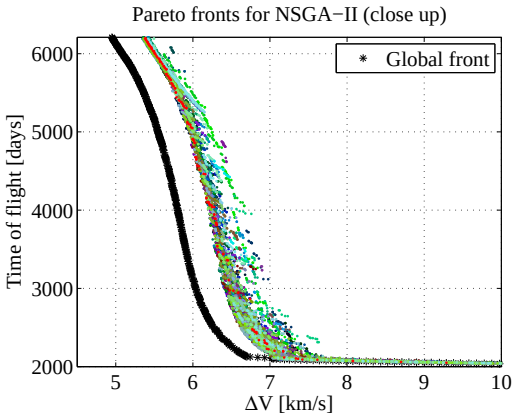

c) NSGA-II

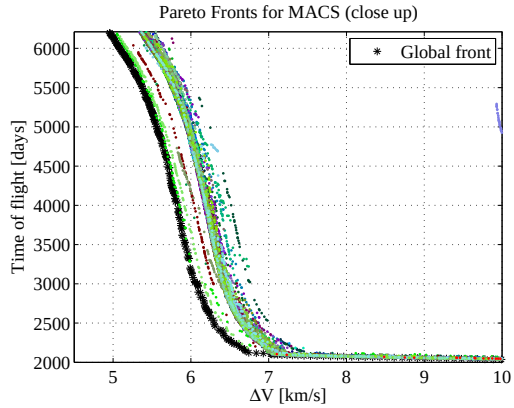

d) MACS

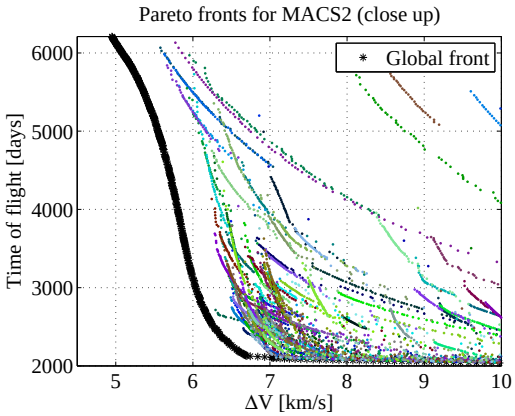

e) MACS2

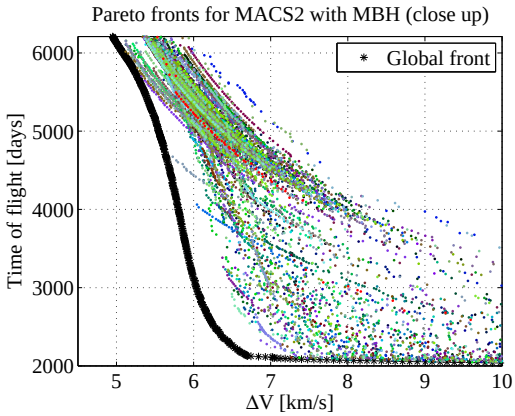

f) MACS2 with MBH step

Figure 2.4: NSGA-II, MACS, MACS2 on the Cassini case: a) NSGA-II and MACS b) MACS2 and MACS2 with MBH step c) NSGA-II close-up d) MACS close-up e) MACS2 close-up f) MACS2 with MBH step close-up.

Figure 2.4 shows the distribution of the Pareto fronts of MACS2 with MBH steps over the 200 runs. The MBH steps effectively contribute to increase the probability of identifying the single objective minimum, leading to an improved convergence also in its neighbourhood. However, the current implementation of MBH steps is less effective at improving other parts of the front and more work is required in this direction.

Algorithm 2.6 Monotonic Basin Hopping.

for all $i = 1 : m$ **do**
  Take a random individual $\mathbf{y}_0 \in \mathcal{D}$
  $j = \{j \in I_\lambda | \lambda_{j,k} = 1, \text{if } k = i, \lambda_{j,k} = 0, \text{if } k \neq i\}$
  Starting from $\mathbf{y}_0$, find a local minimum $\mathbf{y}_{min}$ of f_i with a gradient-based optimiser
  if $\mathbf{f_i}(\mathbf{y}_{min}) <= f_i(\mathbf{x_j})$ **then**
    $\mathbf{x}_j = \mathbf{y}_{min}$
    $\mathbf{f}_j = \mathbf{f}(\mathbf{y}_{min})$
  else
    Take a random number $r \in \mathcal{U}(0, 1)$
    if $r < 1/n$ **then**
      $\mathbf{x}_j = \mathbf{y}_{min}$
      $\mathbf{f}_j = \mathbf{f}(\mathbf{y}_{min})$
    end if
  end if
end for

2.7 Conclusions

This chapter has presented a version of Multi-Agent Collaborative Search based on Tchebycheff decomposition.

Compared to the previous version of MACS a number of heuristics has been revised and in particular there was an inversion of the percentage of agents performing social and individualistic moves. The new version, denominated MACS2, demonstrated remarkable performance on known difficult benchmarks outperforming known algorithms. On the Cassini real case application, and on benchmark function ZDT4, MACS2 falls back behind its predecessor. In both cases there are multiple local Pareto fronts corresponding to strong attractors. From a first analysis it seems that the simple pattern search implemented in MACS2 is not sufficient and is limited by its search along the coordinates only. In MACS the search included random directions and directions derived from DE and PSO heuristics. It seems reasonable to assume that a more flexible set of individualistic moves might further improve MACS2. This is the subject of current developments. In addition, the introduction of MBH steps in the Tchebycheff decomposition framework provided a net improvement of the performance. Also, from the tests performed so far the actual contribution of the utility function is uncertain and more investigations are underway.

The use of a selection operator based on Tchebycheff decomposition, instead, appears to be beneficial in a number of cases. In MACS2, in particular, agents operating at the extreme of the range of each of each objective are always preserved and forced to improve a subproblem.

In summary, the results presented in this chapter have shown MACS2 to be a very efficient MO algorithm compared to other state-of-the-art proposals. Therefore, it is an excellent candidate for the solution of expensive optimisation problems involving Low Thrust dynamics, as will be shown in Chapter 4, Chapter 6, Chapter 7 and Chapter 8.

Chapter 3.Low-Thrust Analytical Formulae

This chapter presents a set of analytical solutions for the perturbed Keplerian motion of a spacecraft under the effect of constant control acceleration. The proposed set of formulae can treat control accelerations that are fixed in either a rotating or inertial reference frame. Moreover, the contribution of the J_2 zonal harmonic is included in the analytical formulae. It will be shown that the proposed analytical theory allows for the fast computation of long, multi-revolution spirals while maintaining good accuracy. The combined effect of different perturbations and of the shadow regions due to solar eclipse is also included. The accuracy and speed of the proposed analytical formulae are compared against a full numerical integration with different integration schemes. This chapter is organised as follows: Section 3.1 will introduce in detail the analytical formulae; Section 3.1.6 will present an analysis of their accuracy compared to numerical integration schemes while Section 3.2 will focus on their applicability for propagating long trajectory arcs.

3.1 Analytical Formulae

Let the state of the spacecraft be expressed in terms of non-singular Equinoctial Elements[98]:

$$\begin{aligned} a \\ P_1 &= e\sin\left(\Omega+\omega\right) \\ P_2 &= e\cos\left(\Omega+\omega\right) \\ Q_1 &= \tan\frac{i}{2}\sin\Omega \\ Q_2 &= \tan\frac{i}{2}\cos\Omega \\ L &= \Omega+\omega+\theta \end{aligned} \tag{3.1}$$

then, the perturbed Keplerian motion is governed by Gauss' planetary equations:

$$\frac{da}{dt}=\frac{2}{B}\sqrt{\frac{a^3}{\mu}}\left[\left(P_2\sin L-P_1\cos L\right)a_r+\Phi\left(L\right)a_\theta\right]$$

$$\frac{dP_1}{dt}=B\sqrt{\frac{a}{\mu}}\left[-a_r\cos L+\left(\frac{P_1+\sin L}{\Phi\left(L\right)}+\sin L\right)a_\theta-P_2\frac{Q_1\cos L-Q_2\sin L}{\Phi\left(L\right)}a_h\right]$$

$$\frac{dP_2}{dt}=B\sqrt{\frac{a}{\mu}}\left[a_r\sin L+\left(\frac{P_2+\cos L}{\Phi\left(L\right)}+\cos L\right)a_\theta+P_1\frac{Q_1\cos L-Q_2\sin L}{\Phi\left(L\right)}a_h\right]$$

$$\frac{dQ_1}{dt}=\frac{B}{2}\sqrt{\frac{a}{\mu}}\left(1+Q_1^2+Q_2^2\right)\frac{\sin L}{\Phi\left(L\right)}a_h$$

$$\frac{dQ_2}{dt}=\frac{B}{2}\sqrt{\frac{a}{\mu}}\left(1+Q_1^2+Q_2^2\right)\frac{\cos L}{\Phi\left(L\right)}a_h$$

$$\frac{dl}{dt}=\sqrt{\frac{\mu}{a^3}}-B\sqrt{\frac{a}{\mu}}\left\{\left[\frac{P_1\sin L+P_2\cos L}{1+B}+\frac{2B}{\Phi\left(L\right)}\right]a_r-\right.$$

$$\left.-\frac{\left(1+\Phi\left(L\right)\right)\left(P_2\sin L-P_1\cos L\right)}{\Phi\left(L\right)\left(1+B\right)}a_\theta+\frac{Q_1\cos L-Q_2\sin L}{\Phi\left(L\right)}a_h\right\} \tag{3.2}$$

with:

$$\begin{aligned}B&=\sqrt{1-P_1^2-P_2^{\,2}}=\sqrt{1-e^2}\\ \Phi\left(L\right)&=1+P_1\sin L+P_2\cos L\end{aligned} \tag{3.3}$$

l is the mean longitude, analogous to the true longitude L, but defined as a function of the mean anomaly M instead of the true anomaly θ:

$$l=\Omega+\omega+M \tag{3.4}$$

a_r, a_θ, a_h, are the components of the thrust acceleration in the radial-transverse-normal (r-θ-h) reference frame, as seen in Figure 3.1, where O is the centre of the central gravitational body, $\hat{i},\hat{j},\hat{k}$ are the unit vectors of the inertial reference frame centred in O, **r** is the position vector and $\hat{t},\hat{r},\hat{h}$ are the unit vectors transversal, radial and out of plane. **u** is the perturbing acceleration vector, which in the radial-transversal reference frame is defined as which can also be expressed in terms of modulus ε, azimuth α and elevation β as:

$$\mathbf{u}=\begin{Bmatrix}a_r\\ a_\theta\\ a_h\end{Bmatrix}=\begin{Bmatrix}\varepsilon\cos\beta\cos\alpha\\ \varepsilon\cos\beta\sin\alpha\\ \varepsilon\sin\beta\end{Bmatrix} \tag{3.5}$$

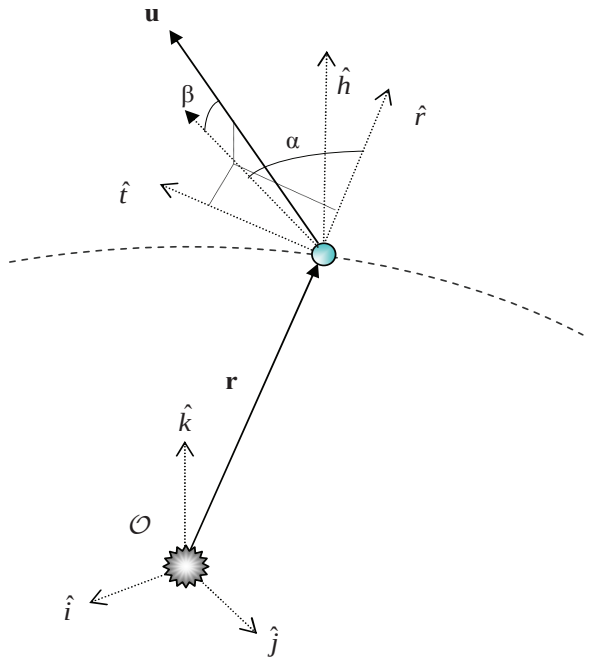

Figure 3.1: Radial-transverse-normal (r- θ -h) reference frame.

If one assumes that the modulus of the perturbative acceleration is small compared to the local gravitational acceleration, one can write:

$$\frac{dt}{dL} \approx \frac{r^2}{h} = \sqrt{\frac{a^3}{\mu}} \frac{B^3}{\Phi^2(L)} \tag{3.6}$$

By substituting (3.6) into Eqs. (3.2) one obtains a system of equations in the longitude L:

$$\begin{aligned}
\frac{da}{dL} &= \varepsilon \frac{2a^3B^2}{\mu}\left[\frac{\left(P_2 \sin L - P_1 \cos L\right)}{\Phi^2(L)}\cos\alpha + \frac{1}{\Phi(L)}\sin\alpha\right]\cos\beta \\
\frac{dP_1}{dL} &= \varepsilon \frac{B^4a^2}{\mu}\left[\left(-\frac{\cos L}{\Phi^2(L)}\cos\alpha + \left(\frac{P_1+\sin L}{\Phi^3(L)} + \frac{\sin L}{\Phi^2(L)}\right)\sin\alpha\right)\cos\beta - P_2\frac{Q_1\cos L - Q_2\sin L}{\Phi^3(L)}\sin\beta\right] \\
\frac{dP_2}{dL} &= \varepsilon \frac{B^4a^2}{\mu}\left[\left(\frac{\sin L}{\Phi^2(L)}\cos\alpha + \left(\frac{P_2+\cos L}{\Phi^3(L)} + \frac{\cos L}{\Phi^2(L)}\right)\sin\alpha\right)\cos\beta + P_1\frac{Q_1\cos L - Q_2\sin L}{\Phi^3(L)}\sin\beta\right] \\
\frac{dQ_1}{dL} &= \varepsilon \frac{B^4a^2}{2\mu}\left(1+Q_1^{\,2}+Q_2^{\,2}\right)\frac{\sin L}{\Phi^3(L)}\sin\beta \\
\frac{dQ_2}{dL} &= \varepsilon \frac{B^4a^2}{2\mu}\left(1+Q_1^{\,2}+Q_2^{\,2}\right)\frac{\cos L}{\Phi^3(L)}\sin\beta
\end{aligned} \tag{3.7}$$

or, in vector form, taking **E** as the first five equinoctial elements as in (3.1):

$$\frac{d\mathbf{E}}{dL} = \varepsilon F\left(\mathbf{E}, L, \alpha, \beta\right) \tag{3.8}$$

As classical Regular Perturbation theory shows (see, for example, Holmes[99] or Sanders, Verhulst and Murdock[100]), one can express the solution of Equation (3.8) as an expansion

in the small parameter ε, with respect to a set of reference conditions $\mathbf{E}_0 = [a_0, P_{10}, P_{20}, Q_{10}, Q_{20}]^T$:

$$\mathbf{E} \approx \mathbf{E}_0 + \varepsilon \mathbf{E}_1 + \varepsilon^2 \mathbf{E}_2 + O\left(\varepsilon^3\right) = \left\{ \begin{array}{c} a_0 + \varepsilon a_1 + \varepsilon^2 a_2 \\ P_{10} + \varepsilon P_{11} + \varepsilon^2 P_{12} \\ P_{20} + \varepsilon P_{21} + \varepsilon^2 P_{22} \\ Q_{10} + \varepsilon Q_{11} + \varepsilon^2 Q_{12} \\ Q_{20} + \varepsilon Q_{21} + \varepsilon^2 Q_{22} \end{array} \right\} + O\left(\varepsilon^3\right) \tag{3.9}$$

Substituting (3.9) into (3.8), and expanding the right side in Taylor series with respect to ε, one obtains:

$$\begin{aligned} &\frac{d\mathbf{E}_0}{dL} + \varepsilon \frac{d\mathbf{E}_1}{dL} + \varepsilon^2 \frac{d\mathbf{E}_2}{dL} + \ldots = 0 + \left. \frac{d\left(\varepsilon F\left(\mathbf{E}_0 + \varepsilon \mathbf{E}_1 + \ldots, L, \alpha, \beta\right)\right)}{d\varepsilon} \right|_{\varepsilon=0} \varepsilon + \\ &+ \left. \frac{d^2\left(\varepsilon F\left(\mathbf{E}_0 + \varepsilon \mathbf{E}_1 + \ldots, L, \alpha, \beta\right)\right)}{d\varepsilon^2} \right|_{\varepsilon=0} \frac{\varepsilon^2}{2} + \ldots \end{aligned} \tag{3.10}$$

By collecting the terms which depend from the same powers of ε, neglecting second and higher order terms, one obtains:

$$\begin{aligned} \frac{d\mathbf{E}_0}{dL} = 0 \Rightarrow \mathbf{E}_0 = const \\ \varepsilon \frac{d\mathbf{E}_1}{dL} = \varepsilon F\left(\mathbf{E}_0, L, \alpha, \beta\right) \end{aligned} \tag{3.11}$$

Therefore the first-order expansion in ε becomes:

$$\mathbf{E}_1\left(L\right) = \mathbf{E}_0 + \varepsilon \int_{L_0}^{L} F\left(\mathbf{E}_0, \mathcal{L}, \alpha, \beta\right) d\mathcal{L} \tag{3.12}$$

To obtain a first-order expansion for the time as a function of L, let one consider Equation (3.6) and apply a similar procedure as done for **E** (Note that, the last equation in (3.2) becomes now redundant and therefore will be ignored from now onwards). First, let one expand the time in the form:

$$t = t_0 + \varepsilon t_1 + \varepsilon^2 t_2 + \varepsilon^3 t_3 + \ldots \tag{3.13}$$

and define the right-hand side of (3.6) as $H(a,P_1,P_2,L)$, then, by expanding H in Taylor series as done previously, one obtains:

$$\frac{dt_0}{dL} + \varepsilon \frac{dt_1}{dL} + \varepsilon^2 \frac{dt_2}{dL} + \ldots \simeq H\left(a_0, P_{10}, P_{20}, L\right) + \left. \frac{dH}{d\varepsilon} \right|_{\varepsilon=0} \varepsilon + \left. \frac{d^2 H}{d\varepsilon^2} \right|_{\varepsilon=0} \varepsilon^2 + \ldots \tag{3.14}$$

and taking only the first order term in ε, one can write:

$$\frac{dt_0}{dL} + \varepsilon \frac{dt_1}{dL} = H\left(a_0, P_{10}, P_{20}, L\right) + \frac{dH}{d\mathbf{E}} \frac{d\mathbf{E}}{d\varepsilon} \varepsilon \tag{3.15}$$

again taking only the first order term in ε, one obtains:

$$\begin{aligned} \frac{dt_0}{dL} &= H\left(a_0, P_{10}, P_{20}, L\right) \\ \varepsilon\frac{dt_1}{dL} &= \varepsilon\left(\left.\frac{dH}{da}\right|_{a_0,P_{10},P_{20}} a_1 + \left.\frac{dH}{dP_1}\right|_{a_0,P_{10},P_{20}} P_{11} + \left.\frac{dH}{dP_2}\right|_{a_0,P_{10},P_{20}} P_{21}\right) \end{aligned} \tag{3.16}$$

These two equations can be integrated in L to obtain an expression in the form:

$$t = t_0 + \varepsilon t_1 \tag{3.17}$$

where:

$$\begin{aligned} t_0(L) &= t_{00} + \int_{L_0}^{L} \sqrt{\frac{a_0^{\,3}}{\mu}} \frac{B_0^{\,3}}{\Phi_0^{\,2}(\mathcal{L})} d\mathcal{L} \\ t_1(L) &= \int_{L_0}^{L} \sqrt{\frac{a_0}{\mu}} B_0 \left\{ \frac{3B_0^{\,2}}{2} \frac{a_1(\mathcal{L})}{\Phi_0^{\,2}(\mathcal{L})} - a_0 \left[\begin{array}{l} \left(\dfrac{3P_{10}}{\Phi_0^{\,2}(\mathcal{L})} + 2B_0^{\,2} \dfrac{\sin\mathcal{L}}{\Phi_0^{\,3}(\mathcal{L})} \right) P_{11}(\mathcal{L}) + \\ \left(\dfrac{3P_{20}}{\Phi_0^{\,2}(\mathcal{L})} + 2B_0^{\,2} \dfrac{\cos\mathcal{L}}{\Phi_0^{\,3}(\mathcal{L})} \right) P_{21}(\mathcal{L}) \end{array} \right] \right\} d\mathcal{L} \end{aligned} \tag{3.18}$$

Note that the zero-order term t_0 is not simply the time t_{00} corresponding to L_0, but includes also the time variation given by the unperturbed Keplerian motion. In addition, the presence of the terms a_1, P_{11}, P_{21} essentially implies a double integration between L_0 and L.

3.1.1 Constant Acceleration in the r-θ-h Frame

If one assumes a constant acceleration modulus and direction in the r-θ-h frame, then Eqs. (3.7) take the following form:

$$\begin{aligned} a^{r\vartheta h} &= a_0 + \varepsilon^{r\vartheta h} \frac{2B_0^{\,2}a_0^{\,3}}{\mu} \cos\beta \left[\left(\frac{1}{\Phi_0(L)} - \frac{1}{\Phi_0(L_0)} \right) \cos\alpha + I_{11}\sin\alpha \right] \\ P_1^{r\vartheta h} &= P_{10} + \varepsilon^{r\vartheta h} \frac{B_0^{\,4}a_0^{\,2}}{\mu} \left[\cos\beta \left(-I_{c2}\cos\alpha + \left(I_{13}P_{10} + I_{s3} + I_{s2} \right)\sin\alpha \right) - P_{20}\left(Q_{10}I_{c3} - Q_{20}I_{s3} \right)\sin\beta \right] \\ P_2^{r\vartheta h} &= P_{20} + \varepsilon^{r\vartheta h} \frac{B_0^{\,4}a_0^{\,2}}{\mu} \left[\cos\beta \left(I_{s2}\cos\alpha + \left(I_{13}P_{20} + I_{c3} + I_{c2} \right)\sin\alpha \right) + P_{10}\left(Q_{10}I_{c3} - Q_{20}I_{s3} \right)\sin\beta \right] \\ Q_1^{r\vartheta h} &= Q_{10} + \varepsilon^{r\vartheta h} \frac{B_0^{\,4}a_0^{\,2}}{2\mu} \left(1 + Q_1^2 + Q_2^2 \right) I_{s3}\sin\beta \\ Q_2^{r\vartheta h} &= Q_{20} + \varepsilon^{r\vartheta h} \frac{B_0^{\,4}a_0^{\,2}}{2\mu} \left(1 + Q_1^2 + Q_2^2 \right) I_{c3}\sin\beta \end{aligned} \tag{3.19}$$

where the terms expressed as I_{xx} are integrals in L in the form I_{cn}, I_{sn} and I_{1n}, with n = 1,2,3, are integrals in L in the form:

$$I_{cn} = \int_{L_0}^{L} \frac{\cos\mathcal{L}}{\Phi_0^{\,n}(\mathcal{L})} d\mathcal{L}; \quad I_{sn} = \int_{L_0}^{L} \frac{\sin\mathcal{L}}{\Phi_0^{\,n}(\mathcal{L})} d\mathcal{L}; \quad I_{1n} = \int_{L_0}^{L} \frac{1}{\Phi_0^{\,n}(\mathcal{L})} d\mathcal{L} \tag{3.20}$$

where Φ_0 is the term in (3.3) evaluated with $P_1=P_{10}$ and $P_2=P_{20}$. The analytical form for these integrals is reported in Appendix A. Regarding the first-order term of the time equation (3.18), as already noted in the previous section, some of the integrals in (3.20) are multiplied by a function of L and again integrated between L_0 and L. For the term depending on a_1, an analytical expression can be found in the form:

$$t_1^{r\vartheta h} = 3\sqrt{\frac{a_0^{\,7}}{\mu^3}} B_0^{\,5} \cos\beta \left(\cos\alpha I_{t1} + \sin\alpha I_{t2}\right) \tag{3.21}$$

where:

$$I_{t1} = \int_{L_0}^{L} \frac{1}{\Phi_0^{\,2}(\mathcal{L})} \left(\frac{1}{\Phi_0(\mathcal{L})} - \frac{1}{\Phi_0(L_0)} \right) d\mathcal{L} \quad I_{t2} = \int_{L_0}^{L} \frac{I_{11}(\mathcal{L})}{\Phi_0^{\,2}(\mathcal{L})} d\mathcal{L} \tag{3.22}$$

The analytical expressions for these integrals are also found in Appendix A. Numerical analysis has shown that neglecting the terms depending on P_1 and P_2 does not introduce a relevant error in the cases analysed in this paper.

3.1.2 Constant Inertial Acceleration

A constant acceleration in the inertial reference frame can be expressed, in the r-θ-h frame, as a function of the longitude L:

$$a_r^{\,In} = \varepsilon^{In} \cos\beta_0 \cos(\gamma_0 - L) \quad a_\theta^{\,In} = \varepsilon^{In} \cos\beta_0 \sin(\gamma_0 - L) \quad a_h^{\,In} = \varepsilon^{In} \sin\beta_0 \tag{3.23}$$

where γ_0 derives from the initial acceleration azimuth α_0 at L_0, as:

$$\gamma_0 = \alpha_0 + L_0 \tag{3.24}$$

Note that the initial azimuth α_0 and elevation β_0 are expressed with respect to the r-θ-h frame at L_0. By substituting (3.23) into (3.7), and after some manipulation, one can obtain an expression analogous to (3.19):

$$\begin{aligned}
a^{In} &= a_0 + \varepsilon^{In} \frac{2B_0^{\,2} a_0^{\,3}}{\mu} \cos\beta_0 \left[-\left(P_{10} I_{12} + I_{s2}\right)\cos\gamma_0 + \left(P_{20} I_{12} + I_{c2}\right)\sin\gamma_0 \right] \\
P_1^{In} &= P_{10} + \varepsilon^{In} \frac{B_0^{\,4} a_0^{\,2}}{\mu} \Big\{ \cos\beta_0 \left[-\left(P_{10} I_{s3} + I_{12} + I_{2s3}\right)\cos\gamma_0 + \right. \\
&\quad \left. + \left(P_{10} I_{c3} + I_{1c1s3}\right)\sin\gamma_0 \right] - \sin\beta_0 P_{20} \left(Q_{10} I_{c3} - Q_{20} I_{s3}\right) \Big\} \\
P_2^{In} &= P_{20} + \varepsilon^{In} \frac{B_0^{\,4} a_0^{\,2}}{\mu} \Big\{ \cos\beta_0 \left[-\left(P_{20} I_{s3} + I_{1c1s3}\right)\cos\gamma_0 + \right. \\
&\quad \left. + \left(P_{20} I_{c3} + I_{12} + I_{2c3}\right)\sin\gamma_0 \right] + \sin\beta_0 P_{10} \left(Q_{10} I_{c3} - Q_{20} I_{s3}\right) \Big\} \\
Q_1^{\,In} &= Q_{10} + \varepsilon^{In} \frac{B_0^{\,4} a_0^{\,2}}{2\mu} \left(1 + Q_1^2 + Q_2^2\right) \sin\beta_0 I_{s3} \\
Q_2^{\,In} &= Q_{20} + \varepsilon^{In} \frac{B_0^{\,4} a_0^{\,2}}{2\mu} \left(1 + Q_1^2 + Q_2^2\right) \sin\beta_0 I_{c3}
\end{aligned} \tag{3.25}$$

where the integral terms I_{1c1s3}, I_{2c3} and I_{2s3} are given in Appendix A. Similarly, the first-order perturbative term in the time equation translates into:

$$t_1^{In} = 3\sqrt{\frac{a_0^{\,7}}{\mu^3}} B_0^{\,5} \cos\beta_0 \left\{ -\frac{\cos\gamma_0}{P_{20}} \left[\left(I_{13} + P_{10} I_{s3} \right) - \frac{\left(1 + P_{10}\sin L_0\right)}{\Phi_0\left(L_0\right)} I_{12} \right] + \sin\gamma_0 \left(I_{s3} - \frac{\sin L_0}{\Phi_0\left(L_0\right)} I_{12} \right) \right\} \quad (3.26)$$

3.1.3 Constant Tangential Acceleration

A constant acceleration along the tangential direction can be expressed, in the r-θ-h frame, as a function of the longitude L:

$$a_r^{\,t} = \varepsilon^t \frac{P_2 \sin L - P_1 \cos L}{D} \quad a_\theta^{\,t} = \varepsilon^t \frac{1 + P_1 \sin L + P_2 \cos L}{D} \quad a_h^{\,t} = 0 \qquad (3.27)$$

where D is expressed as:

$$D = \sqrt{1 + P_1^{\,2} + P_2^{\,2} + 2\left(P_1 \sin L + P_2 \cos L\right)} \qquad (3.28)$$

Again, by substituting (3.27) into (3.7) one obtains:

$$\begin{aligned}
a^t &= a_0 + \varepsilon^t \frac{2 B_0^{\,2} a_0^{\,3}}{\mu} \int_{L_0}^{L} \frac{1}{D_0\left(\mathcal{L}\right)} \left(\frac{2}{\Phi_0\left(\mathcal{L}\right)} - \frac{B_0^{\,2}}{\Phi_0\left(\mathcal{L}\right)^2} \right) d\mathcal{L} \\
P_1^t &= P_{10} + \varepsilon^t \frac{B_0^{\,4} a_0^{\,2}}{\mu} \int_{L_0}^{L} \frac{2\left(P_{10} + \sin\mathcal{L}\right)}{D_0\left(\mathcal{L}\right)\Phi_0\left(\mathcal{L}\right)^2} d\mathcal{L} \\
P_2^{\,t} &= P_{20} + \varepsilon^t \frac{B_0^{\,4} a_0^{\,2}}{\mu} \int_{L_0}^{L} \frac{2\left(P_{20} + \cos\mathcal{L}\right)}{D_0\left(\mathcal{L}\right)\Phi_0\left(\mathcal{L}\right)^2} d\mathcal{L} \\
Q_1^{\,t} &= Q_{10} \\
Q_2^{\,t} &= Q_{20}
\end{aligned} \qquad (3.29)$$

D_0 is simply D evaluated with P_{10} and P_{20}. The three integral terms are more conveniently expressed with respect to the true anomaly θ and eccentricity e, assuming that $\theta \approx L - \left(\Omega_0 + \omega_0\right)$:

$$\begin{aligned}
\int_{L_0}^{L} \frac{1}{D_0\left(\mathcal{L}\right)} \left(\frac{2}{\Phi_0\left(\mathcal{L}\right)} - \frac{B_0^{\,2}}{\Phi_0\left(\mathcal{L}\right)^2} \right) d\mathcal{L} &= \int_{\theta_0}^{\theta} \frac{\sqrt{1 + e_0^{\,2} + 2e_0\cos\vartheta}}{\left(1 + e_0\cos\vartheta\right)^2} d\vartheta = I_a \\
\int_{L_0}^{L} \frac{2\left(P_{10} + \sin\mathcal{L}\right)}{D_0\left(\mathcal{L}\right)\Phi_0\left(\mathcal{L}\right)^2} d\mathcal{L} &= \sin\left(\Omega_0 + \omega_0\right) I_{P1} + \cos\left(\Omega_0 + \omega_0\right) I_{P2} \\
\int_{L_0}^{L} \frac{2\left(P_{20} + \cos\mathcal{L}\right)}{D_0\left(\mathcal{L}\right)\Phi_0\left(\mathcal{L}\right)^2} d\mathcal{L} &= \cos\left(\Omega_0 + \omega_0\right) I_{P1} - \sin\left(\Omega_0 + \omega_0\right) I_{P2}
\end{aligned} \qquad (3.30)$$

where

$$I_{P1} = \int_{\theta_0}^{\theta} \frac{e_0 + \cos\vartheta}{\sqrt{1+e_0^{\,2}+2e_0\cos\vartheta}\left(1+e_0\cos\vartheta\right)^2} d\vartheta$$
$$I_{P2} = \int_{\theta_0}^{\theta} \frac{\sin\vartheta}{\sqrt{1+e_0^{\,2}+2e_0\cos\vartheta}\left(1+e_0\cos\vartheta\right)^2} d\vartheta \tag{3.31}$$

The primitives of I_a, I_{P1} and I_{P2} are available in closed form and are reported in Appendix A. Note that, in (A.14) and (A.15) there are terms which represent incomplete elliptic integrals of the first and second kind, represented as E and F respectively. In this work, E and F are conveniently evaluated numerically using Carlson's Duplication Algorithms[101]. Rearranging the terms in (3.29), one obtains, (omitting the expressions for Q_1 and Q_2):

$$a^t = a_0 + \varepsilon^t \frac{2B_0^{\,2}a_0^{\,3}}{\mu} I_a$$
$$P_1^t = P_{10} + \varepsilon^t 2\frac{B_0^{\,4}a_0^{\,2}}{\mu}\left(\sin\left(\Omega_0+\omega_0\right)I_{P1} + \cos\left(\Omega_0+\omega_0\right)I_{P2}\right) \tag{3.32}$$
$$P_2^t = P_{20} + \varepsilon^t 2\frac{B_0^{\,4}a_0^{\,2}}{\mu}\left(\cos\left(\Omega_0+\omega_0\right)I_{P1} - \sin\left(\Omega_0+\omega_0\right)I_{P2}\right)$$

In the case of tangential thrust, in the first order term of the time equation (3.18) one has terms which depend on the above mentioned elliptic integrals, which appear in (3.30). After some manipulations, one would obtain:

$$t_1^{\,t}(\theta) = \frac{B_0^{\,5}a_0^{\,3.5}}{\mu^{1.5}} \int_{\theta_0}^{\theta} \frac{1}{\Phi_0^{\,2}(\vartheta)} \left\{ 3I_a(\vartheta) - \right.$$
$$\left. - \frac{1}{\Phi_0(\vartheta)_0} \left[\begin{array}{l} \left(6e_0 + 2e_0^{\,2}\cos\vartheta + 4\cos\vartheta\right) I_{P1}(\vartheta) + \\ 4\left(1-e_0^{\,2}\right)\sin\vartheta I_{P2}(\vartheta) \end{array} \right] \right\} d\vartheta \tag{3.33}$$

Expanding the terms in the integral, for example, considering only I_a (as in Eq. (A.14)), the following integral emerges:

$$\int_{\theta_0}^{\theta} \frac{1}{\left(1+e_0\cos\vartheta\right)} \left[\frac{1}{1-e_0} E\left(\frac{\vartheta}{2}, \frac{4e_0}{\left(1+e_0\right)^2}\right) + \frac{1}{1+e_0} F\left(\frac{\vartheta}{2}, \frac{4e_0}{\left(1+e_0\right)^2}\right) - \frac{\sqrt{1+e_0^{\,2}+2e_0\cos\vartheta}\, e_0\sin\vartheta}{\left(1-e_0\right)^2\left(1+e_0\cos\vartheta\right)} - \right.$$
$$\left. - \frac{1}{1-e_0} E\left(\frac{\theta_0}{2}, \frac{4e_0}{\left(1+e_0\right)^2}\right) + \frac{1}{1+e_0} F\left(\frac{\theta_0}{2}, \frac{4e_0}{\left(1+e_0\right)^2}\right) - \frac{\sqrt{1+e_0^{\,2}+2e_0\cos\theta_0}\, e_0\sin\theta_0}{\left(1-e_0\right)^2\left(1+e_0\cos\theta_0\right)} \right] d\vartheta \tag{3.34}$$

an expression for (3.18) with integral terms which have, for example, the following form:

$$\int_{\theta_0}^{\theta} \frac{E\left(\frac{\vartheta}{2}, \frac{4e_0}{\left(1+e_0\right)^2}\right)}{\left(1+e\cos\vartheta\right)} d\vartheta \tag{3.35}$$

Note that the terms $\int_{\theta_0}^{\theta} \frac{E\left(\frac{\vartheta}{2}, \frac{4e_0}{(1+e_0)^2}\right)}{(1+e_0\cos\vartheta)} d\vartheta$, $\int_{\theta_0}^{\theta} \frac{F\left(\frac{\vartheta}{2}, \frac{4e_0}{(1+e_0)^2}\right)}{(1+e_0\cos\vartheta)} d\vartheta$ are not available in closed form. Similar considerations apply to the terms in (3.32) depending on I_{P1} and I_{P2}. Therefore, in this case, it has been chosen to numerically integrate the time equation as in (3.18) with a quadrature method. Numerical tests have shown that, by setting the number of integration nodes at 6 per revolution, adequate accuracy is achieved.

3.1.4 J_2 Perturbation

The inhomogeneous gravity field of the Earth is usually modelled as a series expansion of harmonic functions whose coefficients are experimentally derived in order to match the observed motion of satellites. The strongest contribution to the motion of an Earth-orbiting satellite is given by the first zonal harmonic term, also known as J_2-term[98]. The effect of the J_2 term can be expressed as a perturbative term in the Gauss variational equations. In particular, the components of the J_2 perturbation in the r-θ-h frame can be expressed as[30]:

$$\begin{aligned} a_r^{J_2} &= \frac{3\mu J_2 R^2}{2B^8 a^4}\left[\frac{12}{G^2}\left(Q_1\cos L - Q_2\sin L\right)^2 - 1\right]\Phi^4(L) \\ a_\theta^{J_2} &= \frac{12\mu J_2 R^2}{B^8 G^2 a^4}\left(Q_2\cos L + Q_1\sin L\right)\left(Q_1\cos L - Q_2\sin L\right)\Phi^4(L) \\ a_h^{J_2} &= \frac{6\mu J_2 R^2}{B^8 G^2 a^4}\left(Q_1\cos L - Q_2\sin L\right)\left(1 - Q_1^2 - Q_2^2\right)\Phi^4(L) \end{aligned} \tag{3.36}$$

where R is the planetary radius and G is:

$$G = 1 + Q_1^2 + Q_2^2 \tag{3.37}$$

By substituting (3.36) into (3.7) and with the procedure previously described one can write the first-order variation of the Equinoctial Elements due to the J_2 perturbation. In a compact form, this can be expressed as:

$$\begin{aligned} a^{J_2} &= a_0 + \varepsilon^{J_2}\frac{a_0}{4G_0^2 B_0^6} I_{Ja}\left(L_0, L, P_{10}, P_{20}, Q_{10}, Q_{20}\right) \\ P_1^{J_2} &= P_{10} + \varepsilon^{J_2}\frac{1}{8G_0^2 B_0^4} I_{JP_1}\left(L_0, L, P_{10}, P_{20}, Q_{10}, Q_{20}\right) \\ P_2^{J_2} &= P_{20} + \varepsilon^{J_2}\frac{1}{8G_0^2 B_0^4} I_{JP_2}\left(L_0, L, P_{10}, P_{20}, Q_{10}, Q_{20}\right) \\ Q_1^{J_2} &= Q_{10} + \varepsilon^{J_2}\frac{1 - Q_{10}^2 - Q_{20}^2}{4G_0^2 B_0^4} I_{JQ_1}\left(L_0, L, P_{10}, P_{20}, Q_{10}, Q_{20}\right) \\ Q_2^{J_2} &= Q_{20} + \varepsilon^{J_2}\frac{1 - Q_{10}^2 - Q_{20}^2}{4G_0^2 B_0^4} I_{JQ_2}\left(L_0, L, P_{10}, P_{20}, Q_{10}, Q_{20}\right) \end{aligned} \tag{3.38}$$

where ε^{J_2} is defined as $\varepsilon^{J_2} = J_2 R^2 a_0^{-2}$. G_0 is G as in (3.37), evaluated with $Q_1=Q_{10}$ and $Q_2=Q_{20}$. The integral terms are represented as:

$$
\begin{aligned}
I_{Ja} &= 24\int_{L_0}^{L} \Phi_0^2(\mathcal{L}) \begin{pmatrix} (P_{20}\sin\mathcal{L} - P_{10}\cos\mathcal{L})\left(12(Q_{10}\cos\mathcal{L} - Q_{20}\sin\mathcal{L})^2 - G_0{}^2\right) \\ +2\Phi_0(\mathcal{L})(Q_{10}\cos\mathcal{L} - Q_{20}\sin\mathcal{L})(Q_{20}\cos\mathcal{L} + Q_{10}\sin\mathcal{L}) \end{pmatrix} d\mathcal{L} \\
I_{JP_1} &= 12\int_{L_0}^{L} \Phi_0(\mathcal{L}) \begin{pmatrix} -\cos\mathcal{L}\Phi_0(\mathcal{L})\left(12(Q_{20}\sin\mathcal{L} - Q_{10}\cos\mathcal{L})^2 - G_0{}^2\right) + \\ 8\left(P_{10} + (1+\Phi_0(\mathcal{L}))\sin\mathcal{L}\right)(Q_{20}\sin\mathcal{L} - Q_{10}\cos\mathcal{L})(Q_{20}\cos\mathcal{L} + Q_{10}\sin\mathcal{L}) - \\ 4P_{20}(Q_{10}\cos\mathcal{L} - Q_{20}\sin\mathcal{L})^2(2 - G_0) \end{pmatrix} d\mathcal{L} \\
I_{JP_2} &= 12\int_{L_0}^{L} \Phi_0(\mathcal{L}) \begin{pmatrix} \sin\mathcal{L}\Phi_0(\mathcal{L})\left(12(Q_{20}\sin\mathcal{L} - Q_{10}\cos\mathcal{L})^2 - G_0{}^2\right) + \\ 8\left(P_{20} + (1+\Phi_0(\mathcal{L}))\cos\mathcal{L}\right)(Q_{20}\sin\mathcal{L} - Q_{10}\cos\mathcal{L})(Q_{20}\cos\mathcal{L} + Q_{10}\sin\mathcal{L}) - \\ 4P_{10}(Q_{10}\cos\mathcal{L} - Q_{20}\sin\mathcal{L})^2(2 - G_0) \end{pmatrix} d\mathcal{L} \\
I_{JQ_1} &= 12\int_{L_0}^{L} \Phi_0(\mathcal{L})(Q_{10}\cos\mathcal{L} - Q_{20}\sin\mathcal{L})\sin\mathcal{L}\, d\mathcal{L} \\
I_{JQ_2} &= 12\int_{L_0}^{L} \Phi_0(\mathcal{L})(Q_{10}\cos\mathcal{L} - Q_{20}\sin\mathcal{L})\cos\mathcal{L}\, d\mathcal{L}
\end{aligned}
\tag{3.39}
$$

Their analytical expressions are reported in Appendix A. Note that there is no linear component in L in the expression of I_{Ja} (Eq. (A.17)), confirming the known result that J_2 is not inducing any secular variation of the semi-major axis and thus the energy. There is, on the other hand, a short-term periodic variation of a over one orbital revolution. The remaining equinoctial elements (Eqs. (A.18), (A.19), (A.20) and (A.21)), present both a short-term periodic variation and a secular one, which is linear with respect to L.

3.1.5 Superposition of Perturbations

It has been assumed that the perturbing acceleration is small, and consequently that the variation of the orbital elements induced by this perturbation will similarly be small. For example, one can assume that the variation of the orbital plane due to J_2 and out-of-plane thrust will be small and therefore the Equation (3.23) for the inertial acceleration is still applicable. In this sense, it is also possible to linearly superimpose the four analytical solutions shown in the previous sections to obtain an analytical expansion for the case in which these perturbations are acting together:

$$
\begin{aligned}
a^{tot} &= a_0 + \varepsilon^{r\vartheta h} a_1^{\,r\vartheta h} + \varepsilon^{In} a_1^{\,In} + \varepsilon^{t} a_1^{\,t} + \varepsilon^{J_2} a_1^{\,J_2} \\
P_1^{tot} &= P_{10} + \varepsilon^{r\vartheta h} P_{11}^{\,r\vartheta h} + \varepsilon^{In} P_{11}^{\,In} + \varepsilon^{t} P_{11}^{\,t} + \varepsilon^{J_2} P_{11}^{\,J_2} \\
P_2^{tot} &= P_{20} + \varepsilon^{r\vartheta h} P_{21}^{\,r\vartheta h} + \varepsilon^{In} P_{21}^{\,In} + \varepsilon^{t} P_{21}^{\,t} + \varepsilon^{J_2} P_{21}^{\,J_2} \\
Q_1^{tot} &= Q_{10} + \varepsilon^{r\vartheta h} Q_{11}^{\,r\vartheta h} + \varepsilon^{In} Q_{11}^{\,In} + \varepsilon^{t} Q_{11}^{\,t} + \varepsilon^{J_2} Q_{11}^{\,J_2} \\
Q_2^{tot} &= Q_{20} + \varepsilon^{r\vartheta h} Q_{21}^{\,r\vartheta h} + \varepsilon^{In} Q_{21}^{\,In} + \varepsilon^{t} Q_{21}^{\,t} + \varepsilon^{J_2} Q_{21}^{\,J_2} \\
t^{tot} &= t_{00} + \varepsilon^{r\vartheta h} t_1^{\,r\vartheta h} + \varepsilon^{In} t_1^{\,In} + \varepsilon^{t} t_1^{\,t} + \varepsilon^{J_2} t_1^{\,J_2}
\end{aligned}
\tag{3.40}
$$

3.1.6 Accuracy of the Analytical Expansions

This section contains an analysis of the accuracy and computational cost of the analytical formulae presented in the previous section. Accuracy and computational cost are evaluated against a numeric integration of (3.7) with different integration schemes and accuracies. An initial elliptical orbit, whose orbital parameters are given in Table 3.1, is propagated under the combined effect of J_2 perturbation, an acceleration along the tangential direction of 10^{-4} m/s^2 and an inertial acceleration of 10^{-6} m/s^2 (equivalent to solar radiation pressure acting on a spacecraft with an area to mass ratio of 1/4.56 m^2/kg at 1 AU).

Table 3.1: GTO orbital parameters.

a	e	i	Ω	ω	θ
24478 km	0.73	6°	0°	0°	0°

At first, the motion is propagated for an arc-length up to 2π and the performance of the analytical formulae is evaluated against three numerical integration schemes. This first analysis also provides an evaluation of the suitability of the analytical formulae as fast integration method to be used in the orbit averaging method introduced in Chapter 5. The numerical integration schemes are: a Gauss-Legendre quadrature with a number of nodes between 4 and 24, a Modified Euler method[102] with a number of equally spaced steps between 4 and 16, and an 8th-order, Runge-Kutta method with 13 steps (RK8(7)13)[103]. Note that, the Modified Euler evaluates the integrand function twice per step, therefore the number of function evaluations is double the number of steps. For each method, the integration error is computed as the difference between the analytical formulae and a numerical integration performed with MatLab® *ode113*, implementing an Adams-Bashfort predictor-corrector method, with relative and absolute tolerances equal to 10^{-13}.

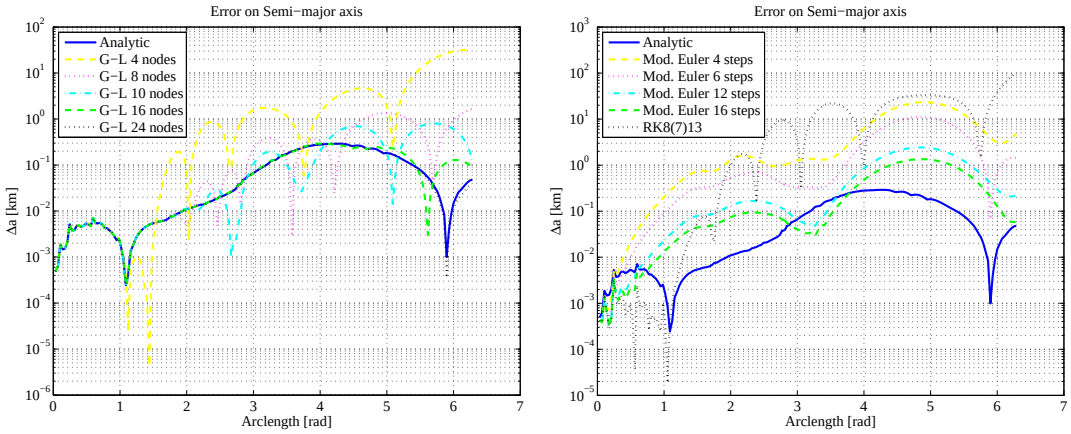

a) **b)**

Figure 3.2: Comparison with numerical integration: error on semi-major axis. a) Gauss-Legendre b) Modified Euler and Runge-Kutta.

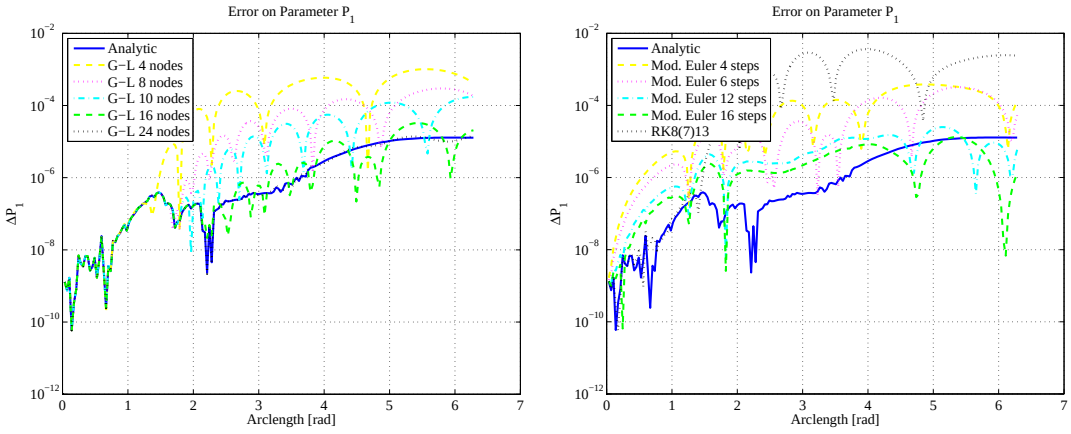

a) **b)**

Figure 3.3: Comparison with numerical integration: error on P_1. a) Gauss-Legendre b) Modified Euler and Runge-Kutta.

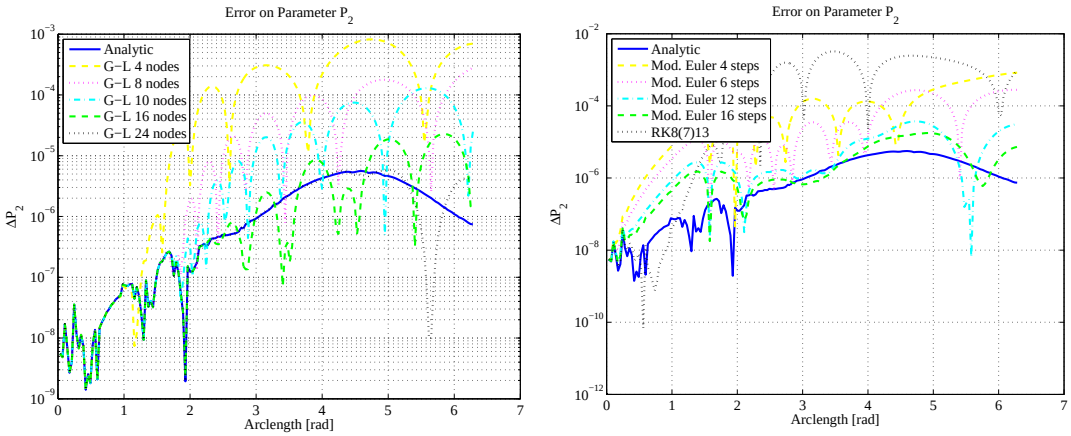

a) **b)**

Figure 3.4: Comparison with numerical integration: error on P_2. a) Gauss-Legendre b) Modified Euler and Runge-Kutta.

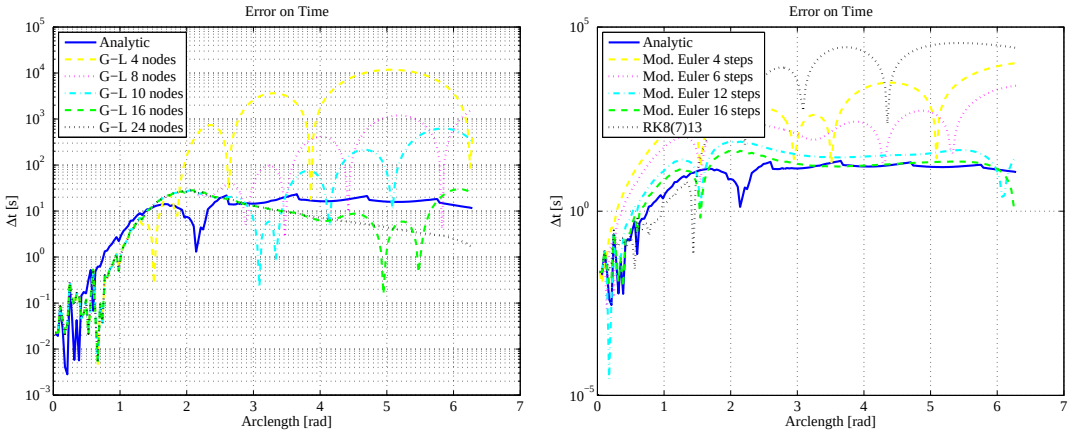

a) **b)**

Figure 3.5: Comparison with numerical integration: error on time. a) Gauss-Legendre b) Modified Euler and Runge-Kutta.

Figure 3.2a shows the error on semi-major axis. One can see that the Gauss-Legendre integration has a rather noisy behaviour already for short arc-length; only the case with 24 nodes shows comparable accuracy to the analytical propagation. Moreover, it has to be noted that Gauss-Legendre quadrature will, at best, have the same accuracy of the analytical step since it is numerically calculating the same integral forms. Figure 3.2b shows a similar comparison with Modified Euler and RK8(7)13 methods and leads to analogous conclusions. The Modified Euler integrator gives good results only with a high number of steps. The RK8(7)13 scheme is extremely accurate for short arc-length, but as this increases, the numerical integral quickly diverges from the true solution. Figure 3.3 and Figure 3.4 show the error on P_1 and P_2 and also reveal that Gauss quadrature can easily accumulate an error which is more than one order of magnitude larger than the analytical formulae. Figure 3.5 shows the error on time. In this case Gauss-Legendre quadrature with a high number of nodes has a slight advantage due to the fact that in the analytical formulae some of the terms depending on P_{11} and P_{21} are neglected. Addressing this issue will be the topic of future improvements.

Figure 3.6 shows the computational cost of the different integration methods. From the figure, one can see that the cost of the analytical propagation is comparable with the Gauss-Legendre quadrature with 8 nodes or Modified Euler with 4 steps. As shown in the previous plots, these two methods are considerably less accurate than the analytical formulae, except for very short arcs. Only Gauss-Legendre with 24 nodes has comparable accuracy but its cost is three times that of the analytical propagation. Note that the analytical formulae in this comparison require the computation of relatively expensive elliptic integrals. If a constant acceleration in a r-θ-h frame is considered instead the computational cost is about a quarter of that of a constant tangential acceleration.

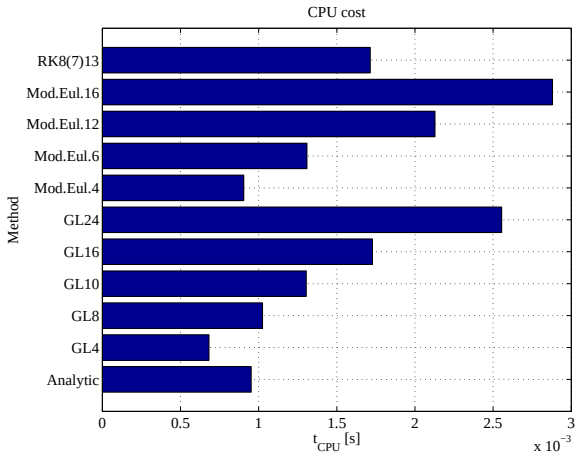

Figure 3.6: Comparison with numerical integration: computational cost.

3.1.7 Accuracy vs. Initial Semi-major Axis and ε

In this section, the behaviour of the error of the analytical formulae is investigated with respect to the initial semi-major axis and the magnitude of the perturbing acceleration. This is assessed by computing the error accumulated over one orbit as a function of the magnitude of the perturbative acceleration ε and of the semi-major axis a_0 of the initial orbit. A number of initial Earth-centred orbits with eccentricity 0.7 and variable a_0 were propagated with different ε, aligned along the tangential direction. Although here, for simplicity, only the tangential thrust case is considered, the same considerations are applicable also for the other acceleration patterns. Figure 3.7 shows the error on the semi-major axis relative to a_0 and as a function of a_0 itself and ε. One can see that for a large initial semi-major axis and ε=10^{-3} m/s^2 the error grows above 1%. However one should consider that 10^{-3} m/s^2 is a performance level hardly attainable with the current Electric Propulsion technology. If the acceleration is instead in the range of 10^{-4}-10^{-6} m/s^2 the resulting propagation error remains below 0.001 for relatively large orbits with semi-major axis up to about 10^5 km. Note also that all orbits in the LEO to GEO class are integrated very accurately, with a relative error lower than 10^{-5}.

A similar behaviour can be observed in Figure 3.8 for P_1 and in Figure 3.9 for the time t. The former is closely related to the orbit eccentricity and therefore it is desirable to keep the error per orbit below 10^{-5}-10^{-6} which, as shown in the graph, can be attained in most cases except for high a_0, large ε combinations. Figure 3.9 shows the error on time divided by the period of the initial osculating orbit and one can see that the perturbed orbit duration is also computed very accurately with the error being just a fraction of the total duration.

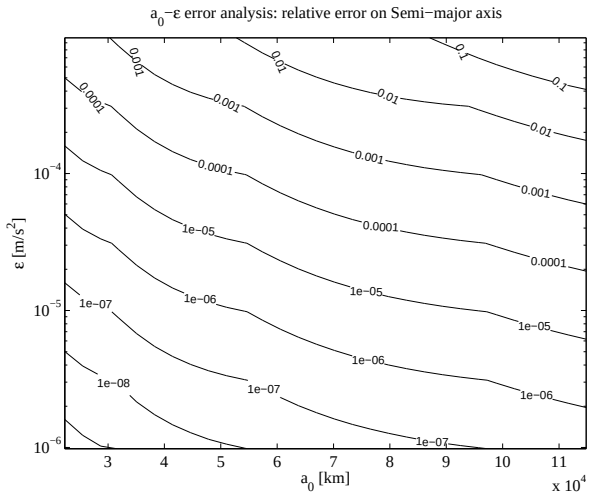

Figure 3.7: Relative error on *a* over one revolution w.r.t. a_0 and ε.

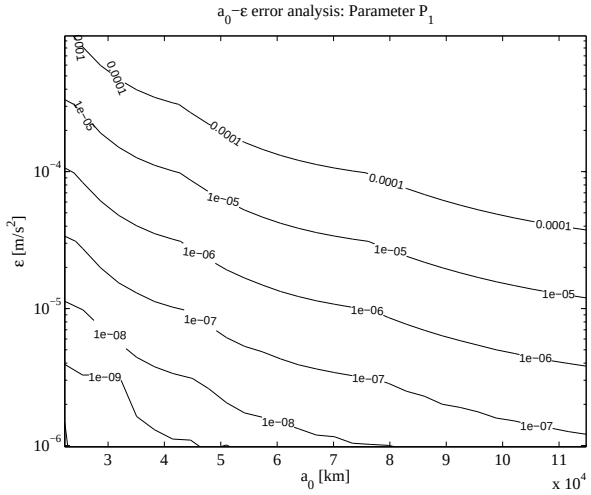

Figure 3.8: Error on P_1 over one revolution w.r.t. a_0 and ε.

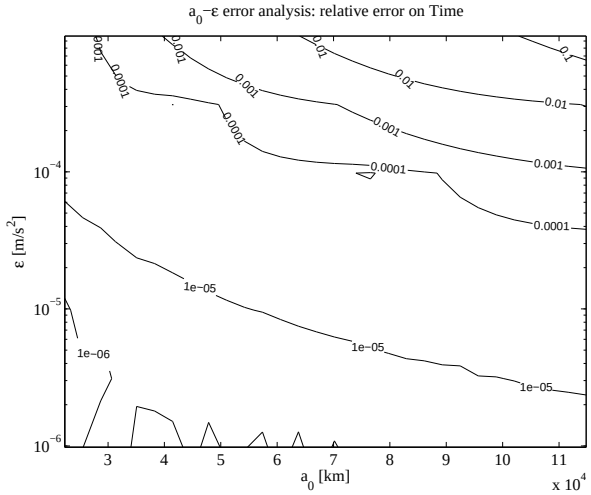

Figure 3.9: Relative error on time over one revolution w.r.t. a_0 and ε.

3.2 Propagation over Long Arcs

In this section, the speed and accuracy of the analytical first-order expansions is further assessed on the propagation of long arcs. For each of the four expansion formulae, an initial orbit around the Earth, with orbital parameters given in Table 3.2, is propagated analytically along an arc of length equal to 20 full revolutions. The difference between the value of the orbital elements along the propagated arc and the result of a full numerical integration of Gauss' variational equations is then computed to give the errors difference Δa, ΔP_1, ΔP_2, ΔQ_1, ΔQ_2, Δt. Both propagations are performed with Matlab and the numerical integration is performed with *ode113* with relative and absolute tolerances were set at 10^{-13}.

Table 3.2: Initial orbit parameters.

a	e	i	Ω	ω	θ
7500 km	0.1	6°	0°	10°	0°

The first test assesses the accuracy and speed of formulae (3.19) and (3.21). The modulus of the acceleration in the r-θ-h frame is 10^{-4} m/s^2, with $\alpha=\pi/2$ and $\beta=\pi/6$. Figure 3.10 shows that the error on the semi-major axis remains contained below 0.12 km after 20 revolutions.

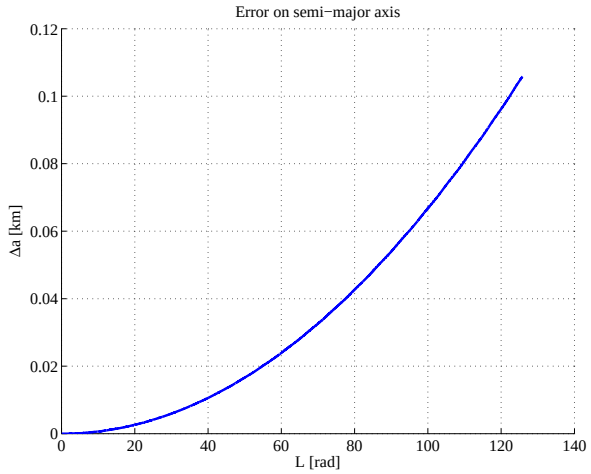

Figure 3.10: Constant r-θ-h acceleration: error on semi-major axis.

Figure 3.11 and Figure 3.12 show that the analytical approximation of P_1 and Q_1 is very close to the numerical solution with errors lower than $3\cdot10^{-7}$. P_2 and Q_2 show similar behaviours but are omitted here for the sake of conciseness.

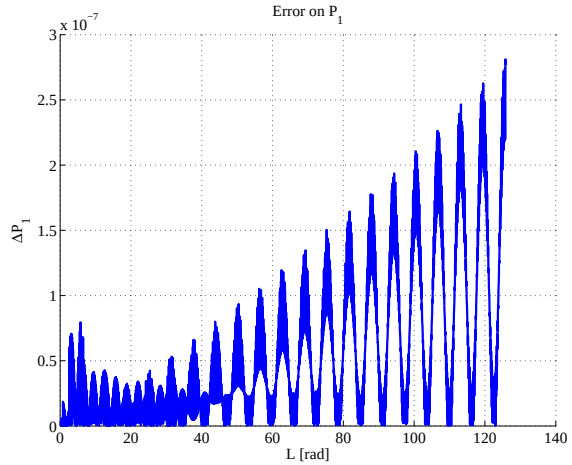

Figure 3.11: Constant r-θ-h acceleration: error on P_1.

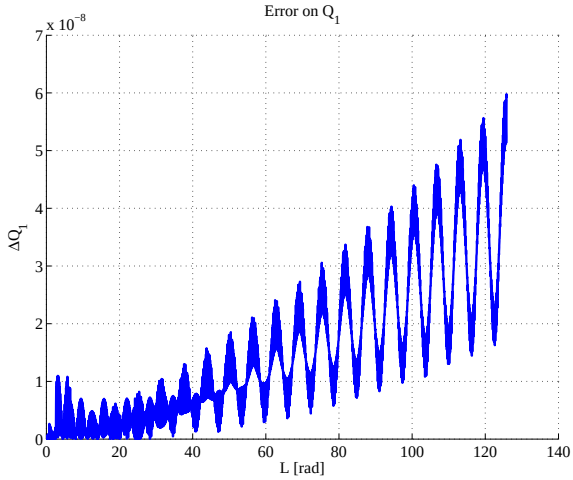

Figure 3.12: Constant r-θ-h acceleration: error on Q_1.

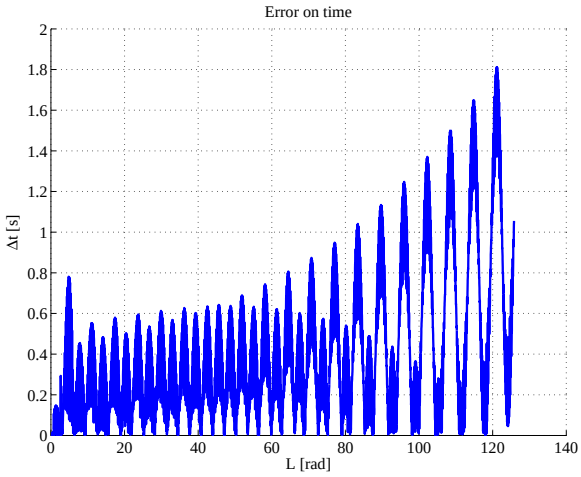

Figure 3.13: Constant r-θ-h acceleration: error on time.

Figure 3.13 shows the difference on time of flight between the approximation computed with Eq. (3.17) and the numerical integration of the time equation. The approximated time of flight accumulates an error that is less than 2 s after 20 orbits (a relative error of $3 \cdot 10^{-4}$). This result demonstrates that the new approximation proposed in Eq. (3.17) reduces the

error by one order of magnitude with respect to the previous formulation proposed in Zuiani et al.[46] for the same ratio of control and local gravity acceleration. Note that a good computation of the time is essential, in particular when one has to use this datum to compute the ΔV corresponding to the propagated thrusting arc.

In this first, test the analytical propagation required $2 \cdot 10^{-4}$ s compared to 0.5 s of *ode113*. However, note that a direct comparison of CPU time is rather difficult, since this value refers to the case in which the tolerance for *ode113* is set at 10^{-13}. On the other hand, if the tolerance were relaxed to 10^{-5} (a relative error comparable to the one of the analytical solutions) the CPU time for *ode113* would be about 0.08 s, which is still two orders of magnitude slower than the analytical propagation.

A second case was used to assess the accuracy of formulae (3.25) and (3.26). The same initial orbit is propagated with a 10^{-4} m/s^2 constant acceleration in the inertial reference frame. Figure 3.14 shows that the error on the semi-major axis is lower than in the previous case (in part due to the fact that the semi-major axis has a periodic behaviour in this case).

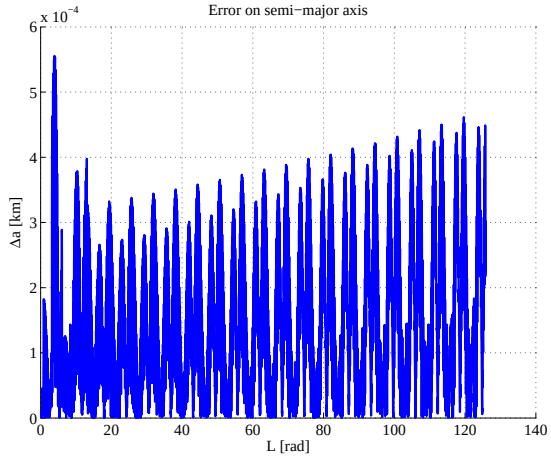

Figure 3.14: Constant inertial acceleration: error on semi-major axis.

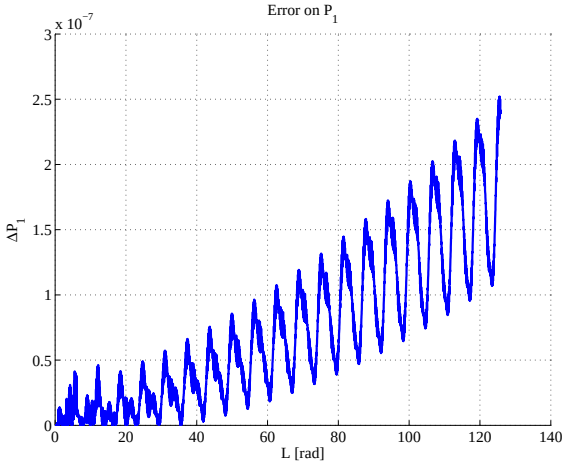

Figure 3.15: Constant inertial acceleration: error on P_1.

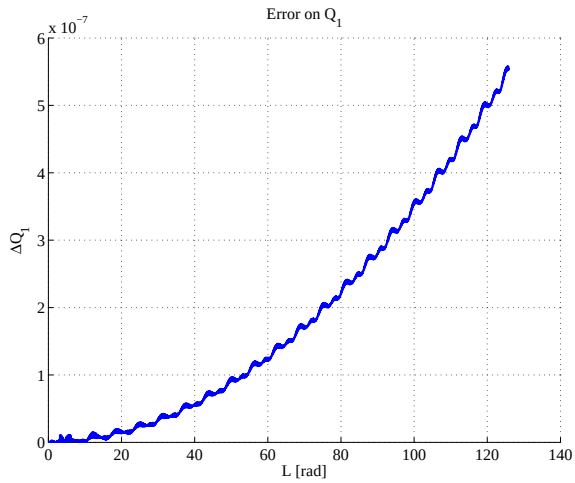

Figure 3.16: Constant inertial acceleration: error on Q_1.

Similarly, Figure 3.15 and Figure 3.16 show that the approximated values for P_1 and Q_1 match quite closely the numerical ones. Analogous considerations apply to P_2, Q_2 and t, the graphs of which are not reported for conciseness.

In the third case, the orbit in Table 3.2 is perturbed with a tangential acceleration of $\varepsilon=10^{-4}$ m/s^2. Figure 3.17 shows the behaviour of the error on semi-major axis and one can see that, from the qualitative point of view, this is remarkably similar to the one in Figure 3.10 for the r-θ-h acceleration.

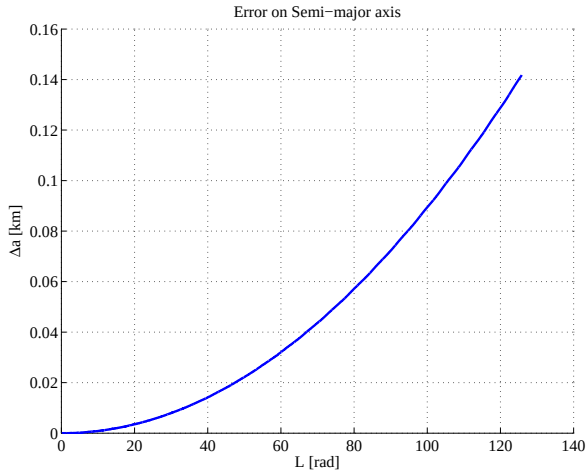

Figure 3.17: Constant tangential acceleration: error on semi-major axis.

The same can be said for the error on P_2 in Figure 3.18, which shows that the error is kept well below 10^{-6} after 20 orbits. The error on time remains below 2s, as seen in Figure 3.19. Note that, in this case the computational cost is higher than in the previous cases due to the elliptic integrals, but it is still lower than for the numerical integration, at around $8\cdot10^{-4}$ s.

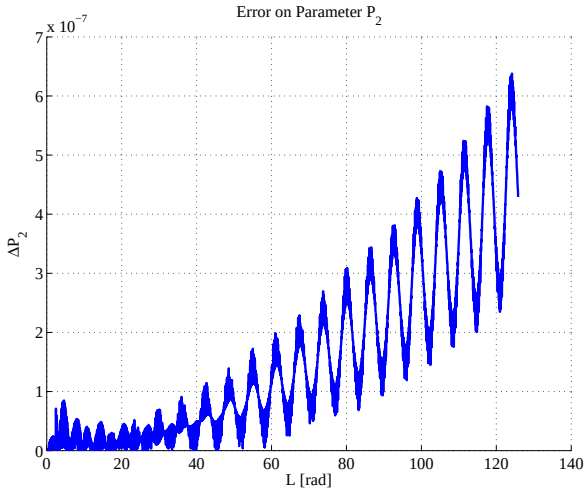

Figure 3.18: Constant tangential acceleration: error on P_2.

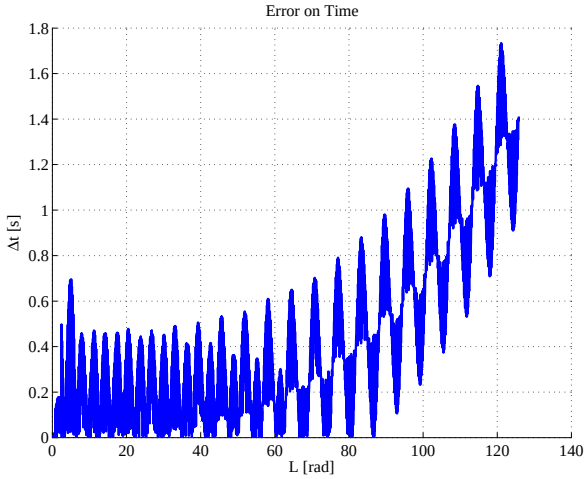

Figure 3.19: Constant tangential acceleration: error on time.

Table 3.3: Initial orbit parameters.

a	e	i	Ω	ω	θ
7197.8 km	0.1	6°	45°	10°	0°

In the last case, the initial orbit in Table 3.3 is propagated under J_2 perturbation only. Note that this orbit has a pericentre altitude of just 100km and has been chosen specifically to show a case in which ε^{J_2} is maximum. Of course, with such a low orbit, in real life one would have to take into account also the relevant contribution of the drag. As in the previous three cases, the general behaviour of the equinoctial elements shows a good match with the results of numerical integration. However, as shown in Figure 3.20, there is a slight, secular increase in the amplitude of the oscillations of the semi-major axis. Figure 3.21 shows that the error on Q_1 (the behaviour for Q_2 is analogous) grows faster than in the other cases. If these parameters are converted to inclination i and right ascension of the ascending node Ω, grows faster than in the other cases, one can see that the error has a long

term deviation. This would negate the known result that J_2 generates no secular variations in the inclination. While this variation is almost negligible along a single orbit, it might become problematic when a long integration interval is considered. Thus, a correction process will be introduced to mitigate the error growth in this and the other analytical solutions.

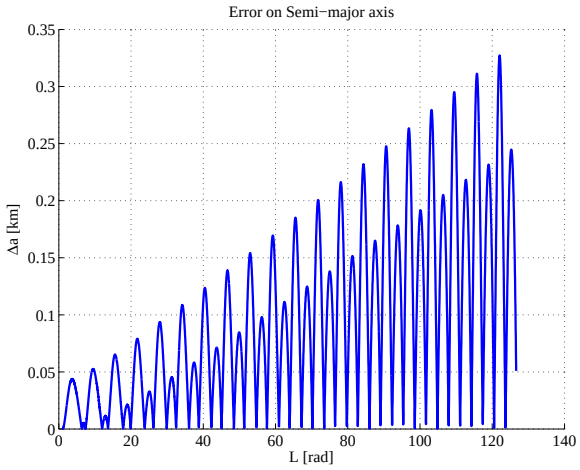

Figure 3.20: J_2 perturbation: error on semi-major axis.

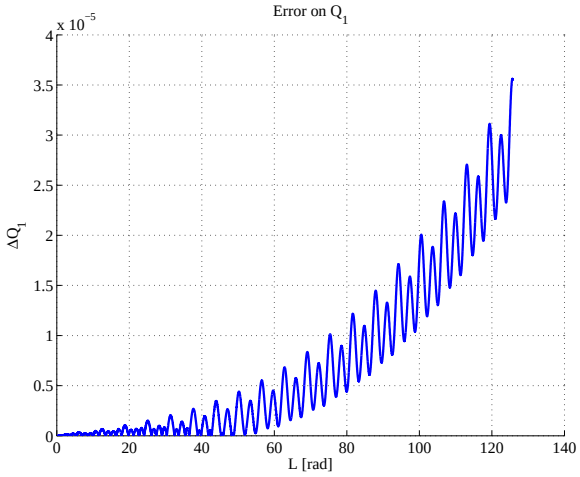

Figure 3.21: J_2 perturbation: error on Q_1.

As underlined in Section 3.1.5, given the limited variations of the orbital elements it is also possible to sum the four first-order expansions seen before into a single approximated solution for Keplerian motion perturbed by constant tangential and inertial acceleration plus J_2 perturbation. Figure 3.24 to Figure 3.27 show the propagation error associated to the combination of the three first-order expansions, for the initial orbit in Table 3.2. The mismatch with numerical integration is not worse than in the cases in which the perturbations are considered separately, confirming that the perturbative effects can be linearly combined. Also by comparing the error on the semi-major axis in Figure 3.20 and Figure 3.24, one can see that, for this specific case of a very low Earth Orbit, the main contribution to the error is actually given by the approximation on the J_2 term.

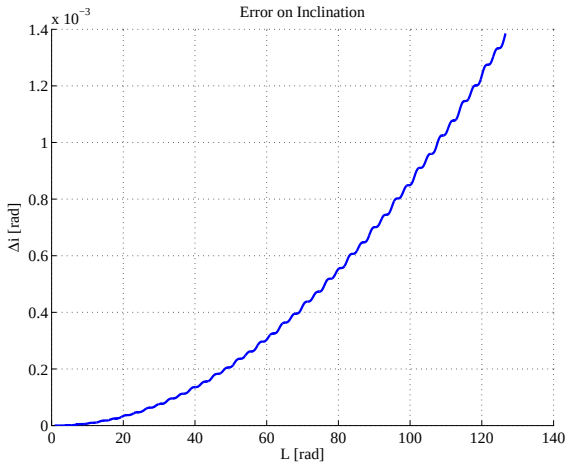

Figure 3.22: J_2 perturbation: error on inclination.

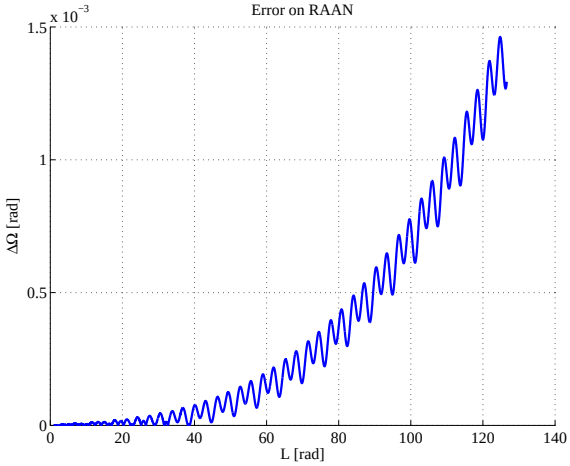

Figure 3.23: J_2 perturbation: error on Ω.

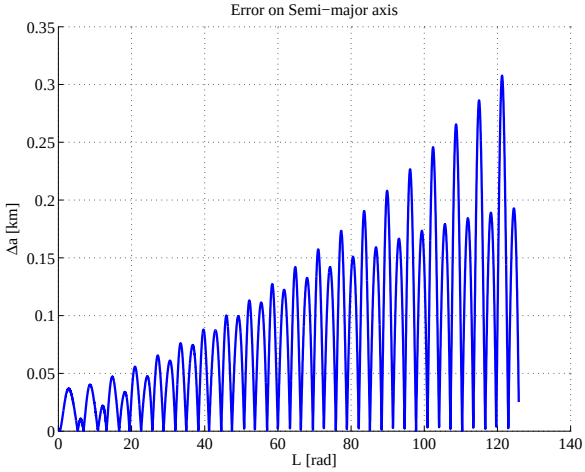

Figure 3.24: Combined perturbations: error on semi-major axis.

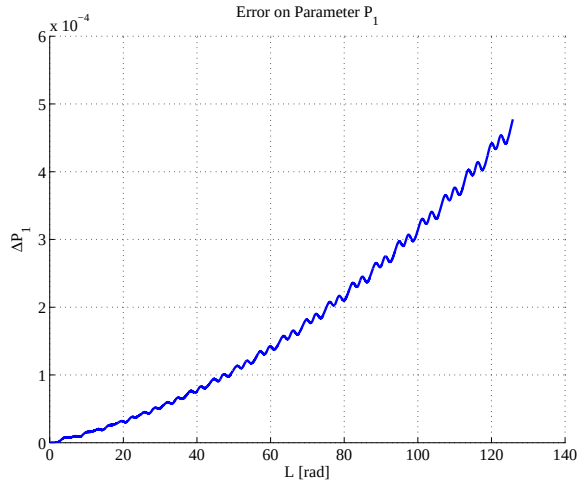

Figure 3.25: Combined perturbations: error on P_1.

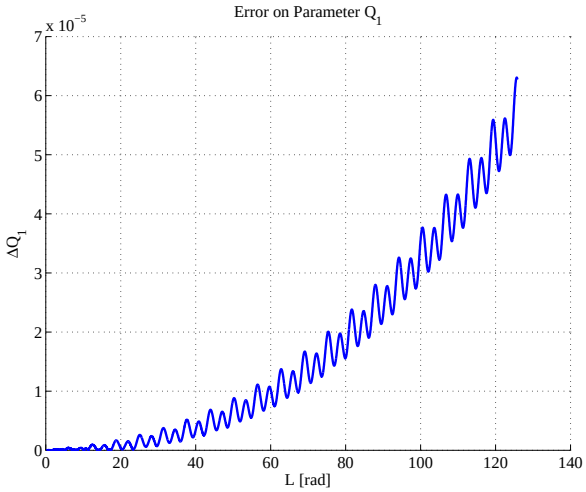

Figure 3.26: Combined perturbations: error on Q_1.

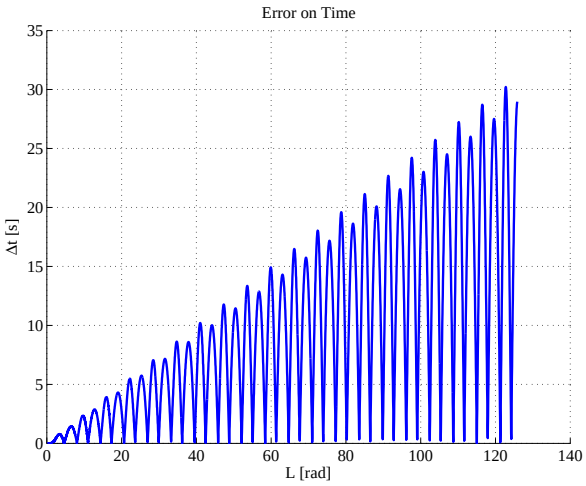

Figure 3.27: Combined perturbations: error on time.

3.2.1 Propagation Error Control over Long Spiralling Arcs

The results in the previous sections show that the propagation error of the proposed analytical solutions remains contained over relatively long arcs provided that ε is small

compared the to the local gravity field. For longer spirals, however, an error control strategy is required to preserve accuracy even for small values of ε.

The propagation error can be controlled by updating the reference condition $\mathbf{E}_0$ in Eq. (3.12) and (3.17) every n orbits. The update consists in taking the value for $\mathbf{E}(L)$ computed at the n-th orbit as the new reference condition $\mathbf{E}_0$ for the following n orbits. This technique, presented in Colombo et al.[42], can be regarded as a *rectification* of the analytical propagation.

The effectiveness of the technique is here demonstrated with the propagation of an initial circular orbit with semi-major axis 7000 km under the effect of an acceleration of $\varepsilon=10^{-4}$ m/s^2, along the tangential direction. The length of the propagation arc is equal to 500 complete revolutions. The frequency of updates is set to n=20, leading to a total of 25 evaluations of the analytical formulae. The analytical propagation required about 0.03 s while a numerical one with *ode113* (Adams-Bashfort, with tolerance set at 10^{-13}) took about 7 s. Figure 3.28 shows the variation of the semi-major axis and confirms that in this case its behaviour is almost linear. The approximation obtained with both rectification and averaging is very good.

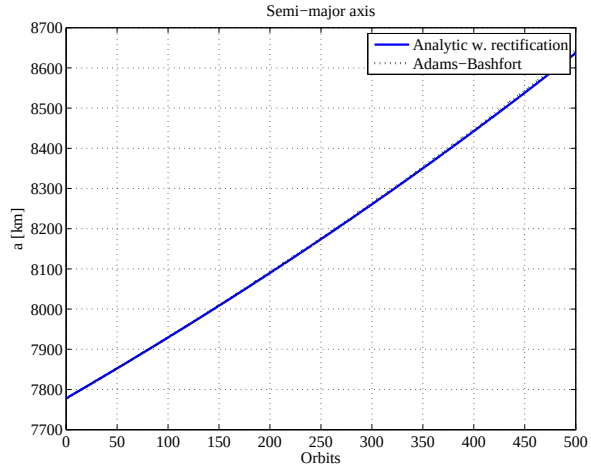

Figure 3.28: LEO propagation: semi-major axis.

Figure 3.29 shows that the relative error in the semi-major axis remains below $5\cdot10^{-4}$.

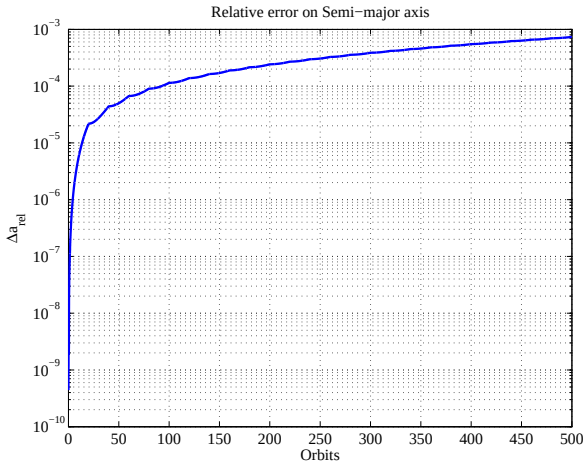

Figure 3.29: LEO propagation: relative error on semi-major axis.

Figure 3.30 shows the effect of the rectification process on the error in eccentricity which remains below $1.2 \cdot 10^{-5}$ after 500 orbits.

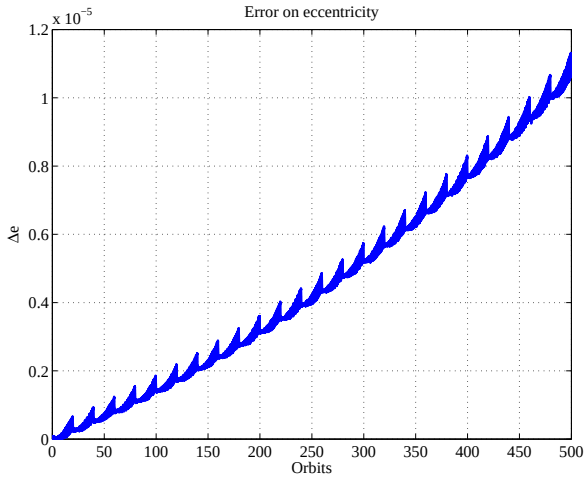

Figure 3.30: LEO propagation: error on eccentricity.

Table 3.4: Rectification strategy

Interval [10^4 km]	a<3	3<a<8.5	8.5<a<10	a>10
Rectifications/ orbit	1	2	4	8

A further test considers the propagation from an initial Geostationary Transfer Orbit (see Table 3.1) until escape condition is reached with an acceleration of $\varepsilon=10^{-4}$ m/s^2 in the tangential direction. This time, due the fact that the transfer is much longer and will span a wide range of different orbit energies, a simple dynamic rule is implemented to define the frequency of rectification. As detailed in Table 3.4, the frequency of rectification is proportional to the value of the semi-major axis. The analytical propagation was compared

to a numerical integration with *ode113*-Adams-Bashfort. The computational times are around 0.6 seconds for the analytical and 15 seconds for *ode113*.

Similarly to the previous case, Figure 3.31, Figure 3.32, Figure 3.33 and Figure 3.34 show, respectively, the variation of semi-major axis, the eccentricity and the relative error on radius modulus and that on phasing. Figure 3.31 shows a very good match between the analytical and numerical propagations, as can also be seen in Figure 3.32 for the eccentricity. The match is very good up to the last few revolutions when the semi-major axis is very large and therefore the analytical formulae become relatively inaccurate. Figure 3.33 shows the relative error on the modulus of the position vector. The figures show that the relative error remains below 10^{-3} for a good part of the spiral and grows above 10^{-2} only towards the end when the semi-major axis grows above $5 \cdot 10^4$km.

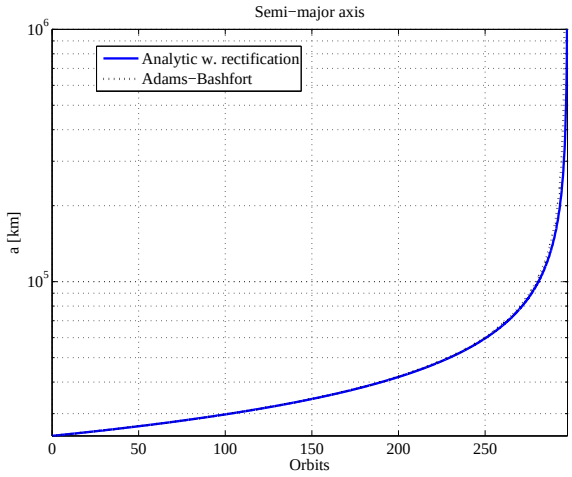

Figure 3.31: GTO propagation: semi-major axis.

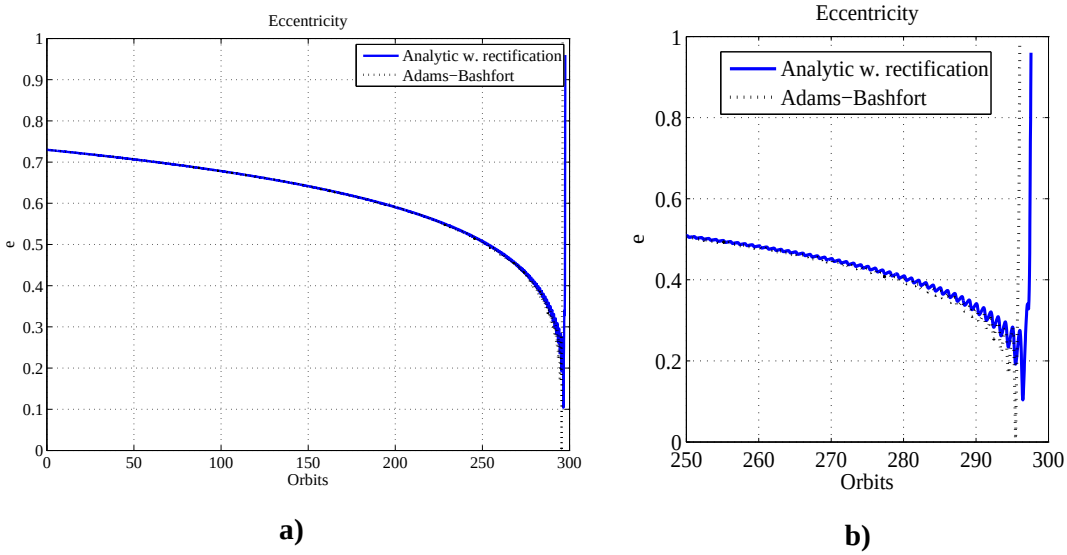

a) **b)**

Figure 3.32: GTO propagation: eccentricity. a) entire trajectory b) close up of last orbits.

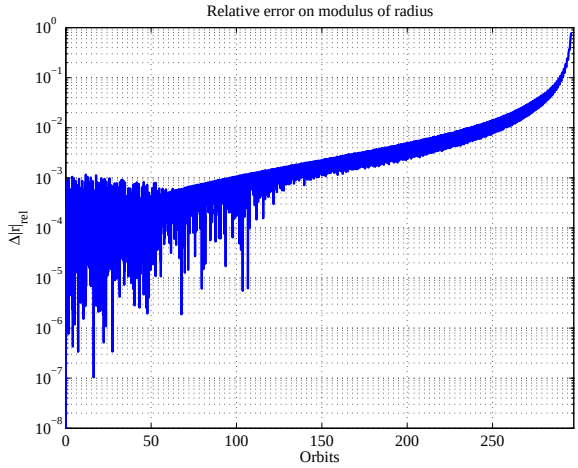

Figure 3.33: GTO propagation: relative error on radius.

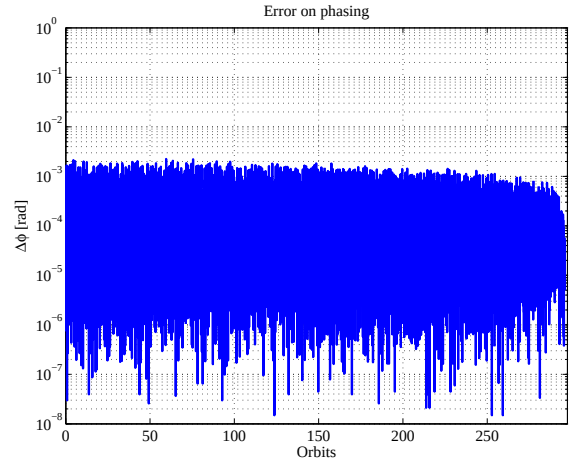

Figure 3.34: GTO propagation: phasing error.

3.3 Conclusions

This chapter has presented a set of analytical solutions for propagating low thrust trajectories under the effect of different perturbing acceleration. In particular, the proposed approach is suitable for treating constant acceleration in the r-θ-h reference frame, constant tangential acceleration, constant inertial acceleration, and J_2 perturbation. The accuracy of the analytical solutions was shown to be suitable for the propagation of relatively long trajectory arcs around the Earth, if the control acceleration level is comparable to the one delivered by current EP engines or other propulsion means falling in the LT class. The set of formulae presented here are the starting point for all the subsequent techniques presented in this dissertation. In particular, in the next two chapters, two additional techniques will be proposed, that will further enhance the scope of application of the analytical formulae.

Chapter 4.Direct Finite Perturbative Element Transcription Method

In this chapter, a direct transcription method for the design of optimal low-thrust transfers with constraint conditions at the boundaries is presented. The trajectory is decomposed into a number of finite elements, along each element, the orbital motion is propagated with the analytical formulation presented in Chapter 3. The trajectory is assumed to be an ε-variation of a Keplerian arc, where ε is a 'small' acceleration term due to the low-thrust action. A fast transcription of the trajectory into a nonlinear programming problem is thus obtained, the accuracy of which is controlled by the number of elements, assuming that every trajectory element remains a first order ε -variation of a Keplerian arc.

It will be shown how this approach is particularly suitable to solve orbital rendezvous problem, such an Earth-Mars, direct transfer. Moreover, thanks to its computational efficiency, it can also be used for the solution of computationally demanding Multi-Objective optimisation problems, where both the mass of propellant and the transfer time need to be minimized. This chapter is organised as follows: Section 4.1 will define the 2PBVP and Section 4.2 will introduce the proposed transcription method to solve it. Section 4.3 will present the case study of an Earth-Mars transfer. The present method is also employed in conjunction with MACS2 to perform a ΔV vs. time-of-flight analysis for a given launch window.

4.1 Problem Definition

Recalling the formalism used in Section 3.1, let one assume that the state of a spacecraft as in orbital motion around a central body is defined in Equinoctial elements as:

$$\mathbf{X} = \begin{Bmatrix} a \\ P_1 \\ P_2 \\ Q_1 \\ Q_2 \\ L \end{Bmatrix} \tag{4.1}$$

From Eq. (3.2) the orbital motion, in vector form, can be expressed as:

$$\dot{\mathbf{X}} = f\left(t, \mathbf{X}, \varepsilon, \alpha, \beta\right) \tag{4.2}$$

If one takes ε as the acceleration modulus delivered by a controllable engine along the directions defined by the angles α and β, the problem is to find the control law that satisfies the boundary conditions:

$$\begin{cases} \mathbf{X}(t_0) = \overline{\mathbf{X}}_0 \\ \mathbf{X}(t_f) = \overline{\mathbf{X}}_f \end{cases} \tag{4.3}$$

with $t_f = t_0 + ToF$ and ToF the time of flight, while minimizing the total ΔV of the transfer:

$$\Delta V = \int_{t_0}^{t_f} \varepsilon(t)\, dt \tag{4.4}$$

In mathematical terms the problem can be formulated as a typical Two-Point Boundary Value Problem as follows:

$$\begin{aligned} &\min_{\varepsilon,\alpha,\beta} J = \int_{t_0}^{t_f} \varepsilon(t)\, dt \\ &s.t. \\ &Eqs.\ (4.2) \end{aligned} \tag{4.5}$$

4.2 Finite Perturbative Element Transcription

The key idea is to exploit the set of analytical formulae presented in Chapter 3 for the propagation of the orbital motion. However, they cannot be directly applied to the solution of problem (4.5), because in the analytical formulae, the control acceleration has to be constant along the integrated trajectory arc. Furthermore, there is no independent control of the accuracy and of the arc length. In order to overcome these two issues the trajectory is decomposed into finite elements, each one representing an arc of prescribed amplitude. On each element, an approximated solution to Eqs. (4.2) is computed by means of the perturbative approach. In particular, it is chosen to use the set of equations (3.25) and (3.26) for the constant acceleration in the r-θ-h reference frame. This set has been preferred to those for the tangential reference because it basically offers the same degree of flexibility at a lower computational (as mentioned in Section 3.1.6) cost since no elliptic integrals are to be computed numerically. All the elements are then linked together to form the complete trajectory. In analogy to Direct Finite Element Transcription[104,20], this novel transcription approach is called Direct Finite Perturbative Element Transcription (DFPET) method. A similar transcription method can be found in the work of Sims and Flanagan[26]. The approach of Sims and Flanagan makes use of a zero-order approximation of the perturbed Keplerian motion by decomposing the trajectory into *n* sub-arcs, with each sub-

arc describing a leg of unperturbed Keplerian motion. The change in momentum due to a continuous thrust is lumped into ΔV discontinuities at the edges of each sub-arc. The main advantage resides in the fast closed-form computation of each Keplerian arc and its variation with respect to the states at the beginning of the arc. By analogy, in DFPET the simple Keplerian model with discrete ΔV impulses is replaced by a first-order perturbed Keplerian model with constant thrust along each sub-arc (see Figure 4.1).

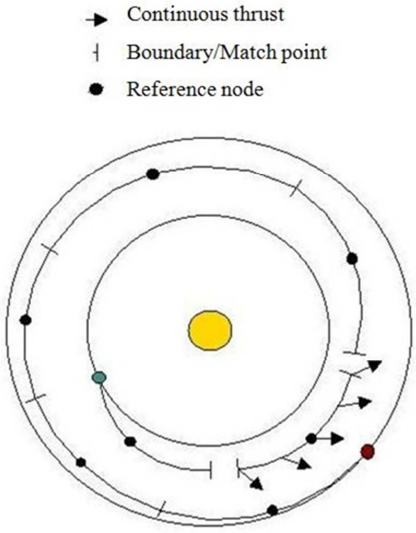

Figure 4.1: LT Direct Finite Perturbative Element Transcription Method.

In DFPET, the i-th arc of amplitude ΔL_i is defined by the following quantities: $\mathbf{X}^{\mathbf{m}}$, the six Equinoctial parameters at the mid-point of the arc and the three control parameters ε, α and β. To obtain the boundary points of the element, the perturbed motion is analytically propagated backward and forward along a subarc with amplitude $\Delta L/2$. The mid-point along the arc ΔL is chosen as the base-point for the analytical propagation to improve accuracy, since the error increases superlinearly with amplitude of the arc and is proportional to ε (see Figure 4.7). Thus, a dual-sided propagation in the form:

$$\begin{cases} \mathbf{X}^{+} = f\left(\mathbf{X}^{\mathbf{m}}, \dfrac{\Delta L}{2}, \varepsilon, \alpha, \beta\right) \\ \mathbf{X}^{-} = f\left(\mathbf{X}^{\mathbf{m}}, -\dfrac{\Delta L}{2}, \varepsilon, \alpha, \beta\right) \end{cases} \tag{4.6}$$

provides a better accuracy than a single forward one over the arc-length of equivalent total length ΔL. All arcs are then interconnected by imposing matching conditions at their boundaries (see Figure 4.2). The proposed dual-sided propagation is different from what is usually done in other Multiple Shooting methods, in which the propagation is carried out only forwards.

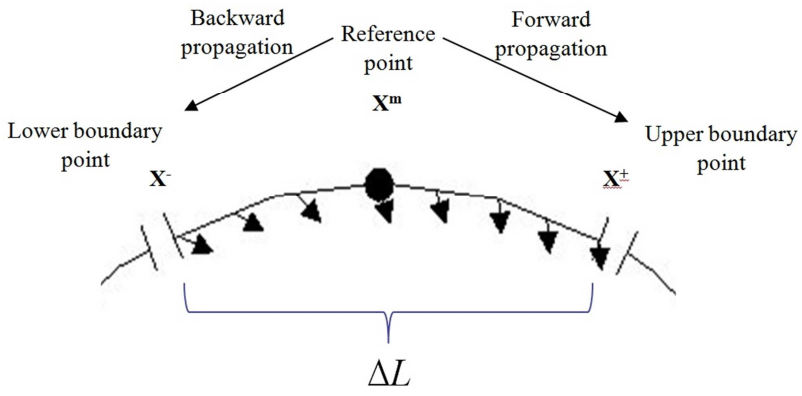

Figure 4.2: DFPET with centred reference node.

4.2.1 Accuracy Analysis

In order to test the integration accuracy of the Perturbative Finite Element Transcription, the backward and forward integration over a single arc was run for a wide range of time intervals, a constant transversal acceleration of $2.5 \cdot 10^{-5} m/s^2$ and an initial circular orbit at 1AU from the Sun. Time intervals ranged from 0.5 up to 100 days. Note that the centred reference node of the Perturbative Finite Element was adjusted in order to match, at the lower boundary, the above mentioned conditions of a 1AU heliocentric circular orbit. For each element size, the computed final state (i.e. the one at the upper boundary) was compared against the result of the integration of Eqs. (3.2) with a simple implementation of the Modified Euler Method[102], and the MatLab® function *ode113* (that implements a variable-order Adams-Bashforth-Moulton Predictor-Corrector method). Other algorithms of the *ode* family (e.g. *ode45*) were also tested, and *ode113* was chosen as being the fastest among them for a given accuracy requirement. The numerical integration was started from the lower boundary of the Perturbative Finite Element. The required relative and absolute accuracies were both set at 10^{-13}, in order to have a very accurate solution to which to compare the results of the propagation with DFPET and the Modified Euler Method. Thus, the results of *ode113* were used as a reference to compute the relative error on the final state as shown in Figure 4.3 and Figure 4.4. Moreover, CPU time for the case in which *ode113* is allowed to use relaxed tolerances (both set at 10^{-3}) is also included in Figure 4.4 for a further comparison.

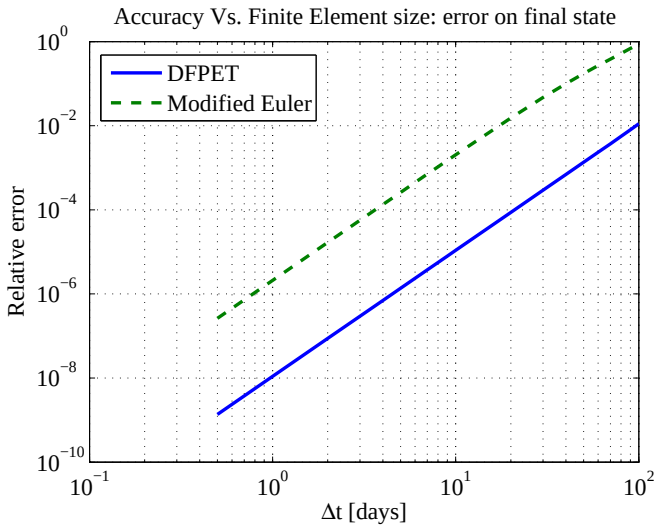

Figure 4.3: Error on final state w.r.t. DFPET size for a heliocentric orbit.

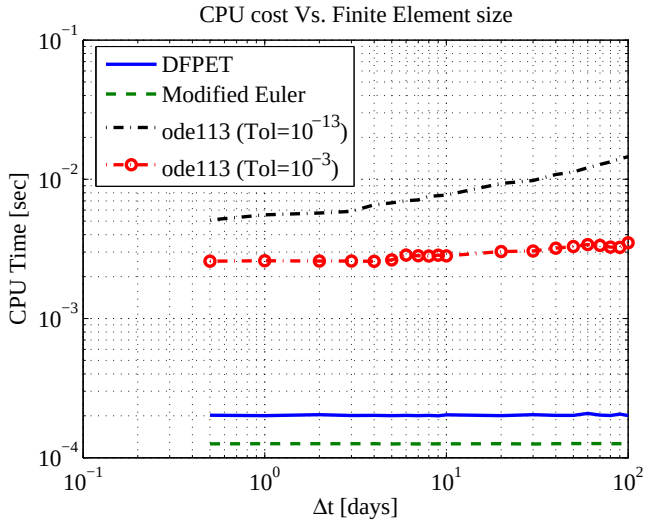

Figure 4.4: CPU cost w.r.t. DFPET size for a heliocentric orbit.

In these tests, the DFPET transcription displays second-order behaviour with respect to temporal size of the element and a good accuracy even with a relatively large size of the element (see Figure 4.3). It should be noted that, in this test, the perturbation force is equivalent to a thrust of 0.5 N continuously acting on a 2000 kg spacecraft. This means that the ratio between the perturbative acceleration and the local gravity is relatively high. Finally, the DFPET method has a computational cost only marginally higher than the Modified Euler method (see Figure 4.4) but still at least one order of magnitude lower than the numerical integration with *ode113*, even with relaxed tolerances.

A similar test was carried out also by propagating a perturbed LEO orbit for an element size ranging from 0.5 to 5 days, roughly equivalent to 50 revolutions.

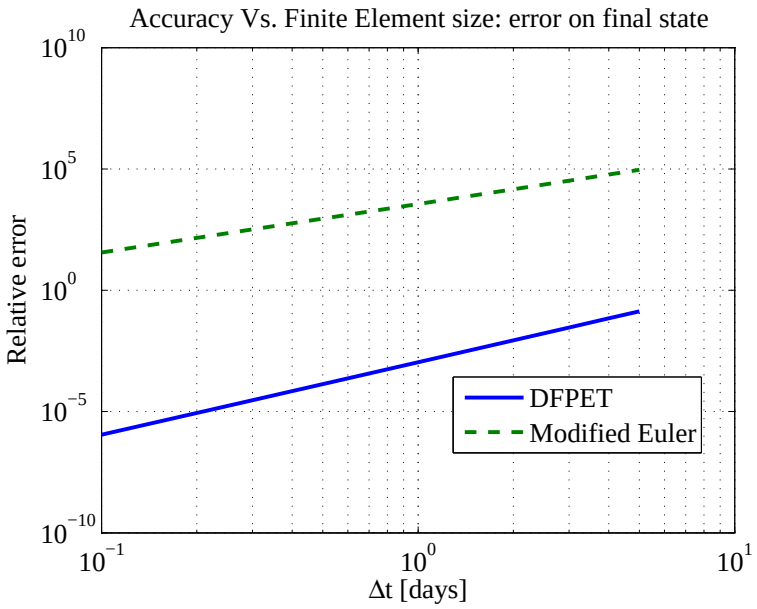

Figure 4.5: Error on final state w.r.t. DFPET size for LEO propagation.

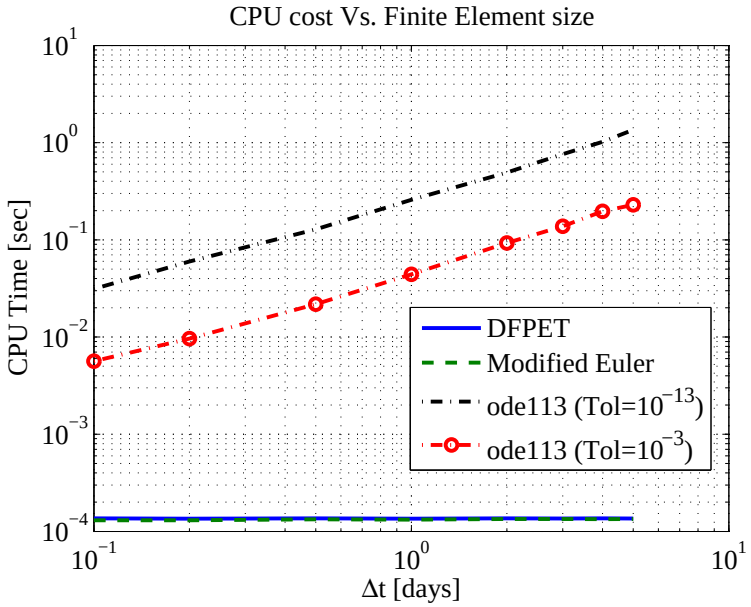

Figure 4.6: CPU cost w.r.t. DFPET size for LEO propagation.

Here the advantage of the analytic propagation is even more evident, as it outperforms the Modified Euler Method (see Figure 4.5), and is at least 60 times faster than the numerical integration with *ode113* (see Figure 4.6). This is easily explained by the fact that in LEO the gravitational force of the Earth is many times higher than the perturbation force. It should also be noted that the analytic propagation is able to provide an accurate estimate even with only one (or even a fraction of) Finite Element per revolution.

Finally, a simple test was performed to evaluate the accuracy with respect to the ratio between the thrust acceleration and the local gravitational force. An initial circular low Earth orbit was propagated analytically for 0.5 days with various levels of transverse

acceleration and the results were again compared against the numerical integration of the same orbit arc with ode113. The relative error in the final state is shown in Figure 4.7.

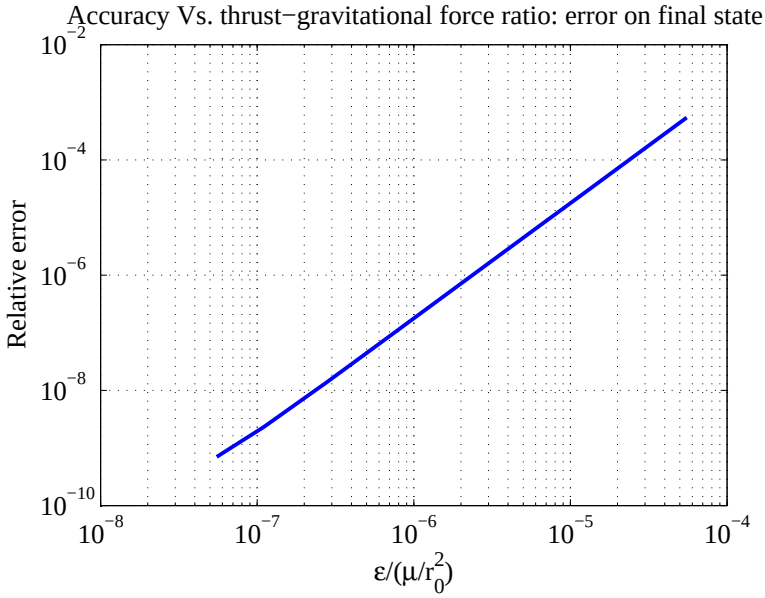

Figure 4.7: Error on final state w.r.t. thrust-gravitational force ratio.

4.2.2 Solution of the 2PBVP Orbit Transfer Problem

The DFPET approach can now be applied to the solution of problem (4.5), leading to the following system of nonlinear algebraic equations:

$$\min_{\mathbf{u}} J = \sum_{i=1}^{n_{FPET}} \varepsilon_i \Delta t_i$$

$$s.t.\ \mathbf{C_{eq}} = \left\{ \begin{array}{c} \mathbf{X}_1^- - \overline{\mathbf{X}}_0 \\ \mathbf{X}_i^+ - \mathbf{X}_{i+1}^-, i = 2,\ldots,n_{FPET}-1 \\ \mathbf{X}_{n_{FPET}}^+ - \overline{\mathbf{X}}_f \\ \overline{ToF} - ToF = \overline{ToF} - \sum_{i=1}^{n_{FPET}} \Delta t_i \end{array} \right\} = 0 \qquad (4.7)$$

$$\varepsilon_i \le \varepsilon_{max},\ i = 1,\ldots,n_{FPET}$$

The decision variables are the control vector components and the first five equinoctial elements of the midpoint of each arc. The vector **u** in Eqs. (4.7) collects all the values of the control vector components for all the arcs. Equality constraints are given by the matching condition between adjacent sub-arcs. The first and last sets of rows in $\mathbf{C}_{eq}$ contain respectively the boundary conditions on the initial and final state and the last row contains the constraint on the time of flight: the required time of flight $\overline{ToF}$ has to match the one computed from the sum of the times of flight of the single sub-arcs as

$ToF = \sum_{i=1}^{n_{FPET}} \Delta t_i = \sum_{i=1}^{n_{FPET}} \left(t_i - t_{i-1} \right)$. Note that continuity conditions with respect to the longitude are automatically satisfied since all the analytical expressions for the variation of the equinoctial elements are already parameterised with respect to L. Therefore, the matching constraints apply only to the remaining five equinoctial elements. Furthermore, the total longitude ΔL_{tot} covered by the trajectory arc is easily determined as $\Delta L_{tot} = L_f - L_0 = \sum_{i=0}^{n_{FPET}} \Delta L_i$. It should also be noted that, to increase the number of complete revolutions of the trajectory, it is sufficient to increase L_f, and thus ΔL_{tot}, by multiples of 2π. In the current implementation only a uniform mesh (with respect to L) was considered.

Limits on the maximum delivered thrust are introduced as limits on the maximum perturbative acceleration. This is not entirely correct since, in fact, while the maximum thrust is constant, the maximum acceleration available gradually increases with time due to a gradual decrease of spacecraft mass. However, for the sake of the calculations in this paper, this approach is acceptable and allows for directly enforcing a reasonable upper limit on a decision variable.

Problem (4.7) was solved by means of the MatLab® function *fmincon*, implementing a Sequential Quadratic Programming (SQP) method. Given n_{FPET} sub-arcs, the problem has $8n_{FPET}$ decision variables and $8(n_{FPET}+1)+1$ scalar equality constraints. Because each control element is decoupled from the others, the Jacobian matrix is highly sparse with the structure shown in Figure 4.8. The figure shows an example with 10 sub-arcs, i.e. with 80 variables and 56 scalar constraints. Size of the full matrix is thus 4480 but it has only 800 non-zero elements.

The sparsity pattern could be divided in three main regions: the left diagonal band, the right diagonal band and the lowermost row. The first corresponds to the derivatives of the constraints between adjacent sub arcs (as in Eqs. (4.7)) w.r.t. the modulus, azimuth and elevation of the thrust acceleration of each sub-arc. The band is composed by five-by-three sub-matrices each of which is basically the Jacobian of the first five Equinoctial elements at the lower (or upper) boundary as a function of ε, α, β. The two zero elements within each sub-matrix correspond to the derivatives of Q_1 and Q_2 w.r.t. α which are always nil as can be easily seen, for example, from Eqs. (3.19).

The second region corresponds to the derivatives of the matching constraints with respect to the reference nodes. Here again one can see a band structure with five-by-five sub-matrices. The two zero elements are in this case the derivatives of the semi-major axis w.r.t. Q_1 and Q_2.

Finally, the lowermost row is composed of the derivatives of the time of flight w.r.t. to all the variables.

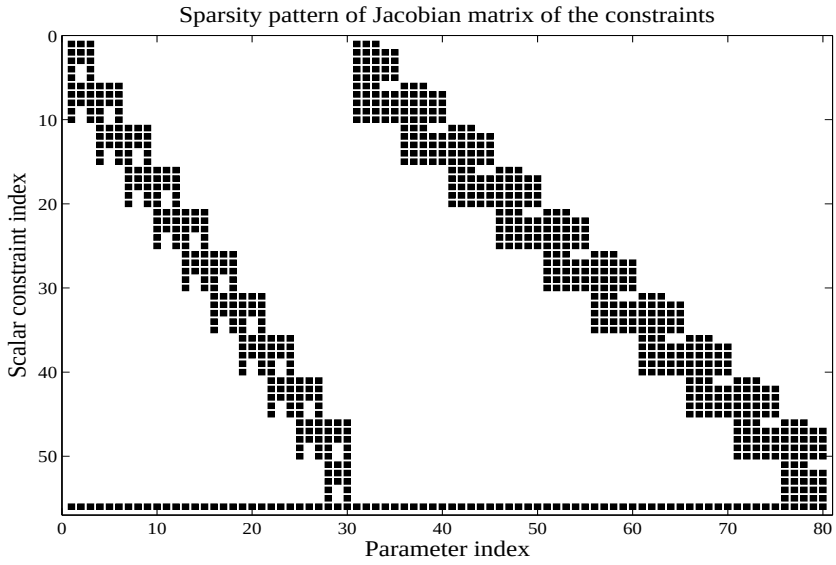

Figure 4.8: Sparsity pattern of the Jacobian of the constraint function.

4.3 Case Study: Low-Thrust Earth-Mars Transfer

To test the proposed transcription method on a realistic transfer problem, a rendezvous transfer from Earth to Mars is considered. The problem is first as a simple boundary value problem and subsequently as a Multi-Objective problem using MACS2.

4.3.1 Earth-Mars Rendezvous Boundary Value Problem

For the simple boundary problem solution, the objective is that of finding a ΔV optimal transfer between Earth and Mars departing from Earth at t_0=5600 MJD2000, with a time of flight of 1095 days, and with 2 complete revolutions. Maximum acceleration was set at $2.5 \cdot 10^{-8}$ km/s^2, equivalent to a thrust of 0.5 N applied to a 2000 kg spacecraft. Initial guess was given by a constant, transversal thrust profile of magnitude half the maximum acceleration. The orbit was modelled with 20 Finite Elements. The problem was solved with the *fmincon* active-set algorithm, with a tolerance of 10^{-8} both on constraint satisfaction and optimality condition.

The solution obtained has a total ΔV of 5.6388 km/s. In order to check the accuracy of the analytical solution, the optimal thrust profile was numerically integrated forward in time to calculate the final state. The relative error between analytical and numerical final state was $3 \cdot 10^{-3}$.

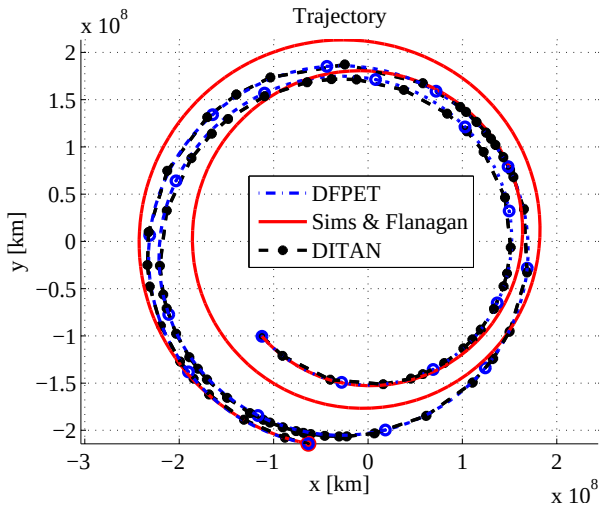

Figure 4.9: Comparison of the optimized trajectories.

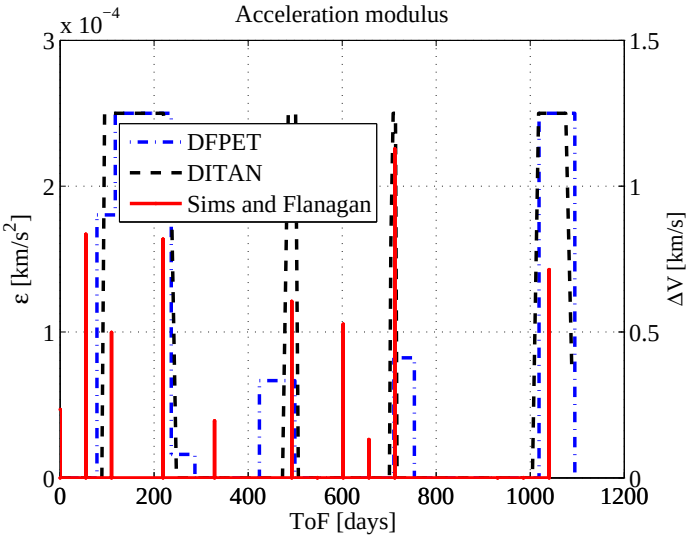

Figure 4.10: Thrust modulus for Earth-Mars LT transfer.

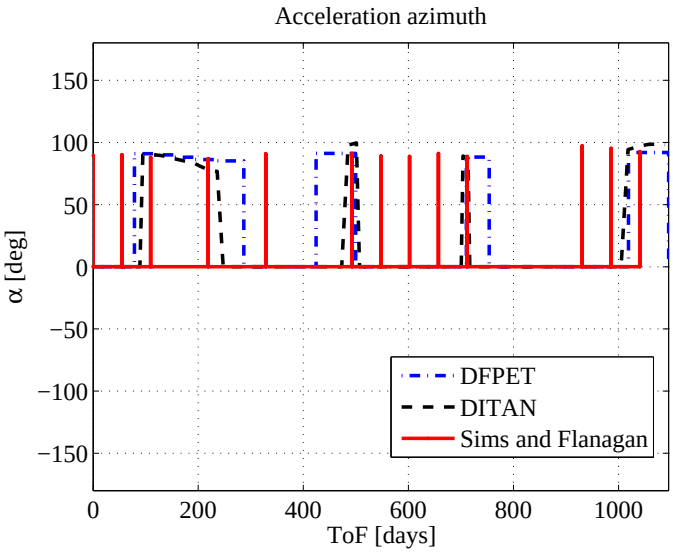

Figure 4.11: Acceleration azimuth α for Earth-Mars LT transfer.

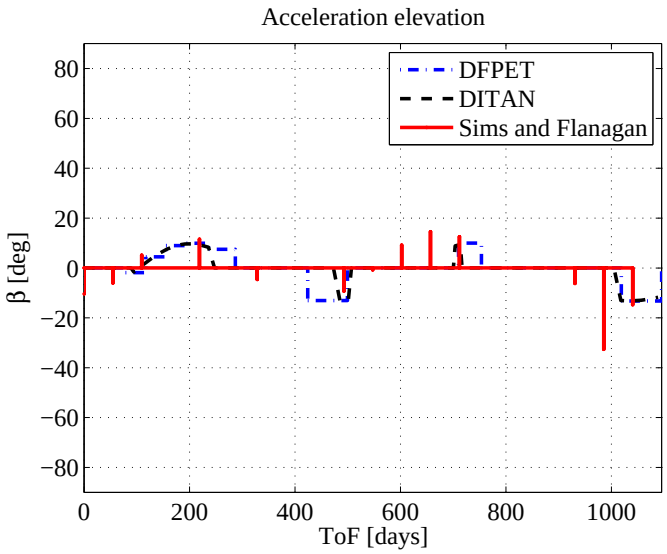

Figure 4.12: Acceleration elevation β for Earth-Mars LT transfer.

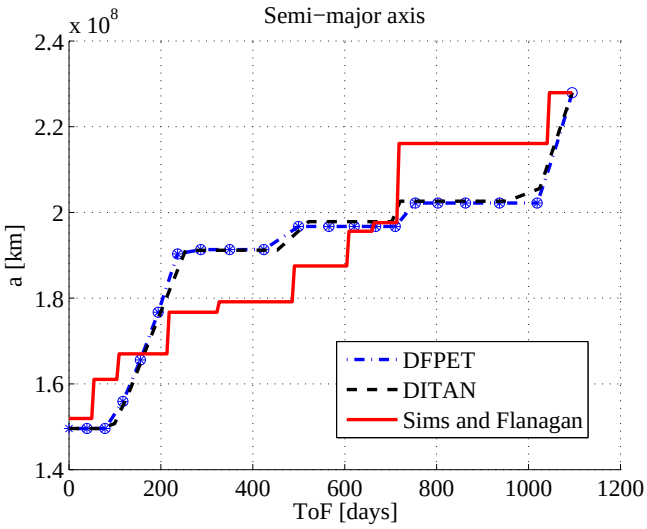

Figure 4.13: Variation of Keplerian Elements for Earth-Mars LT transfer: *a*.

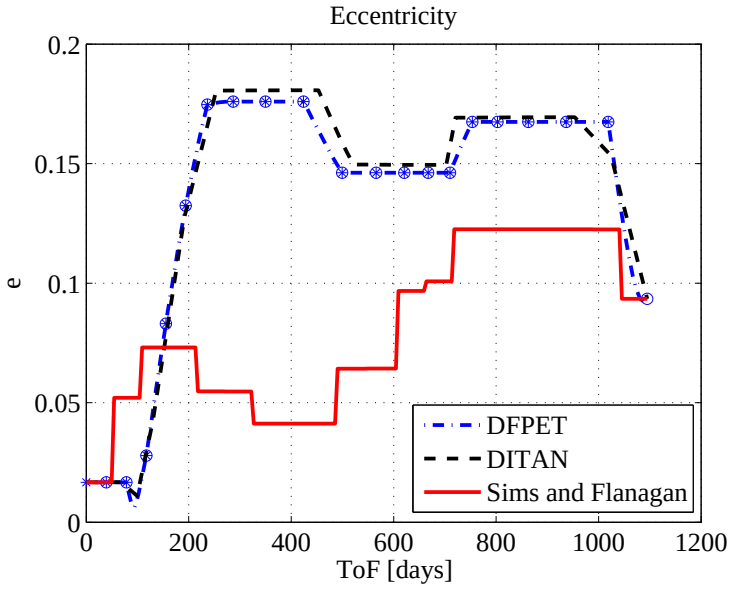

Figure 4.14: Variation of Keplerian Elements for Earth-Mars LT transfer: *e*.

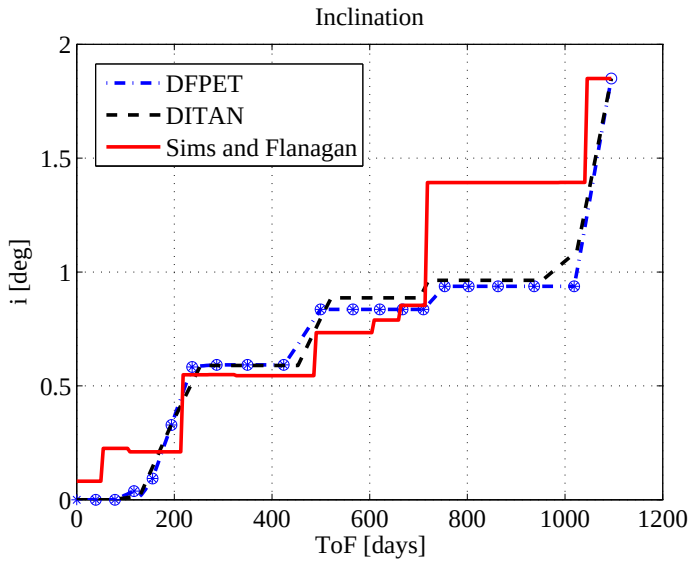

Figure 4.15: Variation of Keplerian Elements for Earth-Mars LT transfer: *i*.

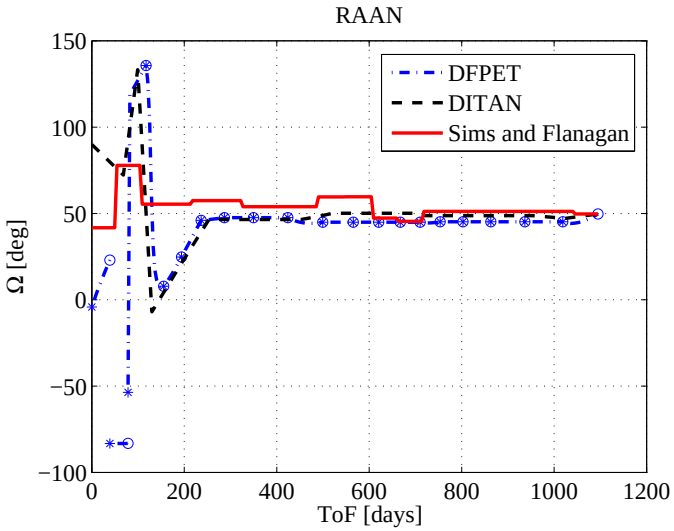

Figure 4.16: Variation of Keplerian Elements for Earth-Mars LT transfer: *Ω*.

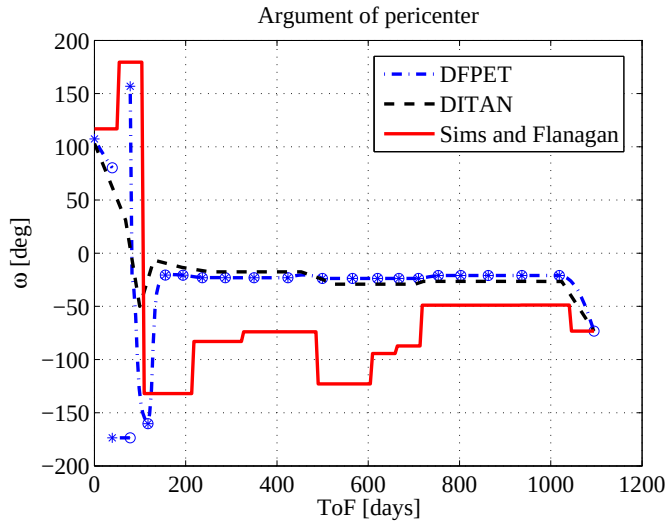

Figure 4.17: Variation of Keplerian Elements for Earth-Mars LT transfer: *ω*.

Figure 4.10 shows the time history of the thrust modulus while Figure 4.11 and Figure 4.12 show its azimuth and elevation respectively. Note that, for ease of visualization of the thrusting or coasting arcs, the angles have been plotted as equal to zero when the corresponding thrust modulus is zero. The thrust profile displays a typical on-off structure with four thrusting arcs concentrated around the pericenter and apocenter. The azimuth angle (see Figure 4.11) is almost constantly at 90º, which translates into a quasi-transverse in-plane component of the thrust. The small out-of-plane component (see Figure 4.12) is due to the small change in inclination between departure and arrival orbit. Figure 4.13 to Figure 4.17 show the time history of the Keplerian elements during the transfer. The semi-major axis increases monotonically (see Figure 4.13), with the largest variations along the first and last thrusting arcs. The inclination (see Figure 4.15) shows also a similar pattern, while the eccentricity (see Figure 4.14) remains constant at about 0.17 for most of the transfer and then decreases to about 0.1 to match the eccentricity of the arrival orbit.

Note that, the discontinuities in both the plots of Ω and ω (see Figure 4.16 and Figure 4.17 respectively) are due to the small initial inclination that causes numerical problems in the derivation of the Keplerian elements from the equinoctial non-singular elements. There is no mismatch in the value of the equinoctial elements instead.

The same problem was solved with an implementation of the Sims and Flanagan method, and with DITAN, an optimal control solver based on a direct transcription with Finite Elements on spectral basis[104,20]. As for the DFPET solution, 20 sub-arcs were used to transcribe the transfer problem with Sims and Flanagan and the resulting nonlinear programming problem was solved with *fmincon* setting the tolerance for both constraint satisfaction and optimality condition to 10^{-8}.

DITAN uses SNOPT [105] as nonlinear programming solver. A first solution was computed with 12 finite elements and the result was then improved by increasing the number of elements to 19. The maximum constraint violation was set to 10^{-8} and the required optimality to 10^{-6}.

Table 4.1: Performance comparisons for three different LT optimisation methods.

	FPET	S&F	DITAN	DITAN (refined)
Elements	20	20	12	19
ΔV [km/s]	5.6388	5.6859	5.6429	5.5401
Iterations	63	240	4602	11064
t_{CPU} [sec]	10.88	21.37	1045.3	3582.73

Table 4.1 summarises optimisation results for the three different methods and shows that both the DFPET and Sims and Flanagan give reliable first guess figures for the ΔV cost of the transfer. On the other hand, it also shows the inherent advantages of the DFPET method compared to Sims and Flanagan. While the total ΔV of the former is only marginally better, its required number of *fmincon* iterations, and thus CPU time, is much lower. Moreover, if one considers the trajectory shape (see Figure 4.9) and thrust modulus (see Figure 4.10) and angles (see Figure 4.11 and Figure 4.12), the DFPET solution compares well with the solution given by DITAN. In this sense, the FPET solution could be considered as a good sub-optimal solution of this transfer problem.

4.3.2 Multi-Objective Earth-Mars Transfer Design

Given its computational efficiency it is also possible to extend the field of application by using the proposed transcription method to solve a Global, Multi-Objective (MOO) Optimisation problem for trajectory design. As a first example, a simple direct, *rendezvous* transfer problem between Earth and Mars is considered. The aim is to find the transfers that are Pareto optimal with respect to the Time of Flight and the total ΔV, within a certain range of departure dates and transfer times. The optimisation parameters in this case are simply the departure date t_0, the *ToF* and the number of revolutions around the Sun. MACS2 was used to generate a number of decision vectors. Then, for each decision vector, problem (4.7) is solved with *fmincon*. The boundary conditions for the solution of problem (4.7) are given by the ephemeris of the Earth at t_0 and those of Mars at (t_0+ToF). The boundaries of the search space for the decision vector of the MOO problem are reported in Table 4.2.

Table 4.2: boundaries for optimization parameters for MO Earth-Mars transfer problem.

	Lower	Upper
t_0 [MJD2000]	5000	5779.94
ToF [days]	100	1500
n_{rev}	1	3

The number of revolutions is handled by MACS2 as a real variable and then is rounded to the nearest integer towards minus infinity when solving problem (4.7). The trajectory was transcribed with 20 finite perturbative elements. The constraints violation and optimality tolerances for *fmincon* where slightly relaxed compared to the tests in the previous sections, with the former set to 10^{-6} and the latter to 10^{-4}.

The MACS2 algorithm was run for 40000 function evaluations. The results of four different runs were combined to extract a good approximation of the Global Pareto Front. Figure 4.18 and Figure 4.19 report the solution points in the parameter space and the Pareto front respectively.

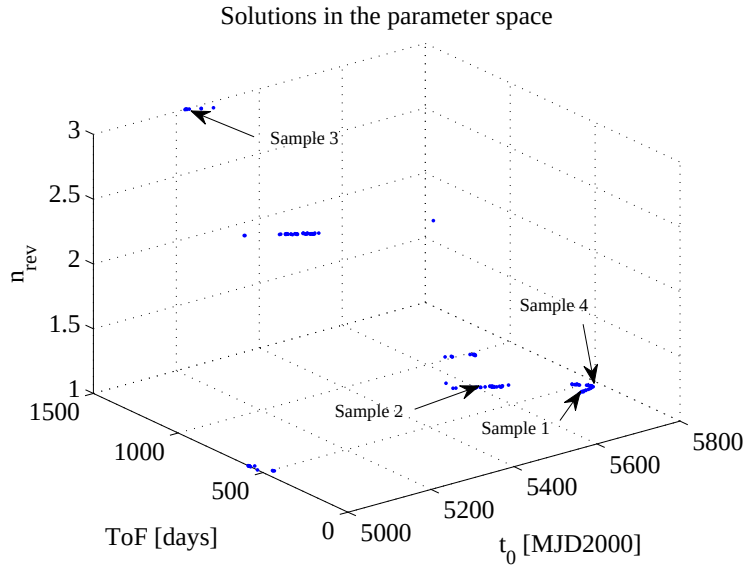

Figure 4.18: Parameters of the solutions for MO Earth-Mars LT transfer problem.

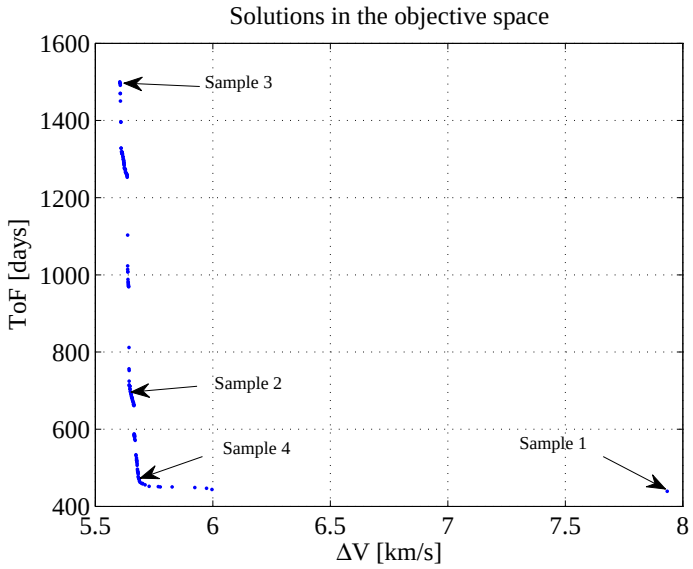

Figure 4.19: Pareto front for MO Earth-Mars LT transfer problem.

The Pareto front presents some discontinuities, which are due to the discrete variable n_{rev}. In particular, the solutions with *ToF* up to 1000 days are all with only one complete revolution, while those with *ToF* between 1000 and 1400 days make two complete revolutions and finally the few over 1400 days make three complete revolutions. Figure 4.20 to Figure 4.27 show the trajectories and corresponding control profiles for three different sample solutions extracted from the Pareto set and reported in Table 4.3:

1. The solution with minimum *ToF*.

2. The solution in the central part of the Pareto Front.
3. The solution with minimum ΔV.

The solution at the knee of the Pareto front: the solution is similar to 1 albeit with a lower ΔV and slightly higher *ToF*.

Table 4.3: Summary of the four sample solutions.

Sample	1	2	3	4
t_0 [MJD2000]	5737.01	5606.82	5222.81	5779.94
t_0 [UTC]	16/09/2015	09/05/2015	20/04/2014	29/10/2015
	12:16:16.32	7:41:13.92	7:33:18.72	03:21:36.00
ToF [days]	439.21	704.25	1500	462.86
n_{rev}	1	1	3	1
ΔV [Km/s]	7.9338	5.6474	5.6047	5.6902

The minimum *ToF* trajectory (see Figure 4.20) reaches Mars in almost exactly one revolution. On the other hand, this requires continuous engine operation for almost the whole transfer, as shown in Figure 4.21, which also translates into a ΔV cost of 7.93 km/s. Note that solutions with a lower *ToF* could be possible, for n_{rev} lower than 1.

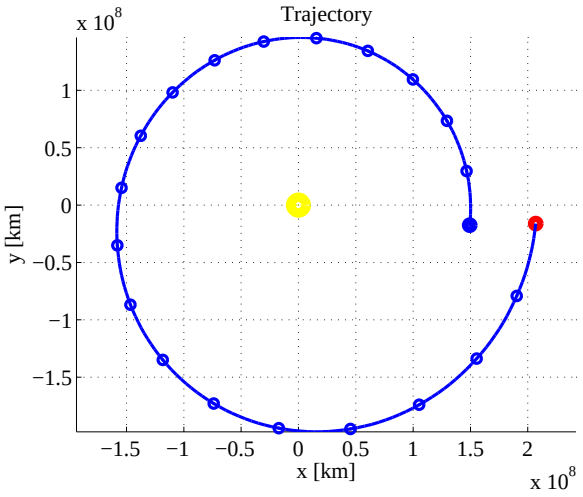

Figure 4.20: Sample solution 1: trajectory.

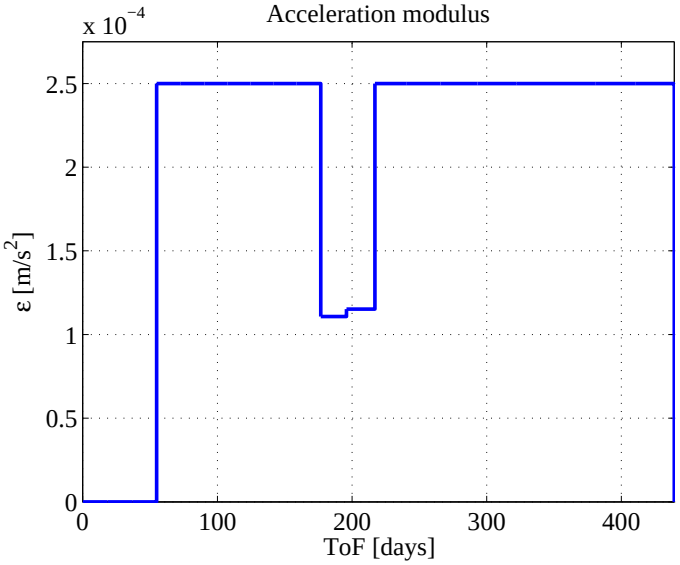

Figure 4.21: Sample solution 1: acceleration modulus.

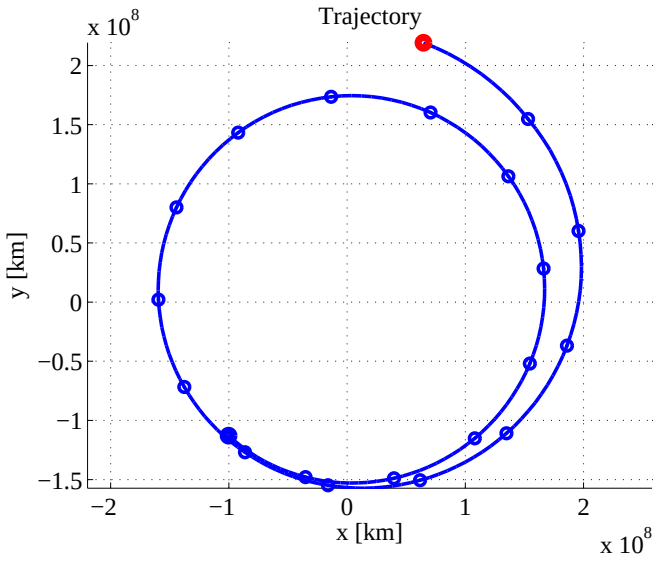

Figure 4.22: Sample solution 2: trajectory.

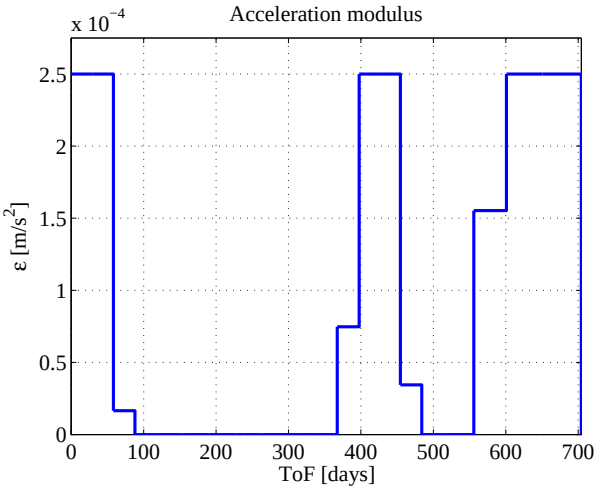

Figure 4.23: Sample solution 2: acceleration modulus.

The second trajectory reaches Mars in 704 days, with one revolution and a half and with three separate thrusting arcs (see Figure 4.22 and Figure 4.23). This allows for a better ΔV cost of 5.65 km/s.

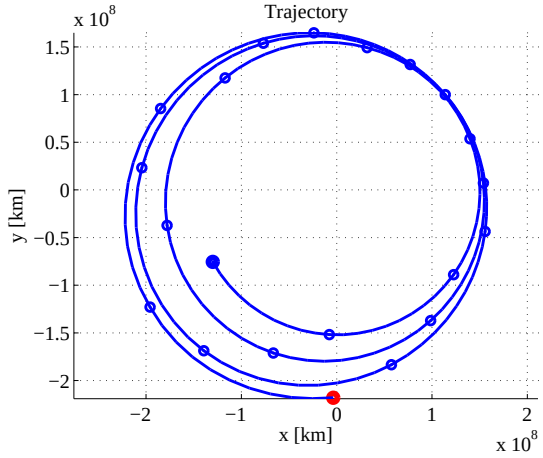

Figure 4.24: Sample solution 3: trajectory.

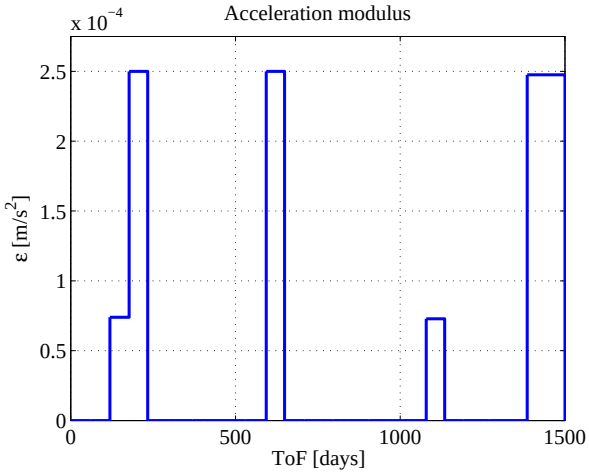

Figure 4.25: Sample solution 3: acceleration modulus.

The minimum ΔV trajectory reaches Mars in 1500 days (the upper bound set for the *ToF*) with slightly more than three revolutions (see Figure 4.24). As shown in Figure 4.25, the four thrusting arcs are concentrated at periapsis and apoapsis, which allows for the mitigation of gravity losses and therefore a low ΔV cost of 5.60 km/s.

The knee solution has a similar phasing between the initial and final positions compared to the minimum *ToF* solution, see Figure 4.26, but due to its higher *ToF* the total ΔV cost is lower. The thrust profile in Figure 4.27 shows three separate thrusting arcs with a lower total thrust time compared to Figure 4.21.

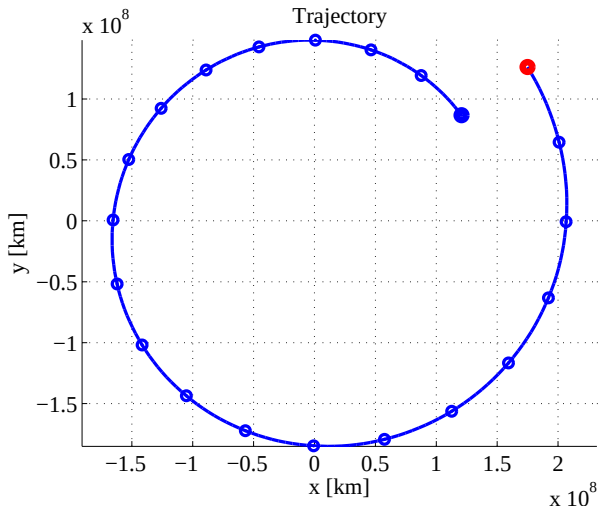

Figure 4.26: Sample solution 4: trajectory.

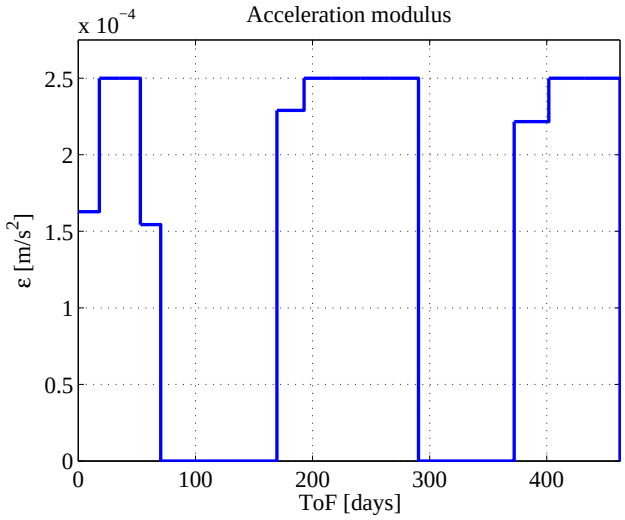

Figure 4.27: Sample solution 4: acceleration modulus.

4.3.3 Transfer between LEO and ISS

The second test case considers a hypothetic orbit transfer between the Ariane 5ATV injection orbit and the ISS orbit, requiring an altitude increase of 95 km. The boundary problem is formulated in an analogous way as the Earth-Mars case, although the ISS motion is modelled as a simple, planar, Keplerian motion and the injection orbit is assumed to be coplanar to the latter. The parameters of the departure LEO are considered fixed, with the exception of the initial true anomaly ϑ_0. Departure time is also considered to be fixed, but the Time of Flight determines the position of the rendezvous with the ISS. It is therefore essential to define the optimal phasing between the departure from LEO and the encounter with the ISS.

The problem is to optimize the ΔV for a transfer with $\vartheta_0 = 210°$, *ToF*=2.02 days and n_{rev}=32. Forty finite perturbative elements were used in the optimisation. The optimised

trajectory has a ΔV of 54.9 m/s. The accuracy is 10^{-5}, a truly remarkable result considering the high number of revolutions.

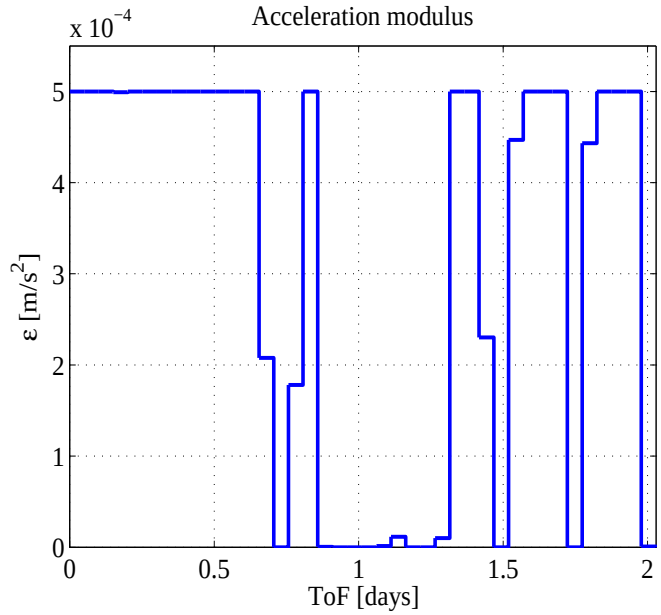

Figure 4.28: Acceleration modulus ε for LEO-ISS LT transfer.

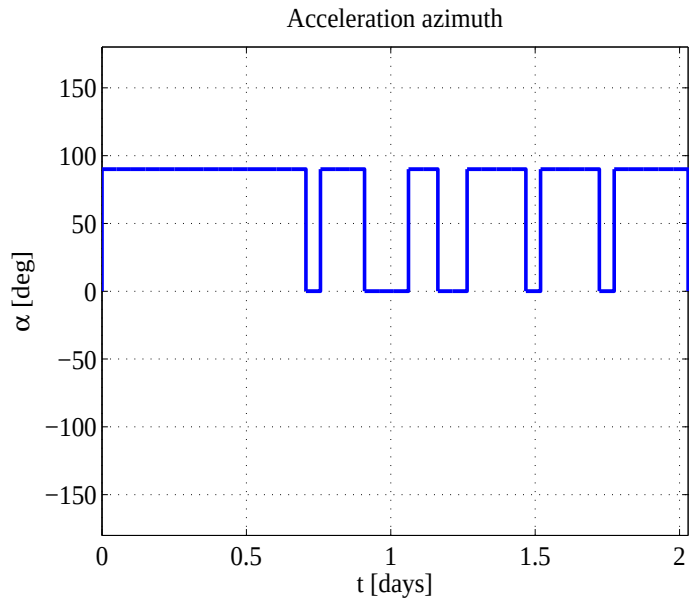

Figure 4.29: Acceleration azimuth α for LEO-ISS LT transfer.

Figure 4.28 and Figure 4.29 show the time history of the acceleration modulus and azimuth respectively (the elevation plot has been omitted since it is constantly null). The acceleration azimuth (see Figure 4.29), is almost constant at 90º, revealing a predominantly transversal and in-plane thrust component, while the thrust modulus in Figure 4.28 shows a long thrusting arc along the initial part of the transfer which accounts for an almost linear increase of the semi-major axis as seen in Figure 4.30. The long interruption of thrusting in the middle part of the transfer is to allow phasing with the target orbit. The eccentricity

(see Figure 4.31) shows a net increase during the transfer to reach the eccentricity of the arrival orbit, albeit it also has a periodic component during the thrusting spirals.

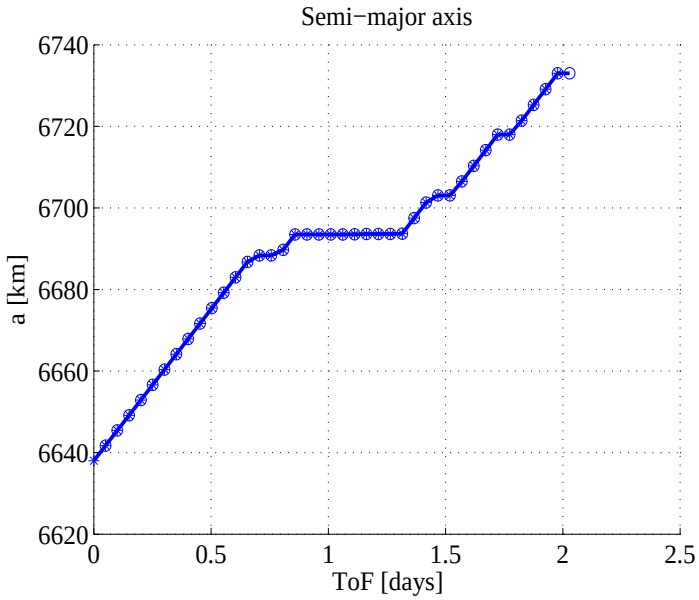

Figure 4.30: Variation of Keplerian Elements for LEO-ISS LT transfer: *a*.

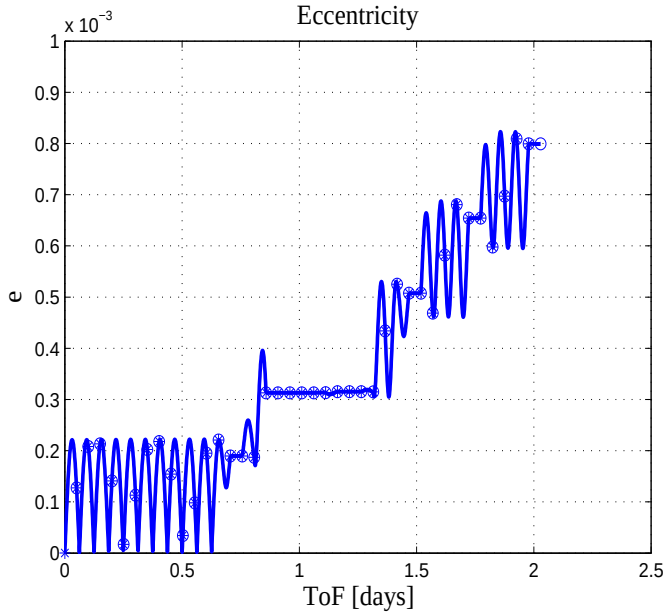

Figure 4.31: Variation of Keplerian Elements for LEO-ISS LT transfer: *e*.

It should be noted, that although *fmincon* converged to a feasible solution, this is hardly the optimal one. This is due to the fact that 40 were used for a transfer with 32 complete revolutions, which means that each trajectory element covers a bit less than a complete revolution. This translates into the fact that the typical *bang-bang* pattern, i.e. with thrusting centered on the apsidal points and coasting elsewhere, cannot be adequately described with such a limited number of elements. While this is not a huge problem in transfers between quasi-circular orbits (as in the present case), it is a key issue in transfers with large variations in the eccentricity. Similar remarks apply also to the control on other

orbital elements, like the argument of perigee. The obvious solution would be to increase the number of trajectory up to at least 4 per revolution, although there would still remain the issue that this would by no means guarantee their proper positioning w.r.t. the apsidal points. Optimisation instances with a higher number of trajectory elements were tried, but there was an unacceptable increase in the computational time and too often *fmincon* did not manage to converge to a feasible solution at all. These computational issues are only exacerbated when one considers that typical transfers in Earth orbit (e.g. LEO to GEO, as shown in the following chapter), normally have hundreds of revolution, which would lead to an intractable number of the degrees of freedom, if the approach described in this chapter is used. The following chapter will therefore propose an alternative approach for tackling this class of trajectory optimisation problems.

4.4 Conclusions

This chapter presented a novel numerical approach for Low Thrust trajectory transcription. The novel approach makes use of a first-order analytical solution of Gauss' planetary equations. The first order analytical solution was demonstrated to provide a fast and relatively accurate propagation of the perturbed Keplerian motion under the effect of a constant thrust. The first order approximation was implemented in a finite element formulation for the solution of two-point boundary value problems that was proven to be more computationally efficient and accurate than other state of the art methods. Furthermore, it was demonstrated how its computational efficiency makes the novel transcription method suitable for the solution of Global and Multi-Objective Optimisation problems for LT trajectory design, in which the 2PBVP needs to be solved thousands of times.

A limitation of the technique presented here is that it is ill suited for modelling transfers with many revolutions around the central body. In such a case, one is confronted with the dilemma of either accepting a large increase in the number of design parameters, which would make the optimisation problem computationally very expensive, or accepting too coarse a discretisation of the trajectory, which in contrast decreases the quality of the solution. Therefore, the next chapter will present rather different techniques specifically target at long spiralling transfers.

Chapter 5.Many-revolution, Low-Thrust Transfers

In this chapter, various techniques are proposed, for treating many-revolution LT transfers with discontinuous control profiles. In particular, an averaging technique is proposed to fast propagate many-revolution transfers under the effect of optimised low-thrust arcs, J_2, light pressure and eclipses. While the examples in Chapter 3 dealt with continuous thrust profiles, in this chapter more general control profiles are considered. A simplified control parameterisation is used to define the thrusting pattern, which ensures enough flexibility to describe complex Low Thrust spirals. The effect of the shadow regions due to solar eclipse is also included in the model. The chapter also presents an application to the optimal design of a low-thrust spiral to transfer a spacecraft from an elliptical to a circular orbit around the Earth. Finally, an example of application to the de-orbiting of space debris from Medium Earth Orbit (MEO) with a combination of Electric Propulsion and Solar Radiation Pressure is shown. The chapter is organised as follows: Section 5.1 will present the proposed model for discontinuous control profiles; Section 5.2 will introduce the proposed averaging technique. These techniques will be then tested in the cases of Section 5.3. Finally, Section 5.4 will discuss in more detail the above-mentioned application of these techniques to the de-orbiting of MEO satellites.

5.1 Discontinuous Control Profiles and Eclipses

In the numerical tests presented in Chapter 3, a simple continuous acceleration was considered. This section proposes a simple approach to introduce bang-zero-bang control profiles and eclipses.

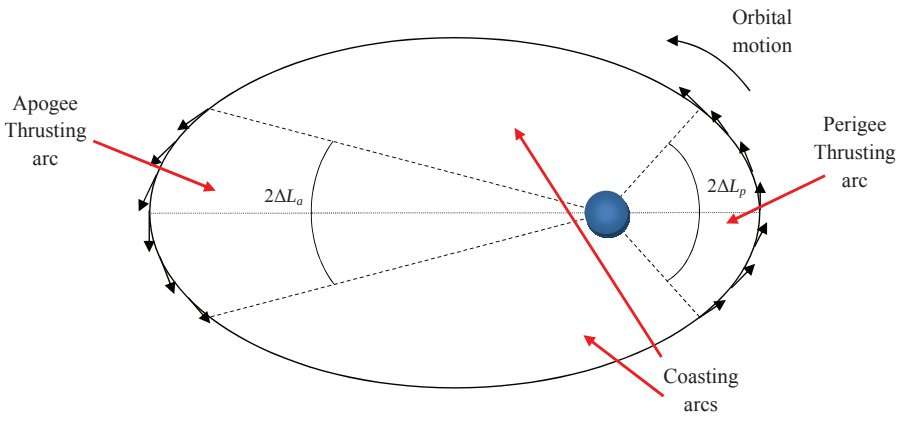

Figure 5.1: Control pattern.

The interest is in the class of low-thrust transfers whose quasi-optimal control corresponds to two thrust arcs. For this class of transfers, each revolution can be divided into 4 sectors, as shown in Figure 5.1: a perigee thrust arc, an apogee thrust arc and two coasting arcs in between. The former, of amplitude ΔL_p, is meant to alter the radius of the apocenter, while the latter, of amplitude ΔL_a, alters the radius of the pericenter. The combined effect of the two thrust arcs can be used to control the inclination and the argument of the pericentre. The variation of the orbital elements along the thrusting arcs is computed with the analytical formulae. A plane change is realised introducing a non-zero elevation angle β_p and β_a. The amplitude of the arcs ΔL_p and ΔL_a, and the angles β_p and β_a, are the quantities to be controlled to match the desired terminal conditions. When a constant thrust is required for each arc, the mass of the spacecraft m_f at the end of a thrust arc can be estimated assuming the control acceleration ε is constant along the thrust arc:

$$m_f = m_i e^{-\frac{\varepsilon \Delta t}{I_{sp} g_0}} \tag{5.1}$$

where m_i is the mass of the spacecraft at the beginning of the thrust arc. The new mass is then used to recompute the control acceleration for the next thrust arc. This introduces a small underestimation of this acceleration, as in reality the latter will increase continuously over time as the mass is consumed.

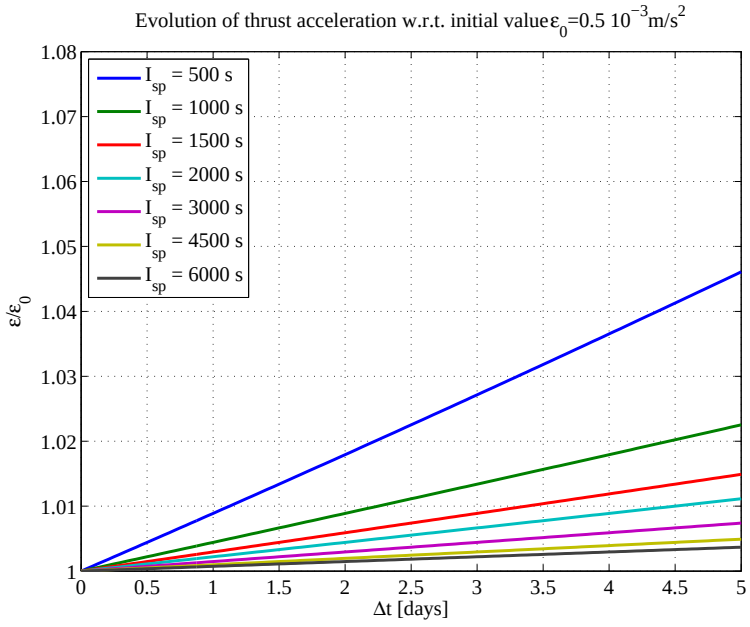

Figure 5.2 Evolution of the thrust acceleration with respect to a reference initial value.

The evolution of the thrust acceleration during a thrusting arc is well described by the equation:

$$\varepsilon(\Delta t) = \frac{1}{\frac{1}{\varepsilon_0} - \frac{\Delta t}{I_{sp} g_0}} \tag{5.2}$$

where ε_0 is the acceleration for Δt=0 . As shown in Figure 5.2, the increase of the acceleration w.r.t. a reference value is rather small for high I_{sp}, being only 1-2% after a few days of thrusting. The error on the magnitude of the thrust acceleration directly translates into an error on the orbital elements and, in this sense, one could also estimate that the latter will be roughly half the error on the acceleration at the end of propagated arc. This is due to the quasi-linear behaviour of the error shown in Figure 5.2, which means that the average error on the acceleration during the thrusting arc is roughly half the error at the final time. Moreover one has to consider that, given the control strategy in Figure 5.1, a single propagated arc will typicall cover a fraction of a revolution, which, in Earth orbit has a period between a few hours and a few days. In light of this, the resulting error is therefore a fraction of a percent and is deemed acceptable in the scope of the present work.

5.1.1 Eclipse Modelling

In the case of long, multi-revolution transfers, the effect of a solar eclipse might be considerable if one takes into account the fact that, for example, during an eclipse the operation of an Electric Propulsion system will, most likely, have to be interrupted due to limitations on power generation and storage. Moreover, eclipses change due to the combined effect of the motion of the Earth around the Sun and the variation of orbit size and orientation due to engine thrust and other perturbative effects. In the case of a full numerical integration, eclipses are computed by checking shadow conditions at each step and eventually activating or deactivating some kind of eclipse flag. This leads to discontinuities in the integrand function. In an analytical approach, like the one here proposed, one can however exploit the fact that the entrance and exit points of the shadow cone (for the sake of simplicity, no distinction is made between umbra and penumbra conditions) can be computed beforehand and then the thrusting arcs can be updated accordingly. Other authors have already proposed a similar approach, see for example Kechichian[33], in which orbits with eccentricity up to 0.2 are considered; Colombo and McInnes[106] also applied a similar method but limited to the planar case. In this work, a cylindrical model for Earth's shadow is adopted (see Figure 5.3), which is perfectly adequate in the case of a spacecraft in Earth orbit.

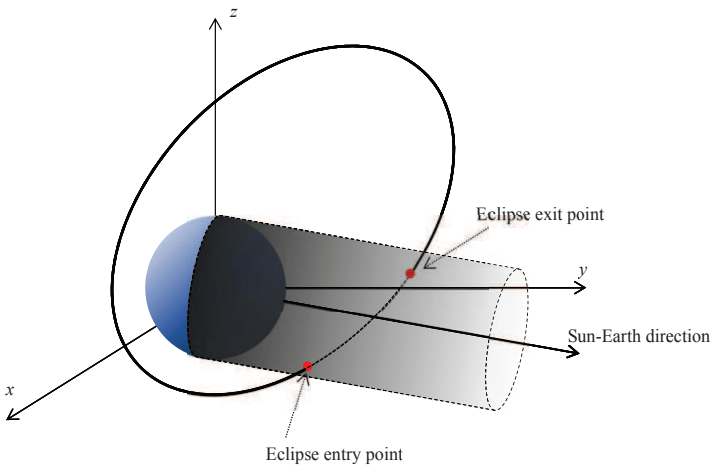

Figure 5.3: Shadow model.

In order to identify the eclipse entry and exit points one has to find the true anomalies of the geometrical intersections between the cylinder and the osculating orbit. The mathematical formulation of this problem can be found in Escobal[107] and Vallado[108] and will not be repeated here. Starting from the osculating orbital elements and the current Sun-Earth vector, this formulation leads to a quartic equation in $cos\theta$, which can be solved either analytically by means of Ferrari's method, as is done in this work, or numerically with a root-finding algorithm. Note that out of the 4 roots of the quartic polynomial, two are spurious. Once the shadow entry and exit points are known, one can correct the thrusting and coasting arcs as shown in Figure 5.4.

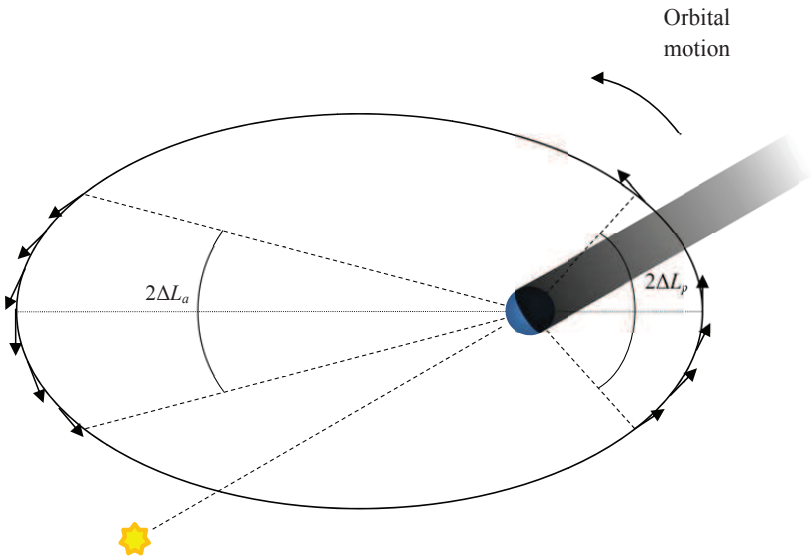

Figure 5.4: Thrust pattern with eclipse region.

Apart from identifying the shadow regions, this formulation also allows one to analytically compute the time spent in the shadow region, t_{ecl}, for each orbit.

5.2 Orbital Averaging

In Chapter 3, a set of analytical formulae for propagating the perturbed Keplerian motion was proposed. As a further step, it is proposed to use these formulae to compute the average variation of the orbital elements over a complete revolution and to numerically propagate the average orbital elements, as it is done in classical averaging techniques (see Ferrier and Epenoy[39,40] and Tarzi et al.[109]). In the proposed averaging technique, the variation of the orbital elements is given by:

$$\begin{aligned}\overline{\mathbf{E}}(t) &= \mathbf{E}_0 + \int_{t_0}^{t} \dot{\mathbf{E}}_{avg}\left(\tau, \overline{\mathbf{E}}(\tau), \overline{\Delta L}_p(\tau), \overline{\Delta L}_a(\tau), \overline{\beta}_p(\tau), \overline{\beta}_a(\tau)\right) d\tau \\ \dot{\mathbf{E}}_{avg} &= \frac{\Delta \mathbf{E}_{2\pi}}{T_{2\pi}}\end{aligned} \tag{5.3}$$

where $\overline{\mathbf{E}}$ represents the vector of the averaged orbital elements. $\Delta\mathbf{E}_{2\pi}$ is the net variation of the orbital elements computed over a complete revolution and $T_{2\pi}$ is the corresponding period. In most orbit averaging techniques, $\Delta\mathbf{E}_{2\pi}$ is computed by numerical quadrature of Gauss' planetary equations over the true anomaly (or longitude). Here $\Delta\mathbf{E}_{2\pi}$ is provided by the evaluation of the analytical formulae at $L=2\pi$. As shown in Section 3.1.6, this is advantageous in terms of computational cost for a comparable accuracy. The terms $\overline{\Delta L}_p$, $\overline{\Delta L}_a$, $\overline{\beta}_p$ and $\overline{\beta}_a$ are the control parameters mentioned in Section 5.1 and are computed as a piecewise linear interpolation with respect to time, from n_{nodes} nodal values, uniformly spaced within the limits of the transfer period. For example, in the case of $\overline{\Delta L}_p$, one can write:

$$\overline{\Delta L}_p(t) = f_{interp}\left(\mathbf{t}_p, \mathbf{\Delta L}_p, t\right) \tag{5.4}$$

where $\mathbf{\Delta L}_p$ is a vector containing the n_{nodes} nodal values, $\mathbf{t_p}$ is the vector which collects the corresponding times at which the nodal values are specified, and f_{interp} defines a piecewise linear interpolation.

An additional equation describes the evolution of the averaged mass:

$$\begin{aligned}\overline{m}(t) &= m_0 + \int_{t_0}^{t} \dot{m}_{avg}\left(\tau, \overline{\Delta L}_p(\tau), \overline{\Delta L}_a(\tau)\right) d\tau \\ \dot{m}_{avg} &= \frac{\Delta m_{2\pi}}{T_{2\pi}}\end{aligned} \tag{5.5}$$

where $\Delta m_{2\pi}$ is computed in discrete steps for each thrusting arc with Eq. (5.1). With a generic control profile as described in Section 5.1, at each revolution one would have to perform as many analytical propagations as the number of thrusting and coasting arcs. One can argue that in such a case, the cost of the analytical propagation might no longer be

advantageous compared to other methods. To assess this, a test analogous to that of Section 3.1.6 was performed, in which the motion is propagated for one revolution under the effect of a tangential thrust for an arc of length $2/3\pi$, followed by a coasting arc of length $\pi/3$ (with J_2 only), another propelled arc of length $2/3\pi$, and finally another coasting arc of length $\pi/3$. Therefore, there are 4 separate propagations to be performed with the analytical formulae. This is an interesting case as it mimics the case of a bang-zero-bang control as described in Section 5.1. The accuracy and computational cost of the analytical solution are compared to a fully numerical integration performed with Gauss-Legendre quadrature, which, in the tests in Section 3.1.6, appeared to be the most competitive method in terms of accuracy and CPU cost. Two slightly different techniques are tested: in the first one, the motion is propagated without splitting the integration interval in the three discontinuous points; in the second one, the orbit is split into four intervals (as is done for the analytical propagation) and Gauss-Legendre quadrature is applied to each of them. The number of nodes for each interval is chosen such that the number of nodes is comparable to the first case when a single integration is performed. In particular, quadrature formulas 16 and 24 nodes have been tested for the single interval case; for the split interval case, three combinations of 5+5+5+5, 7+3+7+3 and 6+6+6+6 nodes were tested.

Figure 5.5 and Figure 5.6 show the error on semi-major axis, P_1, P_2 and time. Even in this case, the analytical propagation is more accurate than the numerical quadrature. Only the Gauss-Legendre quadrature with 6+6+6+6 nodes displays a comparable or better error on the semi-major axis (see Figure 5.5a), although it fares worse in the other cases. Interestingly, 7+3+7+3 has a low error on time during the last arc (see Figure 5.6b) although the other errors are quite high. As already underlined in Section 3.1.6, Gauss-Legendre with 24 nodes has a slight advantage on the calculation of time. However, both Gauss-Legendre with 16 nodes and Gauss-Legendre with 24 nodes show a considerable sensitivity to the positioning of the integration nodes when a discontinuous perturbation is treated within a single interval. In fact, as can be seen in Figure 5.5 and Figure 5.6, the accuracy periodically improves with the length of the integration arc. In terms of computational cost (see Figure 5.7) only Gauss-Legendre with 16 nodes is cheaper than the analytical propagation, while the others are more expensive. These tests confirm the advantage of the analytical propagation, even in the worst case of a propagation arc of length 2π with discontinuities.

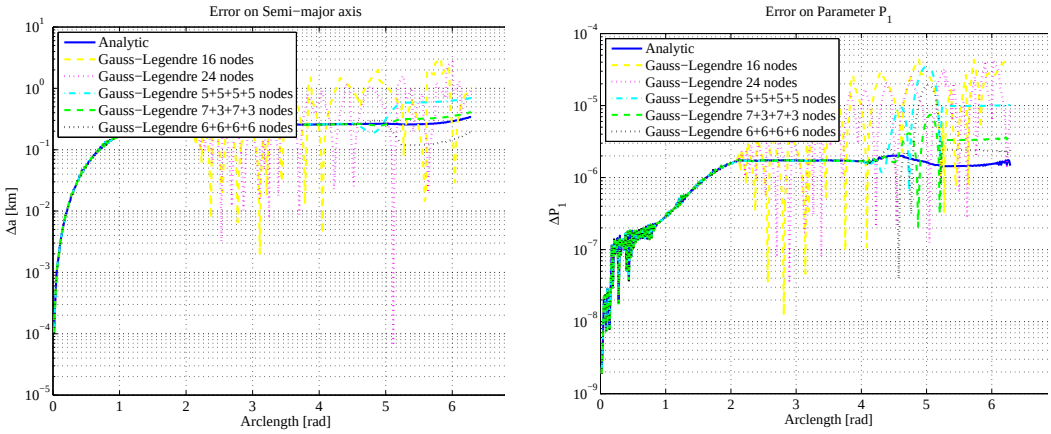

a) **b)**

Figure 5.5: Comparison with numerical integration on discontinuous arcs: a) error on semi-major axis b) error on P_1.

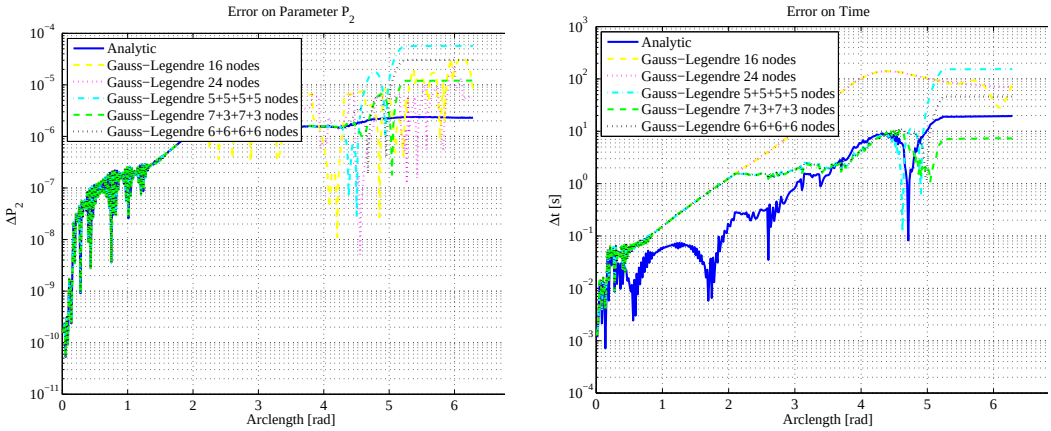

a) **b)**

Figure 5.6: Comparison with numerical integration on discontinuous arcs: a) error on P_2 b) error on time.

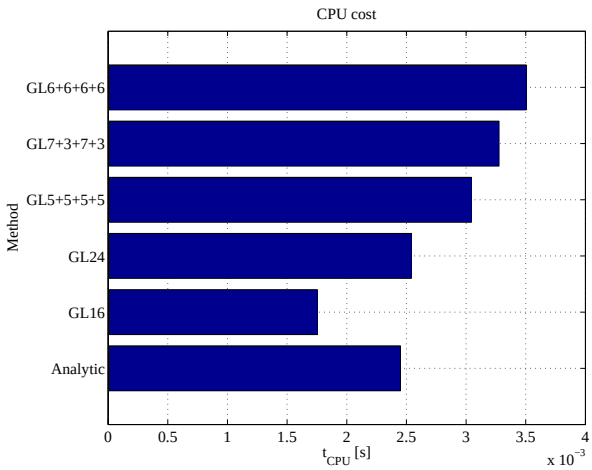

Figure 5.7: Comparison with numerical integration on discontinuous arcs: computational cost.

5.3 Applications

5.3.1 Spiralling with Solar Radiation Pressure and Eclipses

This section presents a comparison between the averaged solution and the rectified solution for the case of a long term propagation of an initial planar elliptical orbit (as in Table 5.1) under the combined effect of a thrust acceleration along the tangential direction, solar radiation pressure (SRP) and Earth oblateness (J_2 effect).

Table 5.1: Initial orbit parameters.

a	e	i	Ω	ω	θ
20000 km	0.5	6°	0°	0°	0°

The initial mass of the spacecraft is 1000 kg, and it is assumed that the engine delivers 10^{-2} N at a specific impulse of 3000 s. The cross section area used to compute the SRP acceleration is 1200 m^2, a value chosen so that the resulting force is about half of the thrust of the engine. At departure, the Sun lies at the Summer Solstice point. The propagation time is set to one and a half years. The SRP direction is considered to be constant along an orbit, therefore allowing the use of the formulas in (3.25) for a constant inertial acceleration. The secular variation in the Sun-Earth direction is used to update the direction of the inertial acceleration. Moreover, eclipses are introduced with the methodology detailed in Section 5.1.1 and the consequent thrust interruptions are accounted for. The averaged propagation is performed with MatLab® *ode23* which implements a Runge-Kutta integration method. The results are compared to a full numerical integration with *ode113*, and to the analytic propagation with rectification every orbit if no eclipse occurs or two times per orbit if an eclipse is present. The CPU time required by the averaged analytic propagation was 1.2 s while the full numerical integration required about 100 s. The rectification required about 7s, showing the additional advantage of the analytic averaging approach. Figure 5.8a shows the long-term, monotonic increase of the semi-major axis due to the tangential thrust. Figure 5.8b shows a close up of a portion of the curve. The dashed curve represents the full numerical integration, the dotted curve represents the analytical propagation with rectification and the solid curve the average solution. Note that the analytical formulas are evaluated only at the end of each revolution and at the transition out of the eclipse. The full numerical integration displays a short-term oscillation of a, due to J_2 and SRP, a secular increment over a revolution. The averaged solution captures accurately the secular components while the analytical solution with rectification keeps

track of the periodic components, although in the figure only the value of the semi-major axis at the eclipse times is plotted.

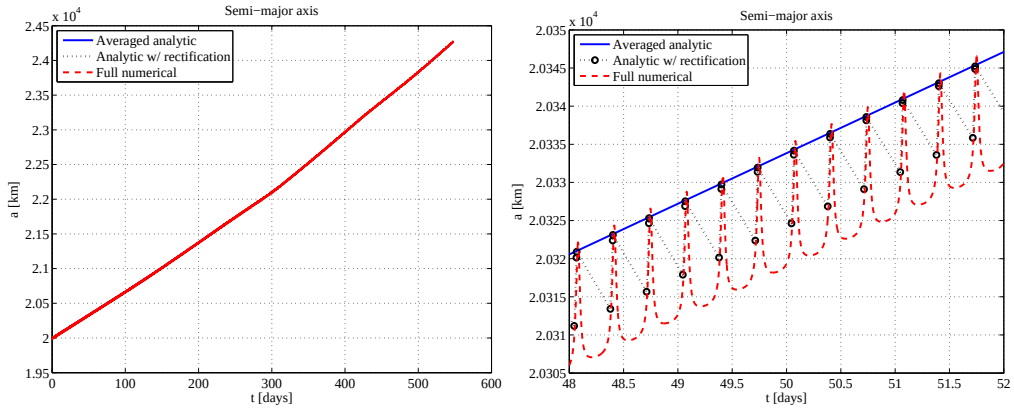

Figure 5.8: Spiralling with SRP: a) semi-major axis; b) Close-up.

Figure 5.9 shows the long term variation of orbital eccentricity due to the combined effects of tangential thrust and SRP. Tangential thrust alone would produce a monotonic decrease of the eccentricity, however, SRP adds a long-term oscillatory component that is linked to the rotation of the Sun-spacecraft vector. SRP also produces a small long term deviation of the inclination due to the relative angle between the Ecliptic plane and the Equatorial plane, in which the initial orbit lies, as shown in Figure 5.10.

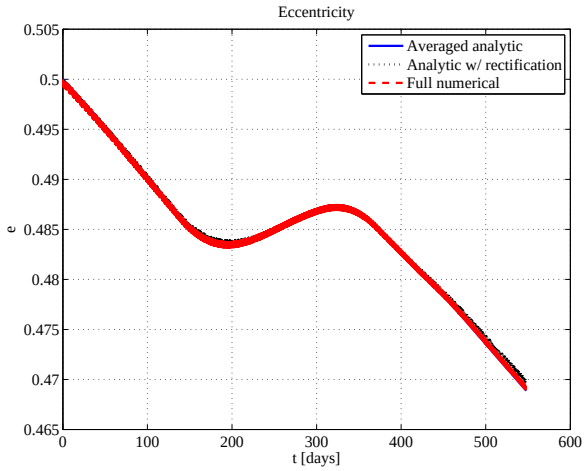

Figure 5.9: Spiralling with SRP: eccentricity.

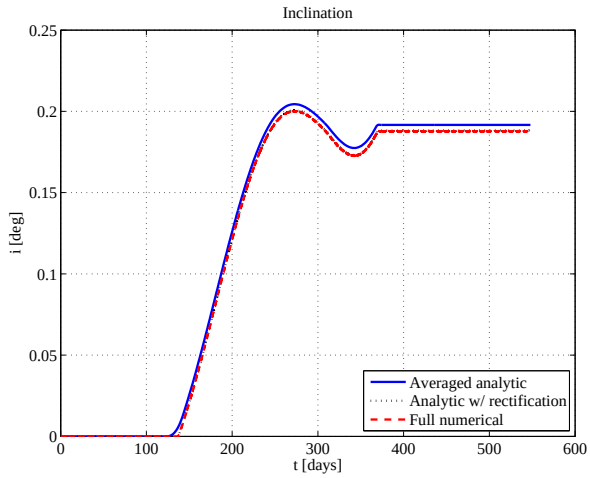

Figure 5.10: Spiralling with SRP: inclination.

5.3.2 GTO to GEO Orbit Circularisation

The previous section demonstrates the advantage of using the proposed analytical formulae for the long propagation of spirals with discontinuous control profiles and eclipses together with their use in conjunction with orbit averaging. In this section a further example will demonstrate how to combine the control parameterisation presented in Section 5.1 with orbit averaging to circularise an initial GTO into a GEO in a specified transfer time. The initial orbit parameters are as in Table 5.2.

Table 5.2: Initial orbit parameters.

a	e	i	Ω	ω	θ
24505.9 km	0.725	7°	0°	0°	0°

The target orbit is a GEO with zero-inclination, therefore a plane change of 7° is also required. The time specified for the transfer is 225 days. Engine thrust is 0.35 N, with a specific impulse of 2000 s. The initial mass of the spacecraft is 2000 kg and mass consumption is also taken into consideration during the transfer using Eq. (5.1). Four nodes each are used to model the variation of ΔL_p, ΔL_a, β_p and β_a, leading to a total of 16 optimisation parameters. The total ΔV is minimised while matching the final semi-major axis, eccentricity and inclination, obtained through the analytical propagator, with those of the target orbit:

$$\begin{aligned} &\min_{\Delta L_p, \Delta L_a, \beta_p, \beta_a} \Delta V \\ &s.t. \\ &\mathbf{E}(t_0) = \mathbf{E}_{GTO} \\ &\mathbf{E}(t_f) = \mathbf{E}_{GEO} \end{aligned} \tag{5.6}$$

This is basically a single-shooting, direct collocation method. The MatLab® *fmincon-sqp* algorithm is used to solve Problem (5.6). The optimisation converges in 8 iterations and 25 seconds (on a Windows 7 platform), and the optimised solution has a ΔV cost of 1.78 km/s. This result compares well with that given, for an identical test problem, by the solver MIPELEC (see Ferrier and Epenoy[40]), which returns a ΔV cost of 1.68 km/s in about 14s of computational time on a UNIX-based Sun workstation. To compare the computational times, one has to consider that MIPELEC is written in FORTRAN77 and a MatLab code is usually at least one order of magnitude slower than an equivalent FORTRAN code.

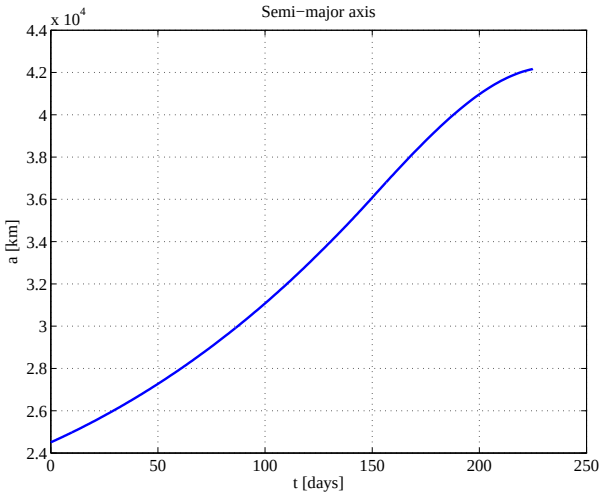

Figure 5.11: Orbit circularisation: semi-major axis.

Figure 5.11, Figure 5.12 and Figure 5.13 show the variation of semi-major axis, eccentricity and inclination respectively. It can be seen that all quantities change monotonically from their initial values to the target ones.

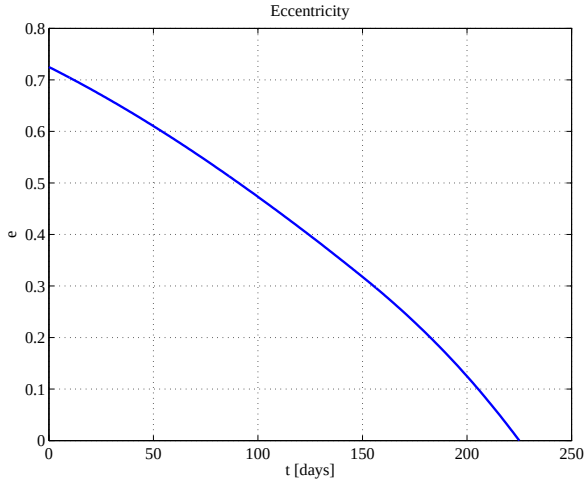

Figure 5.12: Orbit circularisation: eccentricity.

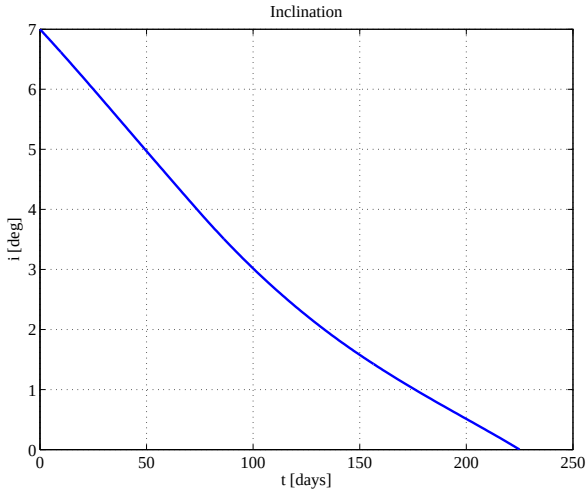

Figure 5.13: Orbit circularisation: inclination.

Figure 5.14 shows the variation of perigee and apogee and it is interesting to see that the perigee rise gradually increases in speed. There is also a slight increase in the apogee radius due to the amplitude of the apogee thrusting arc which is compensated for in the last part of the transfer by a perigee arc (see Figure 5.15), with thrust in the negative tangential direction. Note that, these behaviours are consistent with the results shown in Geffroy and Epenoy[39] and Tarzi et al.[109], even if here a much more simplified model has been used.

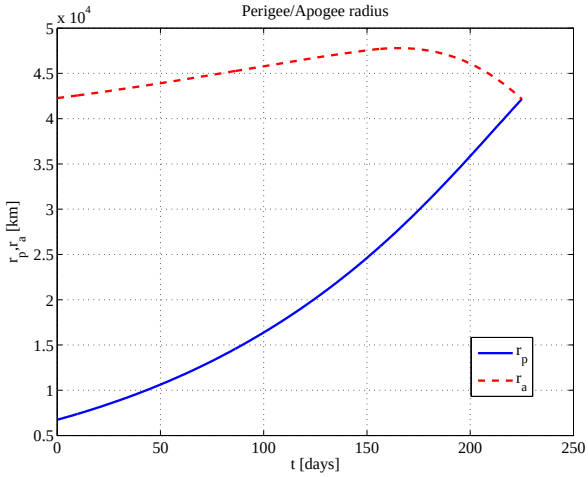

Figure 5.14: Orbit circularisation: perigee and apogee.

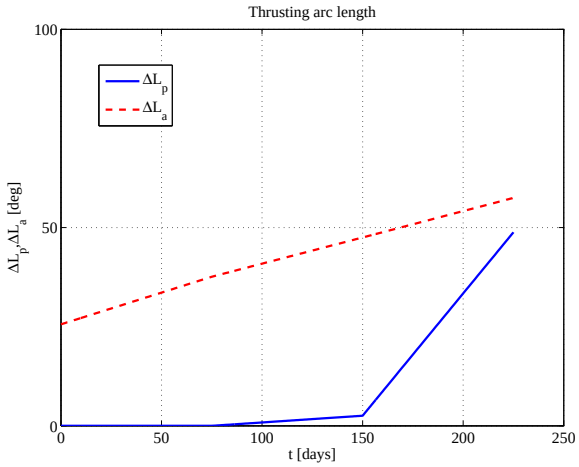

Figure 5.15: Orbit circularisation: thrusting arc length.

Figure 5.16 shows the thrust azimuth α and elevation β in the *t-n-h* reference frame for the perigee and apogee thrusting arcs. It shows that the apogee arc always has a positive tangential component (i.e. energy-increasing), while the opposite is true for the perigee one since it has to compensate for the apogee altitude increase. The plane change effort is concentrated at the apocentre with an out-of-plane component around 15°. Note that the contribution of perigee thrusting to the plane change is only during the final part of the circularisation.

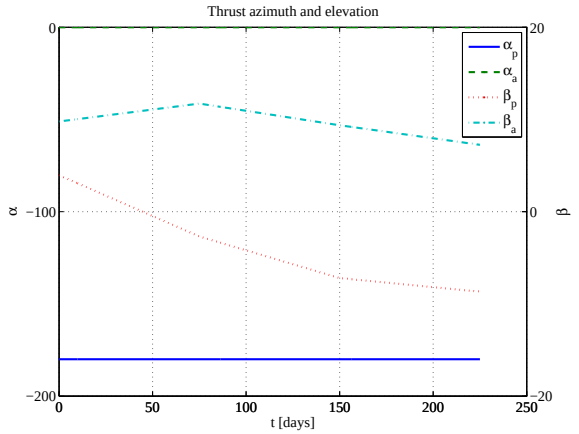

Figure 5.16: Orbit circularisation: thrust azimuth and elevation.

5.4 De-Orbit Analysis for MEO Satellites with Electric Propulsion and SRP

International agreements[115] recommend that certain classes of man-made objects in Earth orbit should re-enter the atmosphere within 25 years after the end of their operational life, in order to mitigate the growth of space debris. Therefore, it is essential to devise some form of disposal strategy already in the early stage of the design of a satellite.

Table 5.3 MEO orbit parameters for GNSS constellation.

a [km]	e	i [deg]	m_0 [kg]
29600	0	55.3	1000

This section, presents the parametric analysis of some Low Thrust disposal options for satellites in Medium Earth Orbit (MEO) combining Electric Propulsion and Solar Radiation Pressure (SRP). The mass and orbit characteristics of a Galileo-type (GNSS) navigation satellite are taken as a reference for all the analyses in this section (see Table 5.3). The objective is that of lowering the perigee of a spacecraft flying on an orbit defined by the orbital elements in Table 5.3, down to an altitude of 200 km at which the atmospheric drag can rapidly lead to a re-entry of the object into the atmosphere. Note that, the spacecraft mass in Table 5.3, is assumed to include the EP system as well as the propellant required for the deorbiting. The engine's specific impulse is assumed to be 3000 s, which is typical for state-of-the-art Electric Propulsion systems.

From a system design point of view, it is interesting to analyse the electric thruster performance requirements (in particular the thrust level) as a function of the required de-orbit time. Moreover, the analysis will explore the effect of combining SRP, by means of an area-to-mass ratio (*A/m*) augmenting device, with EP.

The evolution of the GNSS orbit over time under the effect of a low-thrust action is propagated with the orbital averaging technique developed in Section 5.2. For each revolution the thrust is applied two times, around the pericentre and around the apocentre respectively. The thrust vector is aligned with the velocity vector when thrusting around the pericentre and opposite to the velocity vector with thrusting around pericentre. Moreover, both the apocentre and pericentre thrusting arcs have the same semi-amplitude ΔL_{EP}. This thrusting strategy has the combined effect of decreasing the pericentre and increasing the orbit eccentricity. In order to compute the thrust F_{EP} to achieve the desired pericentre altitude in a given time Δt_{deorb}, one has to solve the following non-linear equation in F_{EP}:

$$h_{peri}\left(\Delta t_{deorb}, F_{EP}, \Delta L_{EP}\right) = 200km \tag{5.7}$$

where h_{peri} is the final achieved perigee altitude. This simple one-dimensional problem was solved with a *bisection* method.

5.4.1 De-orbit with Electric Propulsion

In this section, the GNSS de-orbiting is analysed considering EP propulsion only. The required thrust is derived for a range of de-orbiting times between 0.25 and 25 years and a range of thrusting arc amplitudes between 30° (one-sixth of an orbit) and 180° (i.e. a full orbit). Figure 5.17 shows the required engine thrust to achieve the required pericentre altitude in a range of times between 0.25 and 2.5 years, for different amplitudes of the apogee/perigee thrusting arcs. One can see that, if the thrust is applied continuously for the full orbit (ochre line), the required thrust level is around 0.4 N for the minimum time of 0.25 years and is 0.05 N for 2.5 years. Even in the first case, the required thrust is within the capabilities of current EP systems. Note also that the required thrust level decreases exponentially with the deorbit time, and thus shows a linear behaviour if plotted in a logarithmic scale (see Figure 5.18). Thrusting for a full orbit is less mass efficient, as shown in Figure 5.19, since the required propellant mass Δm, 85 kg, is some 60% higher than in the case in which the thrust is applied only for one sixth of each revolution (blue line). On the other hand, in this latter case, the required thrust is 1.05 N, which is more than double than the full orbit case.

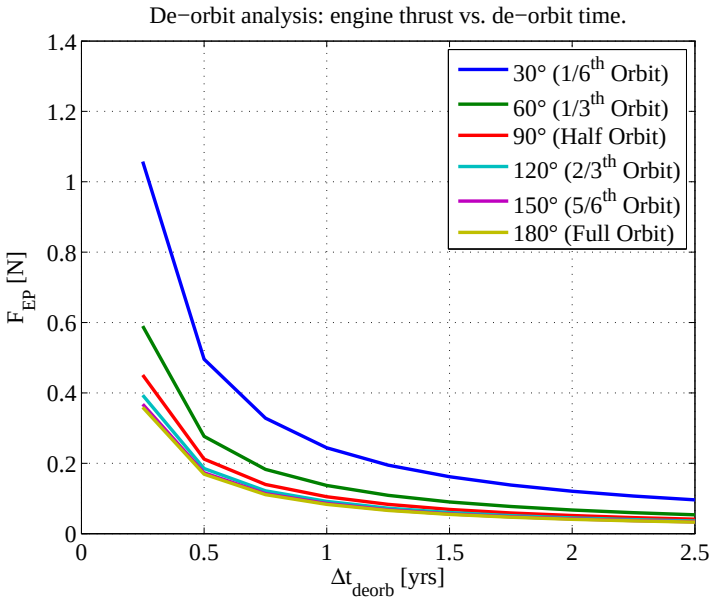

Figure 5.17: De-orbit analysis for deorbit times between 0.25 and 2.5 years: required engine thrust.

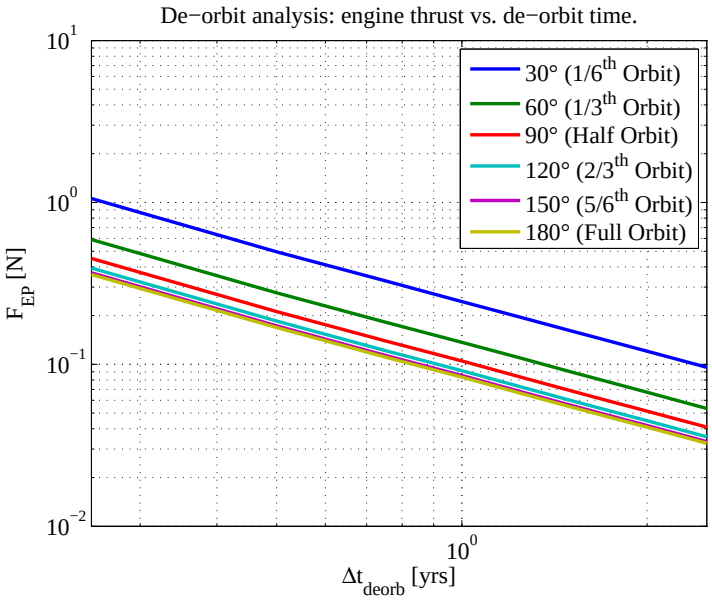

Figure 5.18: De-orbit analysis for deorbit times between 0.25 and 2.5 years: required engine thrust, logarithmic scale.

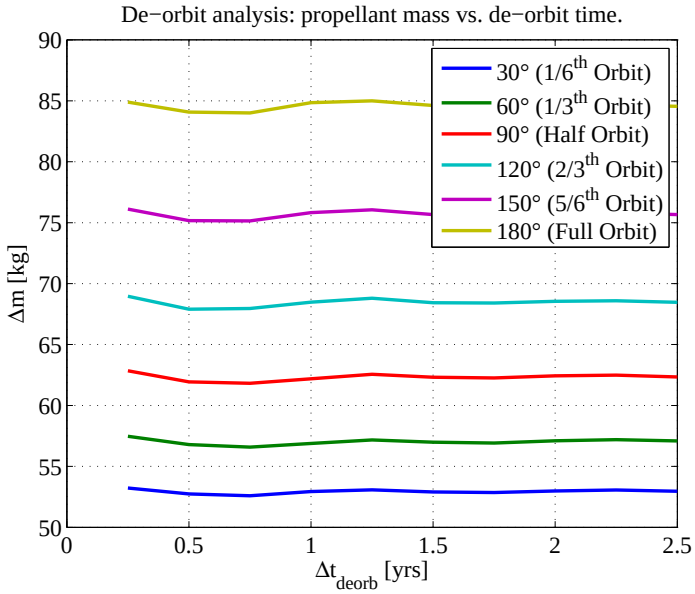

Figure 5.19: De-orbit analysis for deorbit times between 0.25 and 2.5 years: propellant consumption.

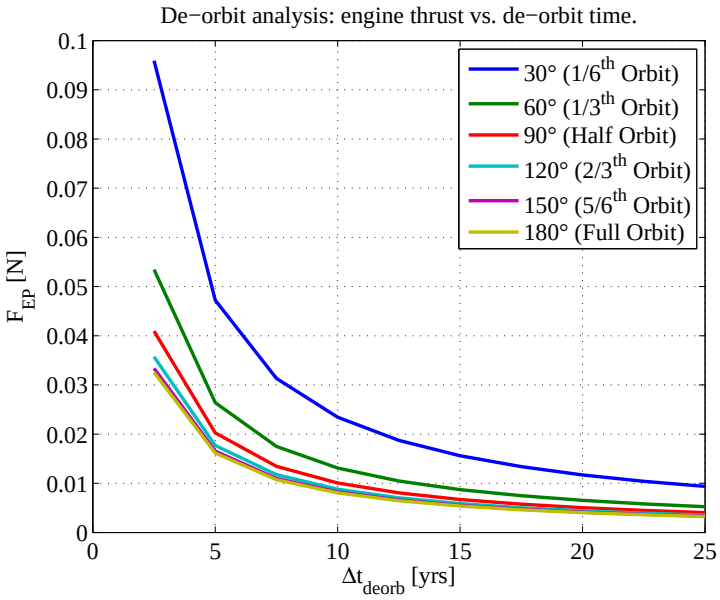

Figure 5.20: De-orbit analysis for deorbit times between 2.5 and 25 years: required engine thrust.

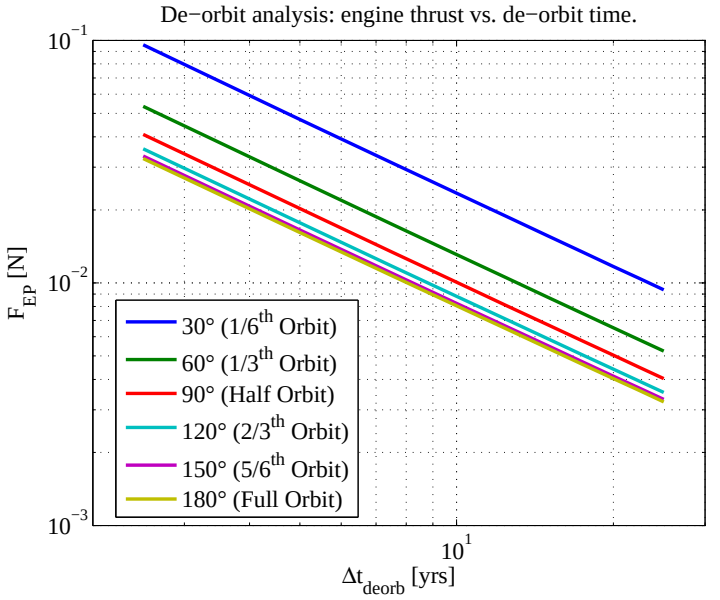

Figure 5.21: De-orbit analysis for deorbit times between 2.5 and 25 years: required engine thrust, logarithmic scale.

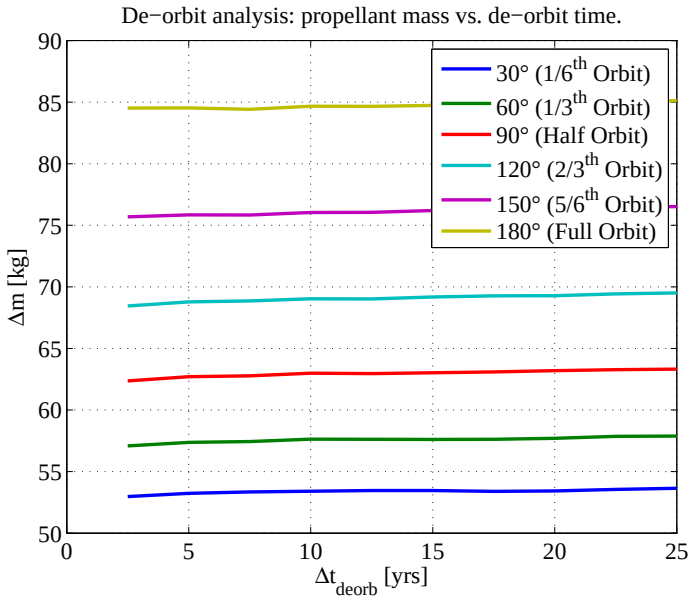

Figure 5.22: De-orbit analysis for deorbit times between 2.5 and 25 years: propellant consumption.

Figure 5.20, Figure 5.21 and Figure 5.22 show analogous results for deorbit times between 2.5 and 25 years. The behaviour of the required thrust level is very similar to that of the previous case, although the values are one order of magnitude smaller. Note, however, that the propellant mass is basically constant with respect to the deorbit time, as shown in Figure 5.19 and Figure 5.22.

5.4.2 De-orbit with EP and SRP

This section considers the case in which the EP and the SRP are concurrently used to deorbit a spacecraft from MEO. The key idea is that of exploiting SRP, in order to naturally increase the orbit eccentricity, as suggested in past works by Colombo, Lücking at al.[110,111,112] This can be achieved thanks to the fact that, in Earth orbit, SRP produces a secular oscillation of the eccentricity, with a period of about one year. The amplitude of the oscillations depends mainly on the initial semi-major axis and eccentricity and on the area-to-mass ratio. It is clear that, if the area-to-mass ratio is large enough the pericentre of the orbit can be brought down to the required value within one year. However, this normally requires relatively large reflective surfaces. A way to reduce the area is to exploit the SRP only for the six months it induces a positive variation of the eccentricity.

If the SRP is used in conjunction with electric propulsion the strategy can be similar to that adopted in Section 5.4.1 but this time the contribution of SRP is also added to the propagation for the six months it is active. The orbital propagation is performed with the averaging approach described in Section 5.3.1 including the effect of eclipses as illustrated in Figure 5.23.

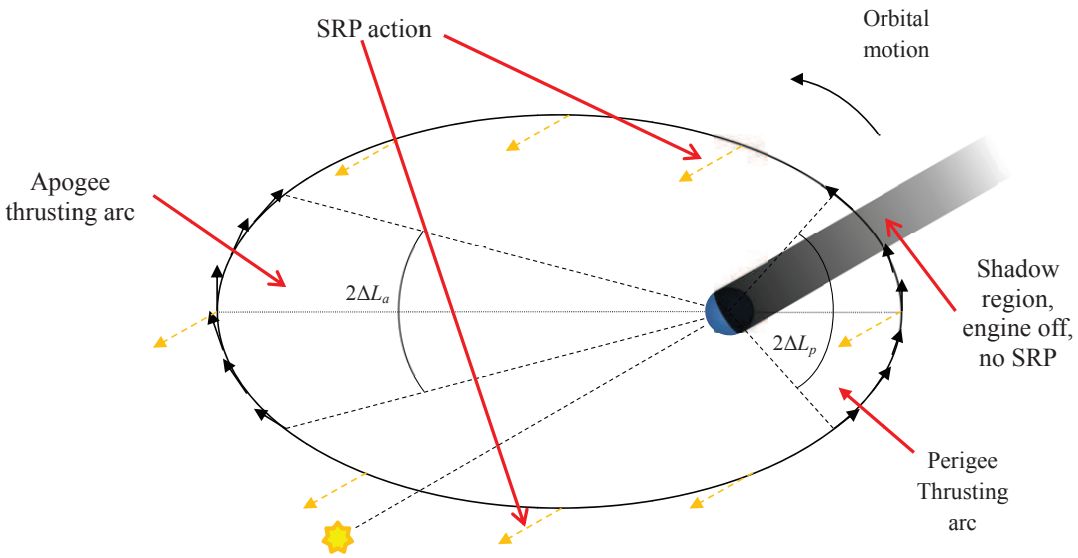

Figure 5.23: Thrusting pattern with SRP and eclipses.

Figure 5.24, Figure 5.25 and Figure 5.26 show the required thrust and mass for a spacecraft with a reference area-to-mass-ratio of 1 m^2/kg. The results are plotted against the EP only case analysed in Section 5.4.1.

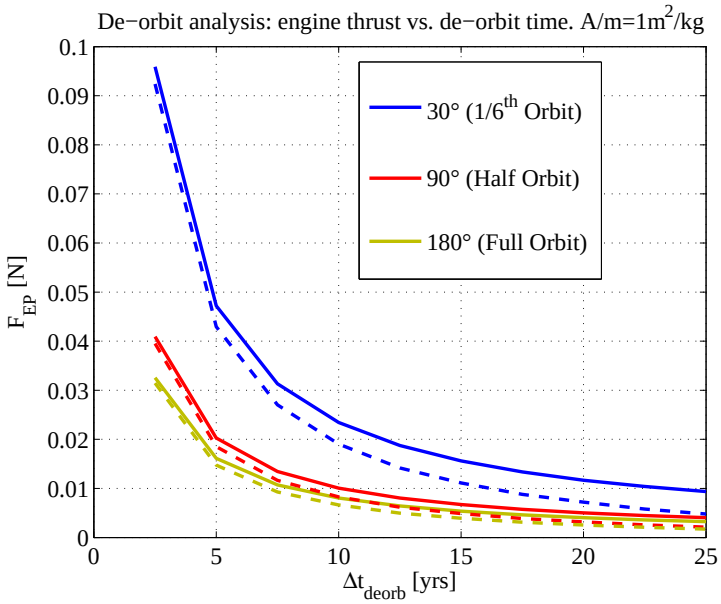

Figure 5.24: De-orbit analysis for deorbit times between 2.5 and 25 years: required engine thrust. Solid line: EP only. Dash line: EP+SRP.

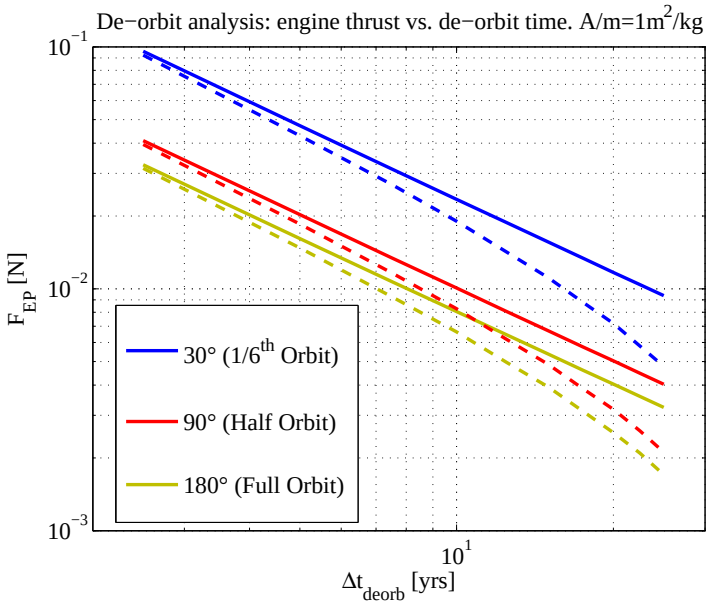

Figure 5.25: De-orbit analysis for deorbit times between 2.5 and 25 years: required engine thrust, logarithmic scale. Solid line: EP only. Dash line: EP+SRP.

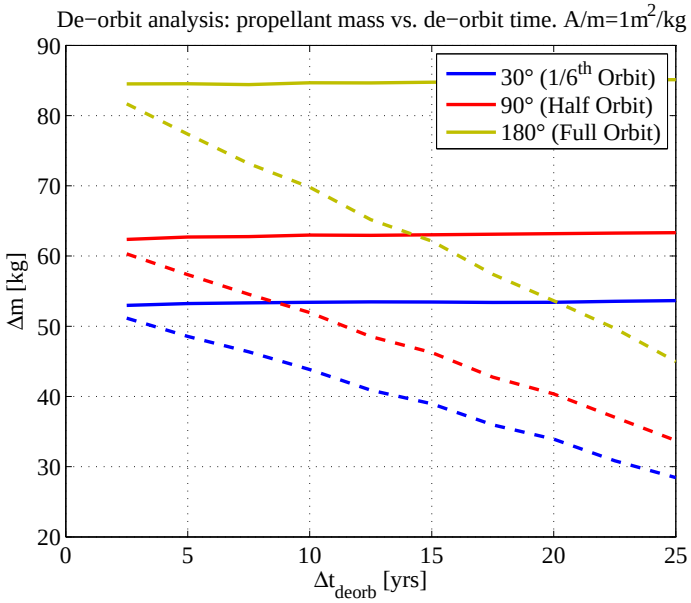

Figure 5.26: De-orbit analysis for deorbit times between 2.5 and 25 years: propellant consumption. Solid line: EP only. Dashed line: EP+SRP.

The results show that the contribution of the SRP consistently helps in reducing thrust and propellant requirements. Moreover, the impact of the SRP contribution increases with the allowed deorbiting time. In this sense, while for 2.5 years the gain due to SRP is negligible, for 25 years, the propellant saving reaches around 50% and the thrust is also more than 50% lower. On the other hand the deployment and control of an area augmentation device (that for a 1000kg spacecraft would translate into 1000 m^2 of reflective surface) implies a higher level of complexity and mass of the mechanisms on board the spacecraft. Such increase in the complexity and mass of the spacecraft is not accounted for in this analysis although one could argue that the saving in propellant mass

is compensated by an increase of the mass of the area augmentation device and related mechanisms.

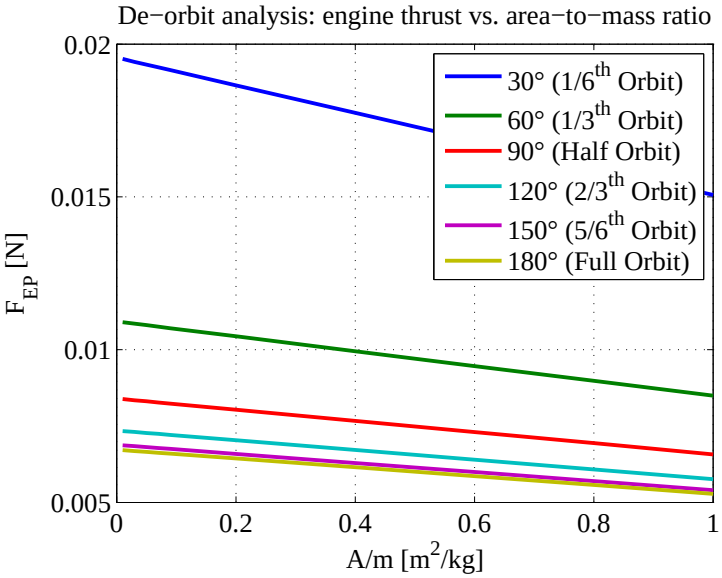

Figure 5.27: Deorbit analysis for 12 years. EP requirements vs. area to mass ratio: required engine thrust.

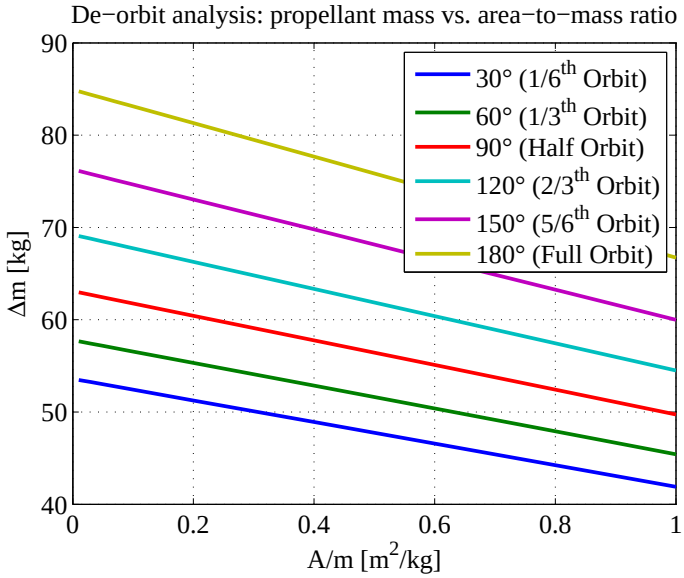

Figure 5.28: Deorbit analysis for 12 years. EP requirements vs. area to mass ratio: propellant consumption.

Figure 5.27 and Figure 5.28 report the behaviour of the required engine thrust and propellant with respect to the area-to-mass ratio for a deorbit in 12 years. As one can see, both thrust and propellant decrease linearly with increasing *A/m*.

5.5 Conclusions

In this chapter, an averaging technique was proposed to control the propagation error and to accurately propagate long spiralling trajectories with discontinuous thrust profiles and eclipses. Moreover, by introducing a simplified parameterisation for the thrusting pattern,

the proposed approach was applied to the optimal design of long spirals with terminal constraints. The test cases examined in this chapter have confirmed the efficiency and accuracy of the proposed techniques. The case dealing the de-orbiting of MEO satellites, in particular, showed their flexibility in propagating the motion under the combined effect of engine thrust and orbital perturbation, and for a very long interval, up to 25 years. The good accuracy displayed in the experimental tests and the fast propagation speed make the proposed analytical theory particularly suitable for the global Multi-Objective optimisation of low-thrust spirals, as will be shown in Chapter 6 and Chapter 7. In particular, the next chapter will extend the de-orbiting of space debris from a single piece to multiple objects

Chapter 6.Multi-Objective Design of Debris Removal Missions

The novel treatment of low-thrust spirals developed in the previous chapters and the MOO algorithm developed in Chapter 2, will be here applied to the design of a multi-target optimal disposal sequence for space debris in Low Earth Orbit. Two slightly different variants of the proposed low-thrust control model are used for the two main phases of a debris removal mission, i.e. the rendezvous with the target object and the de-orbiting trajectory. Furthermore, the chapter introduces a novel technique that builds a surrogate model of the de-orbiting arcs, which helps considerably in reducing the computational cost of evaluating a candidate solution. The chapter is organised as follows: Section 6.1 will give an overview of strategies for Debris removal, while Section 6.2 will briefly outline the IBSC concept and in particular will outline how to compute the thrusting acceleration generated on a given target object; Section 6.3 will analyse an hypothetical mission profile for the removal mission and most important, Subsections 6.3.1 and 6.3.2 will present in detail the proposed trajectory models. Section 6.4 will then show how the mission design problem can be then translated into as a series of Multi-Objective optimisation problems which are solved with a stochastic optimiser. The results are then presented and discussed.

6.1 Space Debris Removal Strategies

One of the most critical issues related to the exploitation of Space around the Earth is the threat posed by space debris. Since the beginning of the space era in the late 1950s, an increasing number of man-made, inert objects has been orbiting the Earth. Recent statistics revealed around 15000 trackable objects, for a total of some 6000 tons of material. Some of these objects are simply spent upper stages of launch vehicles, some others are satellites which are no longer active due to failures or to having reached their end of life. Others, however, are the results of past collisions. It is easy to imagine that even a single collision between two objects is likely to generate tens of smaller objects as a result. The outcome of a collision in an already crowded environment could generate a cascade of collisions generating an exponentially increasing volume of space debris. In fact, the debris produced by a collision is itself likely to collide with other objects, thereby producing other debris which will generate further collisions, and so on. This chain reaction, known as the *Kessler Syndrome*[113], occurs once the rate of generation of debris due to collisions or simple

human-driven additions, exceeds the natural debris removal rate. According to Kessler, this reaction is likely to be ignited once the object density in a certain orbital band reaches a critical point; once started, it will probably render most spacecraft in that orbital band useless within a matter of months or years.

Recent guidelines issued by international spacer regulatory institutions such as the United Nations Committee for the Peaceful Uses of Outer Space (COPUOS)[114] and the Inter-Agency Space Debris Coordination Committee (IADC)[115] prescribe some actions to be followed by national or private agencies putting satellites into orbit in order to mitigate debris growth. For example, it is demanded that every new mission in Low Earth Orbit (LEO) must be planned such that the satellite itself must re-enter in the Earth's atmosphere within 25 years after the end of the mission. Alternatively, for higher orbits like Geostationary orbits, the requirement is for the spacecraft to be placed on a higher *graveyard* orbit. Measures like these, even if strictly applied (and at the moment compliance with them is on a voluntary basis) are only likely to slow down the accumulation of space debris around the Earth. Therefore, active removal actions will probably be needed in the near future to eliminate at least the most dangerous objects.

There have been various proposals on how to remove inert objects from space. They can be generally classified in two major groups: contactless and with direct physical contact. In the latter category one can find methods based on some form of docking with or capturing the object. Once the removing spacecraft and the piece of debris are attached, the latter is dragged into a re-entry trajectory or to a graveyard orbit. Technical problems related to the attitude state of motion of the piece of debris and the fragility of appendices and cover material (including paint) make this removal solution complicated. A potentially interesting solution is represented by Project ROGER[116], developed by EADS/Astrium with the support of ESA. Among contactless solutions on can find what is commonly referred to as the *space broom*[117]. It entails irradiating the target object with a high-power laser which will induce sublimation of the surface material; the ejecta plume will then generate a low thrusting acceleration which will slowly degrade the debris' orbit until it reaches an altitude where atmospheric drag will accelerate its re-entry. Such a technique has the advantage that no physical contact is required, on the other hand current proposals envisage the use of lasers installed on Earth and beaming through the atmosphere. The beam collimation and thrust time is therefore limited and this solution is effective for small-sized objects only. Recent proposals have demonstrated that the use of in-space lasers systems might be more interesting even to remove larger objects[118]. Other proposals involve for example the use of electrodynamic tethers[119], inflatable balloons[120], which are

meant to be lightweight and efficient but require, however, the physical attachment of the device to the target object and are therefore of difficult application to existing debris.

A recent idea simultaneously proposed by Bombardelli et al.[121], Bonnal et al.[122] and JAXA[123] suggested the use of a collimated beam of ions generated by a spacecraft flying in formation with the piece of debris. In the following of the chapter, this concept will be called Ion Beaming Spacecraft (IBSC). The effect of the ion beam is that of producing a thrusting force, equal in magnitude but opposite in direction, on both the IBSC and the piece of debris. This force will induce a thrusting acceleration which can be controlled in order to modify the orbit of the piece of debris. A second ion engine is then fired in a direction opposite to the first one in order to keep the IBSC at a constant distance from the piece of debris. Among the advantages of this concept is the fact that it employs already existing and proven technologies; it does not require any contact with the target, and the fact that a single spacecraft can be used to fetch and deorbit multiple pieces of debris. In[118] one can find a similar concept that uses concentrated solar light instead of ions to generate a thrust and modify the orbit of debris.

Assuming a scenario in which a single IBSC needs to de-orbit multiple pieces of debris, one would need to solve an interesting mission design problem: the optimisation of the de-orbit sequence and trajectories for multiple target objects in minimum time and with minimum propellant. In the hypothetical mission scenario which is analysed in this work, it is assumed that a number of pieces of debris have been shortlisted as priority targets due to the threat they pose to satellites operating in LEO. For example Johnson et al.[124] propose some criteria to choose the object whose removal will be most effective to mitigate the risk of collisions. They underline that an effective removal strategy must be targeted first to large objects in crowded orbits up to 1500 km. Thus, a removal mission by means of an IBSC is planned to be launched from the Earth. Its task is that of removing five objects lying on different low Earth orbits. The design of such a mission is a complex optimisation problem, because it requires the computation of multiple low-thrust, many-revolution transfers. Therefore, this case study proposes an approach to the fast estimation and optimisation of the cost and time duration of the fetch and de-orbit sequences, adopting a MOO approach.

6.2 Ion Beaming System

As shown by Bombardelli et al.[121], the concept behind the Ion Beaming Spacecraft is relatively simple and envisions employing a spacecraft provided with two sets of Ion engines mounted along the same axis but in opposite directions (see Figure 6.1). The jet

from one of the sets will be directed towards the piece of debris and will exert a thrusting force $\mathbf{F_{p1}}$ on it. Due to Newton's third law, an opposite force of same magnitude will also act on the spacecraft itself, but this component will be balanced by the thrust $\mathbf{F_{p2}}$ provided by the other set of Ion engines.

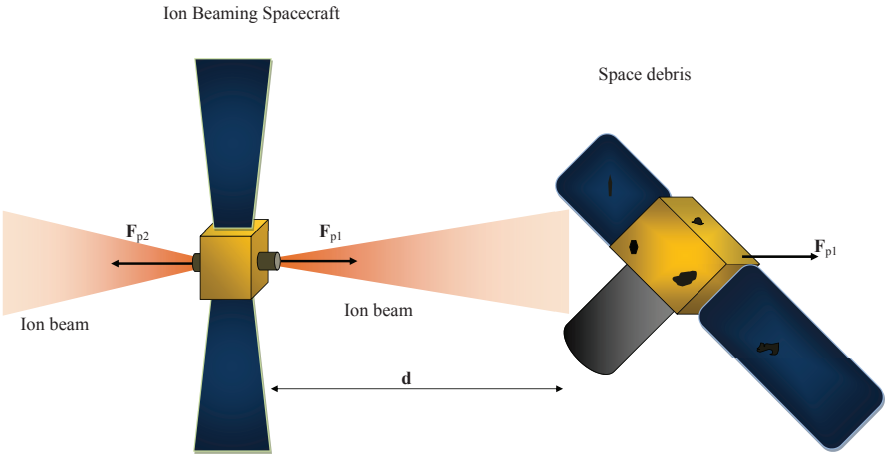

Figure 6.1 Ion Beaming Spacecraft.

Since it is necessary to keep the Shepherd spacecraft at a constant distance from the debris, the thrust $\mathbf{F_{p2}}$ shall be such that the second derivative of the distance d between the two spacecraft is null:

$$\ddot{\mathbf{d}} = \frac{\mathbf{F}_{p2} - \mathbf{F}_{p1}}{m_{IBSC}} - \frac{\mathbf{F}_{p1}}{m_d} = 0 \tag{6.1}$$

Note that in Eq. (6.1) the acceleration terms due to the gravity of the central body have been neglected since it is assumed that the debris and the Shepherd are in close proximity and arranged in a leader-follower configuration. A more accurate and detailed modelling of the proximal motion dynamics of these two bodies is beyond the scope of this study. Thus, in the following sections, the IBSC-debris combination will be treated as a point mass, in order to apply two-body dynamics. By rearranging the terms in Eq. (6.1) one obtains:

$$F_{p2} = F_{p1}\left(1 + \frac{m_{IBSC}}{m_d}\right) \tag{6.2}$$

Under the assumption that the total propulsive power of the IBSC P_{tot} is constant and that the total propulsive thrust is proportional to it F_{tot}, one can write:

$$F_{p1} + F_{p2} = F_{tot} \propto P_{tot} \tag{6.3}$$

thus:

$$F_{tot} = F_{p1}\left(2 + \frac{m_{IBSC}}{m_d}\right) \tag{6.4}$$

Therefore, the maximum acceleration acting on the IBSC-debris combination can be computed as a function of the total available thrust F_{tot}:

$$\varepsilon_{IBSC-debr} = \frac{F_{p1}}{m_d} = \frac{F_{tot}}{2m_d + m_{IBSC}} \tag{6.5}$$

It is assumed here to have a 1000 kg IBSC with a total available thrust of 0.5 N. Such a high thrust would correspond to a substantial power and propulsion system mass, however this is deemed realistic if one considers that the payload of the IBSC is in fact its propulsion and power systems. Hence, the propulsion and power systems might be oversized compared to other applications in which ion engines are used for propulsion only. Note that the validity of the methodology proposed in this paper would not be affected even if lower thrust levels were considered. Thus, in this case, considering for example an 800 kg debris, the magnitude of the acceleration, would be $1.923 \cdot 10^{-7}$ km/s^2. If one considers instead the spacecraft alone, the acceleration achievable would be slightly higher, $5 \cdot 10^{-7}$ km/s^2. Given this order of magnitude, the thrust acceleration can be considered as a perturbative force compared to the Earth's gravitational force and therefore the analytical approach to the propagation of the LT motion can be applied.

6.3 Mission Profile

The objective of this study is that of optimising the performance and cost of a debris de-orbiting mission performed by a single spacecraft. As mentioned in the introduction, it is assumed that there are five pieces of debris of different masses and lying in circular orbits with different radii and orientations. It is assumed that, the IBSC departs from a low-Earth parking orbit, rendezvous with the first object, transfer it to an elliptical re-entry orbit, rendezvous with the second object, transfers it to a second elliptical re-entry orbit, and so on and so forth until all five pieces of debris are removed. One important issue is defining in which order the pieces of debris need to be de-orbited. In the following all possible sequences are generated a priori and optimised one by one.

Each fetch and de-orbit operation is split in two phases:

•A de-orbit phase, in which the perigee of the orbit of the piece of debris is lowered such that the orbit will decay naturally in a relatively short time. In this study it is assumed that this condition is met if the perigee altitude of the debris' orbit is equal or lower than 300 km.

•A transfer phase, in which the IBSC rendezvouses with the next piece of debris (which lies on a circular orbit), after having abandoned the current piece of debris on an orbit with a 300 km perigee altitude.

Given the magnitude of the available thrust acceleration, both phases require a spiral orbit transfer. If a direct transcription approach is used to optimise each spiral the number of parameters that needs to be defined is very high leading to high computational times. The latter fact would make the solution of a Multi-Objective optimisation of all possible de-orbiting sequences computationally intractable. Thus, in this study a simplified, highly efficient, trajectory model is proposed for each one of the two phases.

6.3.1 De-orbiting Trajectory Model

The objective of the de-orbiting phase is that of lowering an initial circular orbit such that its perigee is equal or below 300 km, which basically translates into a perigee lowering manoeuvre. Therefore, it is appropriate to assume that in general, as soon as the initial circular orbit becomes slightly eccentric, one keeps thrusting around the apogee in order to lower the perigee. The thrust level will also be kept at its maximum in order to minimize gravity losses. Moreover, since the de-orbit condition is independent of the final orbit's orientation, one can reasonably assume that the perigee lowering will be performed in-plane. In this sense, the only Keplerian parameters which need to be altered are the semi-major axis and eccentricity. With reference to Gauss' variational equations as in Eq. (3.2), in the case of small eccentricity, a good suboptimal thrust direction can be obtained by thrusting around apogee with a_θ as the only non-zero component of the thrust acceleration. Under these assumptions, one obtains a thrusting pattern very similar to the one in Section 5.1, albeit here there is the apogee thrusting only and the direction is aligned with the transverse rather than the tangential direction, as in Figure 6.2.

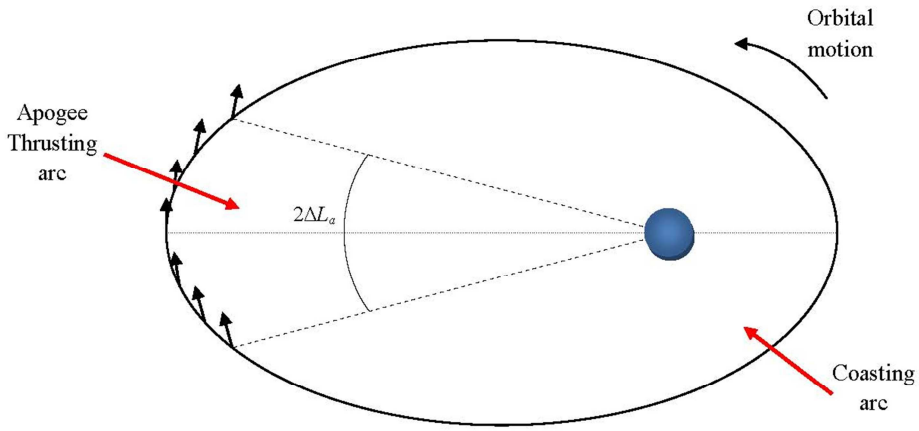

Figure 6.2 Thrusting arc around apogee with thrust directed along transverse direction

The motion around the apogee thrusting arc can therefore be propagated with the formulae in Eq. (3.19). As explained above, the only non-zero component of the

acceleration will be a_θ and since the aim is obtaining a decrease of the orbit energy it will also be in the negative direction. Therefore the acceleration azimuth will be $\alpha=-\pi/2$ and the elevation $\beta=0$ (since, as already mentioned, the motion will be within the initial orbit plane). Note also that, since there is no out-of-plane acceleration component, Q_{11} and Q_{21} are identically zero in this case. Thus, the set of formulae for propagating an apogee thrusting arc can be summarised as:

$$\mathbf{E}^+ = \begin{bmatrix} a \\ P_1 \\ P_2 \end{bmatrix}_{L^+=L_a+\Delta L_a} = \begin{bmatrix} a \\ P_1 \\ P_2 \end{bmatrix}_{L^-=L_a-\Delta L_a} + \varepsilon \begin{bmatrix} a_1\left(2\Delta L_a, \frac{\pi}{2}, 0\right) \\ P_{11}\left(2\Delta L_a, \frac{\pi}{2}, 0\right) \\ P_{21}\left(2\Delta L_a, \frac{\pi}{2}, 0\right) \end{bmatrix} = \mathbf{E}^- + \varepsilon \mathbf{f}\left(2\Delta L_a, \frac{\pi}{2}, 0\right) \quad (6.6)$$

where L_a is the apocentre longitude, L^- and L^+ are the longitudes at the start and end of thrusting respectively. ΔL_a is the semi-amplitude of the apogee thrusting arc. In a similar manner, the thrusting time is computed from Eq. (3.17) as:

$$t_{thrust} = t_0\left(L_a - \Delta L_a, 2\Delta L_a\right) + \varepsilon t_1\left(2\Delta L_a, -\frac{\pi}{2}, 0\right) \quad (6.7)$$

Since the thrust magnitude and direction are fixed, the only free control parameter is the semi-amplitude ΔL_a for each orbit. In order to keep the number of decision variables to a minimum, the semi-amplitude for each orbit is computed from a piece-wise linear polynomial interpolating a limited number of $\Delta L_{a,i}$ over a number of orbits. The nodes $\Delta L_{a,i}$ are equally distributed between orbit 1 and an arbitrary number of orbits (in this paper 1200 was found to be adequate). In this paper the number of interpolating nodes was limited to 2: ΔL_{a1} and ΔL_{af}.

In order to evaluate the time and ΔV needed to de-orbit a piece of debris from its initial orbit with semi-major axis a_{debr0}, given a set of decision (or control) parameters ΔL_{a1} and ΔL_{af}, the following procedure was implemented:

1. Compute the set of initial Equinoctial parameters L_0 and $\mathbf{E}_0 = \begin{bmatrix} a_{debr\,0} & P_{10} & P_{20} \end{bmatrix}^T$ where P_{10} and P_{20} will be null due to the fact that the initial orbit is circular.
2. Initialise the number of orbits, the total ΔV and time of flight to zero:

$$N_{orbit} = 0$$
$$\Delta V = 0$$
$$ToF = 0$$

3. Set $\mathbf{E}^- = \mathbf{E}_0$ and $L_{coast} = L_0$.
4. Initialise the mass of the IBSC:

$$m_{IBSC} = m_{IBSC0}$$

5. While N_{orbit} is smaller than $N_{orbitsmax}$:
    a. $$N_{orbit} = N_{orbit} + 1$$
    b. Interpolate the amplitude of the thrusting arc in the current orbit, i.e. ΔL_a and compute $L^- = L_a - \Delta L_a$ and $L^+ = L_a + \Delta L_a$.
    c. Compute the acceleration $\varepsilon_{IBSC\text{-}debr}$ acting on the IBSC-debris combination from Eq. (6.5).
    d. Compute the time of flight t_{coast} spent coasting from L_{coast} to L^-.
    e. Compute the Equinoctial parameters after the thrusting arc $\mathbf{E}^+$ as in Eq. (6.6).
    f. Compute the current perigee radius r_p and if this is lower than the threshold $\overline{r}_p = 300km$ proceed to step 6, otherwise proceed to step g.
    g. Compute the thrusting time t_{thrust} from Eq. (6.7) and update the total ΔV cost:
    $$\Delta V = \Delta V + \varepsilon_{IBSC-debr} t_{thrust} \tag{6.8}$$
    h. Update the total time of flight:
    $$ToF = ToF + t_{coast} + t_{thrust} \tag{6.9}$$
    i. Update the IBSC mass:
    $$m_{IBSC} = \left(m_{IBSC} + 2m_{debr}\right) \exp\left(-\frac{\varepsilon_{IBSC-debr} t_{thrust}}{I_{sp} g_0}\right) - 2m_{debr} \tag{6.10}$$
    j. Set $\mathbf{E}^- = \mathbf{E}^+$ and $L_{coast} = L^+$
6. Back-track the value of the longitude L_f for which $r_p = \overline{r}_p$ and compute the related and t_{thrust} from Eq. (6.7) and update ToF and ΔV accordingly. Compute the Equinoctial parameters $\mathbf{E}_f$ at L_f from Eq. (6.6).

At this point one gets the ΔV, the time of flight ToF and the semi-major axis and eccentricity of the final orbit (which are easily computed from $\mathbf{E}_f$). It is important to note that, given the simplifications introduced, once one sets the initial mass and orbit of the piece of debris, and the characteristics of the IBSC propulsion system, i.e. F_{tot} and I_{sp}, the de-orbit depends exclusively on the mass of the IBSC m_{IBSC0} at the beginning of the de-orbit phase and the interpolating values for ΔL_a, i.e. ΔL_{a1} and ΔL_{af}. Therefore, it was decided to pre-compute the corresponding ΔV and ToF for a given set of these three parameters and for each piece of debris (i.e. for each m_{debr} and a_{debr0}). Table 6.1 reports upper and lower bounds for $m_{IBSC0,}$ ΔL_{a1} and ΔL_{af}. and the number of samples taken, equally distributed.

Table 6.1 Bounds and number of samples for the de-orbit parameters

	m_{IBSC0}	ΔL_{a1}	ΔL_{af}
Lower bound	m_{dry}+100=350kg	0	0
Upper bound	m_{launch}=1000kg	π	π
Samples	8	50	50

Given the limited number of decision variables, for each piece of debris, one has 20000 de-orbit instances to propagate. Since each instance requires typically $1 \cdot 10^{-2}$ s of CPU time, with a code implemented in MatLab® and running on a 3.16 GHz, 4 GB desktop PC running Windows 7®, the whole computation can be completed in roughly five minutes. The set of de-orbit ΔV and *ToF* is then used to build a response surface, or surrogate model, of the de-orbiting process. Figure 6.3a and Figure 6.3b show examples of two-dimensional surface, respectively for ΔV and *ToF*, with respect to a fixed m_{IBSC0} of 300 kg. One can see that the two quantities show opposite trends, the ΔV being high when the *ToF* is low and vice versa. Figure 6.4a and Figure 6.4b show the final semi-major axis and eccentricity respectively. Note that the minimum *ToF* transfer corresponds to a quasi-circular spiralling trajectory in which the IBSC is thrusting continuously. On the other hand, the minimum ΔV transfer corresponds also to the one with maximum final eccentricity.

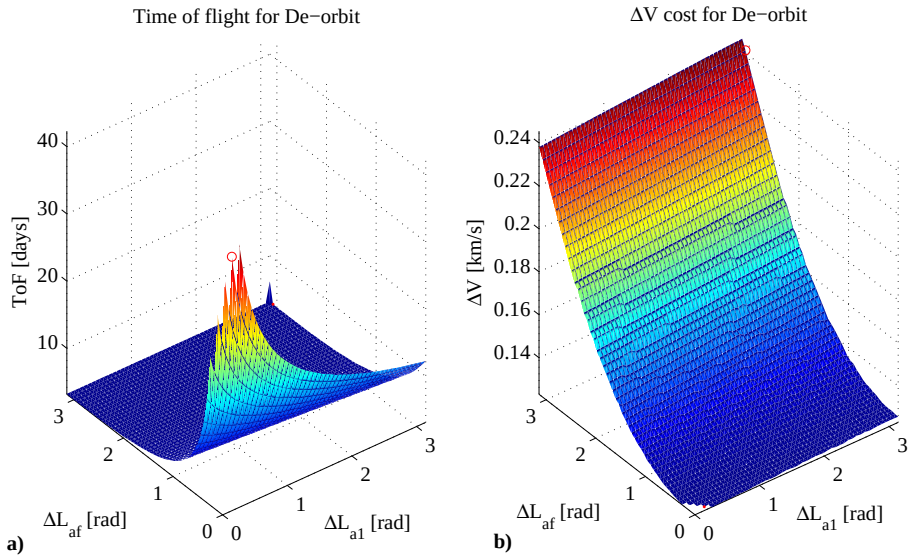

Figure 6.3 a) ΔV and b) *ToF* surfaces with respect to ΔL_{a1} and ΔL_{af} for m_{IBSC0}=300kg, a_{debr0}=7128km and m_{debr}=1200kg m_{IBSC0}=300kg, a_{debr0}=7128km and m_{debr}=120kg

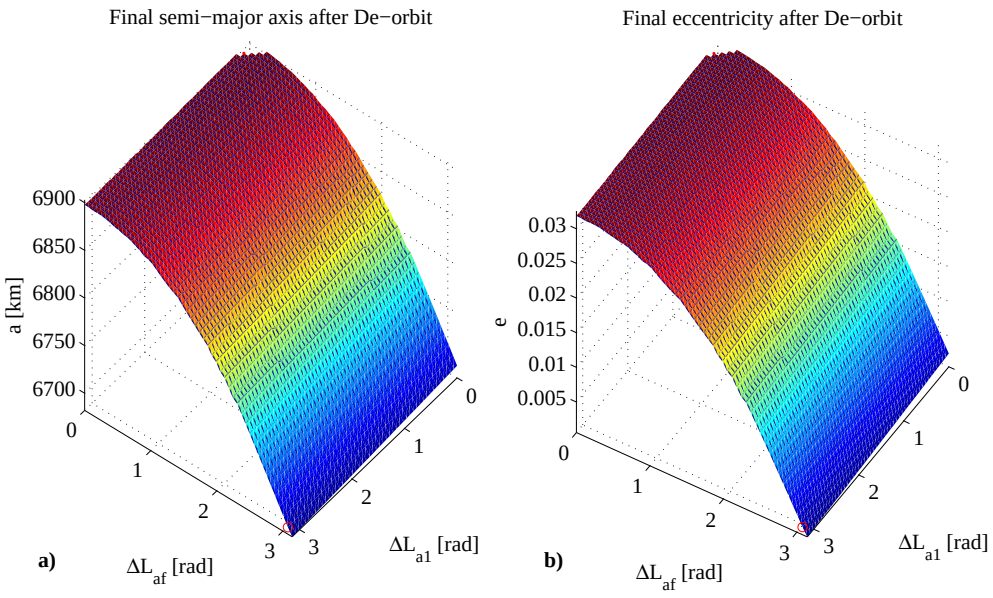

Figure 6.4 a) final semi-major axis and b) eccentricity after de-orbit with respect to ΔL_{a1} and ΔL_{af} for m_{IBSC0}=300kg, a_{debr0}=7128km and m_{debr}=120kg

Now it is desirable that the surrogate model returns the ΔV cost as a function of m_{IBSC0}, m_{debr}, a_{debr0} and *ToF*. From the available data relating the ΔV and *ToF* to the decision variables ΔL_{a1} and ΔL_{af} one can derive the functional relationship between ΔV and *ToF*. Given a triplet m_{IBSC0}, m_{debr}, a_{debr0}, each *ToF* value defines a level curve on the ΔL_{a1} and ΔL_{af} plane (see Figure 6.3a), which can be mapped into a set of ΔV values (see Figure 6.3b). Within this set, one can take the element with minimum ΔV. Thus, for each time of flight, between a minimum and a maximum, one can derive the corresponding minimum ΔV cost. A similar procedure is followed to find the functional relationship between the final semi-major axis and the *ToF*. Note that there is no need to do the same for the eccentricity given the fact that the final perigee radius is fixed at $\overline{r}_p$ and therefore the final *e* can be computed from the final *a*. In this way one can build the two surrogate models:

$$\begin{aligned} \Delta V &= f_{\Delta V,interp}\left(ToF, m_{IBSC0}, m_{debr}, a_{debr0}\right) \\ a_f &= f_{a_f,interp}\left(ToF, m_{IBSC0}, m_{debr}, a_{debr0}\right) \end{aligned} \tag{6.11}$$

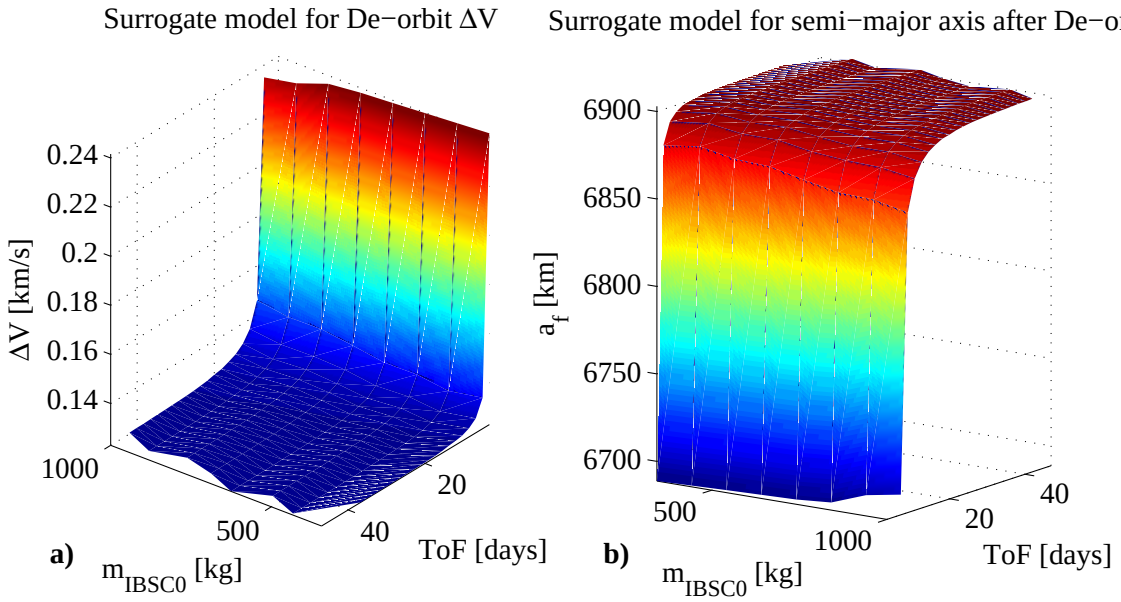

Figure 6.5 3D Plot of surrogate models for, a_{debr0}=7128km and m_{debr}=120kg: a) ΔV; b) a_f

Figure 6.5a and Figure 6.5b show examples of tri-dimensional plots (m_{IBSC0}-*ToF*-ΔV and m_{IBSC0}-*ToF*-a_f respectively) created by evaluating the surrogated models keeping a_{debr0} and m_{debr} fixed. In Figure 6.5a one can see that there is a large *plateau* region corresponding to large time of flights and a smaller region close to the minimum *ToF* where the de-orbit cost increases very steeply and the final semi-major axis in Figure 6.5b similarly decreases. The complete procedure for the creation of the interpolated de-orbit cost models requires few minutes of CPU time and once completed allows for a very fast estimation of the de-orbit cost. The surrogated models will be extremely useful in the Multi-Objective optimisation of debris removal sequences as it will be shown in the following sections.

6.3.2 Orbit Transfer Model

According to the scenario presented in Section 6.3, after having left the debris on a re-entry orbit, the IBSC will have to transfer to the orbit of the next debris and rendezvous with it. The design of such a transfer arc would normally require the solution of a time-fixed 2PBVP, which would be computationally very expensive given the high number of control parameters and constraints involved. A second simplified model was then created to quickly estimate the cost of a low-thrust multi-revolution orbit transfer with boundary constraints. The approach and assumptions presented in this section are similar to those already introduced for the de-orbit model.

First, given the limited acceleration provided by low thrust propulsion systems, one should consider that the orbit transfer will require a high number of multiple revolutions around the Earth, typical in the range of hundreds to few thousands. In this sense, it is

possible to argue that achieving the proper phasing to transfer from the initial to final orbit would not be a major issue. Even a small variation of ω and θ per revolution would be sufficient to attain the required orientation to rendezvous with the piece of debris. Moreover, it is important to bear in mind that, in order to de-orbit the previous debris in the sequence, the IBSC, started from a circular orbit which was subsequently modified into an elliptical one with perigee $\overline{r}_p$. Thus it would be also possible to conveniently adjust the start point of the de-orbit procedure from the circular orbit in order to obtain the proper phasing once this is completed. For all these reasons, it is assumed that in this particular case, the phasing problem will have a negligible effect on the ΔV and time required to rendezvous with the next piece of debris in the sequence. Therefore, in the following it is assumed that it is not necessary to match the arrival ω and θ computed with the simplified model with those of the target object. Matching the target inclination i and RAAN Ω, instead, cannot be ignored without introducing a considerable error in the ΔV cost. In order to match the inclination and RAAN difference, one need to take into account only the geometric angle between planes of the initial and final orbits, which is given by:

$$\Delta i = \arccos\left(-\cos i_0 \cos\left(\pi - i_f\right) + \sin i_0 \sin\left(\pi - i_f\right)\cos\left(\Omega_f - \Omega_0\right)\right) \qquad (6.12)$$

Thus in order to account for Δi, the inclination of the initial orbit is fictitiously set to zero, while the final one is set at Δi. The matching of the RAAN is assured by performing the circularisation properly. The assumption is that the deorbiting of one piece of debris starts at a true anomaly such that the resulting elliptical orbit has the line of apses perpendicular with the line of the nodes of the following piece of debris. Since the orbits of the debris are assumed to be circular, it is always possible to start the deorbiting at the right true anomaly with minimum delay. This hypothesis will be discussed in more detail with some numerical examples in Section 6.4.

With these assumptions, the main issue in designing the multi-revolution transfer will be that of achieving the required change in the apogee and perigee radiuses in order to match those of the final orbit, and to achieve the required rotation of the orbit plane.

The control pattern adopted (shown in Figure 6.6) is therefore very similar to the one seen in Section 6.3.1, but with the addition of a perigee thrusting arc, in order to affect the apogee altitude. The in-plane thrust component is again purely transverse but this time can have either positive or negative sign ($\alpha = \pm\pi/2$) depending whether the perigee (or apogee) needs to be raised or lowered. Since a plane change is required, the out-of-plane component of the thrust acceleration can be non-zero. Thanks to this the control parameters can be reduced to the semi-amplitude of the apogee and perigee thrusting arcs, ΔL_a and

ΔL_p, the sign of the θ component of the thrust acceleration (i.e. the sign of $\alpha_a, \alpha_p = \pm\pi/2$) and the out-of-plane component in the same arcs, β_a and β_p. Define ΔL_{thrust} as half the total thrusting arc length and r_t as the ratio of ΔL_{thrust} which is devoted to apogee thrusting. In order to have a parameterisation which accounts also for the sign of α_a and α_p the following one is proposed:

$$\begin{aligned}
\alpha_a &= \begin{cases} \pi/2 & \Delta L_{thrust} \geq 0 \\ -\pi/2 & \Delta L_{thrust} < 0 \end{cases} \\
\alpha_p &= \begin{cases} \alpha_a & 0 \leq r_t \leq 1 \\ -\alpha_a & 1 < r_t \leq 2 \end{cases} \\
\Delta L_a &= \begin{cases} r_t \left|\Delta L_{thrust}\right| & 0 \leq r_t \leq 1 \\ (2 - r_t)\left|\Delta L_{thrust}\right| & 1 < r_t \leq 2 \end{cases} \\
\Delta L_p &= \left|\Delta L_{thrust}\right| - \Delta L_a
\end{aligned} \tag{6.13}$$

with

$$\begin{aligned}
\Delta L_{thrust} &\in \left[-\pi \quad \pi\right] \\
r_t &\in \left[0 \quad 2\right]
\end{aligned}$$

To define the actual values of ΔL_{thrust} and r_t in each revolution, an interpolating strategy with respect to time as described in Section 5.1 is adopted. Again the number of interpolating nodes can be chosen arbitrarily and is set to 2 in this case, ΔL_{t1}, ΔL_{tf}, r_{t1}, r_{tf}. For β_a and β_p, it is chosen to have a constant value along the entire transfer. The thrusting pattern along each revolution is shown in Figure 6.6.

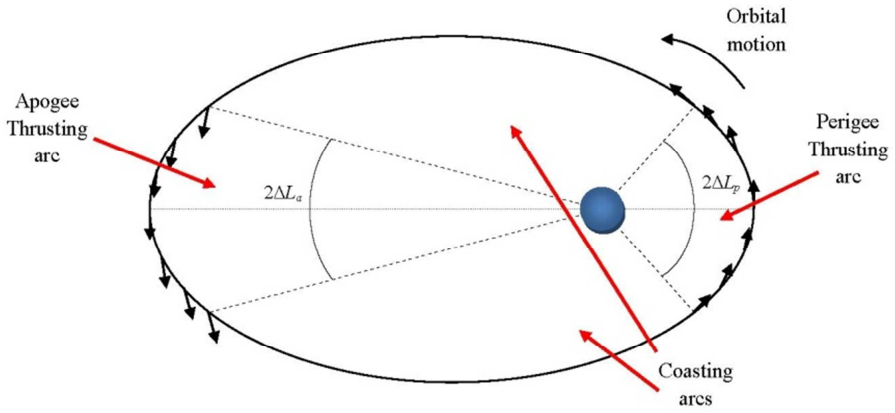

Figure 6.6 Thrusting arcs around apogee and perigee

Given a set of control parameters $\left[\Delta L_{t1} \quad \Delta L_{tf} \quad r_{t1} \quad r_{tf} \quad \beta_a \quad \beta_p\right]$ a multi-revolution transfer with specified duration $\overline{ToF}$, departing from an orbit defined by $\left[a_0 \quad e_0 \quad 0\right]^T$ and

targeted to an orbit defined by $\begin{bmatrix} a_f & e_f & \Delta i \end{bmatrix}^T$, is propagated according to the following procedure:

1. Compute the set of initial Equinoctial parameters L_0 and $\mathbf{E}_0 = \begin{bmatrix} a_0 & P_{10} & P_{20} & Q_{10} & Q_{20} \end{bmatrix}^T$. Q_{10} and Q_{20} will be zero since the initial inclination is arbitrarily set to zero.
2. Compute the set of target Equinoctial parameters $\bar{\mathbf{E}}_f = \begin{bmatrix} \bar{a}_f & \bar{P}_{1f} & \bar{P}_{2f} & \bar{Q}_{1f} & \bar{Q}_{2f} \end{bmatrix}^T$. Note that $\bar{P}_{1f}$ and $\bar{P}_{2f}$ will be zero since in this case the target orbit is a circular one.
3. Initialise the total ΔV and Time of flight to zero:

$$\Delta V = 0$$
$$ToF = 0$$

4. Set $\mathbf{E}_p^- = \mathbf{E}_0$ and $L_{coast,a} = L_0$.
5. Initialise the mass of the IBSC:

$$m_{IBSC} = m_{IBSC0}$$

6. While $ToF < \overline{ToF}$:
   a. Compute the interpolated values for ΔL_t and r_t. Hence calculate α_a, α_p, ΔL_a and ΔL_p from Eq. (6.13).
   b. Compute:

$$\begin{aligned} L_a^- &= L_a - \Delta L_a \quad L_a^+ = L_a + \Delta L_a \\ L_p^- &= L_p - \Delta L_p \quad L_p^+ = L_p + \Delta L_p \end{aligned} \tag{6.14}$$

   c. Compute the current acceleration acting on the spacecraft:

$$\varepsilon_{IBSC} = \frac{F_{tot}}{m_{IBSC}} \tag{6.15}$$

   d. Compute the time of flight $t_{coast,p}$ spent coasting before perigee from $L_{coast,p}$ to L_p^-.
   e. Compute the Equinoctial parameters after the thrusting perigee arc $\mathbf{E}_p^+$ with an expression analogous to Eq. (6.6).
   f. Compute the thrusting time at perigee $t_{thrust,p}$ from Eq. (6.7). If $\left(\overline{ToF} - ToF\right) < t_{thrust,p}$ proceed to step g. Otherwise, break the iterative sequence and go to step 7.
   g. Update ΔV and ToF:

$$\Delta V = \Delta V + \varepsilon_{IBSC} t_{thrust,p} \tag{6.16}$$

$$ToF = ToF + t_{coast,p} + t_{thrust,p} \tag{6.17}$$

   h. Update the IBSC mass:

$$m_{IBSC} = m_{IBSC} \exp\left(-\frac{\varepsilon_{IBSC} t_{thrust,p}}{I_{sp} g_0} \right) \tag{6.18}$$

   i. Set $\mathbf{E}_a^- = \mathbf{E}_p^+$ and $L_{coast,a} = L_p^+$.
   j. Compute the current acceleration on the spacecraft:

$$\varepsilon_{IBSC} = \frac{F_{tot}}{m_{IBSC}} \tag{6.19}$$

k. Compute the time of flight $t_{coast,a}$ spent coasting before apogee from $L_{coast,a}$ to L_a^-.
l. Compute the Equinoctial parameters after the thrusting apogee arc $\mathbf{E}_a^+$ as in Eq. (6.6).
m. Compute the thrusting time at apogee $t_{thrust,a}$ from Eq. (6.7). If $\left(\overline{ToF} - ToF\right) < t_{thrust,a}$ proceed to step n. Otherwise, break the iterative sequence and go to step 7.
n. Update ΔV and ToF:

$$\Delta V = \Delta V + \varepsilon_{IBSC} t_{thrust,a} \tag{6.20}$$

$$ToF = ToF + t_{coast,a} + t_{thrust,a} \tag{6.21}$$

o. Update the IBSC mass:

$$m_{IBSC} = m_{IBSC} \exp\left(-\frac{\varepsilon_{IBSC} t_{thrust,a}}{I_{sp} g_0}\right) \tag{6.22}$$

p. Set $\mathbf{E}_p^- = \mathbf{E}_a^+$ and $L_{coast,p} = L_a^+$.

7. Back-track the point at which $ToF = \overline{ToF}$ and compute the corresponding equinoctial parameters $\mathbf{E}_f = \begin{bmatrix} a_f & P_{1f} & P_{2f} & Q_{1f} & Q_{2f} \end{bmatrix}^T$ and update ΔV accordingly.
8. Compute the mismatch between the actual final conditions and the target orbit:

$$C_{eq} = \begin{bmatrix} a_f - \bar{a}_f \\ e_f - \bar{e}_f = \sqrt{P_{1f}{}^2 + P_{2f}{}^2} - \sqrt{\bar{P}_{1f}{}^2 + \bar{P}_{2f}{}^2} \\ i_f - \bar{i}_f = 2\left(\arctan\sqrt{Q_{1f}{}^2 + Q_{2f}{}^2} - \arctan\sqrt{\bar{Q}_{1f}{}^2 + \bar{Q}_{2f}{}^2}\right) \end{bmatrix} \tag{6.23}$$

Summarizing, the 2PBVP has been reduced to an optimisation problem in the form:

$$\begin{aligned} &\min_{\mathbf{x}} \Delta V \\ &s.t. \; C_{eq} = 0 \\ &with \; \mathbf{x} = \begin{bmatrix} \Delta L_{t1}, \Delta L_{tf}, r_{t1}, r_{tf}, \beta_a, \beta_p \end{bmatrix} \end{aligned} \tag{6.24}$$

Problem (6.24) can be solved with a gradient-based optimisation algorithm like MatLab®'s *fmincon*. Note that, the time of flight $\overline{ToF}$ is specified a priori and therefore it might occur that this duration is too short as to obtain the change in the orbital parameters specified by the boundary constraints. In this case, the problem is infeasible and the optimisation is terminated after a maximum 50 if the constraints are not satisfied.

In the following, an example of transfer from an elliptical orbit with 300 km perigee altitude and eccentricity 0.031 (corresponding to the final orbit of a de-orbiting strategy) to a circular orbit of 1100 km altitude (corresponding to the orbit of the next debris in an

hypothetical removal sequence). Parameters of the two orbits are reported in Table 6.2. Note that the total plane rotation Δi in this case is 10 degrees. The specified time of flight is 70 days.

Table 6.2 Parameters of departure and arrival orbits

	a [km]	e	i [deg]
Departure	6892.24	0.031	0
Arrival	7478.16	0	10

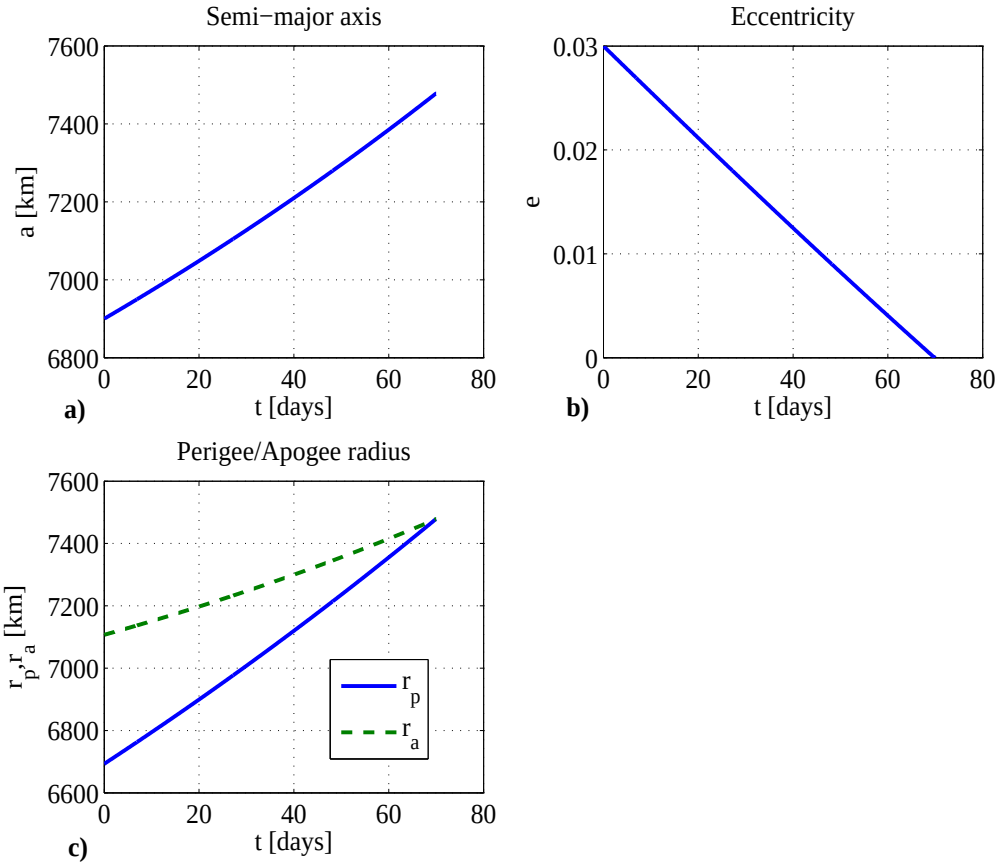

Figure 6.7 a) variation of semi-major axis, b) eccentricity, c) perigee and apogee radiuses for multi-revolution orbital transfer (coplanar case)

First it is considered the case of a coplanar transfer, i.e. Δi=0 will be computed. The optimisation problem was solved with *fmincon* in 6 iterations and less than 10 seconds, returning a minimum ΔV cost of 0.301 km/s, with 1001 revolutions. Figure 6.7a-c report respectively the variation of semi-major axis, eccentricity, apogee and perigee radii. One can see that a is monotonically increasing while e on the other hand is monotonically decreasing to zero. In order to reach the desired circular orbit, the perigee had to be raised by almost 700 km while the apogee had to be raised by some 400 km. This higher effort needed to raise the perigee explains the larger amplitude of apogee thrusting arcs ΔL_a

compared to perigee ones ΔL_p (as shown in Figure 6.8a). The azimuth thrust angles α_p, α_a (see Figure 6.8b) are both positive since both the perigee and apogee are raised. β_p and β_a are obviously zero because the transfer is coplanar and thus Δi is constantly nil.

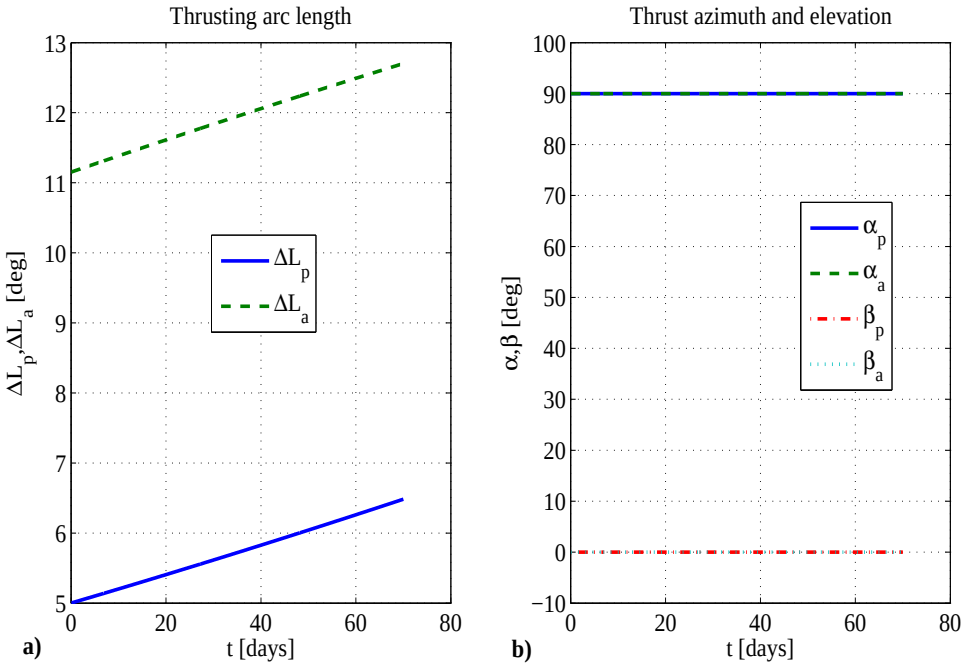

Figure 6.8 Control parameters for multi-revolution orbital transfer (coplanar case): a) thrust arc length; b) azimuth and elevation

The same problem, but this time with the 10º plane change specified in Table 6.2 returns a ΔV of 1.480 km/s with 1004 revolutions. The high cost of out plane manoeuvres is well exemplified by the fact that the ΔV required is more than four times larger than a coplanar transfer. As can be seen in Figure 6.9a, Figure 6.9b, Figure 6.9d, semi-major axis, eccentricity, apogee and perigee radii show a similar behaviour to the coplanar case while this time also the inclination (as in Figure 6.9c) increases monotonically to 10 degrees. By analysing the control parameters in Figure 6.10a one can see that this time the amplitude of the perigee arcs in general larger than the apogee ones, even if, like in the coplanar case, the increase in perigee is much larger than that of the apogee. This fact is explained by the fact that the out-of-plane component at perigee β_p is close to 90º (see Figure 6.10b), meaning that the thrusting action at perigee is mostly devoted to the plane change. In contrast, β_a is smaller in magnitude, around -70º (the opposite sign is due to the fact that it is advantageous to invert the out-of-plane component twice per revolution), therefore with a higher in plane component devoted to perigee raising.

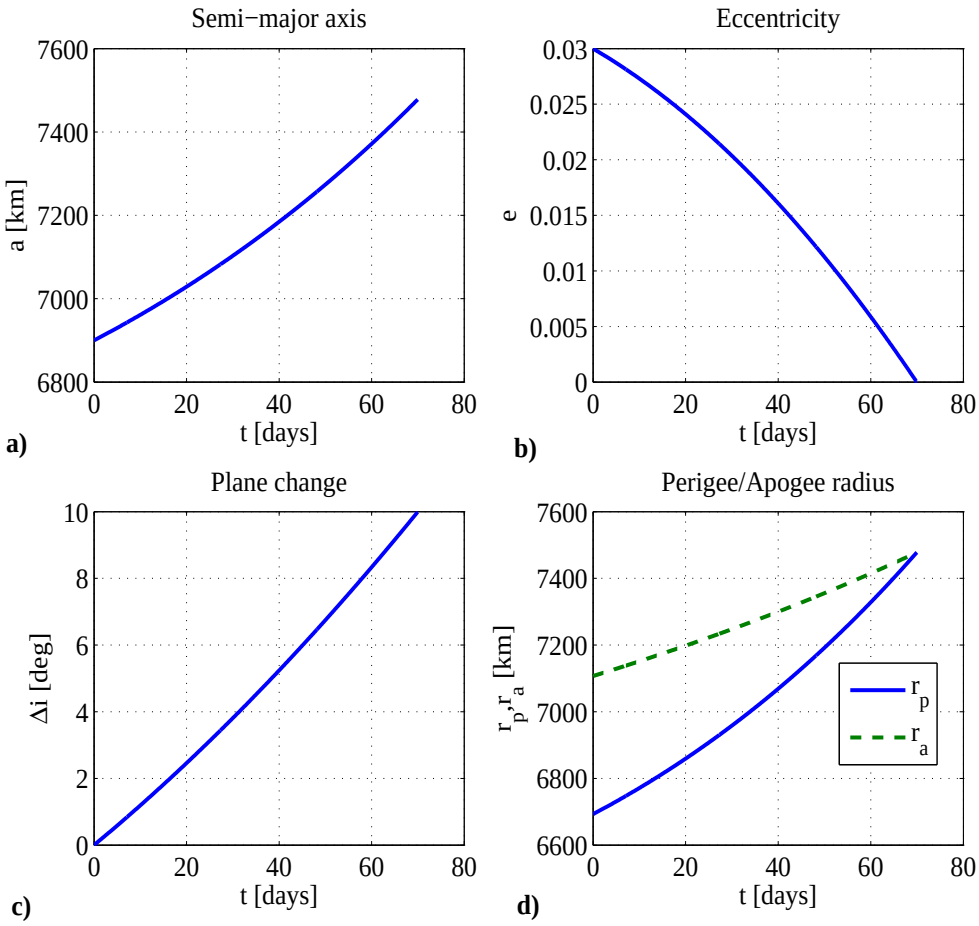

Figure 6.9 a) variation of semi-major axis, b) eccentricity, c) plane change, d) perigee and apogee radiuses for multi-revolution orbital transfer (10º plane change)

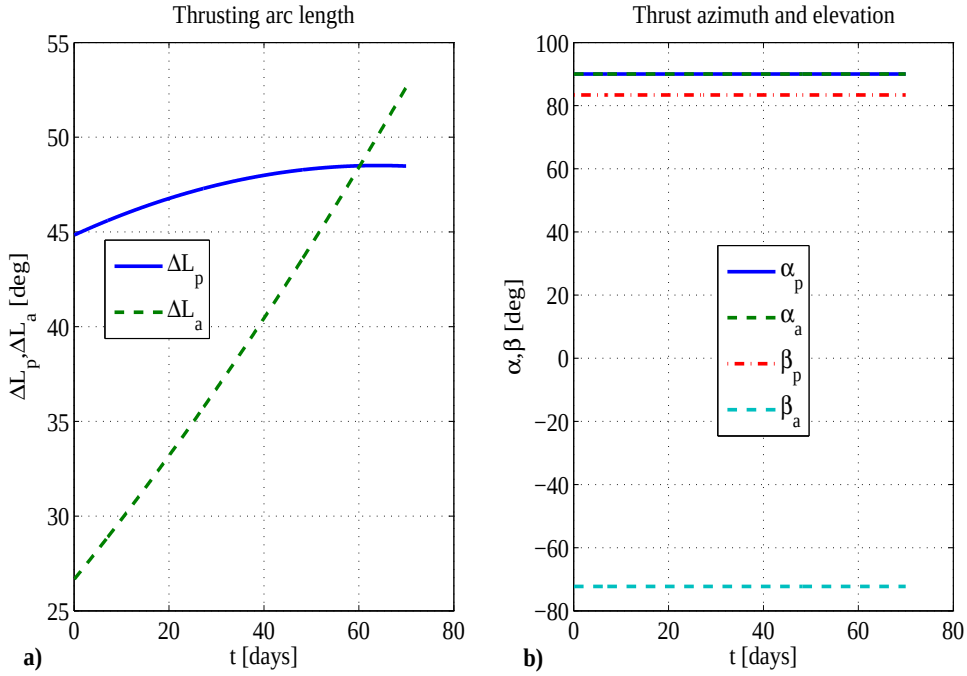

Figure 6.10 Control parameters for multi-revolution orbital transfer (10º plane change): a) thrust arc length; b) azimuth and elevation

6.4 Multi-Objective Optimisation

The aim is now that of optimising the timing and sequence of a removal mission by means of a single IBSC. It is assumed that the spacecraft departs from a LEO with a 250 km semi-major axis altitude and coplanar with respect to the first piece of debris in the sequence. The five target objects have the orbital parameters and mass reported in Table 6.3. The mass and orbital parameters have been chosen arbitrarily while adhering to the observations in Bombardelli and Pelàez[121] and Liou and Johnson[124] that the most dangerous debris are located in LEO and generally weigh a few hundred kilos. Different values for i and Ω are also taken in order to consider the fact that the pieces of debris, in principle, will be orbiting on different planes. Note that $T_{DO,min}$ has been computed with the procedure detailed in Section 6.3.1 and therefore depends on the characteristics of the IBSC. Moreover, it is also important to remark that these are only *best case* figures values which were computed with a *minimum* hypothetical wet mass of 350 kg (much lower than the actual launch mass of 1000 kg). The surrogate models in Eqs. (6.11) can in general consider wet masses between 350 kg and 1000 kg, as shown for example in Figure 6.5a-b.

Table 6.3 Mass, initial orbit parameters and minimum de-orbit time of the debris

Debris nr.	*mass* [kg]	a [km]	e	i [deg]	Ω [deg]	$T_{DO,min}$ [days]
1	500	6828.16	0	1	65	2.67
2	120	7128.16	0	2	150	3.36
3	300	6978.16	0	-2	200	3.68
4	400	7478.16	0	-1	90	11.12
5	800	7178.16	0	0	45	12.25

Table 6.4 reports the relative inclination change between the orbit planes of the 5 different objects, as computed from Eq. (6.12).

Table 6.4 Relative inclination change $|\Delta i|$ [deg] between orbit planes of the debris

Debris nr.	2	3	4	5
1	2.16	1.47	1.95	1
2	-	3.63	2.65	2
3	-	-	2.52	2
4	-	-	-	1

The de-orbit sequence is defined by the order according to which the five pieces of debris are removed, the time needed to rendezvous with T_{RV} and the time to de-orbit T_{DO} each of them. The order is defined by the integer vector:

$$\mathbf{ord} = \begin{bmatrix} i_1 & i_2 & i_3 & i_4 & i_5 \end{bmatrix} \tag{6.25}$$

which collects the indexes of the objects in the a single debris removal sequence. Since there are five objects, there are 120 possible de-orbiting sequences. The other parameters are contained in the vector **x**:

$$\mathbf{x} = \left[T_{RV,i_1} \quad T_{DO,i_1} \quad T_{RV,i_2} \quad T_{DO,i_2} \quad T_{RV,i_3} \quad T_{DO,i_3} \quad T_{RV,i_4} \quad T_{DO,i_4} \quad T_{RV,i_5} \quad T_{DO,i_5} \right] \tag{6.26}$$

The performance of each sequence is assessed according to its total ΔV_{Tot} cost and time of flight ToF_{Tot}. The latter is computed simply as:

$$ToF_{Tot} = \sum \mathbf{x} \tag{6.27}$$

The total ΔV cost is calculated sequentially by adding up the costs of each of the ten phases (rendezvous and de-orbit for each debris). In particular, the cost of the rendezvous ΔV_{RV} is computed by solving the optimisation problem (6.24) and the de-orbit cost ΔV_{DO} is calculated from the surrogated model in Eq. (6.11). The final conditions after de-orbit are also computed from Eq. (6.11) since they will be the departure conditions for the following rendezvous step. The propellant mass consumption is also taken into account and updated throughout the entire sequence computation. In order to have only a real valued optimisation problem, it is chosen here to treat each of the 120 sequences as a bi-objective optimisation problem with **ord** fixed and ten design variables defined in **x**. Therefore, optimisation problem becomes:

$$\min_{\mathbf{x} \in D} \left[ToF_{Tot}(\mathbf{x}) \quad \Delta V_{Tot}(\mathbf{x}) \right] \tag{6.28}$$

The domain D is defined by the upper and lower boundaries defined in Table 6.5. Note that the lower boundaries for de-orbit time are set according to the sequence and the minimum times reported in Table 6.3.

Table 6.5 Optimisation boundaries

Parameter	$T_{RV,i1}$	$T_{DO,i1}$	$T_{RV,i2}$	$T_{DO,i2}$	$T_{RV,i3}$	$T_{DO,i3}$	$T_{RV,i4}$	$T_{DO,i4}$	$T_{RV,i5}$	$T_{DO,i5}$
Lower Bound	5	$T_{DO,min,i1}$	5	$T_{DO,min,i2}$	5	$T_{DO,min,i3}$	5	$T_{DO,min,i4}$	5	$T_{DO,min,i5}$
Upper Bound	100	50	100	50	100	50	100	50	100	50

Each bi-objective optimisation problem is solved with MACS2. MACS2 was run for 40000 function evaluations with 30 agents. Each of the 120 optimisation instances required roughly 6 days of computational time to complete. The outputs are represented by the Pareto optimal solutions w.r.t. ΔV_{Tot} and ToF_{Tot}. Figure 6.11 to Figure 6.15 collect the Pareto fronts according to the number of the first object in the sequence, i.e. the first index in the vector **ord**, as introduced in Eq. (6.25). In each figure, each colour represents the Pareto front corresponding to one of the 24 debris removal sequences starting with the

same object. For example, Figure 6.11 includes the Pareto fronts of sequences 12345, 13245, 14235, 15234, 12435 etc. .

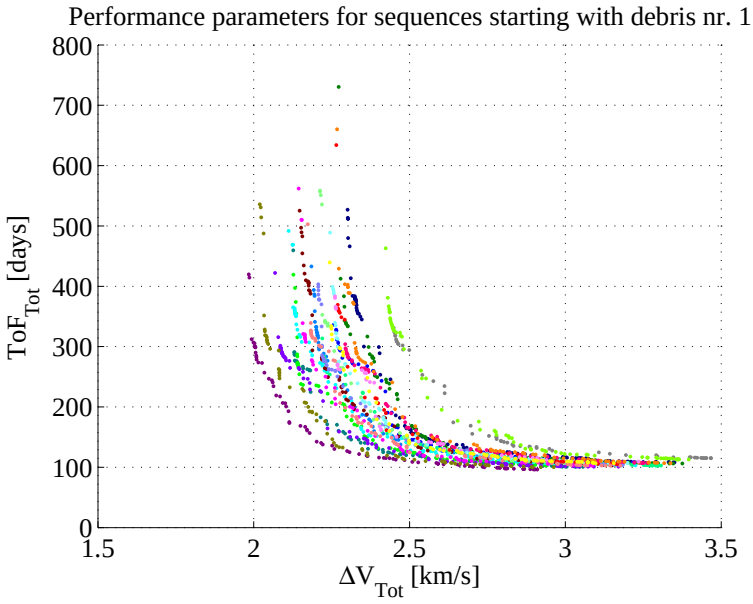

Figure 6.11 Pareto fronts for sequences starting with debris nr.1

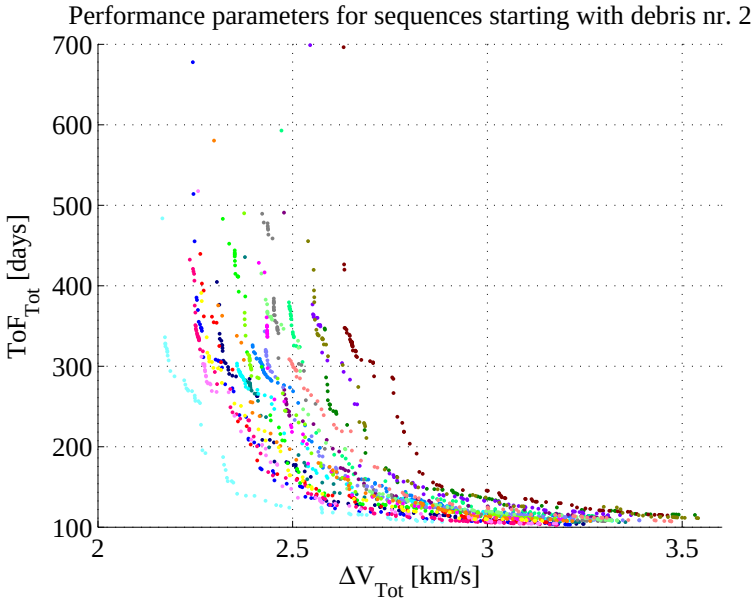

Figure 6.12 Pareto fronts for sequences starting with debris nr.2

From a visual inspection of the fronts it is possible to see that sequences starting from debris nr. 1 seem to present the best ΔV_{Tot}-ToF_{Tot} combination, since for most of them the ΔV cost is comprised between 2 and 2.5 km/s. The corresponding times of flight are comprised roughly between 100 and 500 days. The sequences starting with debris nr. 3 and nr. 2 also have a good ΔV while those starting with nr. 4 and nr. 5 appear to be worst. By combining all the partial Pareto fronts one obtains the globally optimal solutions, as reported in Figure 6.16.

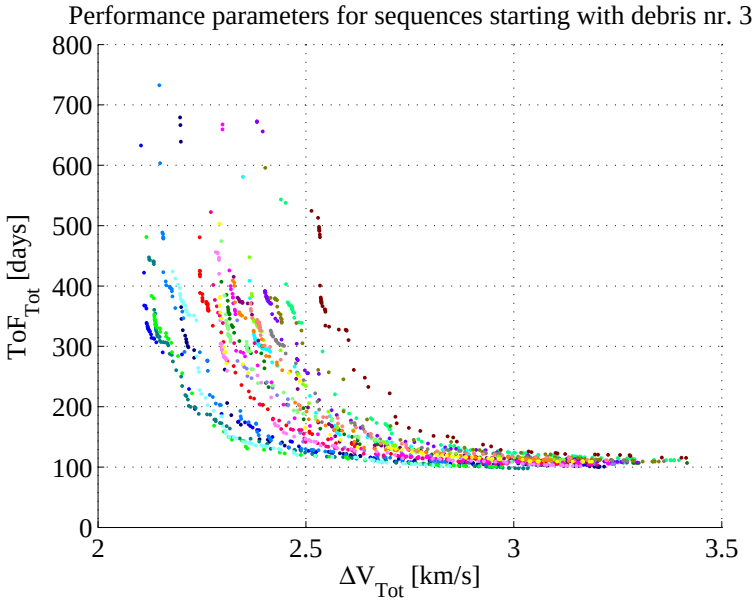

Figure 6.13 Pareto fronts for sequences starting with debris nr. 3

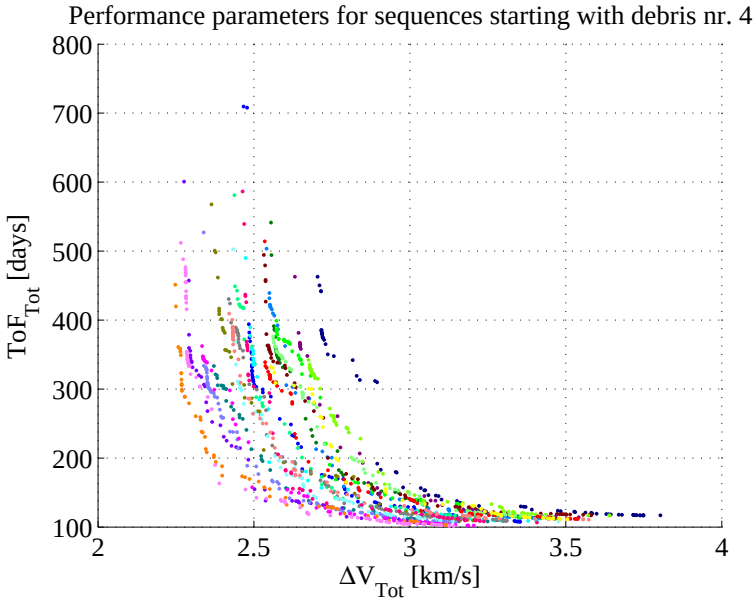

Figure 6.14 Pareto fronts for sequences starting with debris nr. 4

One can see that the global Pareto front is composed by individual solutions belonging exclusively from sequence 13452, which is therefore globally dominant. In order to rank the degree of optimality of each sequence, it is proposed to use an approach inspired by the performance metrics for optimisation algorithms proposed in Chapter 2. Define PF_g as the set of the points of the globally optimal Pareto front while $PF_{\mathbf{ord}}$ is the set of points belonging to the Pareto front corresponding to sequence **ord**. Define then the ranking parameter of sequence **ord** as:

$$Conv(\mathbf{ord}) = \frac{100\sum_{i=1}^{N_{\mathbf{ord}}} \min_{\mathbf{g}_j \in PF_g} \left(\frac{\mathbf{f}_i - \mathbf{g}_j}{\boldsymbol{\delta}} \right)}{N_{\mathbf{ord}}} \qquad (6.29)$$

$$\mathbf{f}_i \in PF_{\mathbf{ord}}, \forall i = 1, \ldots, N_{\mathbf{ord}}$$

Conv is given by averaging the distance of each point of $PF_{\mathbf{ord}}$ from the closest point of PF_g. The closest $PF_{\mathbf{ord}}$ is to PF_g and the lower *Conv* will be. Table 6.6 reports the ranking of the sequences according to *Conv*.

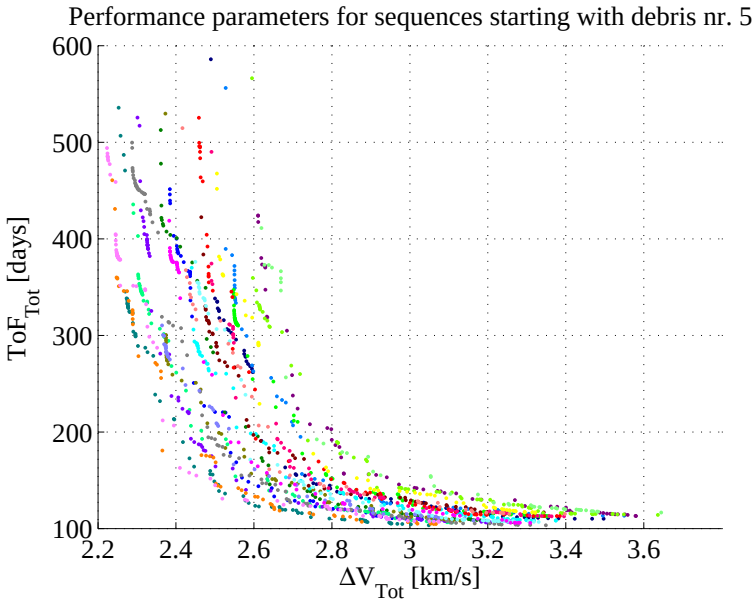

Figure 6.15 Pareto fronts for sequences starting with debris nr. 5

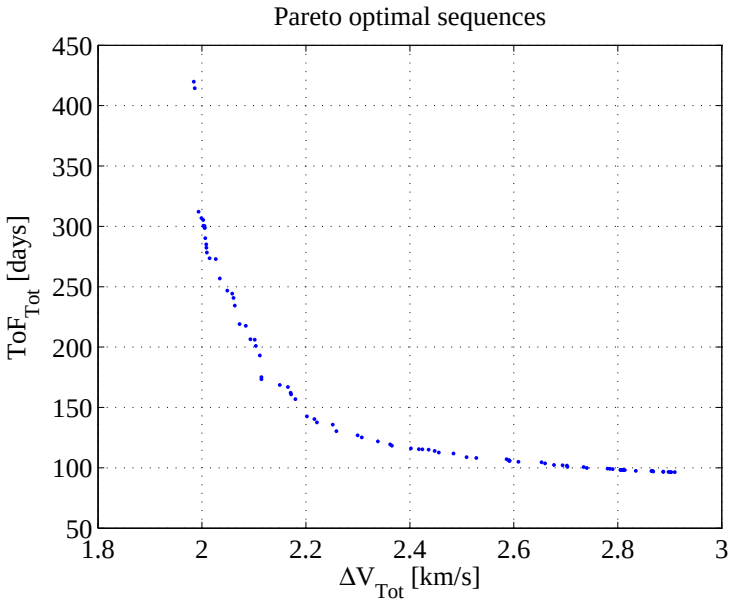

Figure 6.16 Global Pareto front

Table 6.6 Ranking of the de-orbit sequences

Rank	**ord**	*Conv*(**ord**)	Rank	**ord**	*Conv*(**ord**)	Rank	**ord**	*Conv*(**ord**)
1	13452	0	41	42513	21.18	81	52143	31.43
2	13542	5.14	42	15234	21.26	82	32145	31.62
3	13524	6.61	43	32451	21.46	83	54123	31.72
4	12453	6.78	44	52134	21.46	84	54132	31.83
5	12543	7.25	45	34521	21.52	85	42135	32.43
6	31542	9.41	46	35142	21.79	86	52314	32.70
7	31452	9.85	47	35214	21.99	87	42531	33.05
8	34512	11.59	48	34251	22.02	88	21435	33.96
9	24513	12.15	49	52431	22.04	89	54231	34.05
10	15243	12.16	50	45132	22.13	90	23145	34.31
11	12534	12.33	51	54312	23.39	91	23514	34.56
12	31254	12.37	52	21543	23.60	92	53421	34.67
13	15432	13.24	53	24315	23.62	93	25341	34.71
14	35124	13.87	54	41352	23.81	94	14325	34.91
15	13254	14.22	55	43152	23.90	95	41253	35.20
16	31524	14.36	56	12435	24.40	96	32514	35.42
17	15342	14.48	57	34125	24.53	97	14235	35.65
18	13425	16.30	58	15324	24.89	98	32541	36.42
19	24531	16.53	59	53142	24.90	99	51234	36.81
20	14523	16.65	60	23154	25.61	100	42153	36.91
21	14352	16.69	61	53124	25.67	101	51423	38.10
22	34152	17.16	62	51243	25.80	102	54321	38.25
23	25134	17.17	63	43512	25.83	103	45231	40.16
24	12354	17.47	64	31425	25.95	104	51432	40.98
25	14253	17.63	65	12345	25.96	105	41523	41.91
26	31245	17.81	66	21453	26.01	106	45321	44.72
27	15423	17.85	67	52413	26.09	107	32415	45.05
28	51342	17.88	68	51324	26.56	108	42351	45.38
29	14532	18.05	69	35241	26.68	109	43521	45.43
30	25413	18.07	70	25143	26.77	110	53214	45.72
31	54213	18.17	71	24153	26.93	111	43251	45.87
32	35412	18.48	72	34215	27.52	112	23541	46.11
33	21345	19.32	73	21534	28.00	113	52341	46.89
34	25431	19.43	74	32154	29.65	114	41325	47.14
35	13245	19.55	75	43125	30.17	115	41532	47.50
36	35421	19.56	76	23451	30.40	116	53241	48.31
37	25314	19.97	77	24351	30.97	117	23415	48.84
38	45213	19.98	78	45123	31.07	118	42315	48.85
39	45312	20.07	79	24135	31.18	119	43215	52.91
40	21354	20.07	80	53412	31.22	120	41235	65.42

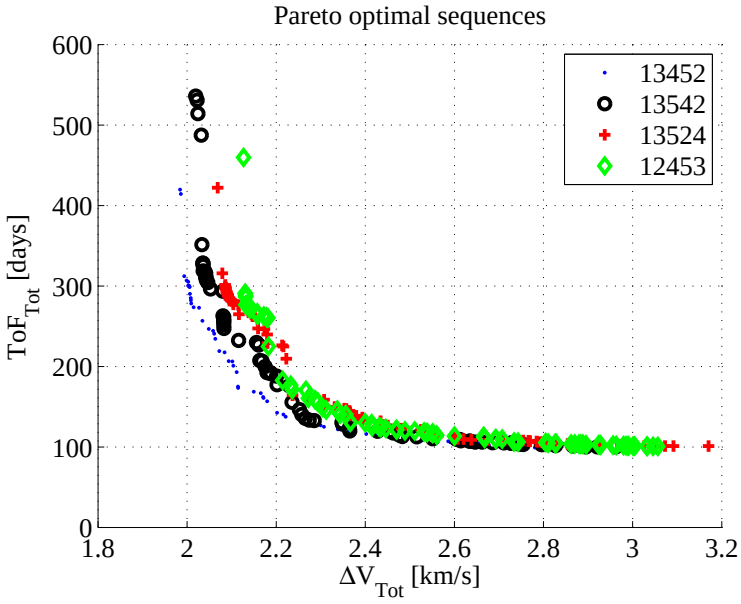

Figure 6.17 Pareto fronts corresponding to the four best sequences according to *Conv*

As one would expect, sequence 13452 has the lowest *Conv* since it coincides with part of the global Pareto front. Sequences 13524, 13542 and 12543 have also a low *Conv* index and thus they are quite close to the globally optimal solution, as shown in Figure 6.17. In general, as already noted before, there is a strong dependence of the *quality* of the sequence from its first element. One can see that the first ranks are occupied mostly by sequences starting with debris nr. 1 and 3, while those with nr. 4 and 5 have highest *Conv* and are therefore occupy predominantly the worst ones. Those starting with nr. 2 are somewhat in the middle. The fact that solutions with nr. 1 and 3 are privileged as first elements in the sequence might be explained from the fact that they lie in the two lowest orbits (see Table 6.3) and therefore are *easier* to reach (Please keep in mind that for the rendezvous with the first debris there is no plane change since it is assumed to depart from a coplanar orbit). Another interesting observation is that the best sequences tend to avoid the largest plane changes. For example, in 13452 the plane changes are 1.47º, 2.52º, 1º and 2º. On the contrary, in the worst one according to *Conv*, i.e. 41235, they are 1.95º, 2.16º, 3.63º and 2º.

Table 6.7 Best ΔV_{Tot} and ToF_{Tot} for each sequence. Best values are in bold. Worst values are underlined.

ord	min(ΔV_{Tot}) [km/s]	min(ToF_{Tot}) [days]	**ord**	min(ΔV_{Tot}) [km/s]	min(ToF_{Tot}) [days]	**ord**	min(ΔV_{Tot}) [km/s]	min(ToF_{Tot}) [days]
12345	2.30	108.17	24513	2.17	106.64	42315	2.53	116.99
12354	2.26	107.81	24531	2.26	105.94	42351	2.63	114.24
12435	2.27	106.25	25134	2.24	102.96	42513	2.28	104.48
12453	2.13	100.63	25143	2.41	109.53	42531	2.36	109.50
12534	2.18	105.81	25314	2.30	107.66	43125	2.42	109.26
12543	2.13	103.26	25341	2.49	107.22	43152	2.34	107.36
13245	2.22	102.72	25413	2.26	104.36	43215	2.67	116.73
13254	2.11	103.03	25431	2.27	107.97	43251	2.56	113.93
13425	2.15	103.12	31245	2.20	100.73	43512	2.43	108.12
13452	**1.98**	**96.35**	31254	2.10	103.46	43521	2.53	111.63
13524	2.07	101.03	31425	2.30	106.79	45123	2.46	106.61
13542	2.02	100.08	31452	2.12	97.810	45132	2.33	102.12
14235	2.45	115.10	31524	2.15	104.32	45213	2.25	102.99
14253	2.21	104.45	31542	2.12	100.52	45231	2.42	110.85
14325	2.42	112.87	32145	2.44	111.30	45312	2.27	101.57
14352	2.21	105.30	32154	2.35	107.73	45321	2.55	111.39
14523	2.25	107.07	32415	2.51	115.31	51234	2.49	110.19
14532	2.27	105.43	32451	2.33	107.85	51243	2.38	107.21
15234	2.29	107.13	32514	2.38	107.70	51324	2.36	106.79
15243	2.14	102.56	32541	2.40	109.14	51342	2.25	103.38
15324	2.27	106.71	34125	2.42	109.68	51423	2.53	113.27
15342	2.17	102.45	34152	2.33	104.78	51432	2.55	112.77
15423	2.26	109.45	34215	2.36	112.19	52134	2.29	106.29
15432	2.24	106.63	34251	2.30	107.17	52143	2.44	108.36
21345	2.31	103.98	34512	2.18	101.86	52314	2.46	116.72
21354	2.24	103.07	34521	2.24	104.80	52341	2.61	112.97
21435	2.58	115.15	35124	2.27	103.81	52413	2.30	106.23
21453	2.38	106.26	35142	2.30	105.62	52431	2.37	108.24
21534	2.40	113.76	35214	2.32	109.19	53124	2.29	103.32
21543	2.32	110.97	35241	2.37	111.19	53142	2.36	108.06
23145	2.47	113.45	35412	2.28	101.50	53214	2.60	114.17
23154	2.36	107.94	35421	2.29	108.91	53241	2.62	116.59
23415	2.63	114.64	41235	2.70	116.91	53412	2.45	106.79
23451	2.48	111.27	41253	2.47	107.83	53421	2.46	112.91
23514	2.55	114.91	41325	2.55	113.15	54123	2.49	112.69
23541	2.54	111.22	41352	2.37	108.25	54132	2.38	105.83
24135	2.42	107.59	41523	2.54	111.57	54213	2.24	104.67
24153	2.43	108.50	41532	2.57	112.14	54231	2.42	115.17
24315	2.38	110.73	42135	2.44	115.59	54312	2.22	107.06
24351	2.42	108.28	42153	2.47	108.75	54321	2.50	116.42

Table 6.7 reports the minimum values for the performance parameters associated to each sequence, i.e. the extreme points of the Pareto fronts. Similar considerations to those made previously also apply to this case, with best values given by sequences starting with nr. 1 and 3 and the worst ones with nr. 4 and 5.

Table 6.8 Debris removal sequence and timing for minimum ΔV_{Tot}.

Phase	*Final Keplerian elements*				*Duration*	ΔV	*mass* [kg]
	a [km]	*e*	*i* [deg]	Ω [deg]	[days]	[km/s]	
Departure	6628.16	0.010	1	65	-	-	1000
Nr. 1 reached	6828.16	0	1	65	5	0.115	996.11
Nr. 1 de-orbited	6752.69	0.011	1	65	22.06	0.043	993.21
Nr. 3 reached	6978.16	0	-2	200	88.10	0.239	985.17
Nr. 3 de-orbited	6826.44	0.022	-2	200	25.96	0.084	980.63
Nr. 4 reached	7478.16	0	-1	90	66.71	0.476	964.88
Nr. 4 de-orbited	7055.54	0.053	-1	90	34.33	0.221	951.69
Nr. 5 reached	7178.16	0	0	45	55.89	0.241	943.91
Nr. 5 de-orbited	6912.18	0.034	0	45	30.77	0.144	931.48
Nr. 2 reached	7128.16	0	2	150	56.98	0.297	922.12
Nr. 2 de-orbited	6901.39	0.032	2	150	33.99	0.124	917.24

Table 6.8 shows details about the best ΔV_{Tot} solution, with sequence 13452. Note that, in general, the ΔV cost of each phase is relatively low, thus leading to the minimum total cost of 1.98 km/s. Correspondingly, their duration is long, meaning that *slow* but more efficient transfers are preferred. This behaviour is also confirmed by the fact that the de-orbit conditions have non negligible eccentricities, which means also that the amplitude of the apogee thrusting arcs during de-orbit (see Figure 6.2) is kept to a minimum. In this way propellant is devoted to lowering the perigee only with minimum variation of the apogee altitude.

By analysing in more detail the ΔV cost breakdown, one can see for example that the highest figures, 0.476 km/s are given by the rendezvous with debris nr. 4 from the de-orbit conditions of debris nr. 3. This high value is justified by the fact that reaching the final orbit radius of 7478.16 requires an apogee raise of 501 km from 6977 km and a perigee raise of 800 km from 6678 km. At the same time there is also a rotation of the orbit plane of 2.52º. By comparison, the rendezvous with nr. 5 after the de-orbit of nr. 4 is comparatively cheaper even if the radius of the target orbit is still high. In this case the perigee raise is 500 km while the apogee on the other hand needs to be lowered by 252 km from 7430 km since piece of debris nr. 4 is released on a relatively eccentric orbit with e=0.053. Plane rotation in this case is only 1º.

Table 6.9 Debris removal sequence and timing for minimum ToF_{Tot}.

Phase	*Final Keplerian elements*				*Duration*	ΔV	*mass* [kg]
	a [km]	*e*	*i* [deg]	Ω [deg]	[days]	[km/s]	
Departure	6628.16	0.010	1	65	-	-	1000
Nr. 1 reached	6828.16	0	1	65	5	0.115	996.11
Nr. 1 de-orbited	6685.24	0.001	1	65	4.04	0.081	990.61
Nr. 3 reached	6978.16	0	-2	200	8.59	0.312	980.14
Nr. 3 de-orbited	6701.87	0.004	-2	200	6.29	0.154	971.87
Nr. 4 reached	7478.16	0	-1	90	14.79	0.664	950.17
Nr. 4 de-orbited	6789.06	0.016	-1	90	17.13	0.362	928.76
Nr. 5 reached	7178.16	0	0	45	7.99	0.281	919.92
Nr. 5 de-orbited	6715.72	0.006	0	45	15.9	0.252	898.39
Nr. 2 reached	7128.16	0	2	150	9.87	0.466	884.28
Nr. 2 de-orbited	6725.90	0.007	2	150	6.75	0.221	875.87

Table 6.9 reports details about the minimum ToF_{Tot} solution, again with sequence 13452. In contrast to what has been remarked for the previous case, here obviously the duration of each phase is kept to a minimum. For example, values for de-orbit times are very close to the minima reported in Table 6.3. Conversely, ΔV costs are higher than those in Table 6.8. Moreover, one can see that the de-orbit trajectories are quasi-circular, which suggests that the thrusting arcs are not restricted to apogee passages but cover almost entirely each revolution (i.e., with reference to Figure 6.2, $\Delta L_a \approx 180°$).

A final note is devoted to the assumption mentioned in Section 6.3.2 that the delay due to phasing will be relatively negligible compared to the total transfer time. First of all, one has to consider that each de-orbit-rendezvous couplet is actually a transfer between two circular orbits with different altitude, phasing and orbit plane. In this sense, the related transfer strategy first lowers the perigee down to 300 km; then, in the second phase the apogee and perigee altitudes are adjusted to match those of the target orbit and at the same time the orbit plane is rotated around the line of nodes. In order to obtain a worst case estimation of the delay, it is chosen to decompose the latter into the contribution determined by the inclination change $t_{wait,\Delta i}$ and the one given by in-plane phasing $t_{wait,\Delta\phi}$. The former stems from the assumption made in Section 6.3.2 that the perigee lowering phase from the initial circular orbit is started such that the lines of apses is perpendicular to the line of nodes defined by the intersection of the orbit planes of the current piece of debris and the next one in the sequence. The maximum wait time is obtained when the line of nodes is aligned with the line of apses and is therefore given by half the orbit period of the departure circular orbit:

$$\max\left(t_{wait,\Delta i}\right) = \pi n_0 \tag{6.30}$$

where n_0 is the angular velocity of the initial circular orbit. After the line of apses is properly aligned in order to reach the target orbit plane, there remains, however, the

problem of in-plane phasing. As a first step, the case of a quasi-circular transfer is considered, noting that this is actually the case for minimum ΔV sequences as the one reported in Table 6.8. If one considers the case of a transfer between two circular coplanar orbits, the phasing of the departure and arrival ones can by expressed as:

$$\begin{aligned} \phi_0 &= n_0 t_{wait,\Delta\phi} + \Delta\phi_{transf}\left(t_{transf}\right) \\ \phi_f &= n_f\left(t_{wait,\Delta\phi} + t_{transf}\right) + \Delta\phi_0 \end{aligned} \tag{6.31}$$

where n is the angular velocity of the current orbit, n_f is the one of the arrival orbit, is introducing along the transfer in order to match the phase of the arrival orbit. $\Delta\phi_0$ is the nominal phase difference between the two orbits at time of departure, computed simply from the initial and final argument of perigee and true anomaly:

$$\Delta\phi_0 = \left(\omega_f - \omega_0\right) + \left(\theta_f - \theta_0\right) \tag{6.32}$$

ϕ_0 and ϕ_f can differ by multiples of 2π, therefore, by combining Eqs. (6.31):

$$t_{wait,\Delta\phi}\left(n - n_f\right) = \Delta\phi_0 + \Delta\phi_{transf} + n_f t_{transf} + 2k\pi \quad k \in \mathbb{Z} \tag{6.33}$$

One can see that, once the transfer type is defined, the left side of Eq. (6.33) is constant and since k is an arbitrary integer, one can write:

$$t_{wait,\Delta\phi} = \frac{\Delta\phi_{Tot}}{\left|n - n_f\right|} \quad \Delta\phi_{Tot} \in \left[0 \quad 2\pi\right] \tag{6.34}$$

and thus the worst case value for the delay t_{wait} is obtained obviously for $\Delta\phi_{Tot} = 2\pi$. Since we are dealing with a LT transfer in which the semi-major axis is continuously varied, also the angular velocity n at a certain point of the transfer is varying accordingly. Also, since it is assumed that the transfer is quasi-circular, one can insert a coasting arc of duration $t_{wait,\Delta\phi}$ at the point in which the ratio $1/\left|n - n_f\right|$ (which depends on the radii of the current and target orbits) is at its lowest. This condition typically occurs when the end of the de-orbit phase is reached.

If the transfer type is not quasi-circular but involves spirals with non-negligible eccentricity, then an arbitrary delay cannot be introduced without altering the position of the lines of nodes. However, it is still possible to introduce an arbitrary number of coasting arcs of duration equal to the orbital period of the osculating orbit, i.e. one full revolution. The phase variation obtained by one such revolution is:

$$\Delta\phi_{2\pi}\left(n\right) = \frac{2\pi\left|n - n_f\right|}{n} \tag{6.35}$$

Note that, given the orbits involved in the transfer, $\Delta\phi_{2\pi}$ will be generally a fraction of 2π. If a worst case phase variation $\Delta\phi_{Tot} = 2\pi$ is to be achieved, the following simple

strategy can be used to estimate the corresponding delay: first, k coasting revolutions are performed when the quantity $|n\text{-}n_f|$ is maximum. In this sense, one can write:

$$k = \left\lfloor \frac{\Delta\phi_{2\pi}(n_k)}{2\pi} \right\rfloor$$
$$n_k = \arg\min_n \Delta\phi_{2\pi}(n) \tag{6.36}$$

This will bring the phase difference to a quantity which is lower than the maximum phase variation per revolution achievable, leaving a residual phase difference;

$$\Delta\phi_{res} = 2\pi - k\Delta\phi_{2\pi}(n_k) \tag{6.37}$$

A last coasting revolution is inserted to delete the residual when the semi-major axis which gives the proper angular velocity n_{res} is reached:

$$n_{res} = \arg(\Delta\phi_{2\pi}(n) = \Delta\phi_{res}) \tag{6.38}$$

The total delay introduced in the worst case is therefore given by the sum of the periods of the coasting revolutions:

$$\max\left(t_{wait,\Delta\phi}\right) = 2\pi\left(\frac{k}{n_k} + \frac{1}{n_{res}}\right) \tag{6.39}$$

By applying the above strategies to the minimum ΔV and minimum time of flight sequences we can obtain a worst case estimation of the additional time introduced by phasing. The maximum delay introduced by the apses alignment in both cases would be 0.14 days. For the minimum time of flight case in Table 6.9 (i.e. quasi-circular sequence), the worst case delay due to $\Delta\phi$ is 2.68 days, leading to a total delay of 2.82 days. This value equates to a 2.93% increase compared to the nominal time of flight of 96.35 days, which can be considered acceptable for a preliminary study. On the contrary, in the case of minimum time of flight sequence as in Table 6.8, the delay due to $\Delta\phi$ would be 4.58 days, and the total delay 4.72 days, corresponding to a 1.12% increase on the nominal time of flight of 419.79 days. For these reasons, neglecting the phasing appears to be an acceptable approximation in this preliminary study.

6.5 Conclusions

This chapter presented a practical application of the novel techniques proposed in this dissertation. They were applied to the design of a multi-target Multi-Objective orbit debris removal mission by means of an IBSC. The models proposed here for the computation of low-thrust many-revolution transfers, allowed for a considerable reduction in control parameters and, at the same time, a fast propagation of the low-thrust motion. The Multi-Objective optimisation minimising both ΔV cost and total removal duration provided

thousands of different debris removal candidate solutions. The analysis of the results showed that the particular removal sequence 13452 is globally optimal. A ranking criterion was proposed to grade all the candidate sequences and identify those that are suboptimal. From the analysis of the sequences it was found that there is a dependency of the quality of the sequence on the first target object. Among the open issues for future developments, there is, for example, the integrating the sequence selection directly into the Multi-Objective optimisation process, thus obtaining a mixed continuous and discrete optimisation problem. This can be crucial when missions with more than 5-10 debris are considered since the enumerative generation of sequence becomes increasingly expensive with the number of potential target objects.

Chapter 7.Low-Thrust Orbit Raising Design for the DESTINY Mission

This chapter presents an overview of the preliminary design of the orbit raising phase for DESTINY, a proposal for a future JAXA interplanetary mission using Low Thrust propulsion. In this case study, the techniques described in the previous chapters are applied to a real-case mission design problem. This case, therefore, provides the evidence of the validity of the proposed techniques as operational tool for space mission design. The chapter is organised as follows: Section 7.1 will give an overview of DESTINY, while Section 7.2 will describe the optimisation problem; Section 7.3 will present the trajectory model used for the orbit raising. Section 7.4 will introduce the formulation of the MOO problem and will show some preliminary results. Section 7.5 will analyse the specific issue of eclipse avoidance during the orbit raising and finally Section 7.6 will show the solutions found with an extended control model, as suggested by these analyses.

7.1 DESTINY Mission Overview

The Demonstration and Experiment for Space Technology and INterplanetary voYage (DESTINY)[9] is a technology demonstrator mission which is currently being developed as a candidate third mission of ISAS/JAXA's small science satellite series. Its main objective is that of gaining flight heritage for a number of novel technologies, which include, among others, the new μ20 Ion engine, the new Epsilon launch vehicle, ultra-lightweight solar panels and an advanced thermal control. In addition, it will also provide a test-bed for new techniques for Low Thrust (LT), interplanetary mission design and operation.

The proposed mission profile for DESTINY, as shown in Figure 7.1, envisions:

1) Injection into an inclined elliptical orbit (with semi-major axis around 20000 km) by means of the Epsilon rocket.
2) Spiralling phase in which the μ20 engine will raise the orbit in order to encounter the Moon.
3) Lunar swing-by.
4) Injection into a Halo orbit at the Sun-Earth L_2 Point.
5) Additionally, if possible, a final escape from L_2 is also desirable.

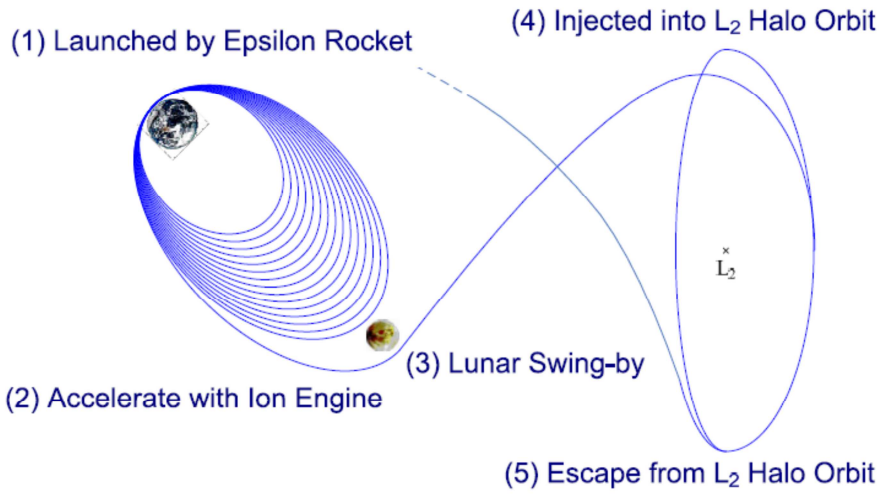

Figure 7.1 DESTINY preliminary mission profile[9].

The early LT orbit raising phase presents an interesting mission design challenge, since many trade-offs are to be made between different performance figures; at the same time, technological limitations on bus design impose a number of constraints on trajectory design. In particular, the time to reach the Moon encounter is upper bounded at 1.5 years but shorter transfer times might also be advantageous. On the other hand, in the latter case, the required ΔV is likely to be higher; while this, given the available fuel and the high efficiency of the μ20 engine, will not prevent reaching the Halo orbit, it will possibly affect the feasibility of the optional post-Halo escape phase. It should also be noted that, during the orbit raising phase, the spacecraft will spend a long period of time within the highly radiative environment of the Van Allen belts. This time should be minimised in order to reduce the total radiation dose and therefore the mass of the required shielding for electronic components. Similarly, eclipse duration during the transfer, influences both trajectory design, since engine operation has to be interrupted while in shadow, and spacecraft bus design, because it imposes constraints on battery sizing. Finally the conditions, in terms of orbit geometry, with which the Moon is encountered, also require trade-off analysis, since they are strongly linked with the trajectory design of the following phase, which will lead DESTINY spacecraft to the designated L_2 Halo orbit.

The presence of many conflicting requirements will be tackled in this work by adopting a Multi-Objective (MO) design approach, in which multiple performance figures are concurrently optimised. The trajectory will be modelled with the parameterisation described in Section 5.1 and it will be propagated with the averaging technique described in Section 5.2, while the Multi-Objective problem will be solved with MACS2 (see Chapter 2).

7.2 Problem Definition

The purpose of this study is that of optimising the strategy for DESTINY's orbit raising phase in order to concurrently minimise four figures of merit: the time of flight *ToF*, the total Ion Engine System operation time *IES*, the time spent within the radiation belt t_{belt} and finally the duration of the maximum eclipse encountered $t_{ecl,max}$. The latter, in addition, is to be kept below 1 h, due to constraints on battery size. The maximum time of flight allowed for the orbit raising phase is 550 days, i.e. about 1.5 years.

As a result of the inputs from the design team of the Epsilon Launch Vehicle, the initial orbit parameters after release from the launcher are assumed to be those reported in Table 7.1.

Table 7.1 DESTINY initial orbit parameters in the J2000 Earth Fixed reference frame.

a (km)	e	i	Ω	ω	M
20953	0.69	32°	21°	124°	5°

Note that, the initial orbital elements are specified with respect to the J2000 Earth Fixed reference frame, i.e. a moving frame, and thus the actual value of Ω in the inertial reference frame is dependent on the launch epoch. After release from the launcher, a 30-day commissioning phase is imposed, in which the spacecraft is not allowed to perform any manoeuver.

The terminal condition to be reached at the end of the orbit phase is a radius of 300000 km at the intersection between the orbit and the current lunar orbital plane. This condition reflects the fact that, at this preliminary stage, it has been decided to uncouple the design of the orbit raising phase from that of the Lunar encounter and subsequent interplanetary phase. Note also that, given the relative angle between the lunar orbit plane and DESTINY's, the intersection between the two can occur quite far from DESTINY's apoapsis and therefore the latter might be much higher than 300000 km.

The preliminary specifications for DESTINY spacecraft are reported in Table 7.2.

Table 7.2 DESTINY spacecraft characteristics.

Initial mass (kg)	Engine thrust (mN)	Specific impulse (s)
400	40	3800

The powerful μ20 engine, mounted on a small spacecraft, produces a relatively high acceleration of 10^{-4} m/s^2. At the same time, the high specific impulse of this ion engine ensures good propellant efficiency.

The design parameters which are to be optimised are the departure epoch and the parameters of the thrust vector (see Section 7.3). For each candidate set for these parameters, the propagation technique presented in the previous section is used to propagate the orbital motion until the terminal condition of 300000 km radius on the lunar orbit plane has been verified, or else when the maximum time of flight allowed, 550 days, has been reached. From this it is possible to compute the total time of flight *ToF*, total engine operation time *IES*, the time within the radiation belt t_{belt} and the duration of the maximum longest eclipse $t_{ecl,max}$. Note that, t_{belt} is defined simply as the time for which the spacecraft is below 20000 km altitude. The candidate parameter sets will be generated by means of a Multi-Objective optimisation algorithm.

7.3 Trajectory Model

The control model chosen for DESTINY's analyses is the one described in Section 5.1 and shown in Figure 5.4. The propagation of the orbital motion is performed as in Eqs. (5.3) and (5.5). An additional equation is added in order to account for the time spent below 20000 km. The time t_{belt} spent below this altitude is also computed in averaged terms:

$$\begin{aligned} \bar{t}_{belt}(t) &= \int_{t_0}^{t} \dot{t}_{belt}\left(\tau, \bar{\mathbf{E}}(\tau)\right) d\tau \\ \dot{t}_{belt} &= \frac{\Delta t_{belt}}{T_{2\pi}} \end{aligned} \tag{7.1}$$

Δt_{belt} is defined as the time spent below 20000 during an orbital revolution, assuming an orbit whose orbital parameters remain constant along the latter. Δt_{belt} can be easily computed as:

$$\Delta t_{belt} = \begin{cases} T_{2\pi}, & a(1+e) \geq r_{belt} \\ 0, & a(1-e) < r_{belt} \\ -t_{kep}(-\theta_{belt}) + t_{kep}(\theta_{belt}), & a(1-e) < r_{belt} \leq a(1+e) \end{cases} \tag{7.2}$$

where r_{belt} is the radius corresponding to the outer edge of the belt, t_{kep} is the time corresponding to the true anomaly θ_{belt}, as computed from Kepler's well-known time equation (see Battin[98]). θ_{belt} is the true anomaly of the radius r_{belt}, given by:

$$\theta_{belt} = \text{acos}\left(\frac{a\left(1-e^2\right) - r_{belt}}{r_{belt} e} \right) \tag{7.3}$$

In order to compute the length of the maximum eclipse $t_{ecl,max}$ the duration t_{ecl} of the eclipse along a single revolution is computed (and stored) during the integration of Eqs. (5.3), assuming the cylindrical shadow model as described in Section 5.1.1 . Note that, this has to be done anyway in the computation of the averaged variation of the orbital elements $\Delta\mathbf{E}_{2\pi}$ in order to account for engine operation discontinuities due to shadow. Then, after the propagation of the orbital motion is completed, the maximum value of t_{ecl} is taken. Note however, that this model is valid under the assumption that the relative position of the shadow region with respect to the orbit plane will not change considerably during an orbital revolution. In other words, the shadow region is assumed to be "frozen" along a single revolution. Given the typical time frame of the Sun's dynamics, this assumption is perfectly valid when the orbital period is comparatively small, roughly up to a few days. For larger orbits, what happens is that the orbital period becomes of the same order of magnitude of the time which takes the orbit plane to cross the shadow region. In this sense, during an orbital period the portion of orbit in shadow changes considerably, and thus the "frozen" model proposed here is no longer applicable. At the same time, however, it also means that there will be just a single eclipse in that revolution and not a sequence of eclipses in close succession as it happens when the orbital period is small. Therefore, it can be assumed that with proper phasing correction at some point before this single eclipse, the latter can be shortened or even avoided altogether. For this reason, it is decided here to ignore these isolated eclipses, in the computation of the maximum eclipse duration, since eclipse avoidance strategies can be easily implemented at a later, more detailed design stage.

As an example of the accuracy of the proposed propagation methodology, a sample trajectory is propagated both with the averaging method and with the full numerical propagation of the equations of motion. The chosen example exibits continuous tangential thrust for the first 200 days or so and then thrusting is localised only on shorter arcs around pericentre. Figure 7.2 shows that the proposed approach describes very accurately the behaviour of the apogee and perigee radius (i.e. semi-major axis and eccentricity), also during the last few orbits when the analytical approach tends to be less reliable due to the large distance from the attracting body. Similarly, Figure 7.3 shows that the evolution of the cumulative eclipse time is also well approximated by the proposed eclipse model.

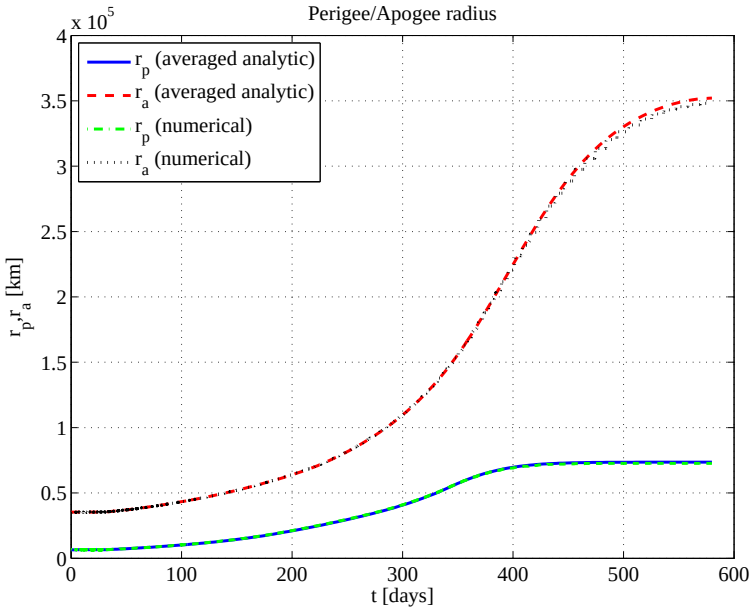

Figure 7.2 Sample propagation: apogee and perigee radius.

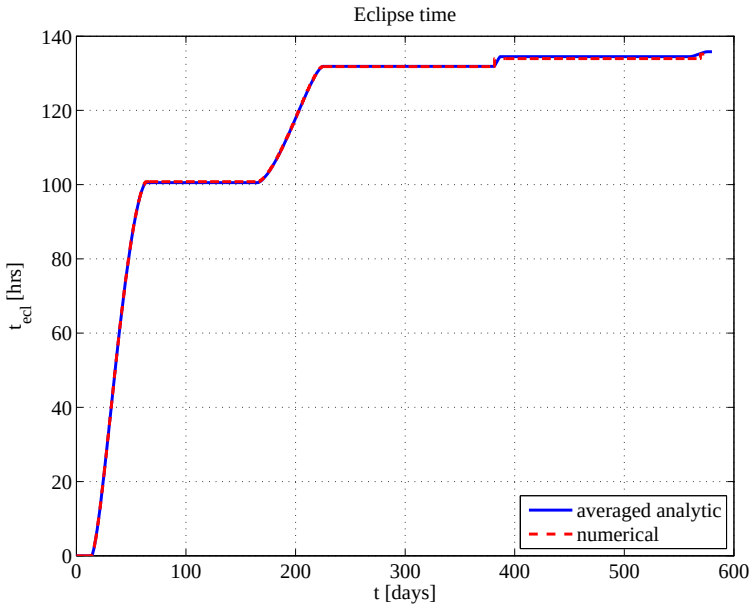

Figure 7.3 Sample propagation: cumilative eclipse time.

7.4 Multi-Objective Optimisation of DESTINY's Orbit Raising

The design of DESTINY's orbit raising phase can be formulated as a Multi-Objective optimisation problem in the form:

$$\min_{\mathbf{x}\in D} \mathbf{f}(\mathbf{x}) \tag{7.4}$$

where **f** is the vector of the objectives:

$$\mathbf{f} = \begin{bmatrix} ToF & IES & t_{belt} & t_{ecl,max} \end{bmatrix} + \mathbf{w}\Delta r_{fin} \tag{7.5}$$

$\mathbf{w}\Delta r_{fin}$ is a penalisation term added to **f** in order to account for the fact that a given candidate transfer might reach a final radius on the Moon's plane r_{fin} lower than the target 30000 radius within the maximum allowed *ToF* of 550 days. Therefore, Δr_{fin} is defined as:

$$\Delta r_{fin} = \min\left(\begin{bmatrix} 0 & 300000 - r_{fin} \end{bmatrix}\right) \tag{7.6}$$

w is simply a weight vector.

x is the parameter vector and *D* is its domain. **x** comprises the departure epoch, decomposed as *date* in MJD2000 and *time* and the semi-amplitudes of the perigee and apogee thrusting arcs, expressed as the values of ΔL_p and ΔL_a at 8 reference nodes, as in Eqs. (5.4). Note that *date* is meant as the integer part of the number of days since epoch 6574.5 MJD2000 (2018/01/01T00:00:00 UTC), while *time* is intended as the number of hours since the midnight of the day defined by *date.*

$$\mathbf{x} = \begin{bmatrix} date & time & \cdots & \Delta L_{p,i} & \cdots & \Delta L_{a,i} & \cdots \end{bmatrix} \quad i = 1,...,8 \tag{7.7}$$

The reason, for which the departure epoch is here expressed as day and hour, is that preliminary tests revealed that the objective functions showed wide oscillations with respect to the departure epoch and that the two scales of these oscillations were of the magnitude of a day and a year. This is related to the orientation of the initial orbital plane with respect to the Ecliptic plane and the lunar plane. Since, as mentioned earlier, the initial orbital elements in Table 7.1 are defined as relative to the Earth, i.e. a rotating reference frame, it follows that Ω in the Equatorial inertial reference frame experiences a short term evolution due to the Earth's rotation around its axis, superimposed to a long term variation due to the Earth's motion in the solar system (plus other secular perturbations). Therefore, by decomposing the departure epoch into *date* and *time*, one is able to decouple these two dynamics. The boundaries for the domain *D* are reported in Table 7.3.

Table 7.3. Boundaries for optimisation parameters.

Variable	*date* (d)	*time* (h)	$\Delta L_{p,i}$ (°)	$\Delta L_{a,i}$ (°)
Lower bound	0	0	0	0
Upper bound	365	24	180	180

In summary, each transfer is described by a total of 18 optimisation parameters. Regarding the performance parameters in the vector **f**, as already mentioned there are four figures of merit which are to be concurrently minimised, *ToF*, *IES*, t_{belt} and $t_{ecl,max}$, which would translate into a 4-objective optimisation problem. In the following sub-section, it is

decided to solve a reduced 3-objective problem first, without $t_{ecl,max}$ as an objective or constraint. This is done because, generally speaking, a 3-objective problem is easier to visualise and analyse. It will also show how the solution set changes, when the fourth objective will be re-introduced and the full optimisation problem solved. In both cases the Multi-Objective optimisation problem in Eq. (7.4) is solved with MACS2.

7.4.1 3-Objective Problem

For this 3-objective problem, MACS2 is set to run for a maximum of $3 \cdot 10^5$ function evaluations. Population size is set at 150 individuals, of which 30 perform social actions.

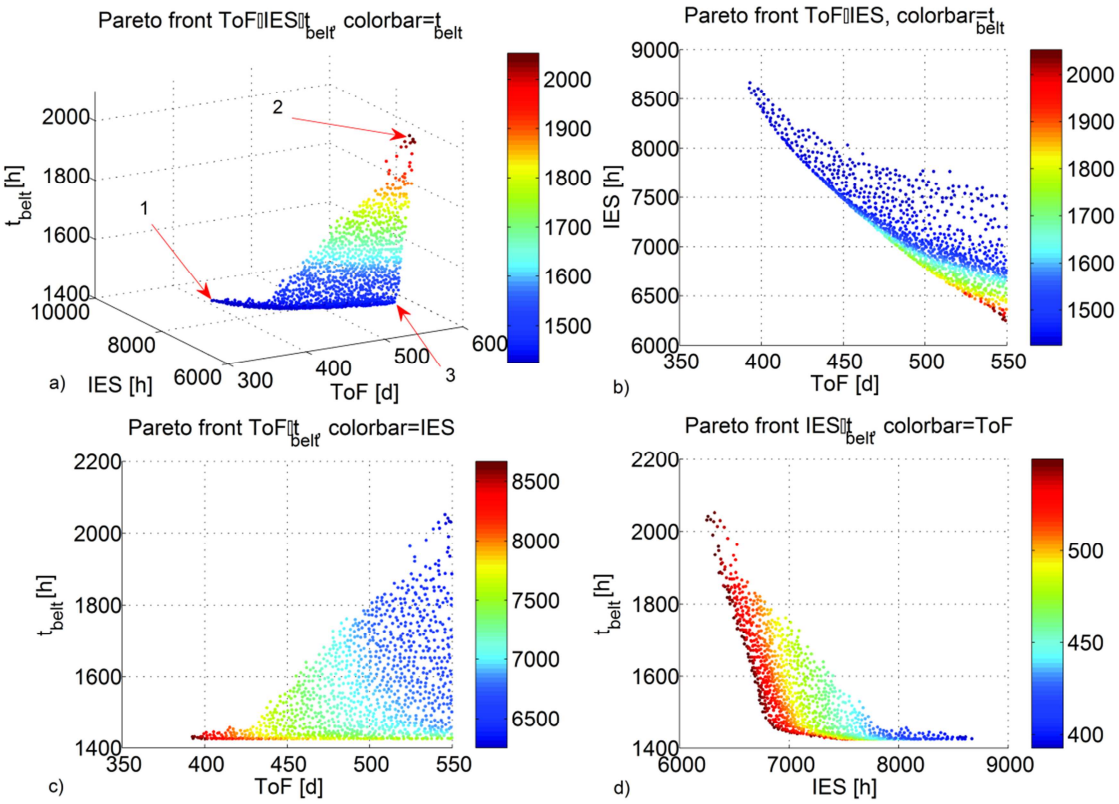

Figure 7.4. 3-Objective problem: a) Pareto front. Projections on the b) *ToF-IES* c) *ToF-*t_{belt} d) *IES-*t_{belt} sub-spaces.

Figure 7.4a shows the optimal objective set. For more clarity, Figure 7.4b-c-d show their projections on the bi-dimensional subspaces. By examining the extreme points for each objective, one can see that, for example, the minimum transfer time is around 400 days, which requires a total of 8600 hours of engine operations. On the other hand, the minimum IES solution requires around 6300 hours for a 550 days transfer. Similarly, the minimum time spent in the radiation belt is above 1400 hours. The *ToF-IES* projection in Figure 7.4b shows the typical pattern of propellant versus transfer time trade-off. This implies that any reduction in propellant consumption is paid for by an increase in transfer time and vice-versa. It is also interesting to note from Figure 7.4d that, in a similar way,

any reduction in propellant consumption below 7300 hours invariably requires an increase in t_{belt}. Moreover, the minimum *ToF* solution is also a minimiser for t_{belt}. The reasons for this will be explained later in this section. Figure 7.5 shows the distribution of the optimal solutions along the launch window and shows that they are aligned along a diagonal line in the date-time space. As mentioned earlier, date and time are determining the initial Ω in the Equatorial reference frame. Given the relative inclination between the Equator and the lunar orbit plane, this parameter consequently affects the elevation of the apsis direction w.r.t. the lunar orbit plane. Since the termination condition is defined at the intersection with this plane, the higher the elevation is, the higher the final semi-major axis will have to be and therefore the longer or the more expensive the transfer will be. Therefore, the optimal solutions line on the diagonal line which corresponds to the initial Ω which gives the lowest elevation of the line of apsis on the lunar orbit plane at the end of the transfer.

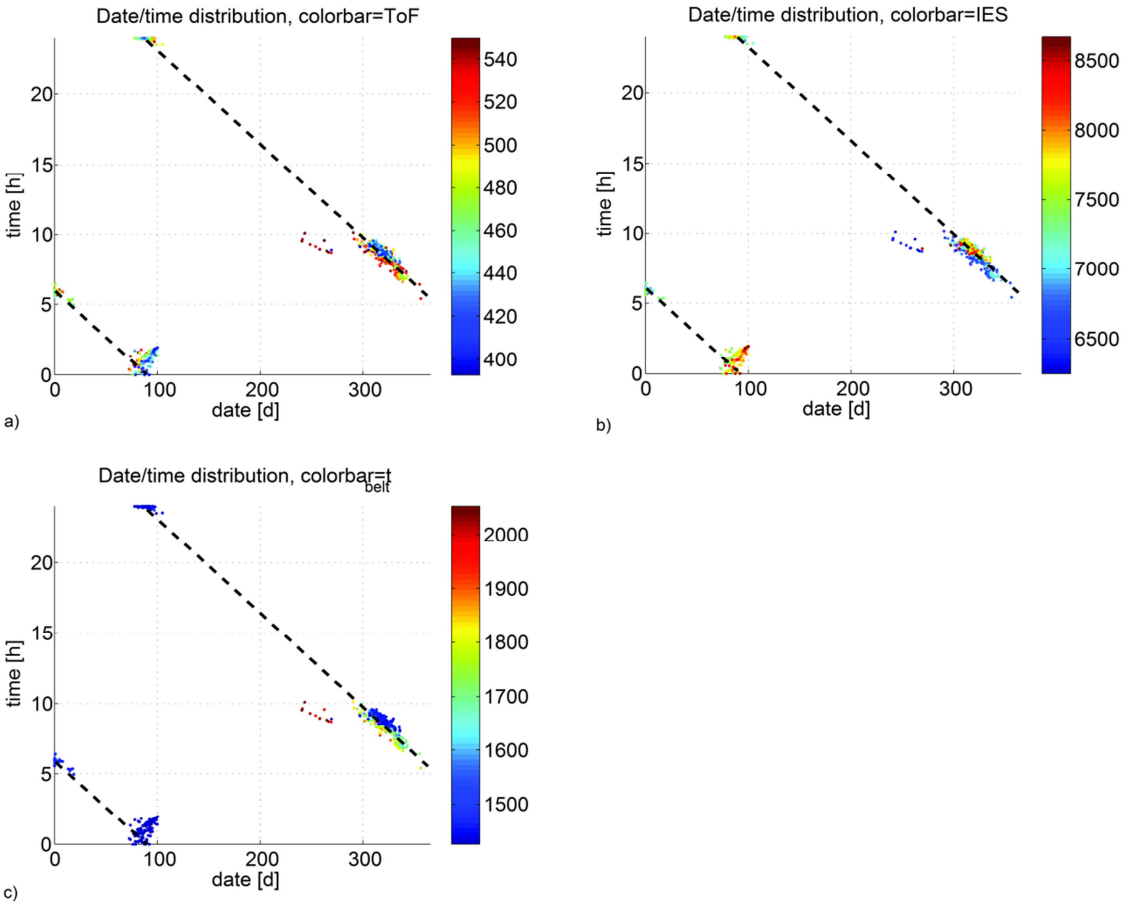

Figure 7.5. 3-Objective problem: distribution of the optimal solutions w.r.t. the departure date: a) *ToF* b) *IES* c) t_{belt}.

From Figure 7.4a one can identify three different classes of solutions: those which minimise time of flight and time in the radiation belt (1); those which minimise propellant cost (2); and finally, those which minimise t_{belt} but at the same time also somewhat minimise *IES* by allowing for the maximum *ToF* of 550 days (3).

Table 7.4 reports a comparison of the three solution types. As one can see solution 1 has the lowest time of flight, 392 days and at the same time also the lowest time spent within the radiation belt, 1431 hours. On the other hand, ion engine operation time is the highest, at 8632 hours. The opposite applies to the second solution, with an engine operation time of just 6349 hours but with the highest admissible time of flight of 550 days and a high t_{belt} of over 2000 hours. The third case is very interesting, for the reason that it has the minimum t_{belt} like the first one, but at the same time its fuel consumption is not as high as the first case, since the time of flight has been allowed to increase up to almost 550 days.

Table 7.4. Summary of sample solutions

	Type	*date* (d)	*time* (h)	*ToF* (d)	*IES* (h)	t_{belt} (h)
1	min(*ToF*)	295	9.2	392	8632	1431
2	min(*IES*)	266	8.7	550	6249	2032
3	min(t_{belt}),max(*ToF)*	329	8.3	550	6865	1457

In order to better understand the differences between the three cases, Figure 7.6, Figure 7.8 and Figure 7.10 show the thrusting arc length and the time history of the perigee/apogee radii for each of them. From Figure 7.6a one can see that the semi-amplitude of the thrusting arc for the minimum *ToF* case is always 180 degrees (except for the initial commissioning phase), which translates into a continuous thrust profile. And as Figure 7.6b shows, perigee and apogee are concurrently raised, with a monotonic decrease of the eccentricity, which reaches 0.2 at the end of the transfer. Note also that the Apogee is around 300000 km when the terminal condition is reached, which confirms what said earlier that the optimal solutions reach the terminal condition with the line of apses lying on the lunar orbital plane.

From Figure 7.7, which plots the trajectory in the J2000 reference frame, one can also clearly appreciate that the typical shape of a continuous tangential thrust trajectory as the orbit shape gradually becomes less eccentric.

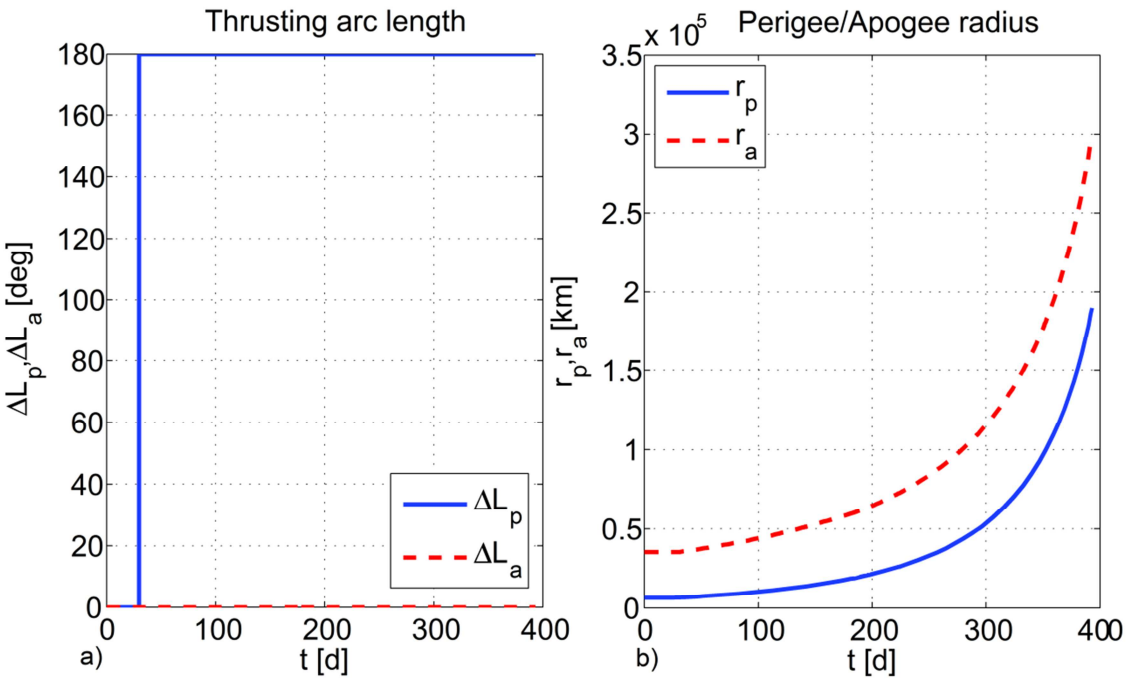

Figure 7.6. Minimum *ToF* solution: a) thrusting arc length; b) perigee/apogee radii.

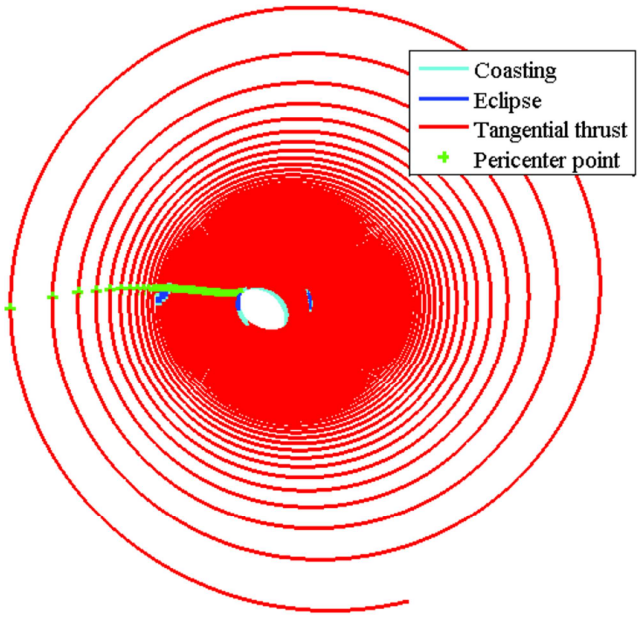

Figure 7.7. Minimum *ToF* solution: trajectory.

From Figure 7.8a, one can see that for the minimum *IES* solution, the thrusting arcs are located always around perigee with a semi-amplitude around 150-160 degrees. Consequently, the rate of increase of the orbit size is much lower (see Figure 7.8b) and at the same time the effort is focused on raising the apogee while the perigee experiences only a comparatively small increase up to around 30000 km, leading to the high t_{belt} mentioned before.

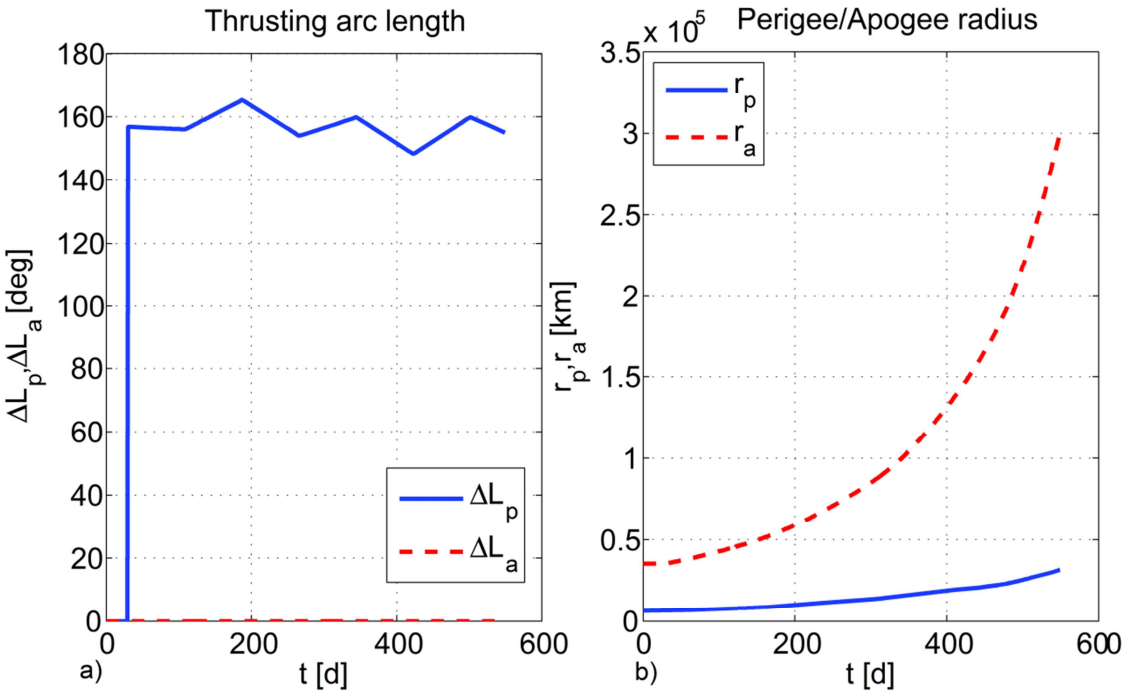

Figure 7.8. Minimum *IES* solution: a) thrusting arc length; b) perigee/apogee radii.

In contrast to the minimum *ToF* case, the long coasting arcs around apocenter lead to a considerable increase in the eccentricity, as shown in Figure 7.9.

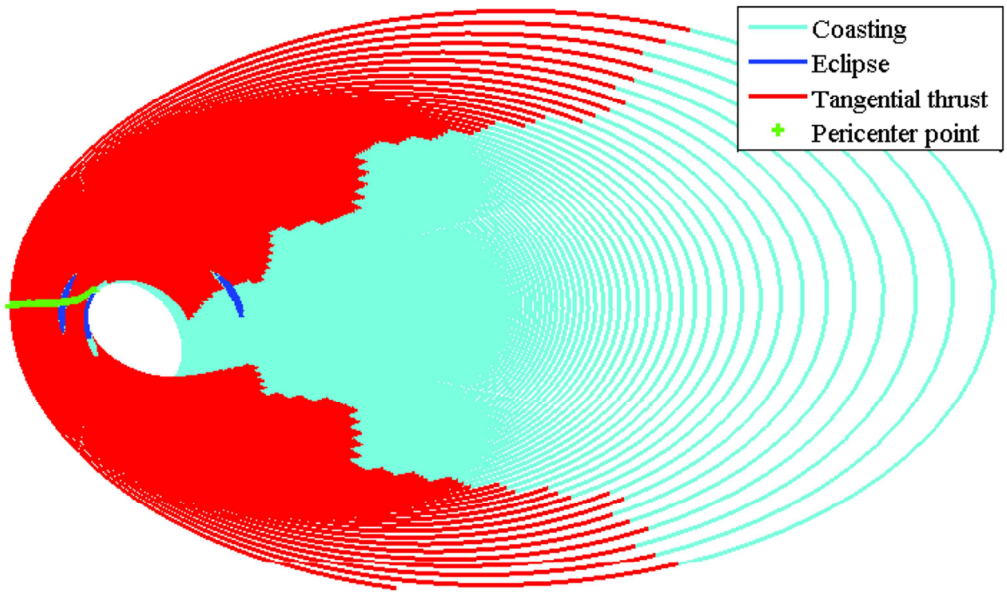

Figure 7.9. Minimum *IES* solution: trajectory.

The control strategy of the third case, as shown in Figure 7.10a, is a mix of the first two. In the first part, the thrust is continuous in order to raise the perigee above the radiation belt as soon as possible. After this has been achieved, at around 250 days, the length of the thrusting arcs is radically reduced in order to save propellant by concentrating on raising the apogee while keeping the perigee almost constant (see Figure 7.10b).

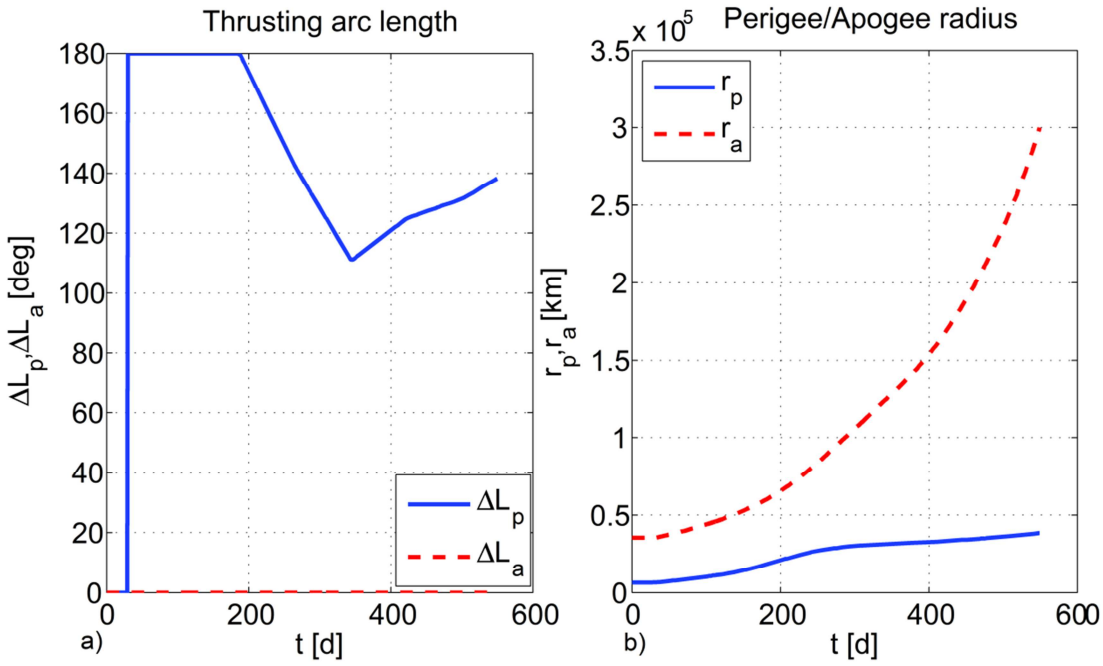

Figure 7.10. Minimum t_{belt}, maximum *ToF* solution: a) thrusting arc length; b) perigee/apogee radii.

Figure 7.11 shows a view of the complete trajectory and clearly reveals the uninterrupted thrusting strategy in the initial part of the trajectory, followed by a phase with long coasting arcs around apocenter which lead to a gradual increase of the eccentricity, which is however lower than in the previous case.

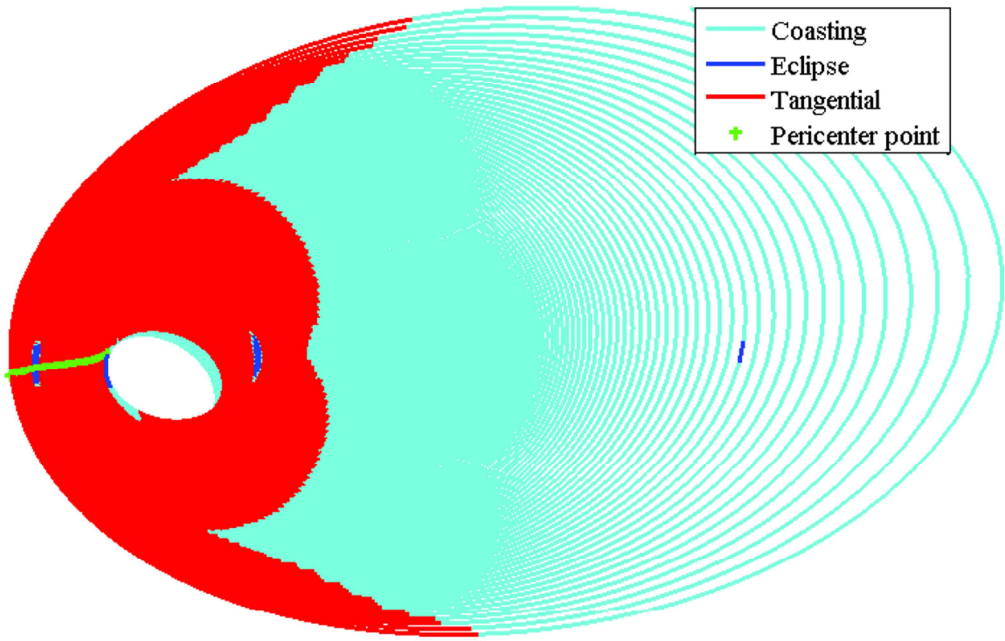

Figure 7.11. Minimum t_{belt}, maximum *ToF* solution: trajectory.

7.4.2 4-Objective Problem

For the 4-objective case, MACS2 is run for a total of $6 \cdot 10^5$ function evaluations.

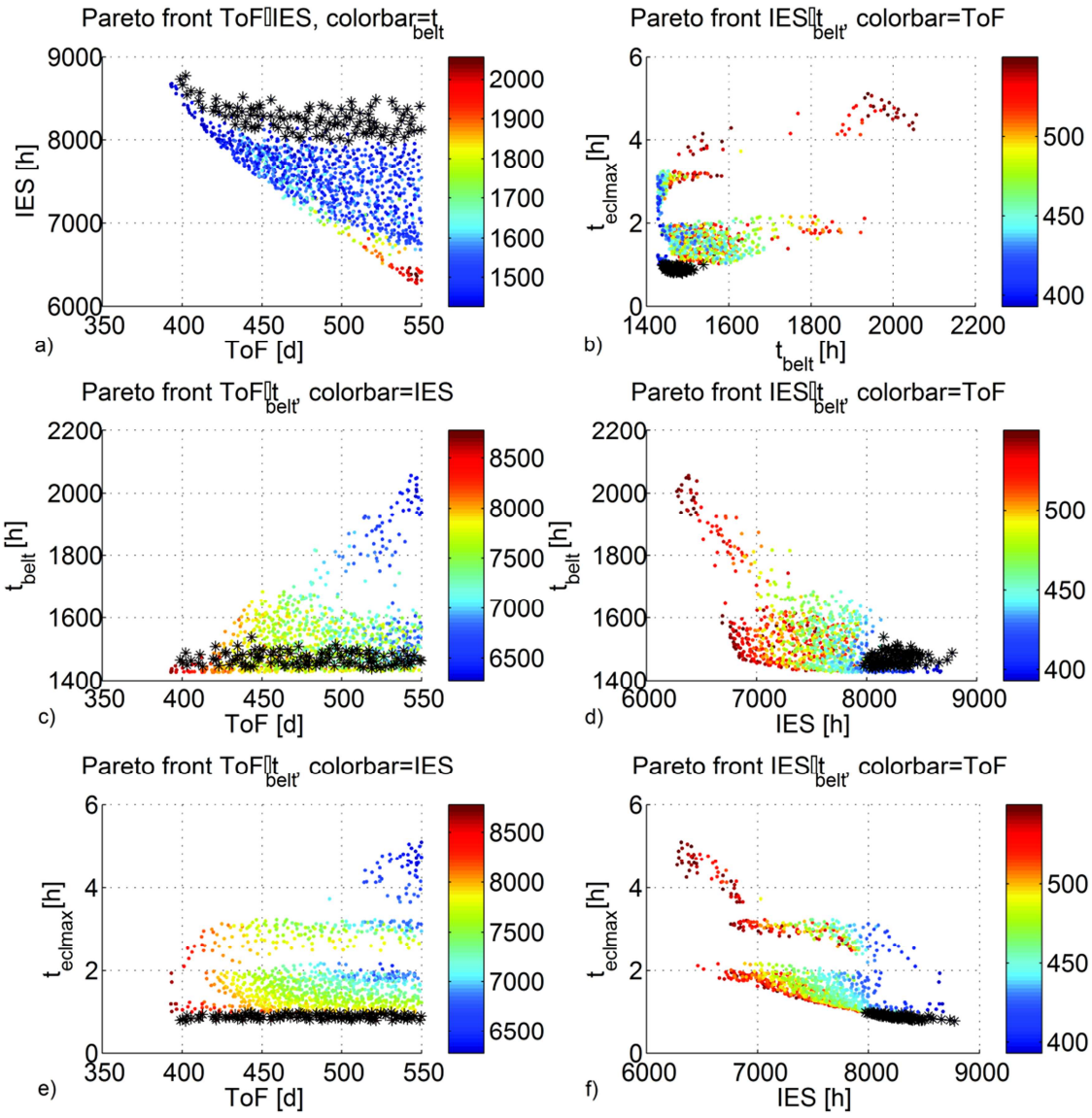

Figure 7.12. 4-Objective problem: Projections of the 4-dimensional Pareto set on the a) *ToF-IES* b) t_{belt}-$t_{ecl,max}$ c) *ToF*-t_{belt} d) *IES*-t_{belt} e) *ToF*-$t_{ecl,max}$ f) *IES*-$t_{ecl,max}$ sub-spaces. Black asterisks denote solutions with $t_{ecl,max} \leq 1$ h.

Figure 7.12 shows the set of the Pareto-optimal solutions, projected onto each of the bi-dimensional sub-spaces. Black asterisks denote the solutions which have the longest eclipse below 1 hour. In this respect, it is immediately apparent that there is no feasible solution with *IES* below 8000 hours (see Figure 7.12a). Similarly, from Figure 7.12b one can see that all these solutions have t_{belt} which is 1600 hours at most. This suggests that, in this case, solutions with a fast initial orbit raising phase are optimal for avoiding eclipses.

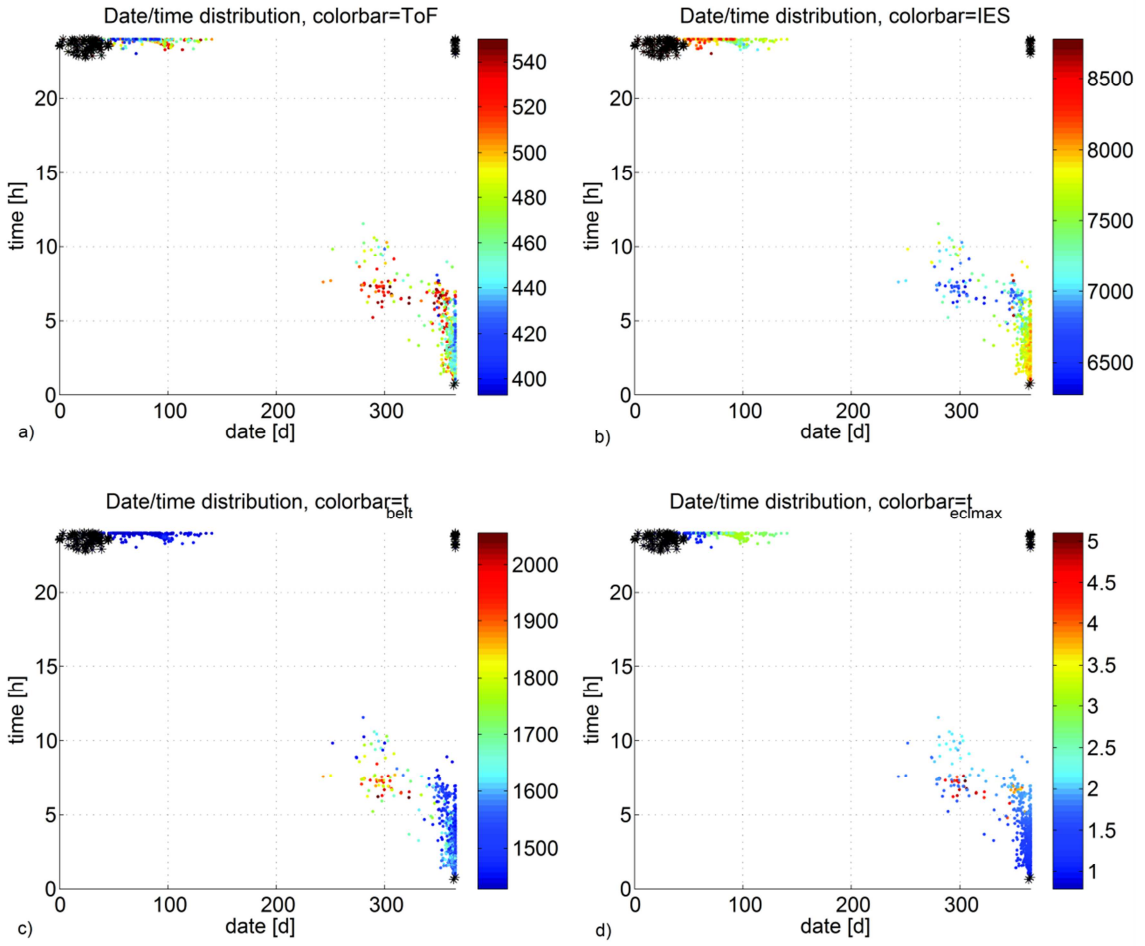

Figure 7.13. 4-Objective problem: distribution of the optimal solutions w.r.t. the departure date: a) *ToF* b) *IES* c) t_{belt} d) $t_{ecl,max}$. Black asterisks denote solutions with $t_{ecl,max}$≤1 h.

Figure 7.13 shows the distribution of the optimal solutions with respect to departure date and departure time. Generally speaking, their distribution is similar to that of the 3-objective case shown in Figure 7.5, as they are roughly aligned along a diagonal line. Solutions with a feasible eclipse, however, are restricted to a very small region around 24/0 h and 365/0 days, at the corners in Figure 7.13 (Note that, due to the annual periodicity of the Earth system, the regions at the four corners of the *date*/*time* plot, are by all practical means contiguous). This clearly shows that the introduction of the upper boundary on the maximum eclipse time is considerably limiting the launch opportunities and their performance, at least under the control model adopted. At the same time, however, it is important to consider that the solution of the Multi-Objective optimisation problem as formulated in (7.4) will return only the globally optimal solutions. This means that feasible, although inferior, solutions might still exist for other departure dates but, since they are dominated by other solutions, they are discarded during the optimisation process. On the other hand, at the preliminary design stage, it is desirable to investigate the existence of feasible solutions in less optimal regions of the launch window as well. This could also provide a good database of back-up solutions, should the optimal period for departure, as

shown in Figure 7.13, become infeasible due to other factors. A simple way to perform this kind of analysis would be to partition the parameter space (see Table 7.3) in a number of subsets along the *date* coordinate, and run separate Multi-Objective optimisation instances in each of them. However, this would require as many optimisation instances as the partitions of the domain *D* and at the same time, the fact that they would run separately would prevent an exchange of information between each of them. Therefore, the following alternative has been adopted, which requires only a single MO instance, and which consists in modifying the 4-Objective problem in (7.4) by adding two *dummy* performance parameters to **f**, as:

$$\mathbf{f} = \left[ToF \quad IES \quad t_{belt} \quad t_{ecl,max} \quad \frac{date}{365} \quad 1 - \frac{date}{365} \right] + \mathbf{w}\Delta r_{fin} \tag{7.8}$$

This modification makes such that a solution, even if it is inferior to another with regard to *ToF*, *IES*, t_{belt} or $t_{ecl,max}$, is still not discarded by the optimisation algorithm as long as its departure date is different from the other. Or, in other words, the optimiser will automatically search for and store the optimal solutions, in terms of *ToF*, *IES*, t_{belt} or $t_{ecl,max}$, *for each departure date*. This modified 4-objective problem, formally a 6-objective one, is again solved with MACS2, with 10^6 function evaluations.

Figure 7.14 shows the distribution of optimal solutions with maximum eclipse duration shorter than 1 hour and reveals the existence of two new clusters of solutions in addition to those already identified in the previous, 4-objective case. One lies in the summer period close to midnight time while the other is in autumn in the 15-20 h range. Although they differ slightly in terms of performance parameters, a number of considerations apply to both groups. First, they both have a higher time of flight than the winter/midnight class, ranging from 480 to 550 days. At the same time, their propellant cost is also quite high, as is t_{belt}, which is between 2000 and 2600 hours. As an example, Table 7.5 reports the relevant parameters for a typical solution in this group, which can be compared to those in Table 7.4. Figure 7.15 plots its thrusting arc length and time history of perigee and apogee radii.

Table 7.5. Sample solution in Summer with feasible eclipse.

date (d)	*time* (h)	*ToF* (d)	*IES* (h)	t_{belt} (h)	$t_{ecl,max}$ (h)
198	23.3	498	8581	2140	0.92

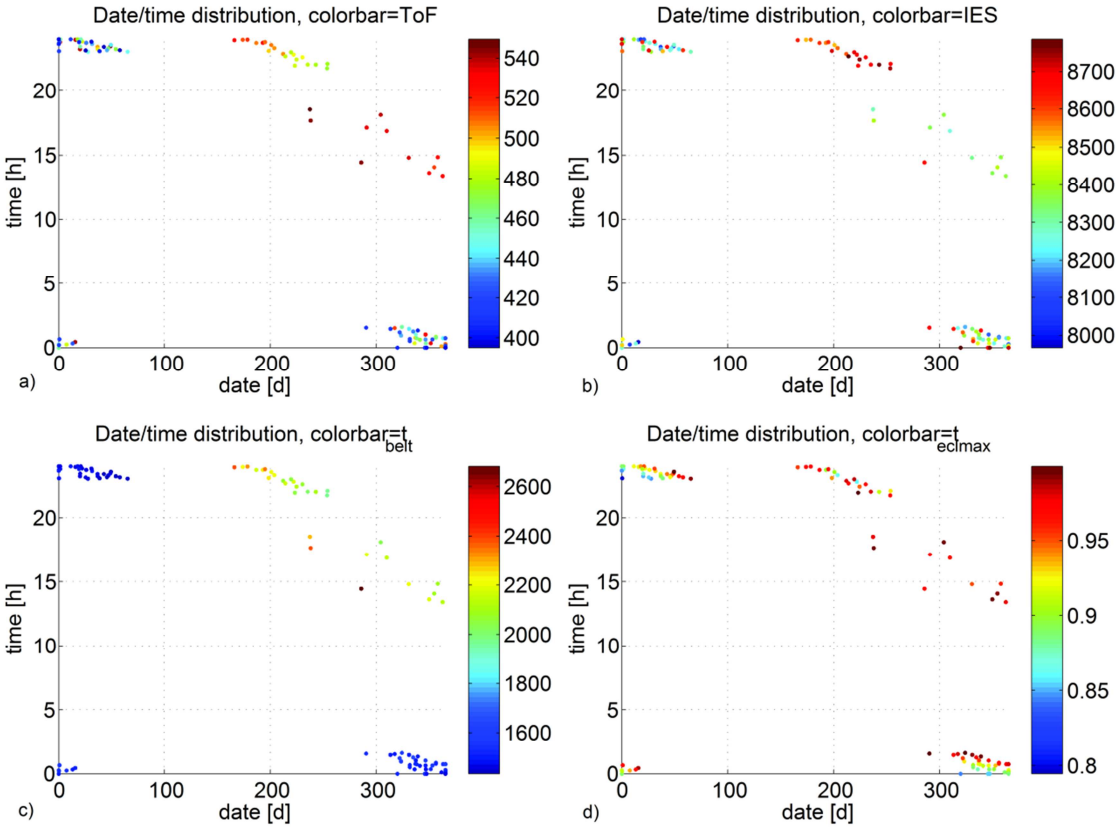

Figure 7.14. Modified 4-Objective problem: distribution of the optimal solutions with $t_{ecl,max}$≤1 h w.r.t. the departure date: a) *ToF* b) *IES* c) t_{belt} d) $t_{ecl,max}$.

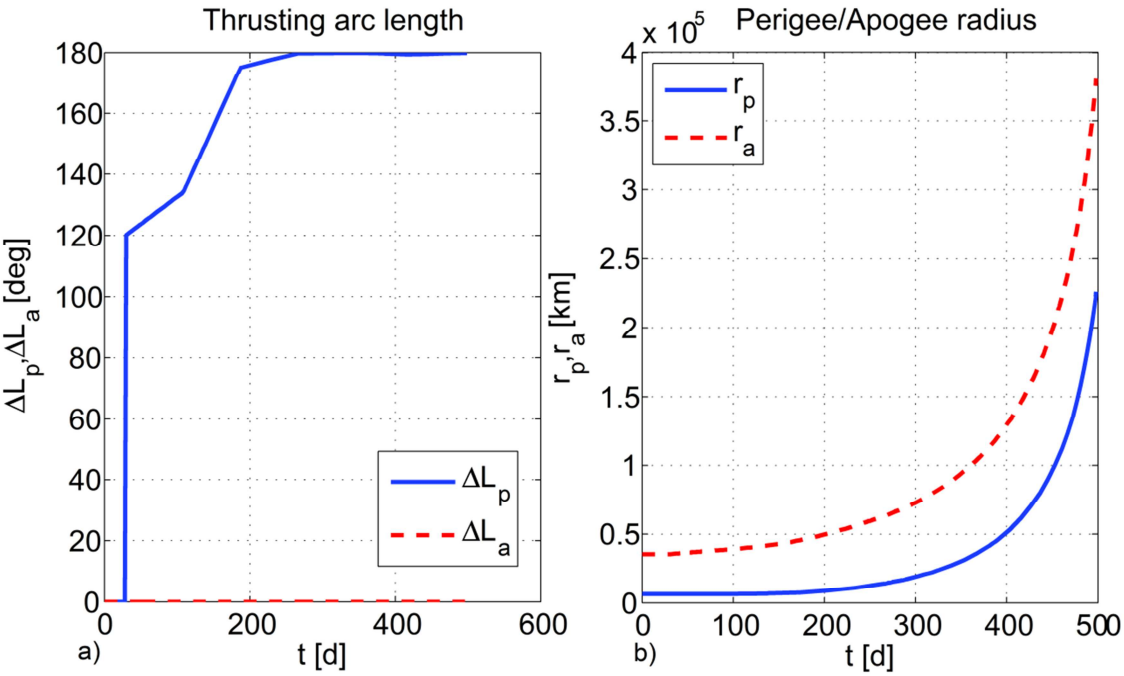

Figure 7.15. Summer solution with feasible eclipse: a) thrusting arc length; b) perigee/apogee radii.

As Figure 7.15a shows, at the beginning, the thrusting arcs are located around perigee with a semi-amplitude of 120 degrees, which then progressively increases to 180 degrees (i.e. continuous thrust) at 250 days. This might seem quite odd at first since it has the

obvious drawback of increasing both the total transfer time and the exposure to the environment of the radiation belts, as testified by Table 7.5. Moreover, the relative geometry between the spacecraft's orbit and the lunar one is far from optimal because, as can be seen in Figure 7.15b, the final apogee is well above 300000km, which means that the intersection with the lunar orbit plane is far from the line of apses. On the other hand, it is important to keep in mind that the driving factor for which this candidate solution has been selected is its low maximum eclipse duration. In this sense, the control profile is meant at altering the geometry relative geometry between DESTINY's orbit and the shadow region in order to minimise eclipse duration. While a more detailed discussion of the specific issues of eclipses during DESTINY's orbit raising and related avoidance techniques will be the topic of a future work, it is still important to introduce here a number of observations. First, one has to consider that, due to the relatively high inclination of DESTINY's orbit with respect to the Ecliptic, and due to the periodicity of the apparent motion of the Sun around the Earth, the shadow region will intersect the orbit plane at more or less regular intervals. Therefore, eclipses are typically encountered in a number of separate phases. In other words, there will be parts of the transfer in which there is one eclipse per orbit, separated by phases in which there are no eclipses at all.

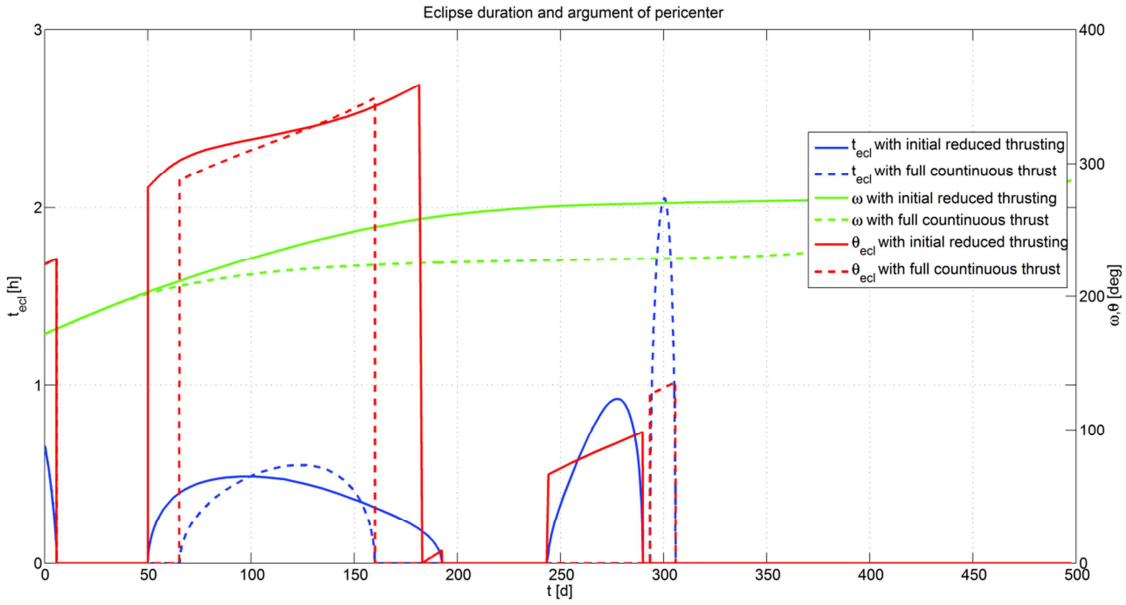

Figure 7.16. Eclipse duration, argument of pericenter and true anomaly of shadow region for two sample solutions.

A visualisation of this can be found in Figure 7.16, which shows the time history of three important quantities: the duration of each single eclipse t_{ecl} (blue line), the argument of perigee ω in the ecliptic reference frame (green line) and finally the true anomaly of the axis of the shadow region θ_{ecl} on the orbit plane (red line). The continuous line refers to the case of the solution in Table 7.5, while the dashed line refers to a trajectory with same

departure epoch as the previous one, but with a simple continuous thrust profile as the one shown in Figure 7.6. As mentioned before, one can recognise three different eclipse phases: a very short one during the commissioning phase, a relatively long one between 50 and 180 days and a shorter one between 240 and 290 days. In the case of the trajectory with reduced thrusting, in none of these three phases the duration of a single eclipse exceeds one hour, making this a feasible trajectory. On the contrary, for the continuous thrust case, in the third sequence of eclipses there is a peak of 2 hours duration. One can seek an explanation for this fundamental difference by examining the time history of θ_{ecl} (the true anomaly of the axis of the shadow region) in each case. Given the eccentricity of DESTINY's orbit, this parameter becomes very important since, the closer to the apocenter the shadow region is, the longer is the time the spacecraft will need to cross it. In the first case, θ_{ecl} is around 90 degrees, which means that the shadow region lies much closer to the pericenter than the apocenter. In the second case, θ_{ecl} is around 130 degrees, i.e. closer to the apocenter and this is the main reason for which eclipses are longer in this case. The cause for the different position of the shadow in the two cases is found if one checks the behaviour of the argument of pericenter: in both cases there is an asymptotic increase of ω with time. However, in the cases with full continuous thrust the transient phase ends earlier and the total variation of ω is some 40 degrees smaller than in the other case, leading to the critical eclipse at 300 days. This variation of ω is essentially due to the J_2 effect. In this sense, while the continuous thrust solution experiences this perturbation for less since it raises the orbit very quickly, the solution with initial reduced thrust spends more time in proximity of the Earth and therefore the J_2 effect acts for longer and leads to a larger rotation of the line of apses. As a side note, note also that, in this case, the second eclipse phase lasts longer and the third one is encountered at an earlier date than in the continuous thrust case. Without entering into too much detail, this is due to the fact the rotation of the line of nodes of the orbit is different in the two cases, again due to the different action of the J_2 perturbation.

In summary, it can be said that this solution is exploiting the J_2 perturbation to passively rotate the line of apses and obtain a favourable relative geometry with the shadow region in order to avoid long eclipses. In order to obtain this, of course, it sacrifices time of flight and transit time in the radiation belt and consequently it is not a globally optimal transfer but nevertheless it constitutes a feasible alternative if a departure date in seasons other than winter becomes imperative.

7.5 Strategies for Eclipse Avoidance

Preliminary results presented in the previous section suggested that a more detailed analysis of the eclipses encountered during the transfer is needed. First, the temporal sequence of the eclipses has been analysed, as shown in Figure 7.17a for a typical trajectory. Figure 7.17b shows the time evolution of the period of the osculating orbit.

One can clearly identify three different uninterrupted sequences of eclipses, one per orbit. The first usually occurs after launch (~0-100 days), when the orbit is very small and consequently its period is also short (~8-12 hours). The second phase usually occurs in the 150-280 days range and in this case the orbital period is typically between 18 and 54 hours. Note also that in this phase the spacecraft is passing through the radiation belts. The third phase occurs between 300 and 460 days and at this point the orbital period is in the range of a few days and can be of the same order of magnitude of the duration of the orbit plane's crossing of the Earth's shadow. In the latter case this translates into the fact that there are one or two consecutive eclipses at most, as one can see for example in Figure 7.17a. Note also that, due to the apparent motion of the Sun around the Earth, the orbit plane crosses the shadow cone once every six months, although in the early phase of the transfer this interval is somewhat shorter due to the plane's rotation caused by J_2 perturbation.

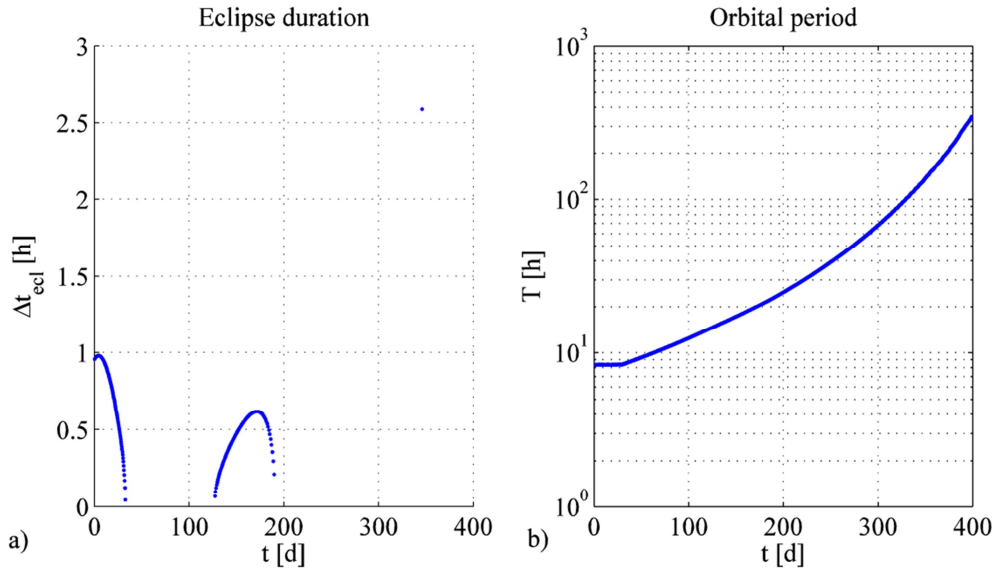

Figure 7.17. a) Eclipse duration. b) Orbital period.

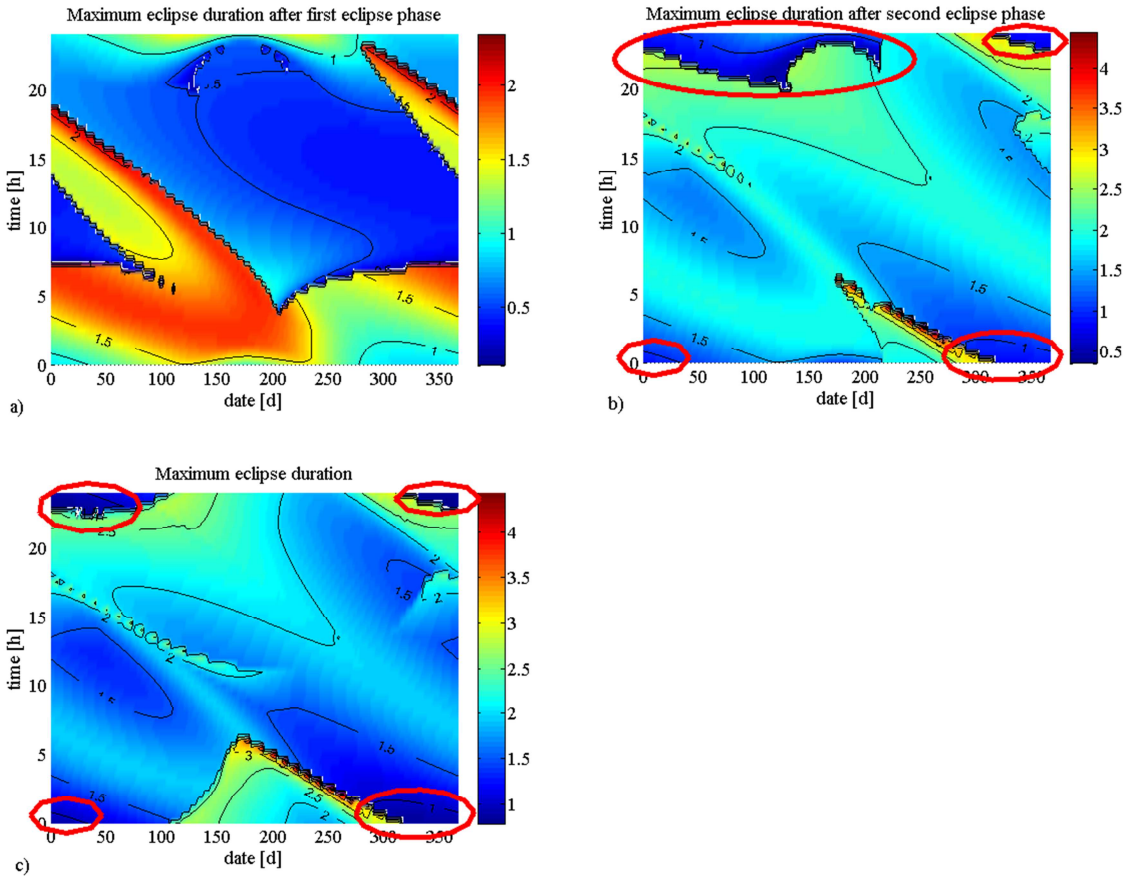

Figure 7.18. Maximum eclipse duration after: a) first b) second c) third eclipse phase.

If, in any one of these phase, a single eclipse exceeds one hour duration, then the entire transfer becomes infeasible. To visualise how this gradually restricts the transfer opportunities, let one compute the duration of the first three eclipse phases, for a with continuous tangential thrust, for different departure dates and times. As Figure 7.18 shows, after each eclipse phase, the feasible regions in the date-time space are progressively reduced down to the winter/midnight range as already seen in the Multi-objective optimisation results presented in the previous sections.

In order to formulate specific control strategies in order to avoid long eclipse it is also essential to understand which are the quantities determining its length and, among them, which can be effectively and easily controlled. Without entering into too much detail, the geometrical quantities which determine the duration of the eclipse are:

- Orbit size and shape, i.e. semi-major axis a and eccentricity e .
- Relative angle between the Sun-Earth direction and DESTINY's orbit plane, i.e. current date and Keplerian parameters inclination i and right ascension of the ascending node Ω.
- in-plane angle between the line of apses and the projection of the Sun-Earth direction, i.e. ω.

Introducing specific strategies to control a and e might be problematic since their time history is already driven by the main design objective, i.e. encountering the Moon within

1.5 years from departure. Controlling i and Ω would require a considerable, out-of-plane, acceleration component, which is inherently expensive even in the case of orbit plane rotations of a few degrees. On the other hand, it might be possible to exert some control on the argument of perigee at a reasonable cost. In order to have a clearer idea on whether this is possible, a graph is created in order to visualise the values of ω which give a feasible eclipse duration for each instant in the time history of a certain transfer. This ω-eclipse plot is created by taking the time history of the Keplerian parameters of a trajectory of interest, obtained obviously by numerical propagation. For each time instant, consider all Keplerian parameters except ω as fixed. Then for values of ω between 0 and 2π, compute the eclipse duration according to the analytical method described in Section 5.1.1. An example of the resulting graph is reported in Figure 7.19, for a trajectory departing on 9 September.

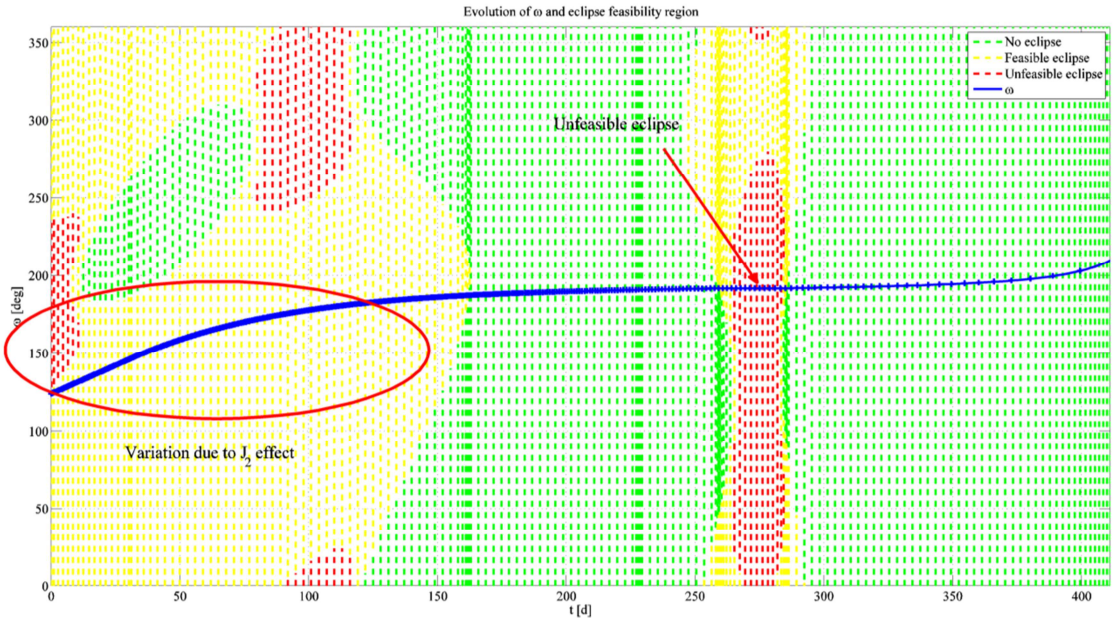

Figure 7.19. ω-eclipse plot for an infeasible trajectory departing on 2018/9/9.

The green regions denote values of ω for which there would be no eclipse; the yellow regions denote values of ω which would give eclipses with duration below 1 hour; finally the red regions indicate values of ω giving infeasible eclipse durations. The blue line is the time history of the argument of perigee of the nominal trajectory, and it can be clearly seen that this transfer encounters a number of infeasible eclipse between 250 and 300 days. Also, one can also see the initial change in ω during the first 100-150 days due to the strong J_2 effect when the spacecraft is in close proximity to the Earth. It is important to remark that these regions have been defined by considering the time history of the other Keplerian parameters as fixed and is therefore subject to change somewhat if the control strategy is modified. However, it already suggests that, if it feasible to alter the argument of perigee by such an amount that it avoids the red regions, then this trajectory can be made feasible.

In order to do this, two different strategies are proposed: a passive ω-control, which exploits J_2 perturbation to change ω, as already suggested by the new solution found in the previous section; an active ω-control, which adopts a thrusting strategy aimed specifically at changing the argument of perigee.

7.5.1 Passive ω-control

Considering the infeasible trajectory shown in the previous section, its continuous tangential thrust profile is altered such that during the first 50 days after end of commissioning phase, thrusting is performed only around pericenter, as shown in Figure 7.20.

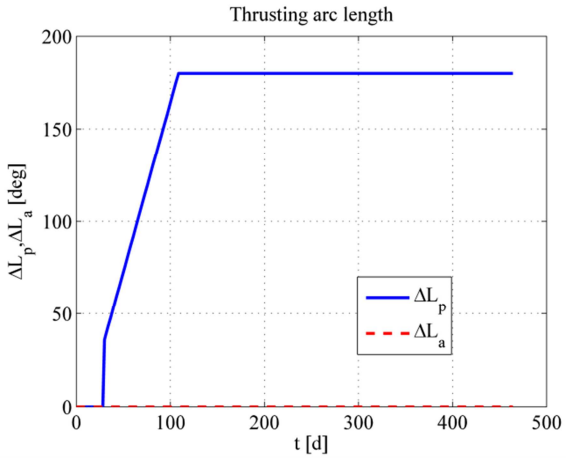

Figure 7.20. Thrusting arc amplitude for passive ω-control.

The ω-eclipse plot consequently takes the form shown in Figure 7.21, where one notes how the initial, reduce thrust phase makes such that more time is spent under the J_2 effect so that the alteration in the argument of perigee is sufficient in avoiding the potentially long eclipse encountered at 250 days.

Note also that, given the longer duration of this transfer, another eclipse phase appears towards the end. However, note that, the orbital period (represented by thick marks on the blue line) appears to be larger than the width of the red band, which translates into the fact that in this case one can have a single, isolated eclipse at most, as mentioned in the previous section. Specific strategies to deal with this single eclipse will be treated in a later section. The obvious drawback of this control strategy is that more time is spent within the radiation belts, since in order to exploit the J_2 effect, the spacecraft has to be relatively close to the Earth.

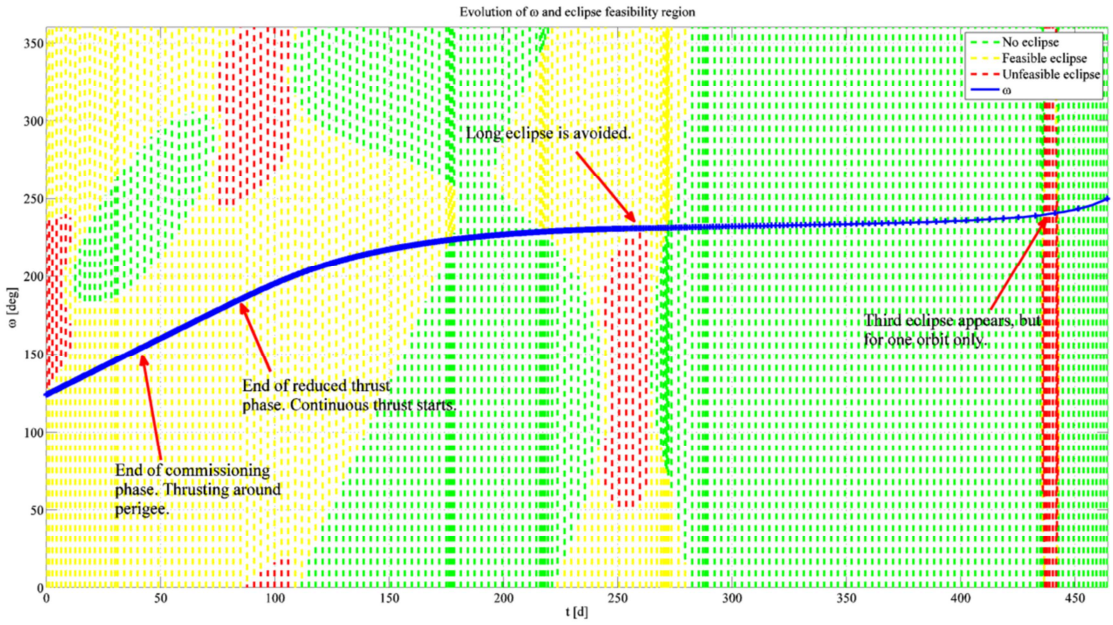

Figure 7.21. ω-eclipse plot with passive ω-control strategy (Trajectory departing on 2018/9/9).

7.5.2 Active ω-control

In order to change the argument of perigee by means of the engine thrust, the tangential thrust control used until now is replaced by a control law which maximises the instantaneous rate of change of ω. Considering Gauss' differential equations for this parameter[98], with in-plane thrust acceleration:

$$\frac{d\omega}{dt}=\frac{\sqrt{a\left(1-e^2\right)}}{e\sqrt{\mu}}\left[-\cos\theta\varepsilon\cos\alpha+\frac{2+e\cos\theta}{1+e\cos\theta}\sin\theta\varepsilon\sin\alpha\right] \tag{7.9}$$

where ε is the modulus of the acceleration and α is its azimuth in the r-θ-h reference frame. Imposing stationariety of (7.9) with respect to α, one obtains:

$$\frac{d}{d\alpha}\frac{d\omega}{dt}=0\Leftrightarrow\cos\theta\left(1+e\cos\theta\right)\sin\alpha+\sin\theta\left(2+e\cos\theta\right)\cos\alpha=0 \tag{7.10}$$

And thus the control law for α in order to maximise/minimise the variation of ω is:

$$\alpha=\tan^{-1}\left(-\tan\theta\frac{2+e\cos\theta}{1+e\cos\theta}\right)+k\pi$$

$$\text{minimum: }\begin{cases}k=0,-\dfrac{\pi}{2}\le\theta\le\dfrac{\pi}{2}\\ k=1,\dfrac{\pi}{2}\le\theta\le\dfrac{3\pi}{2}\end{cases}\quad\text{maximum: }\begin{cases}k=1,-\dfrac{\pi}{2}\le\theta\le\dfrac{\pi}{2}\\ k=0,\dfrac{\pi}{2}\le\theta\le\dfrac{3\pi}{2}\end{cases} \tag{7.11}$$

In order to correct the infeasible trajectory seen in the previous section, this control law replaces the standard tangential acceleration in a phase lasting between 200 and 280 days. In this phase, the control acts exclusively to change the argument of perigee and there is little or no variation of the other orbital elements. This active change in ω can be easily

recognised in Figure 7.22. In this case too, there is a further eclipse phase appearing at the end of the transfer, and similar considerations apply as for the passive ω-control. Note also that, in this case the additional time spent within the radiation belt is likely to be much lower than with previous case, since the ω correction phase starts at 200 when the spacecraft is almost of the belt. On the other hand, however, propellant consumption is likely to be much higher since the ω-control phase does not contribute to raising the orbit energy and therefore is "wasted" from this point of view. Table 7.6 presents a comparison of the performance figures for the two different strategies. In both cases, the time of flight is around 70 days longer than a nominal, full thrust, case. Regarding propellant cost, the passive case even slightly cheaper than the full thrust case, since concentrating the thrusting arcs at perigee in the early phase is more efficient than thrusting along the entire orbit. On the other hand, the increase in time spent within the radiation belt is quite substantial, reaching 2000 hours. Opposite considerations apply to the active case, which has a high engine operation time of 10600 hours but a relatively low radiation belt time of 1700 hours.

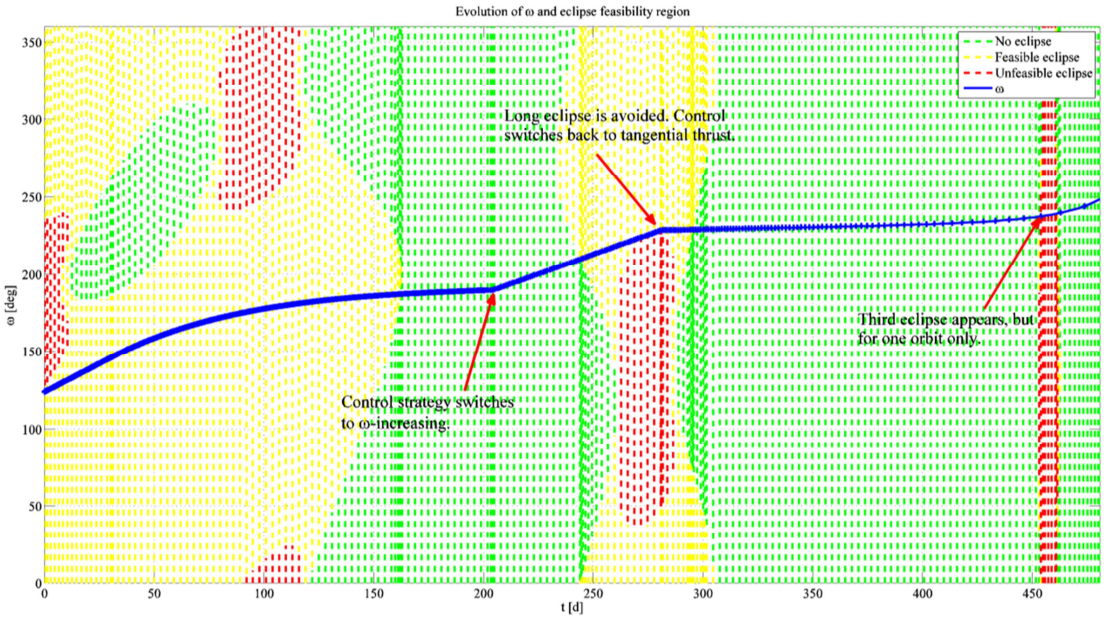

Figure 7.22. ω-eclipse plot with active ω-control strategy (Trajectory departing on 2018/9/9).

Table 7.6. Comparison of ω-control strategies

Case	*ToF* (d)	*IES* (h)	t_{belt} (h)	$t_{ecl,max}$ (h)
Nominal (infeasible)	411	8982	1505	1.70
Passive	484	8849	2001	0.99
Active	481	10633	1711	0.99

7.5.3 Avoidance of Isolated Eclipses

As previously mentioned, it has been chosen to neglect isolated eclipses because it had been assumed that by properly re-phasing the orbit before they happened, it would be possible to avoid them altogether. In order to verify the validity of his claim, let one take the transfer corrected with passive ω-control, as shown in the previous section. First, it is necessary to re-propagate the trajectory in the full dynamical model, in order to ascertain whether the final, isolated eclipse forecasted by the averaged propagator actually occurs or not. As Figure 7.23 shows, there is actually an isolated eclipse of 1.70 hours. A simple way of re-phasing the orbit such that this eclipse is avoided consists in introducing a short coasting arc some time before the eclipse is to be encountered. In this case it is chosen to insert it right after the second phase of eclipses is over, i.e. around 280 days. Figure 7.24 shows the variation of the eclipse duration as a function of the coasting arc duration. One can see that, by inserting a coasting arc of duration between 1.35 and 1.85 days, a proper phasing is obtained such that the duration of the single eclipse is reduced below 1 hour and possibly even avoided altogether.

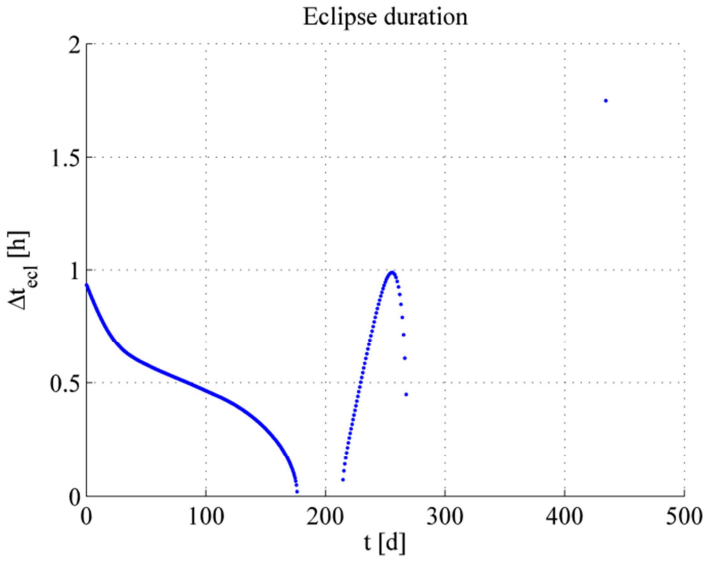

Figure 7.23. Eclipse duration for trajectory departing on 9/9/2018 with passive ω-control strategy.

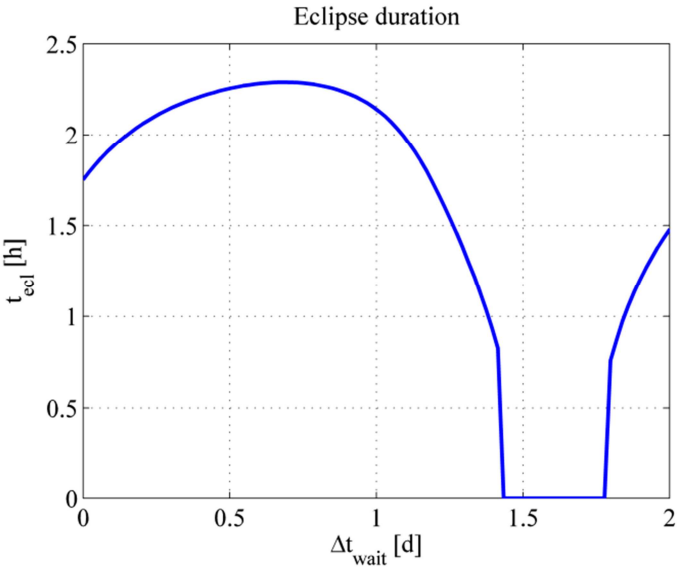

Figure 7.24. Duration of the final isolated eclipse as a function of coasting arc duration.

7.5.4 Final Remarks on Eclipse Avoidance

The results presented in the previous sections provide a good basis for some general guidelines for an integrated strategy for eclipse avoidance. The proposed strategy relies on the combination of three different techniques to avoid the eclipses in different phases of the transfer. In particular:

1. For sequences of eclipses occurring in the early part of the transfer, successful avoidance of long duration can be obtained by adjusting the initial conditions, i.e. launch date and time, in order to obtain favourable orbit geometry with respect to the shadow region and its short term evolution. This proper choice of departure epoch appears the only viable choice for this early phase since it is not possible to introduce any active control, since this would need to begin much in advance before the projected critical eclipse, and adding to this there is the 30-day commissioning phase in which no thrusting is allowed.
2. For the eclipses occurring in the middle part of the transfer, eclipse duration mitigation can be achieved both by proper setting of the initial conditions or, should this not be feasible, by controlling the evolution of the argument of perigee ω. This can be achieved either by exploiting the J_2 perturbation (spending more time in the Earth's proximity) or by using the engine thrust to rotate the line of apses.

The avoidance of eclipses in the last part of the transfer can be achieved by simple phasing adjustments if the duration of the crossing between the orbit plane and the Earth's shadow is shorter than the current orbital period.

7.6 Multi-Objective Optimisation with Extended Control Model

The model used in the Multi-Objective optimisation is thus modified and extended in order to introduce the possibility of controlling the argument of perigee. This is achieved by introducing two different sets of parameters:

- a first set, in order to model a phase of the transfer in which only active, ω-controlling thrust, is used. The parameters used are the start time $t_{0,\omega}$ and its duration Δt_{ω}.
- a second set, which control the asymmetry of the thrusting arc with respect to the line of apses. As described in Section 5.1, nominally the thrusting arcs are symmetrical around the line of apsis. Here, an offset angle η is introduced, in order to allow for arcs which might be asymmetrically arranged with respect to the line of apses, as shown in Figure 7.25. The effect of having an asymmetric arc is that of producing a rotation of the line of apses and therefore a change in the argument of perigee. As has been done for ΔL_a and ΔL_p, this parameter too is defined as a piecewise linear interpolation in time with respect to 8 reference nodes.

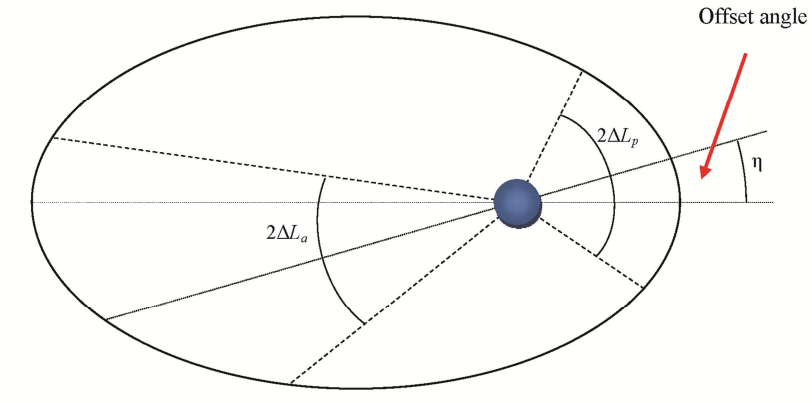

Figure 7.25. Transfer pattern with offset angle.

Now the model includes a total of 20 optimisation parameters and MACS is run with 106 function evaluations.

Figure 7.26 shows the optimal solutions which have both $t_{ecl,max}$ below 1 hour and t_{belt} below 2000 hours. While the distribution of the solutions is not dissimilar to Figure 7.14, there are a number of differences which must be noted. A first remark is for the lower boundaries for the feasible solution. Regarding the results shown in Section 7.4.2 it was commented that there was no feasible solution (eclipse-wise) with a *IES* time below 8000 hours. However, analysis of the new results showed that the threshold has been lowered to slightly less than 7900 hours. Further inspection of the solution showed that this particular class of solutions was adding a slight offset angle at the end of the transfer. The second remark is that the quantity and quality of the solutions in the summer range has improved considerably. If one compares Figure 7.26c (or Figure 7.27c) with Figure 7.14c it is possible to see that, while in the latter hardly any solution had a t_{belt} below 2000 hours, in the former there is a wide range of solutions with this feature. Some of them even have a time in the radiation belt as low as 1650 hours, only marginally higher than the minimum at 1400 hours. This is achieved by exploiting the active ω-control described in the previous section. The obvious drawback is, however, that the IES cost is quite high, being in the

10000-12000 hours range. If one considers solutions with t_{belt} above 2000 hours, then the cost might be reduced below 10000 hours IES, as shown in Figure 7.27b.

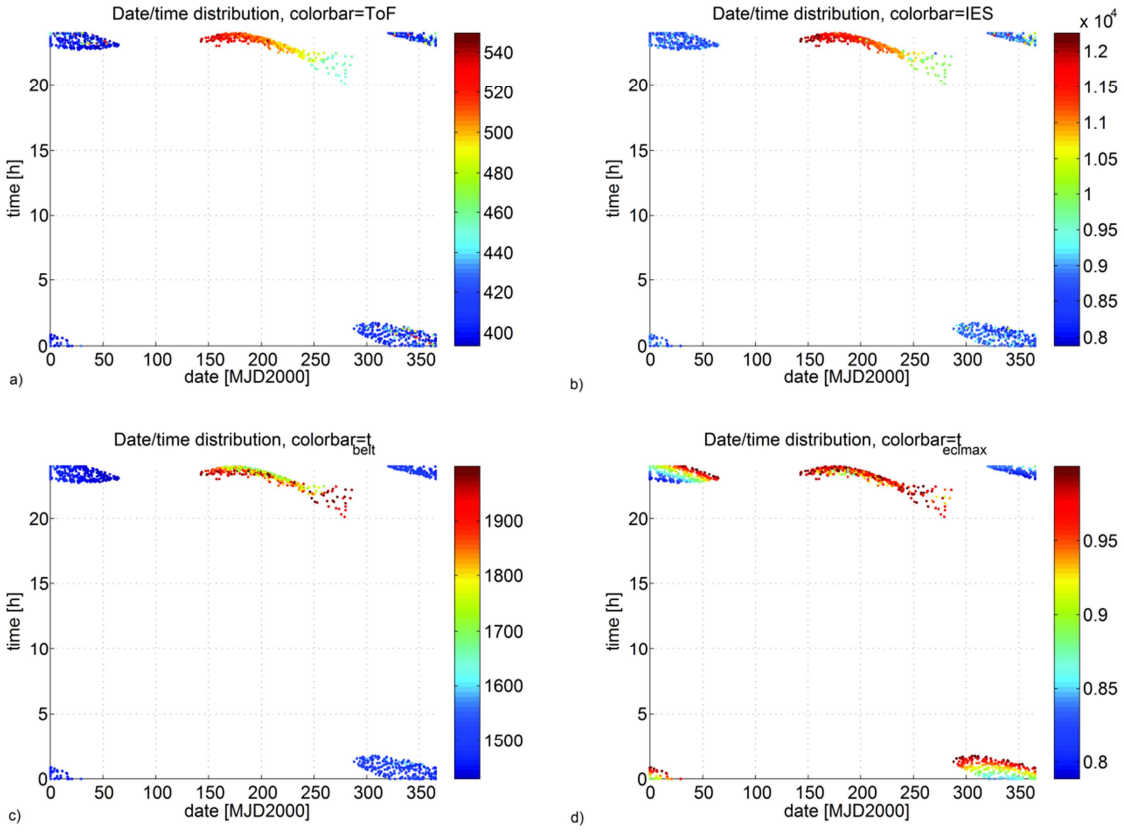

Figure 7.26. Modified 4-Objective problem with extended control model: distribution of the optimal solutions with $t_{ecl,max}$≤1 h and t_{belt}<2000 h w.r.t. the departure date: a) *ToF* b) *IES* c) t_{belt} d) $t_{ecl,max}$.

The minimum t_{belt} summer solution is very similar to the active ω-control solution shown in Section 7.5.2, while the minimum *IES* one resembles the passive one of Section 7.5.1 and therefore they will not be reported here. The minimum time of flight case, however, is quite interesting, since it combines features of both. This solution has a 55-day active ω-control phase right after the commissioning phase (yellow line in Figure 7.28) which has the double of effect of directly changing the argument of perigee and, since the orbit raising is somewhat slowed down, of exploiting J_2 for the same purpose. These combined effects produced the large change in ω required to avoid a long eclipse at 250 days, as shown in Figure 7.29. Again, the obvious drawbacks are a higher *IES* operation time and time in the radiation belt, although the latter is still below 2000 hours (see Table 7.7).

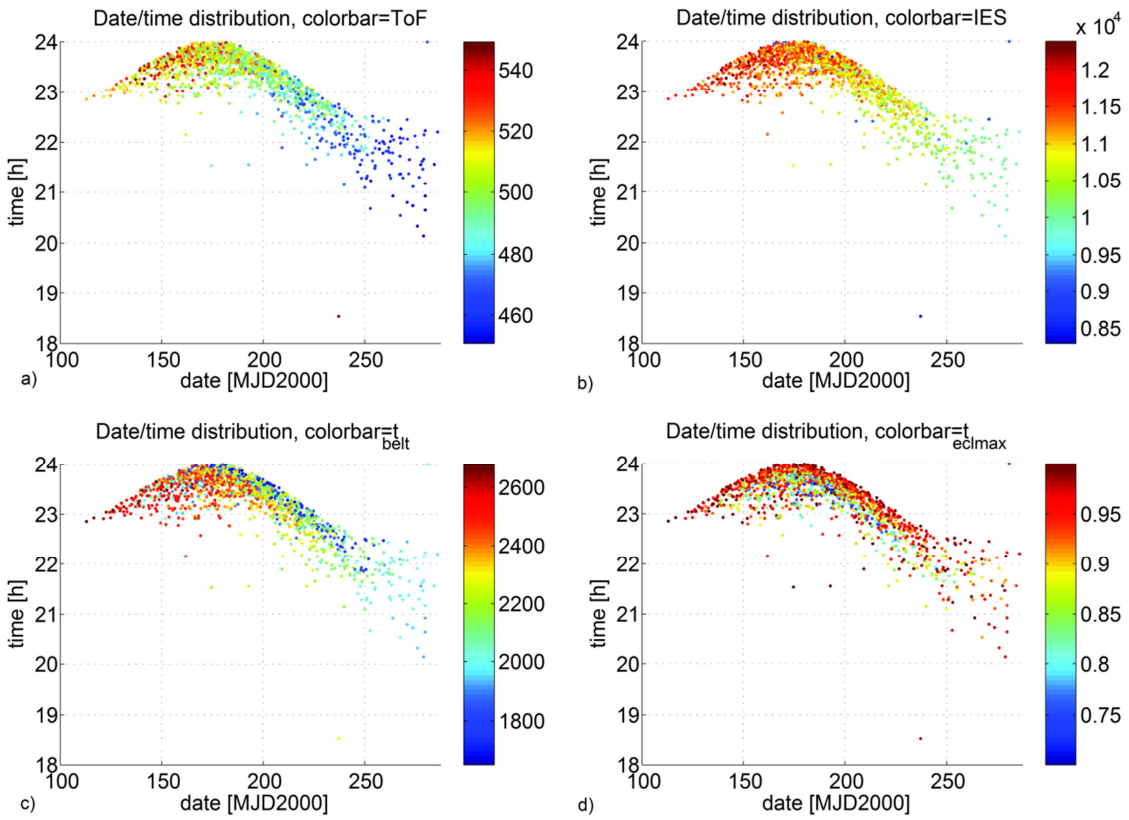

Figure 7.27. Modified 4-Objective problem with extended control model: summer solutions with $t_{ecl,max}$≤1 h w.r.t. the departure date: a) *ToF* b) *IES* c) t_{belt} d) $t_{ecl,max}$.

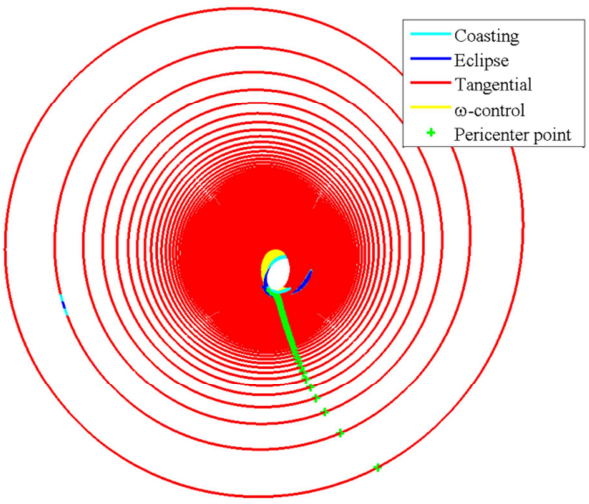

Figure 7.28. Minimum *ToF* summer solution: trajectory.

Table 7.7. Summary of summer solutions

Type	*date* (d)	*time* (h)	*ToF* (d)	*IES* (h)	t_{belt} (h)	$t_{ecl,max}$ (h)
min(*ToF*)	257	21.9	454	9971	1963	0.74
min(*IES*)	237	18.5	547	8289	2294	0.98
min(t_{belt})	190	23.8	501	11202	1658	0.99

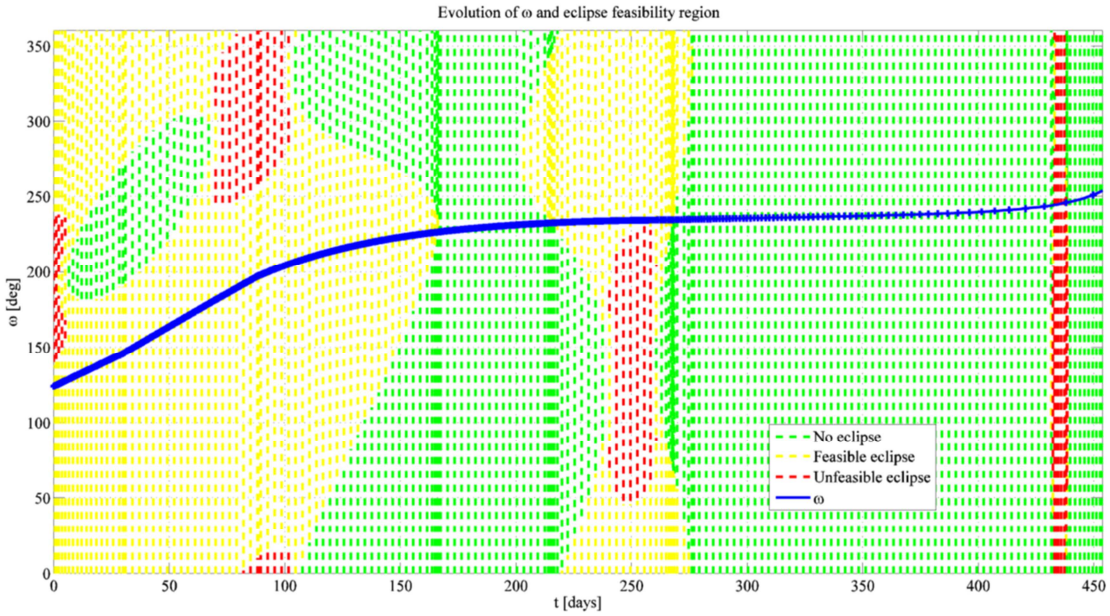

Figure 7.29. Minimum *ToF* summer solution: *ω*-eclipse plot.

7.7 Conclusions

As shown by the results presented here, the application of a Multi-Objective optimisation approach to the design of the initial orbit raising phase for DESTINY produced an extensive database of candidate transfers, widely spread over the launch window. This provided the mission analysts with a wide overview of possible transfer strategies and their inherent trade-offs. Moreover, this design campaign was extremely useful in revealing some the key challenges in designing this particular phase of the mission. Among them, there are the conflicting requirements of minimising the time spent in the radiation belt and the *IES* operation time, or similarly the trade-off between the latter and the transfer time. Most importantly, the upper limit of 1 hour on eclipse duration imposes severe restrictions on the departure epoch. Once this issue was clearly identified, specialised analysis of the eclipse dynamics provided first hints on how to tackle the problem, which were later confirmed by further Multi-Objective optimisation analyses with an extended control model. This led to establishing that the successful avoidance of the long eclipses relies on a combination of proper choice of initial conditions, exploitation of the J_2 effect and active control of the argument of perigee. The results of the Multi-Objective optimisation showed that with the implementation of these techniques it is possible to have transfer opportunities for 75% of a year's launch window. The analysis performed in this case study provides a solid basis for more detailed trajectory design in future design phases of DESTINY.

Chapter 8.Evidence-Based Robust Design of Asteroid Deflection Missions

This chapter presents a novel approach to the robust design of deflection actions for Near Earth Objects (NEO). In particular, the case of deflection by means of Solar-pumped Laser ablation is studied here in detail. The basic idea behind Laser ablation is that of inducing a sublimation of the NEO surface, which produces a low thrust, thereby slowly deviating the asteroid from its initial Earth threatening trajectory. This chapter investigates the integrated design of the Space-based Laser system and the deflection action generated by laser ablation under uncertainty. The integrated design is formulated as a Multi-Objective optimisation problem in which the deviation is maximised and the total system mass is minimised. Both the model for the estimation of the thrust produced by surface laser ablation and the spacecraft system model are assumed to be affected by epistemic uncertainties (partial or complete lack of knowledge). Evidence Theory (see the introduction in Appendix B) is used to quantify these uncertainties and introduce them in the optimisation process. An example of design of the deflection of asteroid Apophis with a swarm of spacecraft is presented.

In order to achieve a fast propagation of the NEO motion under the ablation-induced force, the *rectification* methodology described in Section 3.2.1 is employed. The MOO problem under Uncertainty is solved with a modified version of MACS2.

This chapter is organised as follows: first, some background on NEO threat and mitigation strategy will be provided; then, the mathematical models for trajectory, spacecraft system and deflection action will be introduced; after this, the uncertainties are analysed and quantified through Evidence Theory. A Multi-Objective optimisation problem is then solved to find optimal deflection solutions under uncertainty. The final section also presents an analysis of sensitivity to identify which epistemic uncertainty is the most significant in the context of asteroid deflection with laser ablation.

8.1 NEO Mitigation Strategies

During the last two decades, Near Earth Objects (NEO) have attracted considerable interest from the scientific community in general and in particular in the space field. The reasons for this are twofold: first, from a strictly scientific point of view, asteroids can provide precious data to reconstruct the genesis of the solar system. In this sense, NEOs, in

contrast to other small celestial bodies, are relatively easy to reach and explore, thanks to their small dimensions, lack of atmosphere and vicinity to the Earth. On the exploration side, there is a number of past or ongoing missions aimed at the study of small celestial bodies, such as NEAR[125], Rosetta[126], Deep Space 1[127], Hayabusa[2], Deep Impact[128] and Dawn[4,5].

The second reason instead is linked with the potential threat they represent for our planet. According to the most recent tracking data, over 1000 NEOs have been classified as potentially hazardous to the Earth, i.e. they have an Earth Minimum Orbit Intersection Distance (MOID) of 0.05 AU or less and an absolute magnitude of 22.0 or less[129]. This suggests that the danger of a catastrophic event in the mid to long term is not unrealistic. The historical perspective of past impact events (e.g. Tunguska in 1908) is an important reminder of the dire consequences this could have on our fragile ecosystem.

Therefore, the scientific community has proposed a number of mitigation strategies and techniques to counteract the hazard of a NEO impact. The first serious technical study, Project Icarus[130], dates back to 1967 but only in the 90s the theme has started to be widely explored by scientists and engineers and various strategies have been proposed. Among them we find techniques producing an impulsive change in the asteroid motion such as Nuclear blast[131] and Kinetic Impactor[132], or attached Chemical engines[133]; there are others which produce a continuous low thrust like in the case of using attached Electrical thrusters[133], or electrically propelled gravitational tugs[134], or by means of the low thrust produced by surface Ablation, the latter induced either by solar collectors[135] or laser beam[136]. Other more exotic systems include Mass Drivers[137], which involve the controlled ejection of asteroid's surface material in order to produce a series of small impulsive changes in its motion; there are proposals also for passive methods, like the idea of painting part of the asteroid to modify its optical properties and thus take advantage of the Yarkovsky effect[138].

A recent study[64] presented a quantitative comparison of different deflection methodologies that suggested that surface ablation techniques could represent an advantage compared to other methodologies.

The principle behind the surface ablation strategies is that of inducing the sublimation of the surface material of the asteroid. This will create an ejecta plume and an associate small continuous thrust. This thrust, over extended periods of time, will slowly deviate the asteroids from its initial orbit. Ablation strategies based on direct irradiation with concentrated solar light were proposed by Melosh and Nemchimov[135] who envisioned using a single large solar concentrator to irradiate a relatively small spot on the surface of

the asteroid so that the resulting heat will induce the sublimation. Other authors proposed the use of lasers in conjunction with a nuclear power source[139,140,141,142]. Extensive studies on the dynamics of the deflection with high power lasers were proposed by Park and Mazanek[142] envisaging a single spacecraft with a Micro Wave laser. The combination of solar concentrators with lasers (directly or indirectly pumped) was recently proposed by Maddock and Vasile in 2008[143]. The idea is to use a formation of smaller concentrators, each powering a solar-pumped laser. Thus, the spacecraft could be placed further from the NEOs, in this way also avoiding almost entirely the contamination due to the ejecta plume. Recent numerical and experimental analyses[144,145,143,146,147] have already investigated the basics of the solar-pumped, laser ablation concept. There are, however, some epistemic uncertainties on the physical properties of the asteroid and on some design low Technology Readiness Level (TRL) components of the spacecraft. This work addresses the impact of uncertainties on the performance of the laser system. In order to do so, an approach based on Evidence Theory is introduced[148]. This approach requires the evaluation of several deflected asteroid trajectories, and this is done here by means of the analytical propagator described in Section 3.2.1.

8.2 Trajectory and Deflection Model

In order to assess the performance of the laser ablation approach, a hypothetical asteroid based on 99942 Apophis is considered. Its orbital elements are suitably modified in order for it to intercept the Earth in 2036. The effectiveness of the deflection action is measured by the magnitude of the impact parameter *b* with respect to the Earth at the time of the expected collision, as shown in Figure 8.1, where V_∞ is the incoming velocity of the asteroid and $\mathbf{v}_E$ is the velocity of the Earth.

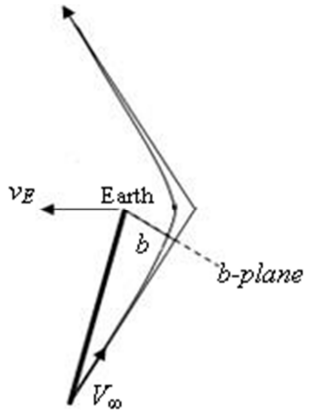

Figure 8.1 Impact parameter.

The impact parameter is computed by projecting the deviated position of the asteroid on the Earth's b-plane at the epoch of the expected impact[149]. In this case study, the undeviated orbit has b=0.

The computation of b requires the variation of the orbital elements due to the deflection action. From the variation of the orbital elements one can use the deflection formulas in[42] or the nonlinear proximal motion equations in[150] to compute the position and velocity relative to the Earth. The variation of the orbital elements is obtained here by integrating Gauss' Variational Equations in non-singular equinoctial elements (as in Eq. (3.2)), by means of the *rectification* method. Note that, as described in Section 8.4, the thrust acceleration is computed by evaluating the ablation model. In particular, the thrust magnitude shows a wide variation with a periodic pattern along the trajectory. In this sense, the ablation model needs to be evaluated quite often in order to detect this variation. The frequency of the rectification of the reference conditions for the analytical formulae therefore follows this rationale, i.e. the frequency with which the model is evaluated dictates the amplitude of the trajectory arcs. The basic idea is to have short arcs when the thrust is high and larger ones when the thrust is low. In order to achieve this, during the propagation the arc length ΔL is dynamically adjusted with the simple law:

$$\Delta L = \min\left[A\exp\left(\frac{-\log_{10}\varepsilon + \log_{10}\varepsilon_{max} + 1}{k} \right) \quad \Delta L_{max} \right] \tag{8.1}$$

where ε is the current value of the thrust acceleration, ε_{max} is the largest value it has assumed so far and A, k and ΔL_{max} are constants which were tuned empirically in order to achieve a good compromise between accuracy and CPU cost compared to the numerical integration. This was done by performing a high number of propagations of the trajectory and ablation models with different candidate sets of tuning parameters. As a result, the set which guaranteed a negligible error on the impact parameter b with respect to the numerical integration at the lowest computational cost was chosen. As an example, using the *rectification* to propagate the trajectory and ablation models implemented in Matlab® on an Intel Core Duo® 3.16 GHz machine running Windows 7® e requires between 0.2 and 2 seconds (depending on the length of the trajectory), compared with up to 30 seconds when using numerical propagation.

8.3 Spacecraft System Model

The solar-pumped laser ablation concept envisions the use of a formation of n_{sc} identical spacecraft, each provided with a solar-pumped laser system. These will be flying in the proximity of the asteroid (see Figure 8.2) with a distance from the asteroid's surface

between 1 and 4 km [151]. Note that the plume shape in Figure 8.2 is a qualitative depiction of the contamination model by Kahle et al.[152] as in Section 8.4.

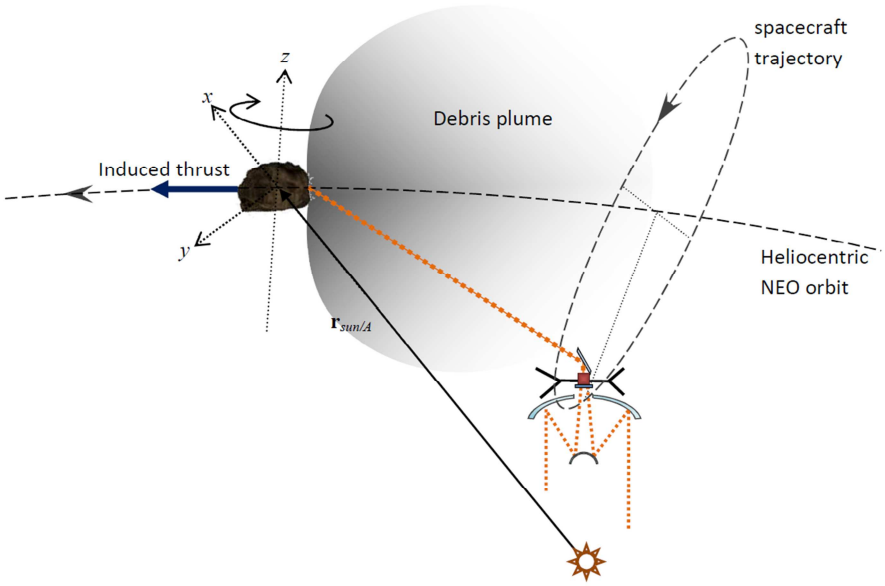

Figure 8.2 Spacecraft's proximal motion with respect to the asteroid.

Each spacecraft in the formation (see Figure 8.3) is composed of a large primary mirror M_1, which focuses the solar rays on a smaller secondary mirror M_2. The solar rays are then conveyed onto a solar array S, which powers a laser plus other subsystems. The laser beam is directed towards the NEO by means of a directional mirror M_d. A set of radiators dissipates the excess heat in order to keep the temperature of the solar array and the laser within operational limits.

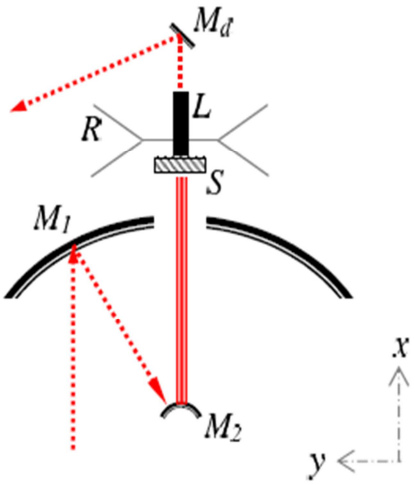

Figure 8.3 Laser spacecraft system.

The dry mass of the spacecraft is computed as:

$$m_{dry} = k_{dry}\left(m_C + m_S + m_M + m_L + m_R + m_{bus}\right) \tag{8.2}$$

where m_C is the mass of the harness, m_S is the mass of the solar arrays, m_M is the mass of the mirrors, m_L is the laser mass, m_R is the radiator mass and m_{bus} is the mass of the bus and the constant k_{dry} represents the margin on dry mass. The masses of the various subsystems are computed with simple analytical formulas. The harness mass is expressed as a fraction of the combined mass of the laser and solar array:

$$m_C = MF_C\left(m_S + m_L\right) \tag{8.3}$$

The radiator mass A_R is proportional to the area needed to dissipate the excess power. MF_C is the mass fraction for harness. The latter is computed from a steady state thermal balance between the Solar input power and the emitted power which is not reported here for the sake of conciseness.

$$m_R = \rho_R A_R \tag{8.4}$$

where ρ_R is the radiator specific mass per surface unit area. The mass of the solar arrays is proportional to their area A_S:

$$m_S = k_S \rho_S A_S \tag{8.5}$$

where ρ_S is the solar array specific mass per surface unit area and the constant k_S represents the margin on solar array mass.

The same applies to the mirror's mass:

$$m_M = k_M \rho_M \left(A_d + A_{M_1} + 2A_{M_2}\right) \tag{8.6}$$

where ρ_M is the mirror specific mass per unit area, k_M is the margin on mirror mass, A_{M1} is the area of the primary mirror and A_{M2} and A_d are the areas of the secondary and directional mirror respectively. They are defined as:

$$\begin{aligned} A_{M_2} &= 0.01 A_{M_1} \\ A_d &= \frac{A_{M_1}}{C_r} \end{aligned} \tag{8.7}$$

where C_r is the concentration ratio, i.e. the ratio between the solar power density on the solar concentrator and that of the spot area on the asteroid. The mass of the laser is proportional to its output power:

$$m_L = k_L \rho_L P_L \eta_L \tag{8.8}$$

where ρ_L is the laser specific mass per input unit power, k_L is the margin on laser mass and the input power P_L depends on the solar input P_{in} and the efficiency of the solar array η_{SA}:

$$P_L = \eta_{SA} P_{in} A_{M_1} \tag{8.9}$$

Finally the total mass of the spacecraft is computed by adding a fixed mass fraction for the propellant:

$$m_{sc} = m_{dry} + 1.1 m_p = m_{dry} + 1.1 MF_p m_{dry} \tag{8.10}$$

where MF_p is the mass fraction for propellant and the factor 1.1 accounts for the mass of the tanks. The total mass of the formation is simply:

$$m_{sys} = n_{sc} m_{sc} \tag{8.11}$$

and the global conversion efficiency of the laser system is given by:

$$\eta_{sys} = \eta_L \eta_{SA} \eta_P \varepsilon_M \tag{8.12}$$

where η_L, η_{SA}, η_P, are the efficiency of the Laser, solar arrays and power bus respectively and ε_M is the emissivity of the mirror. The constants k_{dry}, k_S, k_M, k_L represent system margins that are chosen according to standard practice in space systems engineering and to design maturity[153]. For example, for the dry mass a 20% margin (i.e. k_{dry}=1.2) is used since this is what is normally done in a preliminary mission design study; for the solar arrays, a 15% margin is deemed adequate given the maturity reached by the related technology; for the mirror mass instead, a higher value of 25% was preferred; finally, given the fact that high power lasers for space applications are still in their infancy, a 50% margin must be used for the laser (see Table 8.1). Margins are used when uncertainties are not quantified exactly. In the following, therefore, margin parameters will be equal to 1 when uncertainties are quantified through Evidence Theory.

Table 8.1 System design margins

k_{dry}	k_S	k_M	k_L
1.2	1.15	1.25	1.5

One of the critical aspects of the design of the laser ablation system is that the quantities η_L, η_{SA}, ρ_R, ρ_L and ρ_M are poorly known. This is due to the fact that some of the related technologies are still in an early development stage. In particular, the efficiency and mass of the laser for space application are considered to be quite uncertain. As a matter of fact, there are two methods for powering the laser: in *direct pumping*, the solar energy is used to directly excite the electrons thereby generating the laser beam; on the other hand, in *indirect pumping*, the energy is first converted into electrical power, which then powers a semiconductor laser. Currently, high efficiency (up to 35%) directly pumped lasers have been discussed at a theoretical level, while existing systems achieve only a few percent of power efficiency[145]. Indirect pumping, instead, has shown very good performance albeit

mainly in non-space applications and with lower power outputs. For indirect pumping systems, there is quite some uncertainty on the energy conversion efficiencies that will be achieved in the short or medium term. Efficiencies around 40-50% should be easily attainable even with current proven technology (combining semiconductor laser with fibres) but some laboratory tests have suggested that much higher values, around 65%, are probably achievable, assuming over 80% wall-plug efficiency of the semiconductors and over 80% of the fibres[145]. Solar arrays are also a critical factor in the performance of an indirect pumped laser system. Recent advances in multiple junction cell technology have allowed for efficiencies close to 30% but it is not totally unrealistic to expect that near future improvements will move this threshold as high as 40-50% under concentrated light with partial efficiency recovery through thermocouples.

A third critical element is the radiator. As a matter of fact, given the relatively low power conversion efficiency of the solar arrays-laser combination (from ~10% to ~30% at best), most of the input solar power is rejected as heat and therefore must be dissipated by the radiators. While well proven, high emissivity, radiator technology is already available, the problem lays in the weight per emitting area for large systems. While for small radiator this is around 1 kg/m^2, for large surfaces this could be as high as 4 kg/m^2 [145]. It is clear that these wide ranges on many different parameters can considerably affect the overall size of the laser system and consequently the mass of the laser formation to be put in orbit. At the same time, the lack of detailed knowledge on the physical characteristics of the NEO can markedly affect the system's capability in sublimating enough surface material as to generate enough thrust to deviate the asteroid.

The performance index which is output by the system model is the total system mass of the Laser satellite formation m_{sys}. The input design parameters are the number of spacecraft n_{sc}, the diameter of the primary mirror d_{M1} and the concentration ratio C_r. As already mentioned, the parameters subjected to uncertainties are η_L, η_{SA}, ρ_R, ρ_L and ρ_M.

8.4 Deflection Action Model

As shown in previous works[64,144,145], the yield of the ablation process can be modelled with the simple energy balance (assuming no ionisation):

$$\frac{dm_{\exp}}{dt} = 2n_{sc}v_{rot}\int_{y_0}^{y_{rot}}\int_{t_{in}}^{t_{out}}\frac{1}{E_{sub}}\left(P_{in} - Q_{rad} - Q_{cond}\right)dtdy \tag{8.13}$$

where, $dm_{\exp}/dt$ is the mass flow rate of sublimated material, n_{sc} is the number of spacecraft in the formation, v_{rot} is the linear velocity of the asteroid surface due to its

rotation, E_{sub} is the enthalpy of sublimation. The input power per unit area from the laser is:

$$P_{in} = \eta_{sys} C_r \left(1-\varsigma_A\right) S_0 \left(\frac{r_{AU}}{r_A}\right)^2 \tag{8.14}$$

where ς_A is the albedo of the asteroid, S_0=1367W/m^2 is the solar flux at 1 AU, r_{AU} is the astronomical unit and r_A is the Sun-asteroid distance. Here the assumption is that the amount of reflected laser light is comparable to the amount of reflected visible light. For a highly effective volumetric absorber, experimental evidence has shown that for given asteroid analogue target materials – sandstone, olivine, and a porous composite mixture – that the majority of the incoming laser intensity is absorbed rather than reflected. Energy is emitted in the form of an extended, but contained, exhaust of gas and ejecta. This has been demonstrated for a *90* W continuous wave laser operating at a frequency of 808nm [146,147]. The heat loss due to black body radiation is:

$$Q_{rad} = \sigma \varepsilon_{bb} T^4 \tag{8.15}$$

where σ is the Stefan-Boltzmann constant, ε_{bb} is the black body emissivity, T is the asteroid surface temperature. The loss due to thermal conduction is expressed as[64]:

$$Q_{cond} = \left(T_{subl} - T_0\right)\sqrt{\frac{c_A k_A \rho_A}{\pi t}} \tag{8.16}$$

with T_{sub} as the temperature of sublimation of the surface material and c_A, k_A and ρ_A as its specific heat, thermal conductivity and density respectively. The ablation-induced acceleration can therefore be calculated as:

$$\mathbf{f}_{sub} = \frac{\Lambda \bar{v} \dot{m}_{\exp}}{m_A} \hat{\mathbf{v}}_A \tag{8.17}$$

where $\hat{\mathbf{v}}_A$ is the unit vector along the NEO heliocentric velocity, $\Lambda \approx \frac{2}{\pi}$ is the scattering factor that assumes that the plume is uniformly distributed over an angle of *180* deg, m_A is the asteroid mass and $\bar{v}$ is the average velocity of the ejecta:

$$\bar{v} = \sqrt{\frac{8 k_B T_{subl}}{\pi M_{Mg2SiO_4}}} \tag{8.18}$$

where k_B is the Boltzmann constant and M_{Mg2SiO_4} is the molecular mass of Forsterite. Note that no ionization model is considered here. This assumption is consistent with the sublimation model in Kahle et al. where the power density is analogous to the one used here. A more accurate model is out of the scope of this work, and in fact the proposed methodology is aimed at modelling and propagating uncertainties in order to evaluate the

impact on the quantities of interest, such as the achievable miss distance. An unmodelled component has to be regarded as a source of model uncertainty. More specifically, the incident laser energy absorption and the expansion of the gas depend on the level of ionization (see Phipps et al.[141]). An uncertainty on energy absorption and gas expansion is equivalent to adding uncertainty to the sublimation Enthalpy and to the parameters defining the expansion velocity, as it will be presented in the next section.

The thrust model needs to be completed with a suitable model of the contamination of the optics. In fact the plume of gas and debris coming from the ablation process is expected to flow and impact the spacecraft. The contamination model used here is the one developed by Kahle et al.[152] and further elaborated by Vasile and Maddock[151]. This model assumes that the sublimation of asteroid's surface is analogous to the generation of tails in comets and that the plume will expand as the exhaust gases of a rocket engine (as shown in Figure 8.2). Note that, such a model is not strictly consistent with the hemispherical scattering model used for computing the ablation thrust. Moreover, experimental data[147] is showing that neither the hemispherical model nor the one by Kahle et al., shown in Figure 8.2, accurately represent the expansion of the plume. However, they are used in the present work because each represents the worst case condition for thrust generation and mirror contamination respectively. The density of the expelled gas plume is computed as:

$$\rho_{\exp} = j_C \frac{\dot{m}_{\exp}}{\bar{v} A_{spot}} \left(\frac{d_{spot}}{2r_{S/SC} + d_{spot}} \right)^2 \left(\cos\Theta \right)^{\frac{2}{\kappa-1}} \tag{8.19}$$

where j_C=0.345 is the jet constant, κ=1.4 is the adiabatic index, A_{spot} and d_{spot} are respectively the area and diameter of the Laser spot on the asteroid; $r_{S/SC}$ is the norm of the distance vector of the spacecraft with respect to the spot on the asteroid. Θ is given by:

$$\Theta = \frac{\pi\varphi}{2\varphi_{\max}} \tag{8.20}$$

In the Hill reference frame $\mathbf{r}_{S/SC}$ is defined as:

$$r_{S/SC} = \begin{bmatrix} x - r_{ell} \sin\theta_{v_A} \\ y - r_{ell} \cos\theta_{v_A} \\ z \end{bmatrix} \tag{8.21}$$

where the radius of the ellipsoid is:

$$r_{ell} = \frac{a_I b_I}{\sqrt{\left(b_I \cos\left(\omega_A t + \theta_{v_A} \right) \right)^2 + \left(a_I \, s\,in\left(\omega_A t + \theta_{v_A} \right) \right)^2}} \tag{8.22}$$

x,*y* and *z* are the coordinates of the spacecraft with respect to the asteroid in the Hill reference frame, as shown in Figure 8.4, and a_I and b_I are the axes of the ellipsoid (the asteroid is assumed to be a rotation ellipsoid),.

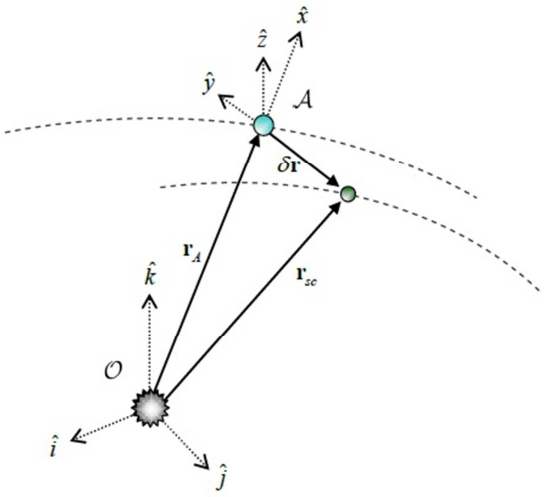

Figure 8.4 Hill reference frame.

The asteroid is assumed to be spinning around the z-axis with angular velocity ω_A. θ_A is the elevation of the spot over the y-axis. The model also assumes that all the particles impacting the mirror condense and stick to it. The variation of the thickness of the contamination layer on the mirror is thus computed as:

$$\frac{dh_{cond}}{dt} = \frac{2\overline{v}\rho_{\exp}}{\rho_{layer}}\cos\psi_{vf} \tag{8.23}$$

where the layer density ρ_{layer} is 1 g/cm^3. The speed of the ejecta is multiplied by 2 to account for the gas expansion in a vacuum. ψ_{vf} is the view factor taken as the angle between the normal of the mirror and the incident flow of gas. Finally, the power irradiated on the asteroid's surface is multiplied by a degradation factor τ:

$$\tau = \exp\left(-2\eta h_{cond}\right) \tag{8.24}$$

where η=10^4 cm^{-1} is the absorption coefficient for Forsterite.

It is important to observe that, according to the relative motion as in Figure 8.2, the mirrors would be exposed to the plume only for roughly half the period of the orbit of the asteroid, i.e. when the spacecraft has positive x coordinate.

Figure 8.5a shows a typical acceleration profile computed without considering the contamination of the mirror. The figure compares the profile obtained from numerical integration of the trajectory and ablation models with a high order Runge-Kutta method, with the one obtained with analytical propagation, with the arc-length adaption rule introduced in Section 8.2. The periodic behaviour is due to NEO's motion around the Sun

which accounts for oscillations in the solar flux captured by the primary mirror. The two integrations are in good agreement and the difference is due to Eq. (8.1). Figure 8.5b and Figure 8.5c show the same case but with the introduction of the contamination model in[150]. One can see that the amplitude of the acceleration oscillation decreases by more than two orders of magnitude already during the first revolution around the Sun and then stabilises at around 10^{-11}-10^{-13} m/s^2 for the rest of the trajectory.

From Figure 8.5 it is important to observe that the analytical propagation approximates very accurately the acceleration profile when its magnitude is high during the first revolution and less correctly when it is decayed for the remainder of the trajectory. This will not affect the accuracy on the computation of the impact parameter since the contribution of the first part will be much more relevant than the second, which will be almost negligible.

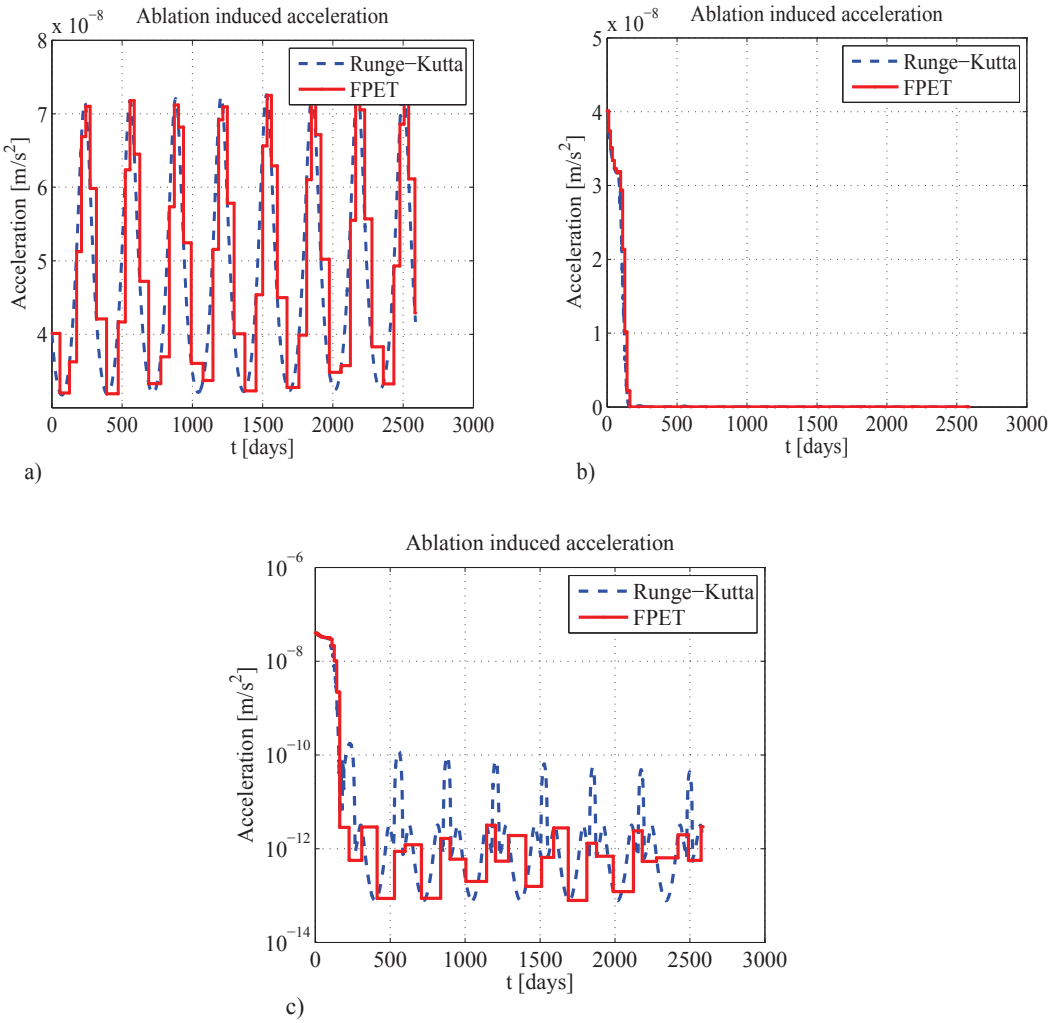

Figure 8.5 Typical acceleration profile: a) without contamination b) with contamination c) with contamination (semi-logarithmic scale).

As will be detailed in Section 8.5, from an analysis of the literature on NEO, one can observe a considerable variability of the physical parameters of asteroids, in particular E_{sub},

T_{sub}, c_A, k_A and ρ_A, which are at the same time quite controversial and very critical to the laser ablation system design.

All these sources of uncertainty are of epistemic nature as they correspond to the present lack of knowledge on the asteroid physical properties. Due to the nature of the uncertainty, probability theory would be inadequate to model and quantify its value, therefore it is here proposed to use Evidence Theory to build a correct uncertainty model and introduce it in the combined optimal design of the deflection and spacecraft system.

8.5 Construction of the Uncertain Intervals

As mentioned in the introduction, Evidence Theory will provide the theoretical framework with which to model uncertainties. An introduction to relevant features of Evidence Theory is available in Appendix B, thogether with the references to the related literature. In this section, the uncertain intervals and the associated BPA for each uncertain parameter are defined. Moreover, the situation in which the estimates about the uncertain intervals and their associated confidence come from different sources will be simulated. In order to do this, in this study the assumption is that the values of uncertain physical and technological parameters stem from the opinion of three different experts, as reported in Table 8.2, Table 8.3 and Table 8.4. Each expert expresses its own opinion on the uncertain intervals and assigns a personal confidence level to each of them. The confidence level represents the perception that experts have in their own level of knowledge. The opinions of the three experts could also be in disagreement with each other. This disagreement can be manifold. In the first instance, the experts can have different opinions on the amplitude of the interval itself and therefore propose slightly different boundaries. Secondly, even if the intervals proposed by different experts are the same, they can associate to them a different confidence and therefore estimate different BPAs. Moreover, some experts can also give a very generic indication that the given parameter can oscillate between a minimum and maximum value with equal confidence, which corresponds to giving a single wide interval with BPA equal to 1. And last, the expert can have no opinion at all on some quantities.

For the technological parameters η_L, η_{SA}, ρ_R, ρ_L and ρ_M, the three experts behaves as follows. Regarding the laser efficiency, *expert a* in Table 8.2 is rather conservative and assigns a high confidence of 70% to the proposition that the efficiency will be between 40% and 50%; he/she is less confident about the possibility of achieving efficiencies comprised between 50% and 60% and therefore the related probability assignment is 30%. *Expert b*, in Table 8.3, on the other hand is probably more realistic and assigns only 30%

confidence to the interval of 40-50% efficiency, while giving 60% to the 50-60% efficiency interval and finally introducing another interval between 60% and 66.4% with a confidence of 10%. *Expert c*, in Table 8.4, is very optimistic about future developments of lasers and therefore assigns 100% confidence to the statement that lasers could reach efficiencies between 55% and 66.4%. For the laser specific mass, *expert a* gives 40% confidence about the specific mass being comprised between 0.005 and 0.01 kg/W while is more oriented towards higher specific masses in the interval of 0.01-0.02 kg/W and therefore assigns 60% confidence to the latter. *Expert b*, on the other hand, is convinced that lightweight laser systems are possible and therefore assign 100% to the 0.01-0.02 kg/W. *Expert c* does not give any opinion on this topic (reported as *n/a* in the table). For the solar array efficiency, *expert a* is again rather sceptical and proposes only one interval between 20% and 30%, obviously with 100% confidence. *Expert b* suggests only a 40% confidence for the 20-30% efficiency range and instead assigns a 60% confidence about achieving higher efficiencies comprised between 30% and 50%. *Expert c* again doesn't express any opinion on the topic (reported as *n/a* in the table). Regarding the mirror specific mass, *expert a* is equally oriented towards values between 0.1 and 0.3 kg/m^2 and 0.3 and 0.5 kg/m^2, therefore confidence will be 50% for both. *Expert b* again proposes only one interval with 100% confidence for values ranging from 0.3 and 0.5 kg/m^2. *Expert c* instead is very optimistic about the development of lightweight mirrors with specific masses between 0.01 and 0.05 kg/m^2. Finally for the radiator, *expert a* suspects that radiator specific mass will be higher for large radiators like those envisioned for laser ablation spacecraft and therefore suggests 40% for values comprised in the 1-2 kg/m^2 and 60% for values between 2 and 4 kg/m^2. *Expert b* doesn't give an opinion on the topic (reported as *n/a* in the table) while *expert c* gives a generic indication that the mirror specific mass will surely be between 1 and 3 kg/m^2.

As already pointed out in Section 8.4, physical properties can differ considerably from one asteroid to the other. At the same time, different sources report different physical parameters for the same asteroid. Moreover, data is currently limited to ground based observations and a limited number of fly-by missions to only a few NEOs, such as Eros, Itokawa, Steins and Lutetia. However, these missions demonstrated that the fundamental nature, composition and geometries of NEOs are highly variable. Any generic group of physical characteristics can introduce a significant error within the analysis. Furthermore substantial error bars in T_{sub}, c_A, k_A and ρ_A also exist from the inferred spectra analysis and shape regularity – including period of rotation, form and shape model, and surface properties[154,155,156]. For example, available source show a range of two orders of magnitude

for the sublimation enthalpy: it is as low as $2.7 \cdot 10^5$ J/kg for some rare E type asteroids composed by carbonaceous and Enstatile Chondrites while it can reach $1.9686 \cdot 10^7$ J/kg for some S type asteroids with Olivine composition. For Silicum based bodies, the values are intermediate, around $5 \cdot 10^6$ J/kg. In this respect, for example, *expert a* gives 100% confidence to enthalpy being generically comprised between values as low as $2.7 \cdot 10^5$ and as high as $6 \cdot 10^6$ J/kg. *Expert b* gives more details, proposing only 20% confidence for a lower range between $2.7 \cdot 10^5$ and 10^6 J/kg for Chondritic objects and assigning instead 80% confidence to enthalpies comprised in the 10^7-$1.9686 \cdot 10^7$ J/kg typical of S-type Olivine asteroids. *Expert c*, while agreeing on the boundaries of this interval, assigns only 30% confidence to it and also is more persuaded about a different lower interval between $4 \cdot 10^6$ and $6 \cdot 10^6$ J/kg, to which he assigns a 70% confidence. Analogously, for the specific heat, most sources reported values between 500 and 600 J/(kg·K), which are typical of Olivine-based S type asteroid but also of M and C types such as Lutetia and Mathilde. It is interesting to note, however, that in some cases like the E type asteroid Steins the estimates can range from 470 up to over 750 J/(kg·K). Thus, *expert a* suggests two uncertain intervals: the first from 375 to 470 J/(kg·K) with 30% confidence, and the second one from 470 to 600 J/(kg·K) with 70% confidence. Also *expert b* proposes this latter range, but with 40% confidence only. He also proposes a higher interval from 600 up to 750 J/(kg·K) with 60% confidence. *Expert c* gives a generic indication that the specific heat will be between 470 and 750 J/(kg·K). For the thermal conductivity, the range spans two orders of magnitude: for common S-type, Olivine bodies and for some E type asteroids it is around 1.47-1.6 W/(m·K); it is as low as 0.2 W/(m·K) for others like M-type Lutetia and C-type Mathilde. In this sense, *expert a* assigns 20% confidence to an interval to a low interval for relatively rare M/C-type bodies with conductivities comprised between 0.2 and 0.5 W/(m·K). On the other hand, he/she gives 80% to the assumption that the conductivity will be between 1.47 and 1.6 W/(m·K). *Expert b* is again rather generic giving just a minimum of 0.2 W/(m·K) and maximum of 2 W/(m·K). *Expert c* is unable to give an opinion (reported as *n/a* in the table). Regarding the density, sources report values comprised between 1100 and 2000 kg/m^3 for most C-type asteroids, and between 2000 and 3700 kg/m^3 for S-types and some M-type ones. According to this, *expert a* thinks that S-type objects will be more common and therefore assigns 70% to the latter interval and 30% to the former. This time too, *expert b* is very vague, giving indications of a lower bound at 1100 kg/m^3 and an upper at 3700 kg/m^3. *Expert c* disagrees with the lower limit and sets it at 2000 kg/m^3 instead. Finally, the sublimation temperature shows a more limited variability, with values around 1700 K for S-type and up to 1812 K for other examples.

This small variability is also reflected in the experts' opinion, since *expert a* assumes the values related to S-type asteroids, between 1700 K and 1720 K, with 100% confidence. *Expert b* proposes a range spanning 1720-1812 K, again with 100% confidence, while *expert c* proposes a wider range from 1700 K to 1812 K.

The three sources of information are data-fused following a similar procedure to the one described by Oberkampf and Helton[157]. As a representative example, the procedure is here applied to the data-fusion of the estimates concerning the laser efficiency. As already discussed, the opinions given by three experts are:

a. Conservative opinion: "The Laser efficiency will be between 40% and 50% with 70% confidence and between 50% and 60% with 30% confidence".
b. Realistic opinion: "The Laser efficiency will be between 40% and 50% with 30% confidence, between 50% and 60% with 60% confidence and between 60% and 66.4% with 10% confidence".
c. Optimistic opinion: "The Laser efficiency will be between 55% and 66.4% with 100% confidence".

These statements, in mathematical terms can be written as:

a. $\begin{cases} {}^{a}U^{1} = [0.4, 0.5] & BPA\left({}^{a}U^{1}\right) = 0.7 \\ {}^{a}U^{2} = [0.5, 0.6] & BPA\left({}^{a}U^{2}\right) = 0.3 \end{cases}$

b. $\begin{cases} {}^{b}U^{1} = [0.4, 0.5] & BPA\left({}^{b}U^{1}\right) = 0.3 \\ {}^{b}U^{2} = [0.5, 0.6] & BPA\left({}^{b}U^{2}\right) = 0.6 \\ {}^{b}U^{3} = [0.6, 0.664] & BPA\left({}^{b}U^{3}\right) = 0.1 \end{cases}$

c. ${}^{c}U = [0.55, 0.664] \quad BPA\left({}^{c}U\right) = 1$

Then, to represent and then combine the data given by the three experts, for each of them a matrix is constructed as follows[157]:

1. First, one has to list all the possible values the experts propose as lower and upper boundaries for the uncertain intervals. In this case the lower boundaries are $[0.4 \quad 0.5 \quad 0.55 \quad 0.6]$ and upper boundaries are $[0.5 \quad 0.6 \quad 0.664]$.
2. Then, a lower triangular matrix A_i is defined for each source of information, which has as many columns as the possible lower boundaries and as many rows as the possible upper boundaries. Thus, each element of this lower triangular matrix represents a certain interval with its lower and upper limits. If the expert has associated a confidence level to that interval, then the element of the matrix

assumes that value and is zero otherwise. For example, the matrix for *expert a* will have the following structure:

	0.4	0.5	0.55	0.6
0.5	0.7	0	0	0
0.6	0	0.3	0	0
0.664	0	0	0	0

In the present case, the three matrices are as follows.

a. $$A_a = \begin{bmatrix} 0.7 & 0 & 0 & 0 \\ 0 & 0.3 & 0 & 0 \\ 0 & 0 & 0 & 0 \end{bmatrix}$$

b. $$A_b = \begin{bmatrix} 0.3 & 0 & 0 & 0 \\ 0 & 0.6 & 0 & 0 \\ 0 & 0 & 0 & 0.1 \end{bmatrix}$$

c. $$A_c = \begin{bmatrix} 0 & 0 & 0 & 0 \\ 0 & 0 & 0 & 0 \\ 0 & 0 & 1 & 0 \end{bmatrix}$$

At this point the three sets of intervals can be combined into a single one by computing the weighted average of matrices as:

$$A = \frac{k_a A_a + k_b A_b + k_c A_c}{3} \tag{8.25}$$

where k_a, k_b, and k_c are weights which can be defined arbitrarily in order to give different influence to each source of information. In this case, all sources are given the same importance and therefore the weights are all set to 1. The resulting matrix is therefore:

$$A = \begin{bmatrix} 0.3333 & 0 & 0 & 0 \\ 0 & 0.3 & 0 & 0 \\ 0 & 0 & 0.3333 & 0.0333 \end{bmatrix}$$

from which one derives the uncertain intervals as:

$$U^1 = [0.4, 0.5] \quad BPA(U^1) = 0.3333$$
$$U^2 = [0.5, 0.6] \quad BPA(U^2) = 0.3$$
$$U^3 = [0.55, 0.664] \quad BPA(U^3) = 0.3333$$
$$U^4 = [0.6, 0.664] \quad BPA(U^4) = 0.0333$$

A similar procedure was followed for the remaining nine uncertain parameters, leading to the results reported in Table 8.5 and Table 8.6. Note that information fusion of different sources for this specific case is still an open problem. The use of a weighted average is

only one possibility. A thorough analysis of the right information fusion technique is out the scope of this work.

Table 8.2: Uncertain parameters estimates from *expert a*.

	Lower	Upper	BPA		Lower	Upper	BPA
c_A [J/KgK]	375	470	0.3	η_L	0.4	0.5	0.7
	470	600	0.7		0.5	0.6	0.3
k_A [W/mK]	0.2	0.5	0.2	η_{SA}	0.2	0.3	1
	1.47	1.6	0.8				
ρ_A [kg/m^3]	1100	2000	0.3	ρ_M [kg/m^2]	0.1	0.3	0.5
	2000	3700	0.7		0.3	0.5	0.5
T_{sub} [K]	1700	1720	1	ρ_L [kg/W]	0.005	0.01	0.4
					0.01	0.02	0.6
E_{sub} [J/kg]	$2.7\cdot10^5$	$6\cdot10^6$	1	ρ_R [kg/m^2]	1	2	0.4
					2	4	0.6

Table 8.3: Uncertain parameters estimates from *Expert b*.

	Lower	Upper	BPA		Lower	Upper	BPA
c_A [J/KgK]	470	600	0.4	η_L	0.4	0.5	0.3
	600	750	0.6		0.5	0.6	0.6
					0.6	0.664	0.1
k_A [W/mK]	0.2	2	1	η_{SA}	0.2	0.3	0.4
					0.3	0.5	0.6
ρ_A [kg/m^3]	1100	3700	1	ρ_M [kg/m^2]	0.3	0.5	1
T_{sub} [K]	1720	1812	1	ρ_L [kg/W]	0.01	0.02	1
E_{sub} [J/kg]	$2.7\cdot10^5$	10^6	0.2	ρ_R [kg/m^2]	n/a		
	10^7	$1.9686\cdot10^7$	0.8				

Table 8.4: Uncertain parameters estimates from *Expert c*.

	Lower	Upper	BPA		Lower	Upper	BPA
c_A [J/KgK]	470	750	1	η_L	0.55	0.664	1
k_A [W/mK]	n/a			η_{SA}	n/a		
ρ_A [kg/m^3]	2000	3700	1	ρ_M [kg/m^2]	0.01	0.05	1
T_{sub} [K]	1700	1812	1	ρ_L [kg/W]	n/a		
E_{sub} [J/kg]	$4\cdot10^6$	$6\cdot10^6$	0.7	ρ_R [kg/m^2]	1	3	1
	10^7	$1.9686\cdot10^7$	0.3				

Table 8.5: Uncertain intervals of NEO physical properties.

	Lower	Upper	BPA
c_A [J/KgK]	375	470	0.1
	470	600	0.3667
	470	750	0.3333
	600	750	0.2
k_A [W/mK]	0.2	0.5	0.1
	1.47	1.6	0.4
	0.2	2	0.5
ρ_A [kg/m^3]	1100	2000	0.1
	2000	3700	0.5667
	1100	3700	0.3333
T_{sub} [K]	1700	1720	0.3333
	1720	1812	0.3333
	1700	1812	0.3333
E_{sub} [J/kg]	$2.7\cdot10^5$	10^6	0.0667
	$2.7\cdot10^5$	$6\cdot10^6$	0.3333
	$4\cdot10^6$	$6\cdot10^6$	0.2333
	10^7	$1.9686\cdot10^7$	0.3667

Table 8.6: Uncertain intervals of technological parameters.

	Lower	Upper	BPA
η_L	0.4	0.5	0.3333
	0.5	0.6	0.3
	0.55	0.664	0.3333
	0.6	0.664	0.0333
η_{SA}	0.2	0.3	0.2
	0.3	0.5	0.3
	0.2	0.5	0.5
ρ_M [kg/m^2]	0.3	0.5	0.5
	0.1	0.3	0.1667
	0.01	0.05	0.3333
ρ_L [kg/W]	0.005	0.01	0.2
	0.01	0.02	0.8
ρ_R [kg/m^2]	1	2	0.2
	1	3	0.5
	2	4	0.3

8.6 Multi Objective Optimization under Uncertainty

Once the uncertainties on system design and asteroid physical characteristics are defined, one can try to find the optimal design of the deflection system under uncertainty. The performance, i.e. the achieved deviation, needs to be maximised while minimising a measure of the cost of the mission, e.g. the mass into space. According to the spacecraft system model presented in previous sections, performance and cost can be optimised with respect to four design parameters: the diameter of the primary mirror d_M, the number of

spacecraft n_{sc}, the warning time t_{warn} (time from the beginning of the deflection action to the time of the expected impact with the Earth) and the concentration ratio C_r. The performance measure to be maximised is the impact parameter b, while the cost measure to be minimised is the total mass of the formation m_{sys}. This leads to a classical Multi-Objective optimisation problem. The impact parameter is computed by means of the deflection and ablation model detailed in Section 8.2 and Section 8.4 while the total system mass is derived as in Section 8.3.

As a first step one can determine the set of Pareto optimal solutions for a fixed value of the uncertain parameters η_L, η_{SA}, ρ_R, ρ_L, ρ_M, E_{sub}, T_{sub}, c_A, k_A and ρ_A. Their value was chosen according to the available literature[154,155,156] and are reported in Table 8.7. Moreover, since at this stage uncertainties are not yet accounted for with Evidence theory, system margins as in Table 8.1 are included in the model, in order to replicate the standard system engineering method to deal with uncertainty.

Table 8.7: Set of fixed values for uncertain parameters.

NEO Physical properties		Technological parameters	
Parameter	Value	Parameter	Value
c_A [J/KgK]	750	η_L	0.6
k_A [W/mK]	2	η_{SA}	0.41
ρ_A [kg/m^3]	2600	ρ_M [kg/m^2]	0.1
T_{sub} [K]	1800	ρ_L [kg/W]	0.005
E_{sub} [J/kg]	$5\cdot10^6$	ρ_R [kg/m^2]	1.4

Table 8.8: Boundaries for optimization parameters.

	Lower	Upper
d_M [m]	2	20
n_{sc}	1	10
t_{warn} [yrs]	1	8
C_r	1000	3000

The multi objective optimisation problem to be solved is:

$$\min_{\mathbf{x}\in D}\left[m_{system}\left(\mathbf{x},\bar{\mathbf{u}}\right) \quad -b\left(\mathbf{x},\bar{\mathbf{u}}\right)\right] \tag{8.26}$$

where $\mathbf{x}$ is the design parameter vector comprising $\mathbf{x}=[d_M, n_{sc}, t_{warn}, C_r]^T$, for which the boundaries are in Table 8.8, and $\bar{\mathbf{u}}$ is the vector of uncertain parameters with values in Table 8.7. The impact parameter b appears with the minus sign since it has to be maximised. For the solution of problem (8.26) system margins are introduced with the values in Table 8.1.

Note that the presence of the discrete variable n_{sc} makes this a mixed integer-nonlinear Multi-Objective optimisation problem. The optimisation problem was solved with MACS2.

When epistemic uncertainties are introduced through Evidence Theory the MOO problem (8.26) has to be reformulated in order to maximise the Belief in the optimal value of impact parameter and total system mass. Formally problem (8.26) would translate into the MOO under uncertainty:

$$\begin{aligned} &\max_{\mathbf{x}\in D} Bel(-b(\mathbf{x},\mathbf{u}) < \nu_b) \\ &\max_{\mathbf{x}\in D} Bel(m_{sys}(\mathbf{x},\mathbf{u}) < \nu_m) \\ &\min \nu_b \\ &\min \nu_m \end{aligned} \tag{8.27}$$

The solution of problem would require the computation of the Belief value for different design parameters and for different values of the thresholds v_b and v_m for all possible values of the uncertain parameters **u** within the uncertain space *U*: for each **x**, set (B.5) needs to be computed for each of the functions *b* and m_{sys} for different v_b and v_m respectively and the cumulative functions (B.6) need to be independently computed for both *b* and $m_{sys.}$. The identification of the set (B.5) would need the computation of the max and min of *b* and m_{sys} over all the focal elements in *U*. However, the number of focal elements in *U* is an exponential function of the number of uncertain parameters[147] which translates into an exponentially increasing number of optimisation problems required to compute the cumulative quantities in (B.6). In practise, however, the full Belief and Plausibility curves are not required and one can study only the worst and best case scenarios.

The best case scenario corresponds to the design, uncertainty vectors and thresholds that yield a Plausibility equal to 0. Below this value of the thresholds the deflection mission is not possible assuming the available body of knowledge of spacecraft systems and asteroid physical properties. The worst case scenario corresponds to the design, uncertainty vectors and thresholds that yield a Belief equal to 1. Above this value of the thresholds the mission is certainly possible, given the current body of knowledge, but would be suboptimal.

The optimal design vector and thresholds that yield a Belief equal to 1 for all possible **u** in *U* can be computed solving the following Multi-Objective *minmax* problem:

$$\min_{\mathbf{x}\in D}\left[\max_{\mathbf{u}\in U} m_{system}(\mathbf{x},\mathbf{u}) \quad \max_{\mathbf{u}\in U}\left(-b(\mathbf{x},\mathbf{u})\right)\right] \tag{8.28}$$

In fact, for a given **x,** the minimum possible threshold value corresponds to the maximum value of m_{sys} and $-b$ over the whole uncertain space *U*, for which boundaries are reported in Table 8.5 and Table 8.6. Because the focal elements in *U* can be overlapping or

can be disconnected, the identification of the maximum of m_{sys} and $-b$ might be problematic as one would need to explore each focal element independently and therefore face an exponential number of optimisation problems. In order to avoid this exponential complexity, all focal elements are collected, through an affine transformation, into the unit hypercube $\bar{U}$ such that they are not overlapping or disconnected.

The optimal design vector and thresholds that yield a Plausibility equal to zero for all possible **u** in U can be computed by solving the following Multi-Objective *minmin* problem:

$$\min_{\mathbf{x}\in D}\left[\min_{\mathbf{u}\in\bar{U}} m_{system}(\mathbf{x},\mathbf{u}) \quad \min_{\mathbf{u}\in\bar{U}}\left(-b(\mathbf{x},\mathbf{u})\right)\right] \tag{8.29}$$

Again as before the focal elements are mapped into the unit hypercube $\bar{U}$ and the search is run over $\bar{U}$. Note that, differently from the case of problem (8.26), system design margins are no longer needed and therefore the values for k_{dry}, k_S, k_M, k_L are all set to 1.

The two mixed integer optimisation problems (8.28) and (8.29) are solved with a variant of MACS2, called MACS2v, as described in the following section.

8.6.1 MACS2v

MACS2v is an algorithm based on MACS2, and is aimed at solving Multi-Objective *minmin*/*minmax* problems. The steps of the algorithm are summarised in Algorithm 8.1.

Algorithm 8.1 MACS2v

1: Initialise Population P_0
2: Apply Algorithm Cross-check on population P_0 and itself
3: Initialise archives A_l and A_g
4: $k = 0$
5: **while** $n_{feval} < n_{feval,max}$ **do**
6: Apply individualistic moves and generate trial population P_t
7: Apply Algorithm Cross-check between population P_t and P_k
8: Apply Algorithm Cross-check between population P_t and archive A_l
9: Update archive A_l
10: $k = k + 1$; $P_k \leftarrow P_t$
11: Apply social moves and generate population P_s
12: Apply Algorithm Cross-check between population P_s and P_k
13: Apply Algorithm Cross-check between population P_s and archive A_g
14: Update archive A_g
15: $P_k \leftarrow P_s$
16: Validate archive A_g
17: **end while**

MACS2v uses the standard MACS framework to explore the design space *D*, which has already been described in detail in Chapter 2. The main differences lay in the fact that now the objective function **J**(**x**) is given by:

$$\mathbf{J}(\mathbf{x}) = \left[\max_{\mathbf{u} \in \bar{U}} f_l(\mathbf{x}, \mathbf{u}) \right]^T \quad l = 1, ..., m \tag{8.30}$$

where m is the number of the objective functions. Therefore, in this algorithm, when a new candidate solution $\mathbf{x}$ is generated, for each f_l, a global optimisation to maximise f_l is run over the space of uncertain parameters U with probability p and the resulting $\mathbf{u}_{max}$ is associated to the new $\mathbf{x}$. If no optimisation is run on U, then the new candidate solution inherits the $\mathbf{u}$ of its parent. Moreover, a number of strategies are implemented, which exploit the knowledge in the current population and in the archive in order to ensure that the $\mathbf{u}$ associated to each $\mathbf{x}$ is a maximiser of f_l. These strategies are described in Algorithm 8.2 and Algorithm 8.3. The first algorithm acts on couples of solutions $[\mathbf{x}_i,\mathbf{u}_i]$ and $[\mathbf{x}_j,\mathbf{u}_j]$, belonging to two different sets S_i and S_j, and cross-checks whether the local maximum $f_l(\mathbf{x}_i,\mathbf{u}_j^*)$, where $\mathbf{u}_j^*$ lies in a neighbourhood of $\mathbf{u}_j$, is higher than $f_l(\mathbf{x}_i,\mathbf{u}_j^*)$; if so, it associates this new point $\mathbf{u}_j^*$ to $\mathbf{x}_i$. Algorithm 8.3 instead is meant to validate the archive and ensures that, for each objective function f_l, its best minimiser $\mathbf{x}_{imin,l}$ found so far is really such. In order to do so, a global search is run over U and the new candidate maximum $\mathbf{u}^g$ is checked against the one currently associated with $\mathbf{x}_{imin,l}$ and, if it gives a higher f_l, it replaces it. The process is repeated until the increase in f_l is below a certain threshold.

Algorithm 8.2 Cross-check

```
Given two generic sets of solutions S_i and S_j
for all {[x_i, u_i]} ∈ S_i do
    for all {[x_j, u_j]} ∈ S_j do
        for all l ∈ {1, ..., m} do
            Compute local maxima f_l(x_i, u_j*) and f_l(x_j, u_i*)
            if f_l(x_i, u_j*) > f_l(x_j, u_i) then
                u_i ← u_j*
            end if
            if f_l(x_j, u_i*) > f_l(x_j, u_j) then
                u_j ← u_i*
            end if
        end for
    end for
end for
```

Algorithm 8.3 Validate

1: Given an archive A_g and $\Delta \to \infty$
2: **for all** $l \in \{1, ..., m\}$ **do**
3: **while** $\Delta < tol$ **do**
4: $i_{min,l} = \arg\min_k f_l(\mathbf{x}_k, \mathbf{u}_k)$
5: Run global search over U and generate putative global maximum $\mathbf{u}_i^g$
6: **if** $f_l(\mathbf{x}_i, \mathbf{u}_i^g) > f_l(\mathbf{x}_i, \mathbf{u}_i)$ **then**
7: $\mathbf{u}_i \leftarrow \mathbf{u}_i^g$
8: **end if**
9: $\Delta = f_l(\mathbf{x}_i, \mathbf{u}_i^g) - f_l(\mathbf{x}_i, \mathbf{u}_i)$
10: **end while**
11: **end for**

8.6.2 Solution of the MO Problems under Uncertainty

The solution of problems (8.28) and (8.29) provides the intervals for both the performance and the design parameters. In particular, the worst case corresponds to the maximum Belief condition:

$$\begin{aligned} &\overline{\mathbf{y}} = [\overline{\mathbf{x}}, \overline{\mathbf{u}}] = \arg\min_{\mathbf{x} \in D} \left[\max_{\mathbf{u} \in \overline{U}} m_{system}(\mathbf{x}, \mathbf{u}) \quad \max_{\mathbf{u} \in \overline{U}} \left(-b(\mathbf{x}, \mathbf{u}) \right) \right] \\ &Bel(\overline{\mathbf{y}}) = 1 \end{aligned} \tag{8.31}$$

The best case instead corresponds to the minimum Plausibility point:

$$\begin{aligned} &\underline{\mathbf{y}} = [\underline{\mathbf{x}}, \underline{\mathbf{u}}] = \arg\min_{\mathbf{x} \in D} \left[\min_{\mathbf{u} \in \overline{U}} m_{system}(\mathbf{x}, \mathbf{u}) \quad \min_{\mathbf{u} \in \overline{U}} \left(-b(\mathbf{x}, \mathbf{u}) \right) \right] \\ &Pl(\underline{\mathbf{y}}) = 0 \end{aligned} \tag{8.32}$$

As a comparison, a *minmin* problem analogous to (8.32) is solved with the reintroduction of system design margins. Finally the 4 optimisation problems are considered both in the case with and without the contamination are solved. In summary, a total of 8 Pareto curves are generated, 4 each for the cases with and without the contamination:

1. *deterministic*, i.e. a bi-objective optimisation problem on $\mathbf{x} \in D$ as in (8.26). The system model does include the margins specified in Table 8.1 and constant values for uncertain parameters u are used as in Table 8.7. The problem is solved with the standard MACS2.
2. *minmax*, bi-objective optimisation problem as in (8.28). The system model doesn't include margins. The problem is solved with the modified MACS2.
3. *minmin*, bi-objective optimisation problem as in (8.29). The system model doesn't include margins. The problem is solved with the modified MACS2.
4. *minmin with margins*, bi-objective optimisation problem as in (8.29). It is analogous to the previous one but this time the system model does include the margins specified in Table 8.1. The problem is solved with the modified MACS2.

Figure 8.6a and Figure 8.6b report the Pareto fronts for the *deterministic*, *minmin* and *minmax* problems, with and without contamination respectively.

Qualitatively, the case with and without contamination are very similar but Figure 8.6a shows that, without contamination, the best deviation achievable is one order of magnitude larger than in the case with contamination (see Figure 8.6b). Since the system model is the same, the range of total system mass is the same in both cases.

The uncertainties in the input parameters translate into a difference between the *minmin* and *minmax* curves of about two orders of magnitude in attainable deviation and one order of magnitude in system mass. The achievable deviation easily reaches 10^5-10^6 km in the best case scenario with a total formation mass below 30000 kg, while in the worst case scenario even with a system mass of 10^5 kg the best achievable deviation does not exceed 10^4 km. This issue is even more apparent in the case with mirror contamination in which the worst case deviation barely reaches 10^3 km. It is important to point out that the huge variability in performance does not imply that the laser ablation is an unreliable deflection method as the type of uncertainty is epistemic. It implies instead that: given the present body of knowledge a reliable deflection mission would require a massive system in orbit, the potential margin for improvement would be considerable, current knowledge on this deflection method is too low to provide an exact quantification of its performance. Note also that the Pareto front for the case *minmin* with margins has higher system mass for the level of deviation attained with respect to the standard *minmin* case.

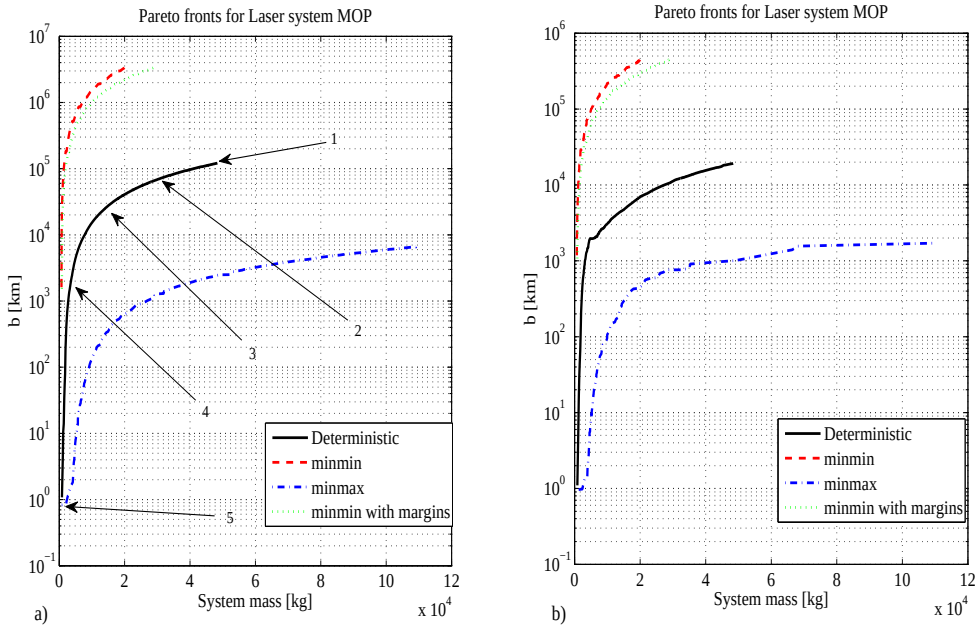

Figure 8.6 Multi objective optimization: Pareto fronts a) no contamination b) with contamination. *b* is represented in logarithmic scale.

Figure 8.7a and Figure 8.7b show the distribution of optimal design solutions in the three case studies, without and with contamination respectively. The plots present the values only for three design variables, i.e. the diameter of the primary mirror, the number of spacecraft and the warning time. The concentration ratio is not reported because all the optimal design points show the maximum allowed concentration ratio allowed, i.e. 3000.

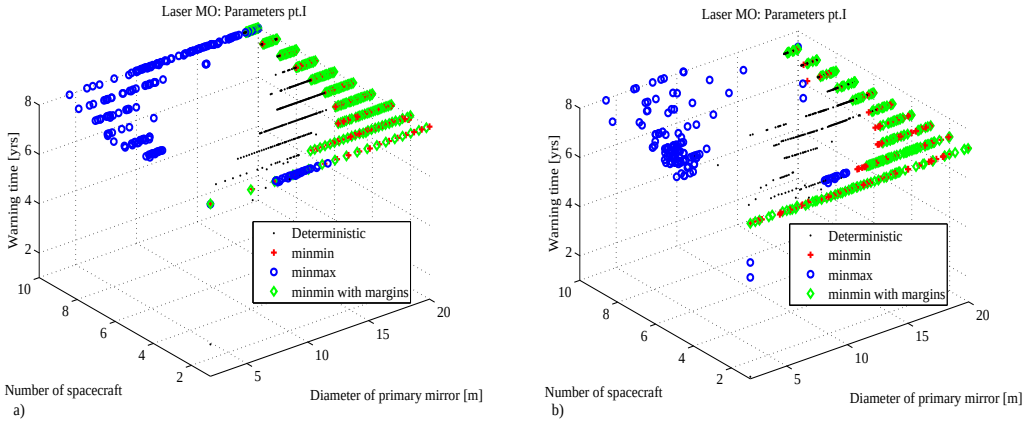

Figure 8.7 Multi objective optimization: Pareto sets a) no contamination b) with contamination.

In Figure 8.7 one can clearly identify two different families of design solutions in the *minmin* and *minmax* case. In the latter, solutions with a high number of spacecraft and a small diameter of the primary mirror are preferred. Arguably, many spacecraft are needed because the physical properties of the asteroid are such that inducing sublimation requires a large amount of power; at the same time the efficiency of the laser system is much lower and in particular the radiator mass per unit area is much higher and therefore it is convenient to have many smaller spacecraft, i.e. with a smaller primary mirror. Coherently with this, for diametrically opposite reasons, in the *minmin* case designs with few spacecraft with large concentrators are preferable. This result brings to an interesting general conclusion: for low performance components a monolithic system is suboptimal with respect to a disaggregated system as the mass of a monolithic system grows faster than the linear growth of the mass of the disaggregated counterpart. Note that, although redundancy was not modelled, the robust analysis suggests that a highly redundant system is preferable in the case of high uncertainty on the design parameters, as it would be logical to expect.

Finally one can note that in the case without contamination the maximum warning time of eight years is always optimal. This is easily explained given the fact that the magnitude of the thrust acceleration is relatively constant (albeit within a minimum and maximum

values, see Figure 8.5a) and therefore the longer this is acting on the NEO, the better. When the contamination of the mirrors is considered, then the optimal warning time is around 7.27 years. In this case, in fact, the acceleration profile essentially is reduced to a single large thrust impulse followed by a perturbation some orders of magnitude smaller than the initial peak (as shown in Figure 8.5b and Figure 8.5c). In this case, thus, the phasing of the initial pulse becomes extremely important (see Colombo et al.[42]).

8.6.3 Belief and Plausibility Analysis

To further analyse the influence of each individual uncertain parameter, five design points from the solution set of the deterministic case in Figure 8.6a were selected. For each of them, the belief and plausibility curves for both the impact parameter *b* and the system mass were reconstructed. The curves were computed with an algorithm based on the evolutionary binary tree technique in Vasile et al.[158]:

1. Given the performance parameter J_i and a constant design parameter vector $\bar{\mathbf{x}}$, the single objective optimisation problems:

$$\begin{aligned} \nu_{\min} &= \min_{\mathbf{u}\in\bar{U}} J_i\left(\bar{\mathbf{x}},\mathbf{u}\right) \\ \nu_{\max} &= \max_{\mathbf{u}\in\bar{U}} J_i\left(\bar{\mathbf{x}},\mathbf{u}\right) \end{aligned} \tag{8.33}$$

are solved with IDEA over the entire uncertain space given by the unit hypercube $\bar{U}$. This returns the upper and lower limit for the performance parameter.

2. n_v values v_j are defined equally spaced in the interval $\left[\nu_{\min} \quad \nu_{\max}\right]$.
3. The initial unit hypercube $\bar{U}$ is partitioned in two sub-hypercubes $\bar{U}^1$ and $\bar{U}^2$. The "cut" is performed such that it coincides with the boundaries of adjacent focal elements which form the hypercube $\bar{U}$. Define Υ as the set of sub-hypercubes $\bar{U}^l$.
4. For each value of the threshold v_j, the following iterative procedure is performed:

   a. $$\begin{aligned} Bel\left(\nu_j\right) &= 0 \\ Pl\left(\nu_j\right) &= 0 \end{aligned}$$

   b. For each sub-hypercube $\bar{U}^l \in \Upsilon$:

      - Solve problem (45) on $\bar{U}^l$ and store $\nu^l_{\min}$ and $\nu^l_{\max}$.
      - If $\nu^l_{\max} \le \nu_j$, then:

$$Bel(\nu_j) = Bel(\nu_j) + BPA(\bar{U}^l)$$
$$Pl(\nu_j) = Pl(\nu_j) + BPA(\bar{U}^l)$$

- Else, if $\nu^l_{\min} < \nu_j < \nu^l_{\max}$, partition $\bar{U}^l$ into two new sub-hypercubes $\bar{U}^{l1}$ and $\bar{U}^{l2}$. Remove $\bar{U}^l$ from Υ and add $\bar{U}^{l1}$ and $\bar{U}^{l2}$.
- Repeat step b. until a termination condition is met, e.g. the maximum number of partitions has been reached or the current $\bar{U}^l$ corresponds to a single focal element and therefore cannot by further divided. Alternatively further subdivisions are also avoided if the BPA of $\bar{U}^l$ is lower than a certain threshold, which means that its contribution to the Belief and Plausibility curves would be negligible.

(Note that step b. is to be skipped if problem (8.33) has already been solved on $\bar{U}^l$ and the results already stored are used instead).

c. For each $\bar{U}^m = \left[\bar{U}^m \in \Upsilon \mid \nu^m_{\min} < \nu_j < \nu^m_{\max}\right]$:

$$Pl(\nu_j) = Pl(\nu_j) + BPA(\bar{U}_m)$$

We report here only the curves for designs 1 and 5, for the case without contamination only. These two are the most relevant since they correspond to the upper and lower edge of the *deterministic* Pareto front (see Figure 8.6a). The curves for the other three design points are qualitatively similar. Figure 8.8a and Figure 8.8b show design point 5, corresponding to the lower left part of the Pareto front, i.e. minimum mass/minimum deviation.

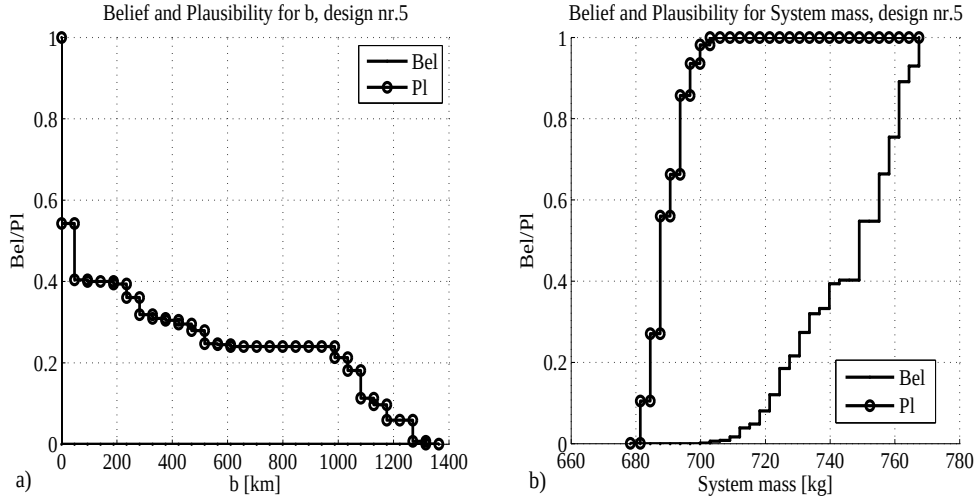

Figure 8.8 Belief/Plausibility curves for design 5: a) impact parameter *b* b) system mass.

The deviation obtained is indeed very small, going from few tens of meters for *Bel*=1 to few thousands for *Pl*=0. At the same time, the curves of the system mass show that it

cannot be lower than 680 kg but also will not exceed 765 kg even in the worst possible condition.

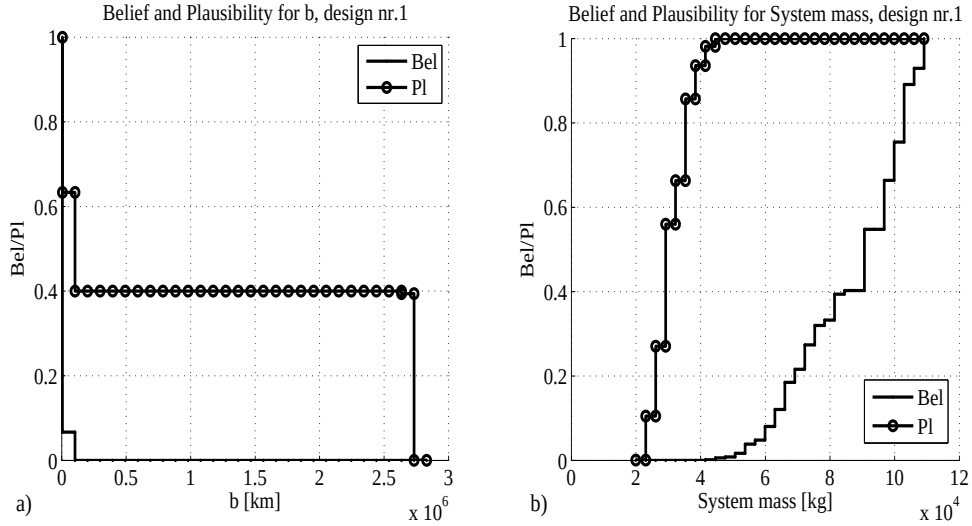

Figure 8.9 Belief/Plausibility curves for design 1: a) impact parameter *b* b) system mass.

Similar observations are applicable to Figure 8.9a and Figure 8.9b, which consider the design point corresponding to maximum deviation and maximum system mass. In this case however, the difference between the condition with *Bel*=1 and *Pl*=0 is much wider: ~10^6-10^4 km for the impact parameter *b* and ~$1.09 \cdot 10^5$-$2 \cdot 10^4$ kg for the mass. This means that in the worst case, a successful deviation is still achievable, albeit with a small margin, but the total launch mass of the formation will be quite high. Note that, in the case of design 1, the performance values for worst and best conditions (*Bel*=1 and *Pl*=0) are coinciding with the values at upper edge of the *minmax* and *minmin* Pareto fronts respectively, as reported in Figure 8.6a. This is explained by the fact that the design points corresponding to the upper edge of the *deterministic*, *minmin* and *minmax* curves are identical and correspond to the point with $n_{sc}=10$, $d_M=20$ m and $t_{warn}=8$ years as in Figure 8.7. However, this is not the case in general (as already discussed in the previous section) and therefore for example the performance values for the Bel=1 and Pl=1 conditions for design points 2 to 4 will be different from the best case and worst case conditions defined by the *minmin* and *minmax* Pareto fronts.

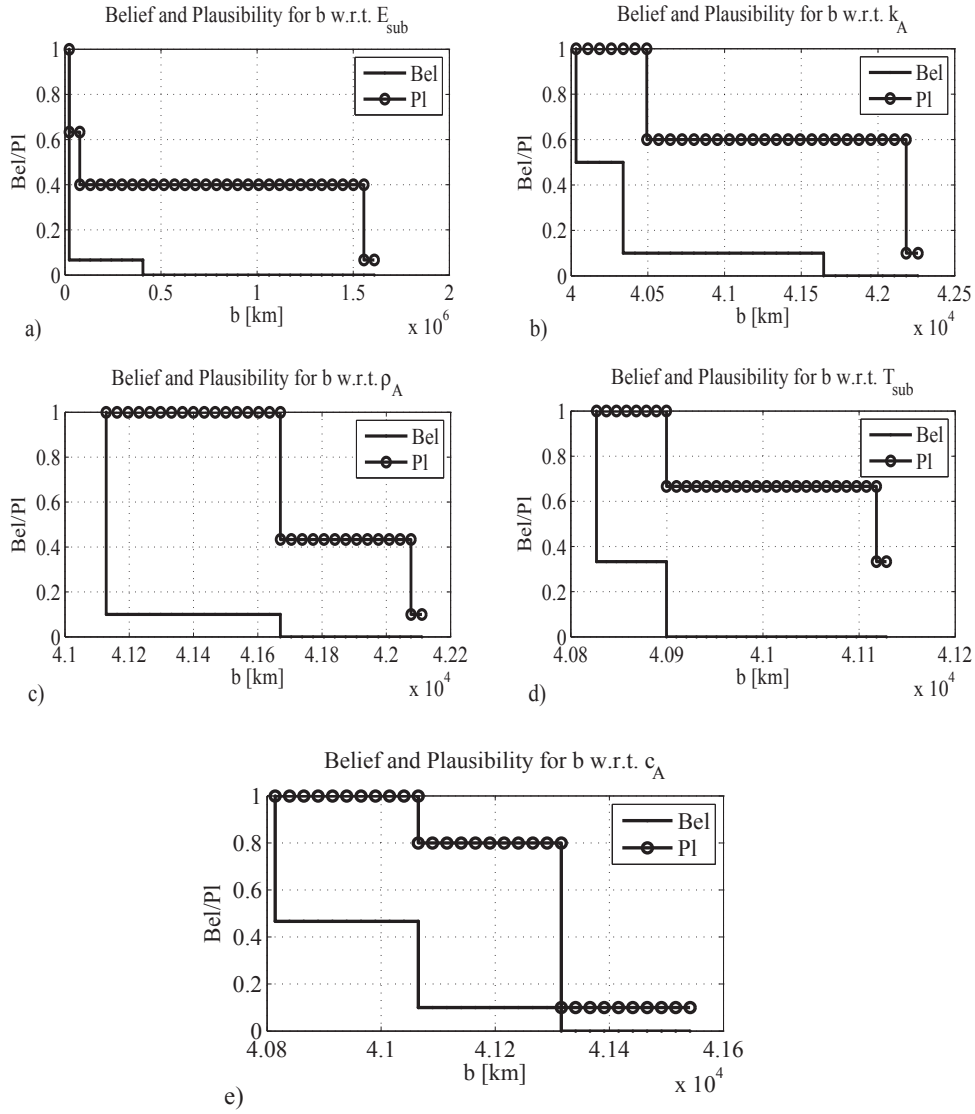

Figure 8.10: Belief/Plausibility curves for *b* w.r.t. the physical parameters.

It is interesting to observe that the Bel/Pl curves for *b* follows a *stepped* trend with three large variations while the mass' curves have a more gradual increase from 0 to 1. This possibly means that the impact parameter is mostly influenced by a single physical parameter rather than by a combination of many of them. In order to identify the most influent parameter, one can calculate the Belief and Plausibility curves for design point 1 with respect to each individual physical parameter while considering the remaining ones as constants with the values in Table 8.7. This analysis does not consider the coupling or interdependency of the parameter and therefore does not provide a complete picture of the impact of one uncertain parameter on the system performance. Nonetheless it gives a qualitative indication of the relative importance of the uncertain parameters. The results are shown in Figure 8.10.

In Figure 8.10a one sees that in the case of the sublimation enthalpy the difference in impact parameters between the points at *Bel*=1 and *Pl*=0 is much greater than in the four other cases (Figure 8.10b to Figure 8.10e).

This shows that the wide boundaries introduced on the enthalpy are a driving factor in determining the wide spreading between the best case and worst case impact parameter *b*. It also means that, with the current knowledge on the value of the sublimation enthalpy (see Table 8.5), a tight enclosure of the performance of the laser ablation system is not possible.

8.7 Conclusions

This chapter presented the combined orbital and system model for the Multi-Objective optimisation under uncertainties of the deflection of an asteroid with laser ablation. A fast and accurate analytical propagation of the low-thrust deflection action, through *rectification*, combined with MACS2, allowed for the fast computation of the Pareto set of optimal solutions for the asteroid deflection problem. The Multi-Objective optimisation without accounting for uncertainty showed that solar-pumped laser ablation can easily achieve considerable NEO deviations with a launch mass within current or near future technological capabilities. The uncertainty on some critical technologies and NEO physical characteristics were modelled and quantified through Evidence Theory. By including these uncertainties in the optimisation process, one can observe that in the worst case scenario the effectiveness of the whole concept is severely compromised. The analysis of the Belief and Plausibility curves has revealed that the sublimation enthalpy is the most critical uncertain parameter, due to its wide range of values which depends on asteroid type and also to the disagreement of different sources. The Optimisation Under Uncertainty (OUU) proposed in this chapter highlighted the key knowledge areas which will require better investigation in the near future. Furthermore, it provides a quantitative measure of which solutions should be adopted to make the deflection mission more robust. A remarkable result emerging from the OUU is that a multi-spacecraft mission is significantly more resilient against uncertainty than a single-spacecraft mission with equivalent power.

Chapter 9.Conclusions

The topic of this dissertation was the Multi-Objective design of LT trajectories and its applications. Among the objectives, enunciated at the beginning of this dissertation, there was the development of an efficient MOO algorithm, of which, MACS2 is the result. Another key objective was the elaboration of a methodology for the fast propagation of LT motion, and this was achieved through the set of analytical formulae and the propagation techniques of rectification and averaging based on them. A third objective was that of devising a simple but flexible parameterisation of the control thrust, which had to be able to model the typical patterns of LT trajectories. This objective was achieved by the control parameterisation proposed in Chapter 5 for Multi-revolution trajectories. For long, rendezvous transfer with few complete revolutions, a different strategy was devised, based on a piecewise constant thrust profile.

The combination of these three techniques forms a powerful and efficient set of tools for the multi-criteria, preliminary design of mission employing LT propulsion techniques. It is expect that this means will find their natural application in the early stages of the design of a space mission. In this regard, the case study on DESTINY presented in Chapter 7 is already a first example of application.

9.1 Summary and Findings

In the following the major findings and advancements are discussed separately along with a summary of the methods and applications developed in this thesis.

9.1.1 Memetic Multi-Objective Optimisation

One of the main paths of research focused on the development of an efficient MOO algorithm, MACS2, which was amply described in Chapter 2. MACS2 hybridised the concept of population-based search with neighbourhood exploration. The former was embodied by the Differential Evolution scheme while for the latter a Pattern Search technique was adopted. In addition, the common selection criterion based on Dominance was supplemented by a criterion based on scalarised Tchebycheff functions. The latter allowed for a more uniform distribution of the points on the Pareto Front. Furthermore, the use of the scalarisation resolves the ambiguity in the selection process based purely on dominance in the case in which dominating solutions cannot be found and there are multiple non-dominated alternatives. The combination of these two selection criteria is

regarded as a key contribution of this research work. The performance of MACS2 was validated in comparative tests with other state-of-the-art optimisation algorithms, on a set of benchmark problems. In these test cases, MACS2 showed an equal or better performance compared to the other algorithms. Of particular interest, was also the good performance of the algorithm on the test cases with more than two objectives.

9.1.2 Approximated Analytical Solution of Perturbed Keplerian Motion

In parallel, a considerable effort was devoted to the reduction of the computational effort required to propagate the orbital motion under the effect of a LT acceleration. The proposed techniques were centred around the set of analytical formulae described in Chapter 3. These were derived, by means of perturbation theory, as a first order solution to the equations of motion. Four different acceleration patterns were considered: constant acceleration in the r-θ-h reference frame, constant tangential acceleration, constant inertial acceleration, and J_2 perturbation. The numerical tests, presented in this dissertation, have shown that the combination of accuracy and computational cost of these formulae renders them advantageous compared to numerical integration schemes, when a low-to-medium fidelity propagation is required. Moreover, the above mentioned acceleration patterns can also be superimposed, allowing for enough flexibility to model more complex thrusting patterns. Compared to other analytical techniques presented by previous authors, the scope of application of the formulae presented here was not restricted to low-eccentricity orbits. Moreover, different thrusting patterns can be treated simultaneously, differently from other formulations which can handle, for example, only tangential[43] or inertially fixed[44] acceleration. The main limitation was the decaying of accuracy with the increase of the propagation interval. In order to mitigate the error growth over very long propagation arcs, a technique was implemented, involving the rectification of the reference conditions used in the analytical formulae. A by-product of this was that, each time the reference conditions are changed, so can be the perturbative acceleration, which allows for better describing time-varying acceleration patterns.

The other approach, described in Chapter 5, combined the analytical formulae with orbital averaging techniques. In particular, the formulae were used for accurately and efficiently computing the variation of the orbital elements over a single orbital revolution. This is an important innovation compared to existing averaging techniques. In the numerical tests of Chapter 5, it was shown that this approach is particularly suited for the propagation of long, multiple-revolution trajectories. The computational advantage, over

other numerical integration techniques, was noteworthy. The test case, described at the end of the chapter, on the de-orbit of MEO satellites, also confirmed the above mentioned flexibility in modelling complex perturbation patterns, like the combination of LT, SRP and J_2 of this case.

9.1.3 Control parameterisation for LT trajectories

Regarding the control parameterisation, the key objective pursued in this dissertation was that of having a reduced number of design parameters to describe the evolution of the control thrust. At the same time, these should allow for enough flexibility to model realistic thrust profiles. The first strategy adopted, presented in Chapter 4, was meant for modelling interplanetary trajectory arcs, with few (if any) complete revolutions around the central body. It envisioned subdividing the trajectory into a number of sub-arcs, each with a constant acceleration vector in the radial-transverse reference frame. The propagation was performed with the rectification method, while the optimisation of the control parameters was done here with a Multiple Shooting method. The numerical tests on Earth to Mars transfer problems have shown that this approach allows for the fast computation of minimum ΔV transfers. The resulting bang-bang thrusting pattern and the ΔV cost was very consistent with the solution obtained with a more expensive, high-fidelity model. Moreover, the 2PBVP solver was combined with MACS2 to perform a Multi-Objective analysis for a given launch window.

For multi-revolution transfers, a different approach was followed, since subdividing the trajectory into a high number of sub-arcs would have led to an excessively large number of design parameters. On the other hand, reducing the number of sub-arcs, for example, even to just one per revolution, would not have allowed to catch the switching pattern over a revolution, which is typical of these transfers. For these reasons, the control parameterisation described in Section 5.1 was introduced, which exploited the assumption that, over each revolution, the thrusting arcs were located only around the pericentre and apocentre and that the in-plane thrust direction was always aligned with the tangential direction, in order to maximise the change in orbit energy. In this way, the thrust control over a single revolution could be described with just a small number of parameters. The long-term evolution of these parameters was conveniently modelled with simple interpolating functions. As a result of this, the final set of design parameters was composed by the parameters of these functions. Additional parameters could be easily introduced to the model, as done, for example, for the out-of-plane acceleration component in the examples of Chapter 5 and in Chapter 6, or for the ω-varying thrusting pattern in Chapter 7.

The optimisation of the control parameters for this thrusting model was performed with a gradient-based method in the test cases of Chapter 5 and in Chapter 6. In the former chapter, the solution of the GEO circularisation problem provided similar results to those found in the available literature.

9.1.4 Active Debris Removal

Three case studies were presented in more detail to assess the validity of the proposed methodologies. Chapter 6 presented the interesting case of the MO design of a multi-rendezvous mission for debris removal. A surrogate model was introduced for describing the deorbiting arcs, while the rendezvous arcs were modelled with the control parameterisation described above. The propagation was performed with the *rectification* method. This features effectively allowed for lowering the computational cost of evaluating each candidate trajectory. Then, the solution of the MO instances with MACS2 identified the most convenient fetch-and-deorbit sequences.

9.1.5 Long-spiral Mission Design

Chapter 7 applied the techniques for MO, LT trajectory optimisation to the preliminary design of a JAXA mission, DESTINY. The MO formulation enabled to tackle the peculiar combination of design requirements and system-derived constraints for this mission. In particular, the first MO runs immediately revealed the criticality of the issue of eclipse mitigation, which severely limited the transfer opportunities. The flexibility of the proposed trajectory model was again put to test, since it was easily expanded in order to introduce a thrusting pattern which maximises the change of argument of perigee. Further MO runs clearly showed the effectiveness of this modification in extending the range of transfer opportunities. The performance of MACS2 was also put to a test since it had to deal with 3- to 6-objective (although in the latter case 2 objectives were spurious) with a relatively high number of design parameters. The complex dynamics of this orbit raising trajectory were realistically modelled with orbital averaging. It is also interesting to note that, in this case study, a further step was taken with regard to the parameter optimisation: differently from the previous examples, in which the control parameter optimisation was taken care of by a gradient-based algorithm, in this case MACS2 acted directly both on the control and in other parameters, like departure epoch and time of flight. In summary, the data obtained from the MO analysis of the trajectory, by means of the proposed tools, gave the mission designer a wide overview of the relative merits of the various transfer options.

9.1.6 Asteroid Deflection Under Uncertainty

In Chapter 8, the interdisciplinary design of a spacecraft constellation for NEO impact mitigation was formulated as a MOO problem. The LT-like dynamics of the NEO deviating trajectory were conveniently propagated with the analytical formulae. Epistemic and technological uncertainties, due to various sources, were introduced into the model through Evidence Theory. A specialised variant of MACS2, tailored for OUU, was developed and used to solve the MOO problems. These gave, at a glance, a good overview of the worst-case and best-case scenario, as well as identifying the most critical sources of uncertainty for the performance of the spacecraft constellation.

9.2 Future Work

The work in this thesis paved the way to several possible new developments. MACS2 has shown to be a powerful framework for implementing effective memetic strategies. Possible improvements will include mixing different local search strategies to improve the performance in the case of multimodal functions as the Cassini trajectory one. A possible path, which has already showed some promise in the context of this work, is that of the hybridisation with the Monotonic Basin Hopping methods.

Another important development field for the MOO algorithm would be that of introducing heuristic for the explicit treatment of constraints. Note that, in this dissertation, problem constraints were treated implicitly by the MOO algorithms, for example with penalties on the objective function (see, for example, Section 7.4). An explicit mechanism for tackling constraints within the optimisation process would extend the field of application of the proposed techniques to optimisation problems of even higher complexity.

The multi-rendezvous problem presented in Chapter 6 also suggested a further extension of the MOO algorithm to mixed continuous/discrete optimisation problem. This involves the concurrent optimisation both of discrete parameters (e.g. the debris sequence in this case) and of the continuous ones (thrust profile parameters, departure/rendezvous times etc.). A tool to solve such a mixed problem would, for example, allow solving an optimisation problem similar to that of Chapter 6 but with a higher number of target debris. In the case Chapter 6 this was limited to five because each of the 125 possible sequences had to be treated separately.

Finally, as for the analytical formulae, future research can be aimed at further extending the range of acceleration patterns. In particular, an approximate solution for 3^{rd} body perturbation could be highly desirable. Some previous works[159, 160] might provide an important starting point.

Appendix A.Analytical Integrals

The integrals which appear in the equations in Chapter 3 are expressed as:

$$I_{11}\left(L_0, L, P_{10}, P_{20}\right) = -\frac{2}{B}\left[\Lambda_0\left(\mathcal{L}\right)\right]_{L_0}^{L} \tag{A.1}$$

$$I_{12}\left(L_0, L, P_{10}, P_{20}\right) = \left[-\frac{2}{B^3}\Lambda_0\left(\mathcal{L}\right) - \frac{1}{P_{20}B^2}\frac{P_{10} + \left({P_{10}}^2 + {P_{20}}^2\right)\sin\mathcal{L}}{\Phi_0\left(\mathcal{L}\right)}\right]_{L_0}^{L} \tag{A.2}$$

$$I_{13}\left(L_0, L, P_{10}, P_{20}\right) = \frac{1}{2}\left[\begin{array}{l} -\dfrac{2\left(2 + {P_{10}}^2 + {P_{20}}^2\right)}{{B_0}^5}\Lambda_0\left(\mathcal{L}\right) + \\ -\dfrac{1}{P_{20}{B_0}^2}\left(\dfrac{P_{10} + \left({P_{10}}^2 + {P_{20}}^2\right)\sin\mathcal{L}}{{\Phi_0}^2\left(\mathcal{L}\right)}\right. \\ \left. + \dfrac{P_{10}\left(2 + {P_{10}}^2 + {P_{20}}^2\right) + 3\left({P_{10}}^2 + {P_{20}}^2\right)\sin\mathcal{L}}{B_0\Phi_0\left(\mathcal{L}\right)}\right) \end{array}\right]_{L_0}^{L} \tag{A.3}$$

$$I_{c2}\left(L_0, L, P_{10}, P_{20}\right) = \left[\frac{2P_{20}}{{B_0}^3}\Lambda_0\left(\mathcal{L}\right) + \frac{1}{{B_0}^2}\left(\frac{P_{10} + \sin\mathcal{L}}{\Phi_0\left(\mathcal{L}\right)}\right)\right]_{L_0}^{L} \tag{A.4}$$

$$I_{s2}\left(L_0, L, P_{10}, P_{20}\right) = \left[\frac{2P_{10}}{{B_0}^3}\Lambda_0\left(\mathcal{L}\right) - \frac{1}{P_{20}{B_0}^2}\left(\frac{{P_{20}}^2 - 1 - P_{10}\sin\mathcal{L}}{\Phi_0\left(\mathcal{L}\right)}\right)\right]_{L_0}^{L} \tag{A.5}$$

$$I_{c3}\left(L_0, L, P_{10}, P_{20}\right) = \frac{1}{2}\left[\frac{6P_{20}}{{B_0}^5}\Lambda_0\left(\mathcal{L}\right) + \frac{1}{{B_0}^2}\left(\begin{array}{l}\dfrac{P_{10} + \sin\mathcal{L}}{{\Phi_0}^2\left(\mathcal{L}\right)} + \\ \dfrac{3P_{10} + \left(1 + 2\left({P_{10}}^2 + {P_{20}}^2\right)\right)\sin\mathcal{L}}{{B_0}^2\Phi_0\left(\mathcal{L}\right)}\end{array}\right)\right]_{L_0}^{L} \tag{A.6}$$

$$I_{s3}\left(L_0, L, P_{10}, P_{20}\right) = \frac{1}{2}\left[\frac{6P_{10}}{{B_0}^5}\Lambda_0\left(\mathcal{L}\right) + \frac{1}{P_{20}{B_0}^2}\left(\begin{array}{l}\dfrac{1 - {P_{20}}^2 + P_{10}\sin\mathcal{L}}{{\Phi_0}^2\left(\mathcal{L}\right)} + \\ \dfrac{P_{10}\left(3P_{10} + \left(1 + 2\left({P_{10}}^2 + {P_{20}}^2\right)\right)\sin\mathcal{L}\right)}{{B_0}^2\Phi_0\left(\mathcal{L}\right)}\end{array}\right)\right]_{L_0}^{L} \tag{A.7}$$

$$I_{t1} = \left(I_{13} - \frac{I_{12}}{\Phi_0\left(L_0\right)}\right) \tag{A.8}$$

$$I_{t2}\left(L_0,L,P_{10},P_{20}\right)=\frac{1}{2\left(1-P_{20}\right)B_0{}^3}\left[\begin{array}{l}2\left(P_{20}-1\right)\Lambda_0{}^2\left(\mathcal{L}\right)+\\ \cos\left(2\Lambda_0\left(\mathcal{L}\right)\right)\left(2P_{10}B_0\Lambda_0\left(\mathcal{L}\right)-\left(P_{10}{}^2+P_{20}{}^2\right)+P_{20}\right)+\\ -\sin\left(2\Lambda_0\left(\mathcal{L}\right)\right)\left(2P_{10}B_0+\left(\left(P_{10}{}^2+P_{20}{}^2\right)-P_{20}\right)\Lambda_0\left(\mathcal{L}\right)\right)\end{array}\right]_{L_0}^{L} \quad \text{(A.9)}$$

$$\Lambda_0\left(L\right)=\operatorname{atan}\left(\frac{1}{B}\left(-P_{10}+\left(P_{20}-1\right)\tan\left(\frac{L}{2}\right)\right)\right) \quad \text{(A.10)}$$

$$I_{2c3}\left(L_0,L,P_{10},P_{20}\right)=\frac{1}{B_0{}^4}\left[\begin{array}{l}\frac{P_{10}{}^2-2P_{20}{}^2-1}{B_0}\Lambda_0\left(\mathcal{L}\right)-\\ \frac{\left(\begin{array}{l}\Phi_0\left(\mathcal{L}\right)\left(P_{10}\left(2-3P_{10}{}^2+P_{10}{}^4+\left(5P_{10}{}^2-3\right)P_{20}{}^2+4P_{20}{}^4\right)+\right.\\ \left(P_{10}{}^2-P_{10}{}^4-P_{20}{}^2+3P_{10}{}^2P_{20}{}^2+4P_{20}{}^4\right)\sin\mathcal{L}\left.\right)+\\ B_0{}^2\left(P_{10}\left(-1+P_{10}{}^2-2P_{20}{}^2\right)+\left(P_{20}{}^2-P_{10}{}^2B_0{}^2\right)\sin\mathcal{L}\right)\end{array}\right)}{4P_{20}\left(P_{10}{}^2+P_{20}{}^2\right)\Phi_0{}^2\left(\mathcal{L}\right)}\end{array}\right]_{L_0}^{L} \quad \text{(A.11)}$$

$$I_{1c1s3}\left(L_0,L,P_{10},P_{20}\right)=\frac{1}{B_0{}^2}\left[\begin{array}{l}-\frac{3P_{10}P_{20}}{B_0{}^3}\Lambda_0\left(\mathcal{L}\right)+\\ \frac{\left(\begin{array}{l}\left(-1+P_{20}{}^2+P_{10}\left(-2+P_{10}{}^2+P_{20}{}^2\right)\sin\mathcal{L}\right)-\\ \Phi_0\left(\mathcal{L}\right)\left(-P_{10}{}^4+P_{10}{}^2\left(-4+P_{20}{}^2\right)+\right.\\ \left.2\left(P_{20}{}^2-1\right)^2-P_{10}\left(-2+5\left(P_{10}{}^2+P_{20}{}^2\right)\right)\sin\mathcal{L}\right)\end{array}\right)}{2\Phi_0{}^2\left(\mathcal{L}\right)}\end{array}\right]_{L_0}^{L} \quad \text{(A.12)}$$

$$I_{2s3}\left(L_0,L,P_{10},P_{20}\right)=\left[\begin{array}{l}\frac{P_{20}{}^2-2P_{10}{}^2-1}{B_0{}^5}\Lambda_0\left(\mathcal{L}\right)-\\ \frac{\left(\begin{array}{l}\Phi_0\left(\mathcal{L}\right)\left(P_{10}\left(2-5P_{10}{}^2+\left(3P_{10}{}^2-5\right)P_{20}{}^2+3P_{20}{}^4\right)+\right.\\ \left(P_{10}{}^2-4P_{10}{}^4-P_{20}{}^2-3P_{10}{}^2P_{20}{}^2+P_{20}{}^4\right)\sin\mathcal{L}\left.\right)-\\ B_0{}^2\left(P_{10}\left(1-P_{20}{}^2\right)+\left(P_{10}{}^2-P_{20}{}^2B_0{}^2\right)\sin\mathcal{L}\right)\end{array}\right)}{2P_{20}B_0{}^2\left(P_{10}{}^2+P_{20}{}^2\right)\Phi_0{}^2\left(\mathcal{L}\right)}\end{array}\right]_{L_0}^{L} \quad \text{(A.13)}$$

$$I_a=\left[\frac{1}{1-e_0}E\left(\frac{\vartheta}{2},\frac{4e_0}{\left(1+e_0\right)^2}\right)+\frac{1}{1+e_0}F\left(\frac{\vartheta}{2},\frac{4e_0}{\left(1+e_0\right)^2}\right)-\frac{\sqrt{1+e_0{}^2+2e_0\cos\vartheta}e_0\sin\vartheta}{\left(1-e_0\right)^2\left(1+e_0\cos\vartheta\right)}\right]_{\theta_0}^{\theta} \quad \text{(A.14)}$$

$$I_{P1}=\frac{1}{e_0\left(1-e_0\right)}\left[\begin{array}{l} E\left(\frac{\vartheta}{2},\frac{4e_0}{\left(1+e_0\right)^2}\right)-\frac{1}{\left(1+{e_0}^2\right)\left(1+e_0\right)^2}F\left(\frac{\vartheta}{2},\frac{4e_0}{\left(1+e_0\right)^2}\right)+ \\ +\frac{1}{2\left(1+e_0\right)}\log\left(\frac{\sqrt{1+{e_0}^2+2e_0\cos\vartheta}+e_0\sin\vartheta}{\sqrt{1+{e_0}^2+2e_0\cos\vartheta}-e_0\sin\vartheta}\right)+ \\ -\frac{\sqrt{1+{e_0}^2+2e_0\cos\vartheta}e_0\sin\vartheta}{\left(1+e_0\right)\left(1+e_0\cos\vartheta\right)} \end{array}\right]_{\theta_0}^{\theta} \tag{A.15}$$

$$I_{P2}=-\frac{1}{e_0\left(1-{e_0}^2\right)}\left[\frac{2}{\sqrt{1-{e_0}^2}}\operatorname{atan}\left(\frac{\sqrt{1+{e_0}^2+2e_0\cos\vartheta}}{\sqrt{1-{e_0}^2}}\right)+\frac{\sqrt{1+{e_0}^2+2e_0\cos\vartheta}}{\left(1+e_0\cos\vartheta\right)}\right]_{\theta_0}^{\theta} \tag{A.16}$$

$$I_{Ja}\left(L_0,L,P_{10},P_{20}\right)=-\left[\begin{array}{l} -3\left(\begin{array}{l} G_0^2P_{20}(4+P_{10}^2+P_{20}^2)-2P_{20}(18+3P_{10}^2+5P_{20}^2)Q_{10}^2+ \\ 4P_{10}(6+P_{10}^2+3P_{20}^2)Q_{10}Q_{20}-2P_{20}(6+3P_{10}^2+P_{20}^2)Q_{20}^2 \end{array}\right)\cos\mathcal{L}+ \\ 6\left(G_0^2(P_{10}-P_{20})(P_{10}+P_{20})+4(1+3P_{20}^2)Q_{10}^2-4(1+3P_{10}^2)Q_{20}^2\right)\cos(2\mathcal{L})+ \\ \left(\begin{array}{l} G_0^2(3P_{10}^2P_{20}-P_{20}^3)+3P_{20}(12-3P_{10}^2+5P_{20}^2)Q_{10}^2+ \\ 18P_{10}(4+P_{10}^2+P_{20}^2)Q_{10}Q_{20}-3P_{20}(12+9P_{10}^2+P_{20}^2)Q_{20}^2 \end{array}\right)\cos(3\mathcal{L})+ \\ 18\left(P_{20}(Q_{10}-Q_{20})+P_{10}(Q_{10}+Q_{20})\right)\left(P_{10}(Q_{20}-Q_{10})+P_{20}(Q_{10}+Q_{20})\right)\cos(4\mathcal{L})+ \\ 3\left(\begin{array}{l} -2P_{10}^3Q_{10}Q_{20}+6P_{10}P_{20}^2Q_{10}Q_{20}+ \\ P_{20}^3(Q_{10}-Q_{20})(Q_{10}+Q_{20})+3P_{10}^2P_{20}(-Q_{10}^2+Q_{20}^2) \end{array}\right)\cos(5\mathcal{L})+ \\ -3\left(\begin{array}{l} G_0^2P_{10}(4+P_{10}^2+P_{20}^2)-2P_{10}(6+P_{10}^2+3P_{20}^2)Q_{10}^2+ \\ 4P_{20}(6+3P_{10}^2+P_{20}^2)Q_{10}Q_{20}-2P_{10}(5P_{10}^2+3(6+P_{20}^2))Q_{20}^2 \end{array}\right)\sin(\mathcal{L})+ \\ -12\left(\begin{array}{l} G_0^2P_{10}P_{20}+6P_{10}^2Q_{10}Q_{20}+ \\ 2(2+3P_{20}^2)Q_{10}Q_{20}-6P_{10}P_{20}(Q_{10}^2+Q_{20}^2) \end{array}\right)\sin(2\mathcal{L})+ \\ \left(\begin{array}{l} G_0^2(P_{10}^3-3P_{10}P_{20}^2)+3P_{10}(12+P_{10}^2+9P_{20}^2)Q_{10}^2+ \\ -18P_{20}(4+P_{10}^2+P_{20}^2)Q_{10}Q_{20}-3P_{10}(12+5P_{10}^2-3P_{20}^2)Q_{20}^2 \end{array}\right)\sin(3\mathcal{L})+ \\ 36\left(P_{20}Q_{10}+P_{10}Q_{20}\right)\left(P_{10}Q_{10}-P_{20}Q_{20}\right)\sin(4\mathcal{L})+ \\ 3\left(\begin{array}{l} 6P_{10}^2P_{20}Q_{10}Q_{20}-2P_{20}^3Q_{10}Q_{20}+ \\ 3P_{10}P_{20}^2(Q_{10}-Q_{20})(Q_{10}+Q_{20})+P_{10}^3(-Q_{10}^2+Q_{20}^2) \end{array}\right)\sin(5\mathcal{L}) \end{array}\right]_{L_0}^{L} \tag{A.17}$$

$$
I_{JP_1}(L_0, L, P_{10}, P_{20}) = -\left[\begin{array}{l}
-12P_{20}\left(G_0^2 + 2(-4 + Q_{10}^2 + Q_{20}^2)(Q_{10}^2 + Q_{20}^2)\right)\mathcal{L} + \\
6\left(\begin{array}{l} G_0^2 P_{10} P_{20} - 10P_{10}^2 Q_{10} Q_{20} + \\ 2P_{10}P_{20}(Q_{10}^4 + 2(-5 + 2Q_{10}^2)Q_{20}^2 + 3Q_{20}^4) \\ -2Q_{10}Q_{20}(2 + P_{20}^2(-5 + 2Q_{10}^2 + 2Q_{20}^2)) \end{array}\right)\cos\mathcal{L} + \\
6\left(\begin{array}{l} G_0^2 P_{10} + 4(P_{10}(Q_{10}^2 - 4Q_{20}^2) + \\ -P_{20}Q_{10}Q_{20}(-4 + Q_{10}^2 + Q_{20}^2)) \end{array}\right)\cos(2\mathcal{L}) + \\
2\left(\begin{array}{l} G_0^2 P_{10} P_{20} + 17P_{10}^2 Q_{10} Q_{20} + \\ P_{10}P_{20}(-5Q_{10}^2 + 2Q_{10}^4 - 7Q_{20}^2 - 2Q_{20}^4) \\ +Q_{10}Q_{20}(28 + P_{20}^2(15 - 4Q_{10}^2 - 4Q_{20}^2)) \end{array}\right)\cos(3\mathcal{L}) + \\
18\left(2P_{20}Q_{10}Q_{20} + P_{10}(-Q_{10}^2 + Q_{20}^2)\right)\cos(4\mathcal{L}) + \\
6\left(P_{20}Q_{10} + P_{10}Q_{20}\right)\left(-P_{10}Q_{10} + P_{20}Q_{20}\right)\cos(5\mathcal{L}) + \\
-3\left(\begin{array}{l} G_0^2(4 + P_{10}^2 + 3P_{20}^2) - 20Q_{10}^2 - 28Q_{20}^2 + \\ 6P_{10}^2(Q_{10}^2 - 3Q_{20}^2) - 8P_{10}P_{20}Q_{10}Q_{20}(-6 + Q_{10}^2 + Q_{20}^2) \\ +2P_{20}^2(6Q_{10}^4 - 7Q_{20}^2 + 2Q_{20}^4 + Q_{10}^2(-19 + 8Q_{20}^2)) \end{array}\right)\sin(\mathcal{L}) + \\
-6\left(G_0^2 P_{20} + 20P_{10}Q_{10}Q_{20} + 2P_{20}(-7Q_{10}^2 + Q_{10}^4 + Q_{20}^2 - Q_{20}^4)\right)\sin(2\mathcal{L}) + \\
\left(\begin{array}{l} G_0^2(P_{10} - P_{20})(P_{10} + P_{20}) + Q_{10}^2(28 + 11P_{10}^2 + P_{20}^2(21 - 4Q_{10}^2)) \\ -4P_{10}P_{20}(Q_{10} + 2Q_{10}^3)Q_{20} - (28 + 23P_{10}^2 + 9P_{20}^2)Q_{20}^2 + \\ -8P_{10}P_{20}Q_{10}{}^3Q_{20} + 4P_{20}^2 Q_{20}^4 \end{array}\right)\sin(3\mathcal{L}) + \\
18\left(2P_{10}Q_{10}Q_{20} + P_{20}(Q_{10}^2 - Q_{20}^2)\right)\sin(4\mathcal{L}) + \\
3\left(P_{20}(Q_{10} - Q_{20}) + P_{10}(Q_{10} + Q_{20})\right)\left(P_{10}(-Q_{10} + Q_{20}) + P_{20}(Q_{10} + Q_{20})\right)\sin(5\mathcal{L})
\end{array}\right] \qquad \text{(A.18)}
$$

$$I_{JP_2}(L_0,L,P_{10},P_{20}) = -\left[\begin{array}{l}
12P_{10}\left(G_0^2+2(-4+Q_{10}^2+Q_{20}^2)(Q_{10}^2+Q_{20}^2)\right)\mathcal{L}+\\
-3\left(\begin{array}{l}G_0^2(4+3P_{10}^2+P_{20}^2)-28Q_{10}^2+2(-10Q_{20}^2+3P_{20}^2(-3Q_{10}^2+Q_{20}^2)+\\-4P_{10}P_{20}Q_{10}Q_{20}(-6+Q_{10}^2+Q_{20}^2)+\\P_{10}^2(2Q_{10}^4-19Q_{20}^2+6Q_{20}^4+Q_{10}^2(-7+8Q_{20}^2)))\end{array}\right)\cos\mathcal{L}+\\
-6\left(G_0^2P_{20}-4(P_{20}(4Q_{10}^2-Q_{20}^2)+P_{10}Q_{10}Q_{20}(-4+Q_{10}^2+Q_{20}^2))\right)\cos(2\mathcal{L})+\\
\left(\begin{array}{l}G_0^2(P_{10}-P_{20})(P_{10}+P_{20})+Q_{10}^2(28+23P_{20}^2+P_{10}^2(9-4Q_{10}^2))+\\4P_{10}P_{20}(Q_{10}+2Q_{10}^3)Q_{20}-(28+21P_{10}^2+11P_{20}^2)Q_{20}^2+\\8P_{10}P_{20}Q_{10}{}^3Q_{20}+4P_{10}^2Q_{20}^4\end{array}\right)\cos(3\mathcal{L})+\\
18\left(2P_{10}Q_{10}Q_{20}+P_{20}(Q_{10}^2-Q_{20}^2)\right)\cos(4\mathcal{L})+\\
3\left(P_{20}(Q_{10}-Q_{20})+P_{10}(Q_{10}+Q_{20})\right)\left(P_{10}(Q_{20}-Q_{10})+P_{20}(Q_{10}+Q_{20})\right)\cos(5\mathcal{L})+\\
6\left(\begin{array}{l}G_0^2P_{10}P_{20}-2(2+5P_{20}^2)Q_{10}Q_{20}-2P_{10}^2Q_{10}Q_{20}(-5+2Q_{10}^2+2Q_{20}^2)\\+2P_{10}P_{20}(3Q_{10}^4+Q_{20}^4+2Q_{10}^2(-5+2Q_{20}^2))\end{array}\right)\sin(\mathcal{L})+\\
-6\left(G_0^2P_{10}+20P_{20}Q_{10}Q_{20}+2P_{10}(-7Q_{20}^2+Q_{20}^4+Q_{10}^2-Q_{10}^4)\right)\sin(2\mathcal{L})+\\
-2\left(\begin{array}{l}G_0^2P_{10}P_{20}+(28+17P_{20}^2)Q_{10}Q_{20}+P_{10}^2Q_{10}Q_{20}(15-4Q_{10}^2-4Q_{20}^2)\\-P_{10}P_{20}(7Q_{10}^2+2Q_{10}^4+5Q_{20}^2-2Q_{20}^4)\end{array}\right)\sin(3\mathcal{L})+\\
18\left(-2P_{20}Q_{10}Q_{20}+P_{10}(Q_{10}^2-Q_{20}^2)\right)\sin(4\mathcal{L})+\\
6\left(P_{20}Q_{10}+P_{10}Q_{20}\right)\left(P_{10}Q_{10}-P_{20}Q_{20}\right)\sin(5\mathcal{L})
\end{array}\right]_{L_0}^{L} \tag{A.19}$$

$$I_{JQ1}(L_0,L,P_{10},P_{20}) = -\left[\begin{array}{l}
6Q_{20}\mathcal{L}+\\
3\left(P_{20}Q_{10}-3P_{10}Q_{20}\right)\cos\mathcal{L}+\\
3Q_{10}\cos(2\mathcal{L})+\\
\left(P_{20}Q_{10}+P_{10}Q_{20}\right)\cos(3\mathcal{L})+\\
3\left(-P_{10}Q_{10}+P_{20}Q_{20}\right)\sin(\mathcal{L})+\\
-3Q_{20}\sin(2\mathcal{L})+\\
\left(P_{10}Q_{10}-P_{20}Q_{20}\right)\sin(3\mathcal{L})
\end{array}\right]_{L_0}^{L} \tag{A.20}$$

$$I_{JQ2}(L_0,L,P_{10},P_{20}) = -\left[\begin{array}{l}
-6Q_{10}\mathcal{L}+\\
3\left(P_{10}Q_{10}-P_{20}Q_{20}\right)\cos\mathcal{L}+\\
-3Q_{20}\cos(2\mathcal{L})+\\
\left(P_{10}Q_{10}-P_{20}Q_{20}\right)\cos(3\mathcal{L})+\\
3\left(-3P_{20}Q_{10}+P_{10}Q_{20}\right)\sin(\mathcal{L})+\\
-3Q_{10}\sin(2\mathcal{L})+\\
-\left(P_{20}Q_{10}+P_{10}Q_{20}\right)\sin(3\mathcal{L})
\end{array}\right]_{L_0}^{L} \tag{A.21}$$

Appendix B.Evidence Theory

Evidence Theory [161 ,157, 162 , 163 , 164], or Dempster-Shafer Theory, is a mathematical framework to model epistemic uncertainty and can be interpreted as a generalisation of classical probability theory. Epistemic uncertainties are typical of the preliminary phase of the design of a space mission since the experts from each engineering discipline involved are asked to provide reasonable estimations regarding the size, mass, power consumption or performance of individual components. The whole design process can be mathematically represented as a multidisciplinary optimisation problem in which a number of design parameters are uncertain or their values derive from opinions or estimations.

In Evidence Theory, the values of uncertain or vague design parameters are expressed by means of intervals with associated belief (degree of confidence in the range of values). Each expert participating in the design assigns an interval and a belief according to their opinion or rare experimental data. Evidence Theory treats these epistemic uncertainties better than probability theory since there is no reason to prefer one distribution function over another. Ultimately, all the pieces of information associated to each interval are fused together to yield two cumulative values, Belief and Plausibility, that express the confidence range in the optimal design point. In particular the value of Belief expresses the lower limit on the probability that the selected design point remains optimal (and/or feasible) even under uncertainties. More precisely it represents the lowest level of confidence in the computed value of the cost function (and/or the constraints).

B.1.Definition of Uncertainty

Uncertainties are usually classified in two distinct categories, aleatory and epistemic uncertainty. According to Helton[165], the definition of each type is:

- Aleatory Uncertainty arises from what is considered to be an inherent randomness in the behavior of the system under study. Also known as: Stochastic uncertainty, Type A uncertainty, Irreducible uncertainty, Variability, Objective uncertainty.
- Epistemic Uncertainty arises from a lack of knowledge about a quantity that is assumed to have a fixed value in the context of a particular analysis. Also known as: Subjective uncertainty, Type B uncertainty, Reducible uncertainty, State of Knowledge uncertainty, Ignorance.

- Error, also called numerical uncertainty, which is defined as "a recognizable deficiency in any phase or activity of modelling and simulation that is not due to lack of knowledge"[162]. Such uncertainties are well-known, and a good estimation of the error is generally available. This point distinguishes errors from epistemic uncertainties. Aleatory uncertainties are due to the random nature of input data while epistemic ones are generally linked to incomplete modelling of the physical system, the boundary conditions, unexpected failure modes, etc.

In the case of preliminary space mission design, analysts face both types of uncertainty. For example, the initial velocity of the spacecraft, the gravity model or the solar radiation, all present aleatory uncertainties. On the other hand, a good deal of the parameters defining the characteristics of spacecraft subsystems are not known a priori and their value cannot be computed because it depends on other unknown parameters. Therefore their value has to be first estimated on the basis of previous experience or educated guesses by a group of experts. The uncertainty associated to those parameters is therefore epistemic.

B.2. Quantification of Uncertainty in Evidence Theory

Let one define the *frame of discernement* $\mathcal{U}$ as the set of mutually exclusive elementary propositions. A possible elementary proposition can be for example

$$E = u_1 \in [\underline{u_1}_i, \overline{u_1}_i] \tag{B.1}$$

which translates into "*the parameter u_1 is comprised a certain interval* $[\underline{u_1}_i, \overline{u_1}_i]$ ". E is therefore an element of $\mathcal{U}$.

Let one define the power set $2^{\mathcal{U}}$ as a set collecting subsets of $\mathcal{U}$. One can assign, to each proposition in $2^{\mathcal{U}}$, a Basic Probability Assignment (BPA), defining the level of confidence in the proposition itself. This corresponds to the probability of an event in classical probability theory. The properties which apply to the BPA are as follows:

$$\begin{gathered} BPA(E) > 0, \forall E \in 2^{\mathcal{U}} \\ BPA(E) = 0, \forall E \notin 2^{\mathcal{U}} \\ BPA(\varnothing) = 0 \\ \sum_{E \in 2^{\mathcal{U}}} BPA(E) = 1 \end{gathered} \tag{B.2}$$

Therefore, the BPA is a function that maps the power set into [0;1]. The elements of $2^{\mathcal{U}}$ are solely defined by their associated BPA being strictly positive, and are commonly called Focal Elements (FE).

Unlike probability theory, unions and intersections of subsets of $\mathcal{U}$ are not necessarily included in the power set. This means that, given two events *F* and *G*, evidence on the event $F \cup G$ and $F \cap G$ does not give or require information on either events *F* and *G*. In contrast to probability theory, the complement of an element of $\mathcal{U}$ is not necessarily in the power set. This translates into the fact that an expression similar to $P(E)=1-P(\bar{E})$, is not necessarily true in Evicence Theory. One the contrary, an expression like the following can apply:

$$\sum_i BPA(E^i) + \sum_{i,j} BPA(E^i \cup E^j) = 1 \tag{B.3}$$

With reference to Equation (B.1), this for example means that the intervals can not only be disconnected, but also overlapping. Therefore, the power set $2^{\mathcal{U}}$ and the BPA are less structured than their counterparts of probability theory and allow for greater flexibility in representing incomplete or contradictory information.

If the space uncertain parameters is multidimensional, the power set is composed by the Cartesian product of elements of the power sets of each parameter's frame of discernment: $2^{(\mathcal{U}1,\mathcal{U}2)}=2^{\mathcal{U}1}\times 2^{\mathcal{U}2}$. Given two focal elements $FE_i^1 = u_1 \in [\underline{u_{1_i}}, \overline{u_{1_i}}]$ and $FE_j^2 = u_1 \in [\underline{u_{1_j}}, \overline{u_{1_j}}]$, for variable u_1 and u_2 respectively, the associated BPA of $FE_i^1 \times FE_j^2$ is the product of the BPA of the two corresponding focal elements:

$$BPA\left((u_1,u_2) \in [\underline{u_{1_i}}, \overline{u_{1_i}}] \times [\underline{u_{2_j}}, \overline{u_{2_j}}]\right) = BPA\left(u_1 \in [\underline{u_{1_i}}, \overline{u_{1_i}}]\right) \cdot BPA\left(u_2 \in [\underline{u_{2_j}}, \overline{u_{2_j}}]\right) \tag{B.4}$$

This also means that, the total number of focal elements for all uncertain parameters is given by the product of the number of focal elements for each parameter.

B.3.Belief and Plausibility

Differently from Probability Theory, Evidence Theory uses two complementary quantities to measure the cumulative confidence, or belief, in a given proposition: Belief and Plausibility. To explain their meaning, let one consider a performance parameter *y*, which is a function *f* of the design parameters **x** and of the uncertain parameters **u**. The set of all *y* which are below a certain threshold *v* is defined as:

$$Y_v = \{y : y = f(\mathbf{x},\mathbf{u}) < v, \mathbf{x} \in D, \mathbf{u} \in U\} \tag{B.5}$$

then the Belief and Plausibility associated to the proposition $y<v$ are:

$$\begin{aligned} Bel(Y_v) &= \sum_{j \in I_B} BPA(U^j) \\ Pl(Y_v) &= \sum_{j \in I_P} BPA(U^j) \end{aligned} \tag{B.6}$$

with

$$I_B = \left\{ j : U^j \subset f^{-1}(Y_v) \right\}$$
$$I_P = \left\{ j : U^j \cap f^{-1}(Y_v) \neq 0 \right\} \tag{B.7}$$

It should be noted that I_B is always a subset of I_P, i.e. $I_B \subseteq I_P$ and in this sense Belief and Plausibility can be interpreted as respectively the lower and upper boundary for the likelihood of an event.

To better illustrate how focal elements contribute to Belief and Plausibility, let one consider the focal elements in Figure B.1. The purple dotted line represents the set Y_v. All focal elements which are fully contained in Y_v (in green in the figure) belong to the set I_B, while those which at least intersect it (the blue and the green elements), belong to set I_B.

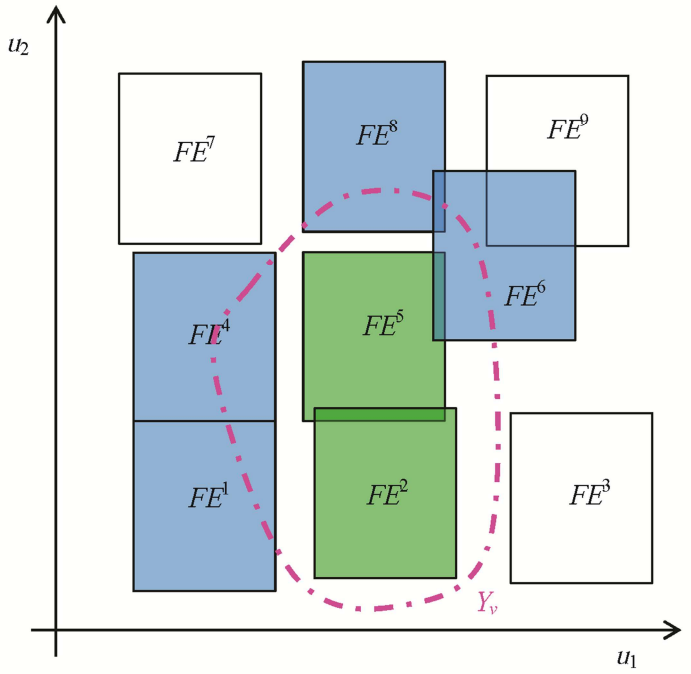

Figure B.1: Focal Elements, Belief and Plausibility sets.

Differently from the probability of an event and its opposite, Belief and Plausibility are not strictly complementary. Instead the following relationships apply, as also shown in Figure B.2:

$$Bel(A) + Bel(\bar{A}) \leq 1$$
$$Pl(A) + Pl(\bar{A}) \geq 1$$
$$Bel(A) + Pl(\bar{A}) = 1 \tag{B.8}$$

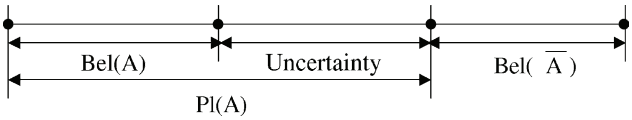

Figure B.2: Belief and Plausibility

References

[1] http://nmp.jpl.nasa.gov/ds1/ (retrieved on 28 April 2013).

[2] http://www.jaxa.jp/projects/sat/muses_c/index_e.html (retrieved on 27 April 2013).

[3] http://www.esa.int/Our_Activities/Observing_the_Earth/GOCE (retrieved on 28 April 2013).

[4] http://dawn.jpl.nasa.gov/ (retrieved on 27 April 2013).

[5] Russell, C.T., Capaccioni, F., Coradini, A., De Sanctis, M.C., Feldman, W.C., Jaumann, R., Keller, H.U., McCord, T.B., McFadden, L.A., Mottola, S., S., Pieters, C.M., Prettyman, T.H., Raymond, C.A., Sykes, M.V., Smith, D.E. and Zuber, M.T.: "Dawn mission to Vesta and Ceres", Earth Moon Planets, Vol. 101, No. 1–2, 65–91 (2007).

[6] Tsuda, Y., Yoshikawa, M., Abe, M., Minamino, H. and Nakazawa, S.: "System design of the Hayabusa 2 - Asteroid sample return mission to 1999 JU3", Acta Astronautica, Vol. 91, 356-362 (2013).

[7] http://sci.esa.int/science-e/www/area/index.cfm?fareaid=30 (retrieved on 27 April 2013).

[8] http://en.wikipedia.org/wiki/Jupiter_Icy_Moons_Orbiter (retrieved on 28 April 2013).

[9] Kawakatsu, Y. and Iwata, T.: "DESTINY Mission Overview - A Small Satellite Mission for Deep Space Exploration the Technology Demonstration", The 13th International Space Conference of Pacific‐basin Societies, (2012).

[10] http://messenger.jhuapl.edu/ (retrieved on 27 April 2013).

[11] http://spaceflight.nasa.gov/shuttle/support/researching/aspl/vasimr.html (retrieved on 22 November 2013).

[12] Chang Diaz, F.R., Hsu, M.M., Braden, E., Johnson, I. and Yang, F.T.: "Rapid Mars transit with exhaust-modulated plasma propulsion", NASA Technical Paper 3539 (1995).

[13] Bramanti, C., Walker, R., Sutherland, O., Boswell, R., Charles, C., Frigot, P., Orlandi, M., del Amo, J. and Fearn, D.: "The Innovative Dual-Stage 4-Grid Ion Thruster Concept-Theory and First Experimental Results", Paper IAC-06-C4.4.7, 57th International Astronautical Congress, Valencia, Spain (2006),

[14] Betts, J.T.: "Survey of Numerical Methods for Trajectory Optimization", Journal of guidance, control, and dynamics, Vol.21, No.2, 193-207 (1998).

[15] Conway, B.A.: “A brief survey of methods available for numerical optimization of spacecraft trajectories”, 61th International Astronautical Congress of the International Astronautical Federation, Prague, Czech Republic, IAC-10-C1.2.1 (2010).

[16] Ranieri, C.L., Ocampo, C.A.: “Optimization of roundtrip, time-constrained, finite burn trajectories via an indirect method, Journal of Guidance, Control and Dynamics”, Vol.28 No.2, 306-314 (2005).

[17] Betts, J.T.: “Very low-thrust trajectory optimization using a direct SQP method”, Journal of Computational and Applied Mathematics, Vol. 120, No. 1, 27-40 (2000).

[18] Betts, J.T., Erb, S.O.: “Optimal Low-Thrust trajectories to the moon”, SIAM Journal on Applied Dynamical Systems, Vol.2, 144 (2003).

[19] Conway, B.A., Tang, S.: “Optimization of low-thrust interplanetary trajectories using collocation and nonlinear programming”, Journal of Guidance, Control, and Dynamics, Vol.18, No.3, 599-604 (1995).

[20] Vasile, M.: “Finite elements in time: a direct transcription method for optimal control problems”, AIAA/AAS Astrodynamics Specialist Conference, 2-5 August 2010, Toronto, Ontario, Canada (2010).

[21] Petropoulos, A.E., Longuski, J.M.: “Shape-Based Algorithm for the Automated Design of Low-Thrust, Gravity-Assist Trajectories”, Journal of Spacecraft and Rockets, Vol.41, No.5, 787-796, 2004.

[22] Wall, B.J., Conway, B.A., “Shape-based approach to low-thrust rendezvous trajectory design”, Journal of Guidance, Control and Dynamics, Vol.32, No.1, 95-101 (2009).

[23] Vasile, M., De Pascale, P., Casotto, S.: “On the optimality of a shape-based approach based on pseudo-equinoctial elements”, Acta Astronautica, Vol.61, No.1-6, 286-297 (2007).

[24] Novak, D.M., Vasile, M.: “Improved Shaping Approach to the Preliminary Design of Low-Thrust Trajectories”, Journal of Guidance, Control and Dynamics, Vol.34, 128-147 (2011).

[25] Azimov, D., Bishop, R.H.: “Planetary capture using low-thrust propulsion”, 16th International Symposium on Space Flight Dynamics. Pasadena, California (2001).

[26] Sims, J.A., Flanagan, S.N.: “Preliminary Design of Low-Thrust Interplanetary Missions”, Paper AAS 99-338 (1999).

[27] Vavrina, M.A., Howell, K.C.: “Global Low-Thrust Trajectory Optimization through Hybridization of a Genetic Algorithm and a Direct Method”, AIAA/AAS Astrodynamics Specialist Conference, 18-21 (2008).

[28] Yam, C.H., Di Lorenzo, D.D., Izzo, D.: Low-thrust trajectory design as a constrained global optimization problem, Proceedings of the Institution of Mechanical Engineers, Part G: Journal of Aerospace Engineering, Vol. 225, No. 11, 1243-1251 (2011).

[29] Kechichian, J.A.: "Reformulation of Edelbaum's low-thrust transfer problem using optimal control theory", Journal of Guidance, Control, and Dynamics, Vol. 20, No. 5, 988-994 (1997).

[30] Kechichian, J.A.: "The treatment of the earth oblateness effect in trajectory optimization in equinoctial coordinates", Acta Astronautica, Vol. 40, 69-82, Elsevier (1997).

[31] Kechichian, J.A.: "Low-Thrust Eccentricity-Constrained Orbit Raising", Journal of Spacecraft and Rockets, Vol. 35, No. 3, 327-335 (1998).

[32] Kechichian, J.A.: "Orbit Raising with Low-Thrust Tangential Acceleration in Presence of Earth Shadow", Journal of Spacecraft and Rockets, Vol. 35, No. 4, 516-525 (1998).

[33] Kechichian, J.A.: "Low-thrust inclination control in presence of Earth shadow", Journal of Spacecraft and Rockets, Vol. 35, No. 4, 526-532 (1998).

[34] Kechichian, J.A.: "The streamlined and complete set of the nonsingular J2-perturbed dynamic and adjoint equations for trajectory optimization in terms of eccentric longitude", The Journal of the Astronautical Sciences, Vol. 55, No. 3, 325-348 (2007).

[35] Evtushenko, Yu. G.: "Investigation of the motion in a central field under the action of a constant tangential acceleration" (in Russian), Prikl. Mat. Mekh., Vol. 30, No. 3 (1966).

[36] Beletsky, V.V.: "Essays on the Motion of Celestial Bodies", Birkhäuser Verlag (1999).

[37] Kluever, C.A. and Oleson, S.R.: "Direct approach for computing near-optimal low-thrust Earth-orbit transfers", Journal of Spacecraft and Rockets, Vol. 35, No. 4, 509-515, AIAA (1998).

[38] Gao, Y., Kluever, C.A.: "Orbit Raising with Low-Thrust tangential thrust", Journal of Guidance, Control and Dynamics, Vol. 15, No. 6, 1503-1507 (2005).

[39] Geffroy, S. and Epenoy, R.: "Optimal low-thrust transfers with constraints, generalization of averaging techniques", Acta Astronautica, Vol. 41, Nr 3, 133-149 (1997).

[40] Ferrier, C., Epenoy, R.: "Optimal control for engines with electro-ionic propulsion under constraint of eclipse", Acta Astronautica, Vol. 48, No. 4, 181-192 (2001).

[41] Petropoulos, A.E.: "Simple Control Laws for Low-Thrust Orbit Transfers", Vol. 116, 2031-2047 (2003).

[42] Colombo, C., Vasile, M. and Radice, G.: "Semi-analytical solution for the optimal low-thrust deflection of Near-Earth Objects", Journal of Guidance, Control and Dynamics, Vol. 32, No. 3, 796-809, AIAA (2009).

[43] Bombardelli, C., Baù, G. and Peláez, J., "Asymptotic solution for the two-body problem with constant tangential thrust acceleration", Celestial Mechanics and Dynamical Astronomy, Vol. 110, No. 3, 1-18, Springer (2011).

[44] Lantoine, G., Russell, Ryan P.: "The Stark Model: an exact, closed-form approach to low-thrust trajectory optimization", 21st International Symposium on Space Flight Dynamics (2009).

[45] Lantoine, G., Russell, Ryan P.: "Complete closed-form solutions of the Stark problem", Celestial Mechanics and Dynamical Astronomy, Vol. 103, No. 4, 333-366 (2011).

[46] Zuiani, F., Vasile, M., Palmas, A. and Avanzini, G.: "Direct Transcription of Low-Thrust trajectories with Finite Trajectory Elements", Acta Astronautica, Vol.72, March–April 2012, 108-120 (2012).

[47] Coverstone-Carroll, V.L., Hartmann, J.W. and Mason, W.J.: "Optimal multi-objective low-thrust spacecraft trajectories", Computer methods in applied mechanics and engineering, Vol. 186, No.2, 387-402 (2000).

[48] Srinivas, N. and Deb., K.: "Multi-objective optimization using non-dominated sorting in genetic algorithms", Evolutionary computation, Vol. 2, No. 3, 221-248 (1994).

[49] Sauer Jr., C.G.: "Optimization of multiple target electric propulsion trajectories", Paper N. 76-205, AIAA 11th Aerospace Sciences Meeting, Washington DC (1973).

[50] Lee, S., von Ailmen, P., Fink, W., Petropoulos, A.F. and Terrile, R.J.: "Design and optimization of low-thrust orbit transfers", 2005 IEEE Aerospace Conference, 855-869 (2005).

[51] Schütze, O., Vasile, M., Junge, O., Dellnitz, M., Izzo, D.: "Designing optimal low-thrust gravity-assist trajectories using space pruning and a multi-objective approach", Engineering Optimization, Vol. 41, No. 2, 155-181 (2009).

[52] Kemble, S.: "Interplanetary mission analysis and design", Springer (2006).

[53] Vasile, M.: "Robust mission design through evidence theory and Multi-Agent Collaborative Search", Annals of the New York Academy of Sciences, Vol.1065, No.1, 152-173 (2005).

[54] Vasile, M., Zuiani, F.: "Multi-Agent Collaborative Search: an agent-based memetic Multi-Objective optimization algorithm applied to space trajectory design", Proceedings of

the Institution of Mechanical Engineers, Part G: Journal of Aerospace Engineering, Vol.25, No.11, 1211-1227 (2011).

[55] Zuiani, F., Vasile, M.: "Multi-Agent Collaborative Search with Tchebycheff decomposition and Monotonic Basin Hopping steps", BIOMA2012, Bohinij, Slovenia (2012).

[56] Zuiani, F. , Vasile, M.: "Multi agent collaborative search based on tchebycheff decomposition", Computational Optimization and Applications, Vol. 56, No. 1, 189-208 (2013).

[57] Zuiani, F., Vasile, M.: "Preliminary design of debris removal missions by means of simplified models for Low-Thrust, many revolution transfers", International Journal of Aerospace Engineering (2012).

[58] Zuiani, F., Vasile, M., Gibbings, A.: "Evidence-based robust design of deflection actions for Near Earth Objects", Celestial Mechanics and Dynamical Astronomy, Vol. 114, No. 1, 107-136 (2012).

[59] Zuiani, F., Kawakatsu Y., Vasile, M.: "Multi-Objective optimisation of many-revolution, Low-Thrust orbit raising for DESTINY mission", Paper AAS 13-257, 23rd AAS/AIAA Space Flight Mechanics Meeting, Kauaii, Hawaii, U.S.A. (2013).

[60] Zuiani, F.: "Multi-Objective optimisation of many-revolution, Low-Thrust orbit raising for DESTINY mission", JSPS short-term fellowship final report (2013).

[61] Vasile, M.: "A behavioral-based meta-heuristic for robust global trajectory optimization", IEEE Congress on Evolutionary Computation (CEC 2007), 2056-2063 (2007).

[62] Vasile, M. and Locatelli, M.: "A hybrid multiagent approach for global trajectory optimization", Journal of Global Optimization, Vol. 44, No. 4, 461-479 (2009).

[63] Maddock, C.A., Vasile, M.: "Design of optimal spacecraft-asteroid formations through a hybrid global optimization approach", International Journal of Intelligent Computing and Cybernetics, Vol.1, No.2, 239-268 (2008).

[64] Sanchez, J.P., Colombo, C., Vasile, M., Radice, G.: "Multi-criteria comparison among several mitigation strategies for dangerous near earth objects", Journal of Guidance, Control and Dynamics, Vol.32, No.1, 121-142 (2009).

[65] Zhang Q., Li H.: "MOEA/D: A multiobjective evolutionary algorithm based on decomposition", IEEE Transactions on Evolutionary Computation, Vol.11, No.6, 712-731 (2007).

[66] Sindhya K., Sinha A., Deb K., Miettinen K.: “Local search based evolutionary multi-objective optimization algorithm for constrained and unconstrained problems”, Transactions of the IEEE Congress on Evolutionary Computation (CEC’09), 2919-2926 (2009).

[67] Miettinen, K.: “Nonlinear multiobjective optimization”, Springer (1999).

[68] Fliege, J., Grana Drummond, L.M., Svaiter, B. F.: “Newton's method for multiobjective optimization”, SIAM Journal on Optimization, Vol. 20, No. 2, 602-626 (2009).

[69] Fliege, J., Svaiter, B.F.: “Steepest descent methods for multicriteria optimization”, Mathematical Methods of Operations Research, Vol. 51, No.3, 479-494 (2000).

[70] Kirkpatrick, S., Gelatt, J.D. and Vecchi, M.P.: “Optimization by simulated annealing”, Science, New Series, Vol. 220, No. 4598, 671-680 (1983).

[71] Storn, R., Price, K.: “Differential evolution--a simple and efficient heuristic for global optimization over continuous spaces”, Journal of global optimization, Vol.11, No.4, 341-359 (1998).

[72] Neri, F., Tirronen, V.: “Recent advances in differential evolution: a survey and experimental analysis”, Artificial Intelligence Review, Vol.33, No.1-2, 61-106 (2010).

[73] Hansen, N., Ostermeier, A.: “Completely derandomized self-adaptation in evolution strategies”, Evolutionary computation, Vol.9, No.2, 159-195 (2001).

[74] Kennedy, J., Eberhart, R.: “Particle swarm optimization”, Proceedings of the IEEE International Conference on Neural Networks, Vol.4, 1942-1948 (1995).

[75] Dorigo, M., Blum, C.: “Ant colony optimization theory: A survey”, Theoretical computer science, Vol.344, No.2, 243-278 (2005).

[76] Knowles, J., Corne, D.: “Approximating the nondominated front using the Pareto archived evolution strategy”, Evolutionary computation, Vol.8, No.2, 149-172 (2000).

[77] Coello Coello, C. A., Toscano Pulido, G., Lechuga, M.S.: “Handling multiple objectives with particle swarm optimization”, IEEE Transactions on Evolutionary Computation, Vol.8, No.3, 256-279 (2004).

[78] Deb, K., Pratap, A., Agarwal, S., Meyarivan .M.T.: “A fast and elitist multiobjective genetic algorithm: NSGA-II”, IEEE Transactions on Evolutionary Computation, Vol.6, No.2, 182-197 (2002).

[79] Ishibuchi H., Yoshida T.: “Hybrid Evolutionary Multi-Objective Optimization Algorithms”, Soft Computing Systems: Design, Management and Applications, 163-172, IOS Press (2002).

[80] Erfani T., Utyuzhnikov S.: “Directed search domain: a method for even generation of the Pareto frontier in multiobjective optimization”, Engineering Optimization Vol.43, No.5, 467-484 (2011).

[81] Kumar A., Sharma D., Deb K.: “A hybrid multi-objective optimization procedure using PCX based NSGA-II and sequential quadratic programming”, Transactions of the IEEE Congress on Evolutionary Computation (CEC’07), 3011-3018 (2007).

[82] Lara A., Sanchez G., Coello Coello C.A., Schütze O.: “HCS: A new local search strategy for memetic multiobjective evolutionary algorithms”, IEEE Transactions on Evolutionary Computation, Vol.14, No.1, 112-132 (2010).

[83] Rigoni E., Poles S.: “NBI and MOGA-II, two complementary algorithms for multi-objective optimizations”, Practical Approaches to Multi-Objective Optimization, Internationales Begegnungs- und Forschungszentrum für Informatik (IBFI), Schloss Dagstuhl, Germany, http://citeseerx.ist.psu.edu/viewdoc/summary?doi=10.1.1.89.6798 (2005).

[84] Eiben, A.E. and Smith, J.E.: “Introduction to evolutionary computing”, Springer (2003).

[85] Back, T., Fogel, D.B. and Michaelwicz, Z.: “Handbook of evolutionary computation”, IOP Publishing (1997).

[86] Vasile, M., Locatelli, M.: “A hybrid multiagent approach for global trajectory optimization” Journal of Global Optimization, Vol.44, No.4, 461-479 (2009).

[87] Vasile, M., Minisci, E., Locatelli, M.: “An inflationary differential evolution algorithm for space trajectory optimization”, IEEE Transactions on Evolutionary Computation, Vol.15, No.2, 267-281 (2001).

[88] Laumanns, M. and Thiele, L. and Deb, K. and Zitzler, E.: “Combining Convergence and Diversity in Evolutionary Multiobjective Optimization”, Evolutionary computation, Vol.10, No.3, 263-282 (2002).

[89] Schütze, O., Laumanns, M., Tantar, E., Coello, C.A.C., Talbi, E.G.: “Computing gap free Pareto front approximations with stochastic search algorithms”, Evolutionary Computation, Vol.18, No.1, 65-96 (2010).

[90] Zhang, Q., Suganthan, P.N.: “Final report on CEC’09 MOEA competition”, IEEE Congress on Evolutionary Computation (CEC'09) (2009).

[91] Zhang, Q., Zhou, A., Zhao, S., Suganthan, P.N., Liu, W., Tiwari, S., “Multiobjective optimization test instances for the CEC 2009 special session and competition”, Technical Report of the Special Session on Performance Assessment of Multi-Objective

Optimization Algorithms, University of Essex, Colchester, UK and Nanyang Technological University, Singapore (2008).

[92] Zitzler, E. and Thiele, L. and Laumanns, M. and Fonseca, C.M. and da Fonseca, V.G.: "Performance assessment of multiobjective optimizers: An analysis and review", IEEE Transactions on Evolutionary Computation, Vol.7, No.2, 117-132 (2003).

[93] Minisci, E.A., Avanzini, G.: "Orbit transfer manoeuvres as a test benchmark for comparison metrics of evolutionary algorithms", Transactions of the IEEE Congress on Evolutionary Computation (CEC'09), 350-357 (2009).

[94] Vasile, M., Minisci, E., Locatelli, M.: "Analysis of Some Global Optimization Algorithms for Space Trajectory Design", Journal of Spacecraft and Rockets, Vol.47, No.2, 334-344 (2010).

[95] Tseng, L.Y., Chen, C.: "Multiple trajectory search for unconstrained/constrained Multi-Objective optimization", Transactions of the IEEE Congress on Evolutionary Computation (CEC'09), 1951-1958 (2009).

[96] Liu, M., Zou, X., Chen, Y., Wu, Z.: "Performance assessment of DMOEA-DD with CEC 2009 MOEA competition test instances", Transactions of the IEEE Congress on Evolutionary Computation (CEC'09), 2913-2918 (2009).

[97] Leary, R.H.: "Global Optimization on funneling landscapes", Journal of Global Optimization, Vol.18, No.4, 367-383 (2000).

[98] Battin, R.H.: "An introduction to the mathematics and methods of astrodynamics", AIAA Education Series (1987).

[99] Holmes, M. H.: Introduction to the foundations of applied mathematics, Springer (2009).

[100] Sanders, J.J.A., Verhulst, F., Murdock, J.A.: Averaging methods in nonlinear dynamical systems, Springer (2007).

[101] Carlson, B.C.: "Computing elliptic integrals by duplication", Numerische Mathematik, Vol.33, No. 1, 1-16 (1979).

[102] Hahn, G.D.: "A modified Euler method for dynamic analyses", International Journal for Numerical Methods in Engineering, Vol.32, No.5, 943-955, (1991).

[103] Prince, P.J., Dormand, .J.R.: "High order embedded Runge-Kutta formulae", Journal of Computational and Applied Mathematics, Vol.7, No.1, 67-75, Elsevier (1981).

[104] Vasile M. Bernelli-Zazzera F.: "Optimizing Low-Thrust and Gravity Assist Manoeuvres to Design Interplanetary Trajectories", The Journal of the Astronautical Sciences, Vol.51, No.1, January-March (2003).

[105] Gill, P.E., Murray, W., Saunders, M.A.: “SNOPT: An SQP algorithm for large-scale constrained optimization”, SIAM Journal on Optimization, Vol.12, No.4, 979-1006 (2002).

[106] Colombo, C. and McInnes, C.: “Orbital Dynamics of "Smart-Dust" Devices with Solar Radiation Pressure and Drag”, Journal of Guidance, Control and Dynamics, Vol. 34, No. 6, 1613-1631 (2011).

[107] Escobal, P.: “Methods of Orbit Determination”, New York, John Wiley and Sons (1965).

[108] Vallado, D.A.: “Fundamentals of Astrodynamics and Applications”, 3rd edition, Space Technology Library, Springer (2007).

[109] Tarzi, Z, Speyer, J., Wirz, R.: Fuel optimum low-thrust elliptic transfer using numerical averaging, Acta Astronautica, Vol. 86, 95-118 (2013).

[110] Colombo C., Lücking C. and McInnes C. R.: "Orbital dynamics of high area-to-mass ratio spacecraft with J_2 and solar radiation pressure for novel Earth observation and communication services", Acta Astronautica, Vol. 81, No. 1, 137–150 (2012).

[111] Lücking C., Colombo C., and McInnes C. R.: “A passive satellite deorbiting strategy for Medium Earth Orbit using solar radiation pressure and the J_2 effect”, Acta Astronautica, Vol. 77, Aug.–Sept. 2012, 197-206 (2012).

[112] Lücking C., Colombo C., and McInnes C. R.: “Solar Radiation Pressure-Augmented Deorbiting: Passive End-of-Life Disposal from High-Altitude Orbits”, Journal of Spacecraft and Rockets, Vol. 50, No. 6, 1256-1267 (2013).

[113] Kessler, D.J., Johnson, N.L., Liou, J.C. and Matney, M.: “The Kessler Syndrome: Implications to Future Space Operations”, Proceedings of the 33rd Annual American Astronautical Society, Rocky Mountain Section, Guidance and Control Conference, 6-10 (2010).

[114] Committee on Peaceful Uses of Outer Space (COPOUS), Scientific and technical sub-committee, Working group on Space debris: Progress report of the working group on space, U.N. Doc. A/AC.105/C.1/L.284 (2006).

[115] Inter-Agency Space Debris Coordination Committee: “IADC space debris mitigation guidelines”, revision 1, (2007).

[116] Bischof, B., Kerstein, L., Starke, J., Guenther, H., Foth, W. et al.: “Roger-Robotic geostationary orbit restorer”, Proceedings of the 8th ESA Workshop on Advanced Space Technologies for Robotics and Automation, The Netherlands (2004).

[117] Phipps, C.R. and Reilly, J.P.: “ORION: Clearing near-Earth space debris in two years using a 30-kW repetitively-pulsed laser”, Proceedings-SPIE The International Society for Optical Engineering, 728-731 (1997).

[118] Vasile, M., Maddock, C. and Saunders, C.: “Orbital debris removal with solar concentrators”, 61st International Astronautical Congress (IAC 2010), Prague, Czech Republic (2010).

[119] Bombardelli, C., Herrera, J., Iturri, A., and Pelaez, J.: “Space Debris Removal with Bare Electrodynamic Tethers”, Proceeding of the 20th AAS/AIAA Spaceflight Mechanics Meeting, San Diego, California, USA (2010).

[120] Lücking, C., Colombo, C., McInnes, C.: “A passive high altitude deorbiting strategy”, 25th Annual IAA/USU Conference on Small satellites (2011).

[121] Bombardelli, C. and Pelàez, J.: “Ion Beam Shepherd for Contactless Space Debris Removal”, Journal of Guidance, Control, and Dynamics, Vol. 34, No. 3 (2008).

[122] Ruault, J.M., Desjean, M.C., Bonnal, C. and Bultel, P.: “Active Debris Removal (ADR): From identification of problematics to in flight demonstration preparation”, 1st European Workshop on Active Debris Removal (2010).

[123] Kitamura, S.: “Large Space Debris Reorbiter using Ion Beam Irradiation”, 61st International Astronautical Congress (IAC 2010), Prague, Czech Republic, Paper IAC-10.A6.4.8 (2010).

[124] Liou, J.C. and Johnson, N.L.: “A sensitivity study of the effectiveness of active debris removal in LEO”, Acta Astronautica, Vol. 64, No. 2-3, 236-243 (2009).

[125] McAdams, J.V., Dunham, D.W., Mosher, L.E., Ray, J.C., Antreasian, P.G., Helfrich, C.E., Miller, J.K.: “Maneuver history for the NEAR mission—launch through Eros orbit insertion”, Proceedings of the AIAA/AAS Astrodynamics Specialist Conference, Paper AIAA-2000-4141 (2000).

[126] Glassmeier, K.H., Boehnhardt, H., Koschny, D., Kührt, E., Richter, I.: “The Rosetta mission: flying towards the origin of the solar system”, Space Science Review, Vol. 128, No. 1–4, 1–21 (2007).

[127] Rayman, M., Varghese, P., Lehman, D., Livesay, L.: “Results from the Deep Space 1 technology validation mission”, Acta Astronautica, Vol. 47, No. 2, 475–487 (2000).

[128] Hampton, D., Baer, J., Huisjen, M., Varner, C., Delamere, A., Wellnitz, D., A’Hearn, M., Klaasen, K.: “An overview of the instrument suite for the deep impact mission”, Space Science Review, Vol. 117, No. 1–2, 43–93 (2005).

[129] Jet Propulsion Laboratory, Near Earth Object Program, http://neo.jpl.nasa.gov/neo/groups.html (2014). Accessed 26 January 2014.

[130] "Project Icarus", MIT Press, Cambridge, MA (1968).

[131] Smith, P.L., Barrera, M.J. et al.: "Deflecting a Near Earth Object with Today's Space Technology", AIAA planetary Defense Conference, Orange County, CA, AIAA Paper 2004-1447 (2004).

[132] McInnes, C.: "Deflection of Near-Earth Asteroids by Kinetic Energy Impacts from Retrograde Orbits", Planetary and Space Science, Vol. 52, No. 7 (2004).

[133] Scheeres, D.J., Schweickart, R.L.: "The Mechanics of Moving Asteroids", AIAA planetary Defense Conference, Orange County, CA, AIAA Paper 2004-1447 (2004).

[134] Lu, E.T., Love, S.G.: "Gravitational Tractor for Towing Asteroids", Nature, Vol. 438 (2005).

[135] Melosh, H.J., Nemchinov, I.V., Zetzer, I.I.: "Non-nuclear Strategies for Deflecting Comets and Asteroids", Hazards Due to Comets and Asteroids, Univ. of Arizona (1994).

[136] Campbell, J.W., Phipps, C., Smalley, L., Reilly, J., Boccio, D.: "The Impact Imperative: Laser Ablation for Deflecting Asteroids, Meteoroids, and Comets from Impacting the Earth", AIP Conference Proceedings, Vol. 664 (2003).

[137] Olds, J., Charania, A., Schaffer, M.G.: "Multiple Mass Drivers as an Option for Asteroid Deflection Missions", 2007 Planetary Defense Conference, Washington, D.C., Paper 2007 S3-7 (2007).

[138] Spitale, J.N.: "Asteroid Hazard Mitigation using the Yarkovsky Effect", Science, Vol. 296, No. 5565, (2002).

[139] Phipps, C.: "Laser Deflection of NEO's", Report of the NASA Near-Earth-Object Interception Workshop, January 14-16 (1992).

[140] Phipps, C.: "Laser Deflection of near Earth asteroids and comet nuclei", Proceedings of the International conference on Lasers 96 (1997).

[141] Phipps, C.: "Can Lasers play a role in Planetary Defense?", AIP Conference Proceedings 1278, 502-508 (2010).

[142] Park, S.Y., Mazanek, D.D.: "Deflection of Earth-crossing asteroids/comets using rendezvous spacecraft and laser ablation", Journal of Astronautical Sciences, Vol. 53, No. 1, 21-37 (2005).

[143] Maddock, C.A., Vasile, M.: "Design of optimal spacecraft-asteroids formation through a hybrid global optimization approach", International Journal of Intelligent Computing and Cybernetics, Vol. 1, No. 2 (2008).

[144] Vasile, M., Maddock, C.A., Summerer, L.: "Conceptual design of a multi-mirror system for asteroid deflection", 27th International Symposium on Space Technology and Science (2009).

[145] Vasile M., Maddock C., Radice G., McInnes C.: "NEO Deflection though a Multi-Mirror System", ESA Call for Proposals: Encounter 2029, Final Report for Ariadna Study Contract 08/4301, Technical officer: Summerer L. (2009).

[146] Gibbings, A., Vasile, M., Hopkins, J.M., Burns, D., Watson, I.: "Exploring and Exploiting Asteroids with Laser Ablation", UK Space Conference, Warwick, UK, 4th-5th July (2011).

[147] Gibbings, A., Vasile, M., Hopkins, J.M., Burns, D.: "On testing Laser ablation processes for asteroid deflection", 2011 IAA Planetary Defence Conference, Bucharest, Romania, 9-12th May (2011).

[148] Vasile, M. and Croisard, N.: "Robust Preliminary Space Mission Design under Uncertainty", Computational Intelligence in Expensive Optimization Problems, 543-570, Springer (2010).

[149]Vasile, M. and Colombo, C.: "Optimal impact strategies for asteroid deflection", Journal of Guidance, Control, and Dynamics, Vol. 31, No. 4 (2008).

[150] Vasile, M. and Maddock, C.A.: "On the deflection of asteroids with mirrors", Celestial Mechanics and Dynamical Astronomy, Vol. 107, No. 1, 265-284 (2010).

[151] Vasile, M., Maddock, C., and Radice, G.: "Mirror formation control in the vicinity of an asteroid", AIAA/AAS Astrodynamics Specialist Conference and Exhibit, 18-21 August 2008, Honolulu, Hawaii (2008).

[152] Kahle, R., Kuhrt, E., Hahn, G., Knollenberg, J.: "Physical limits of solar collectors in deflecting Earth-threatening asteroids", Aeropace science and technology, Vol. 10, No. 3 (2006).

[153] Wertz, J.R. and Larson, W.J.: "Space mission analysis and design", Microcosm (1999).

[154] Britt, D.T., Yeomans, D., Housen, K. and Consolmagno, G.: "Asteroid Density, Porosity, and Structure, Asteroids III", Vol. 1, 485-500 (2002).

[155] Pieters, C.M. and McFadden, L.A.: "Meteorite and Asteroid Reflectance Spectroscopy: Clues to Early Solar System Processes", Annual Review of Earth and Planetary Sciences, Vol. 22, 457-497 (1994).

[156] Price, S.D.: "The surface properties of asteroids, Advances in Space Research", Vol. 33, No. 9, 1548-1557, Elsevier (2004).

[157] Oberkampf, W., Helton, J.: "Investigation of Evidence Theory in Engineering Applications", AIAA-Paper 2002-1569 (2002).

[158] Vasile, M., Minisci, E., Zuiani, F., Komninou, E., Wijnands, Q.: "Fast Evidence-based Systems Engineering", Paper IAC-11.D1.3.3, 62nd International Astronautical Congress, Cape Town, South Africa, 3rd-7th October (2011).

[159] Lane, M.T.: "On analytic modeling of lunar perturbations of artificial satellites of the earth", Celestial Mechanics and Dynamical Astronomy, Vol. 46, No.4, 287-305 (1989).

[160] Luu, K., Sabol, C.: "Effects of perturbations on space debris in supersynchronous storage orbits", AFRL-VS-PS-TR-1998-1093, Air Force Research Laboratory (1998).

[161] Klir, G.J., Smith, R.M.: "On Measuring Uncertainty and Uncertainty-Based Information: Recent Developments", Annals of Mathematics and Artificial Intelligence, Vol. 32, No. 1-4 (2001).

[162] Agarwal, H., Renaud, J.E., Preston, E.L. and Padmanabhan, D.: "Uncertainty quantification using evidence theory in multidisciplinary design optimization", Reliability Engineering & System Safety, Vol. 85, No. 1, 281-294, Elsevier (2004).

[163] Beyer, H.G. and Sendhoff, B.: "Robust optimization--a comprehensive survey", Computer methods in applied mechanics and engineering, Vol. 196, No. 33, 3190-3218, Elsevier (2007).

[164] Vasile, M. and Croisard, N:: "Robust Preliminary Space Mission Design under Uncertainty", Computational Intelligence in Expensive Optimization Problems, 543-570, Springer (2010).

[165] Helton, J.C.: "Uncertainty and sensitivity analysis in the presence of stochastic and subjective uncertainty", Journal of Statistical Computation and Simulation, Vol. 57, No. 1-4, 3-76 (1997).